TUDelft

Delft University of Technology

Spinful Andreev States in Superconducting Circuits

Wesdorp, J.J.

Important note
To cite this publication, please use the final published version (if applicable).
Please check the document version above.

SPINFUL ANDREEV STATES IN SUPERCONDUCTING CIRCUITS

Jaap Joachim Wesdorp
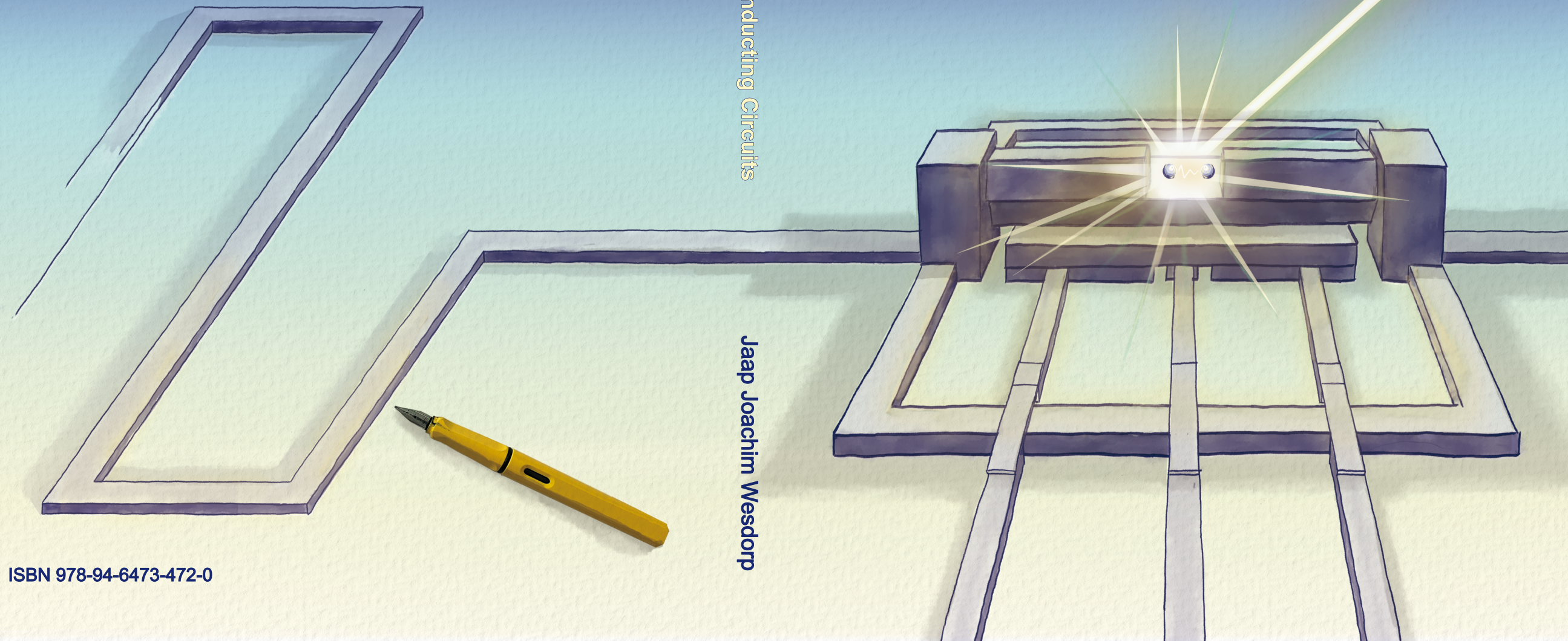
Spinful Andreev States in Superconducting Circuits

Spinful Andreev States in Superconducting Circuits

Proefschrift

ter verkrijging van de graad van doctor
aan de Technische Universiteit Delft,
op gezag van de Rector Magnificus prof. dr. ir. T.H.J.J. van der Hagen,
voorzitter van het College voor Promoties,
in het openbaar te verdedigen
op vrijdag 26 april 2024 om 10.00 uur

door

Jaap Joachim WESDORP

Master of Science in Applied Physics,
Technische Universiteit Delft, Nederland,
geboren te Columbia, Verenigde Staten.

Dit proefschrift is goedgekeurd door de

promotor: Prof. ir. L.P. Kouwenhoven
copromotor: Dr. C.K. Andersen

Samenstelling promotiecommissie:

Rector Magnificus,	voorzitter
Prof. ir. L.P. Kouwenhoven,	Technische Universiteit Delft, Nederland
Dr. C.K. Andersen,	Technische Universiteit Delft, Nederland

Onafhankelijke leden:

Dr. A. Chatterjee,	Technische Universiteit Delft, Nederland
Prof. dr. V. Fatemi,	Cornell University, United States of America
Prof. dr. A.L. Yeyati ,	Universidad Autónoma de Madrid, España
Prof. dr. ir. Y.M. Blanter,	Technische Universiteit Delft, Nederland

Andere leden:

Dr. ir. G. de Lange,	Microsoft Research, Nederland

Reserve leden:

Prof. dr. ir, L.M.K Vandersypen	Technische Universiteit Delft, Nederland

Contents

Summary

The growing understanding of the physics of superconductor-semiconductor nanostructures is a key driver for the development of emerging quantum technologies. The elementary excitations of these hybrid nanostructures are Andreev bound states. To further our knowledge about their intricate physics, new tools must be used to study them. This thesis describes the use of magnetic-field compatible superconducting circuits to study and manipulate Andreev bound states and their spin in hybrid superconducting-semiconducting nanowire Josephson junctions.

First, we provide an introduction to the physical models describing Andreev bound states in superconducting circuits and the general methodology used for the circuit design, device fabrication and experimental setups in the experiments of this work.

We then move on to an initial set of two experiments in Chapters 4 and 5, where we inductively shunt a superconducting resonator with a nanowire-based radio-frequency superconducting quantum interference device (rf-SQUID). This allows us to study Andreev bound states in InAs/Al nanowire Josephson junctions using circuit quantum electrodynamics techniques under various external conditions.

In Chapter 4 we use pulsed detection of Andreev bound state parity to demonstrate parity selective spectroscopy. The main result of this Chapter was the discovery of microwave-induced parity polarization, that allows one to set the bound state parity in-situ using microwave pulses. We then study the evolution of the microwave spectrum of Andreev bound states in a magnetic field in Chapter 5. Here we find a multitude of phenomena that arise because of the rich interplay between spin-orbit coupling, the Zeeman effect, superconductivity, and electron-electron interactions. We observe evidence of spin-polarizing microwave transitions, the anomalous Josephson effect, and transitions involving triplet Andreev spins.

In Chapter 6 we explore an alternative material and junction fabrication method in combination with the same circuitry. Specifically, we excite Andreev bound states in InSb/Al Josephson junctions defined by shadow-wall lithography. We observe low density, high-transparency Andreev bound states in a range of devices and reproduce the directly spin-polarizing microwave transition observed in Chapter 5. The results of this Chapter demonstrate the viability of combining hybrid circuit quantum electrodynamics with advanced material combinations and fabrication geometries.

In the final experiment, Chapter 7, we move back to InAs/Al based junctions. This Chapter uses previous results from Chapter 5 and works demonstrating the use of a single superconducting spin as a quantum bit, as a stepping stone. Here, we embed two superconducting spin qubits in a single SQUID and demonstrate strong longitudinal coupling between them over a distance much larger than their wavelengths.

The results and methods developed in this dissertation pave the way for continued exploration of the intricating physics of superconducting spins and demonstrate early steps towards their use as a new platform for quantum computing.

Samenvatting

Het groeiende begrip van de fysica van supergeleider-halfgeleider nanostructuren is een belangrijke motor voor de ontwikkeling van opkomende kwantumtechnologieën. De elementaire excitaties van deze hybride nanostructuren zijn Andreev toestanden. Om onze kennis over hun ingewikkelde fysica te vergroten, moeten nieuwe hulpmiddelen worden gebruikt om ze te bestuderen. In dit proefschrift bestuderen we Andreev toestanden en hun spin in hybride supergeleider-halfgeleider nanodraad Josephson juncties. Dit doen we met behulp van supergeleidende circuits die functioneren in een magnetisch veld.

We beginnen we met een inleiding tot de fysieke modellen die Andreev toestanden in supergeleidende circuits beschrijven, en vervolgen met de algemene methodiek die gebruikt wordt voor het ontwerpen van de circuits, de fabricage ervan en het opzetten van de meetopstellingen. Vervolgens gaan we verder met een eerste reeks van twee experimenten in Hoofdstuk 4 en 5. Hierin aarden we een supergeleidende resonator via een radiofrequentie supergeleidend kwantuminterferentieapparaat (rf-SQUID. *eng*) dat een In-As/Al nanodraad bevat met een Josephson junctie. Dit maakt het mogelijk om Andreev toestanden in zo'n draad te bestuderen met behulp van circuit kwantumelektrodynamica technieken onder verschillende externe omstandigheden.

In Hoofdstuk 4 detecteren we de pariteit van Andreev toestanden met microgolfpulsen. Dit gebruiken we om spectroscopie te demonstreren die selectief is voor een bepaalde pariteit van de Andreev toestanden. Het belangrijkste resultaat van dit Hoofdstuk was de ontdekking van de mogelijkheid tot polarisatie van de pariteit door microgolfpulsen. In Hoofdstuk 5 bestuderen we de evolutie van het microgolfspectrum van Andreev toestanden in een magnetisch veld. Hier vinden we een groot aantal verschijnselen die ontstaan als gevolg van het rijke samenspel tussen spin-baankoppeling, het Zeemaneffect, supergeleiding en elektron-elektron-interacties. We meten tekenen van spin-polariserende microgolftransities, het afwijkende Josephson-effect en microgolftransities waarbij triplet Andreev-spins betrokken zijn.

In Hoofdstuk 6 onderzoeken we het gebruik van een junctie fabricagemethode met alternatieve materialen in combinatie met dezelfde circuits. We exciteren Andreev toestanden in InSb/Al Josephson-juncties gedefinieerd door schaduwmuurlithografie. We meten Andreev toestanden met lage dichtheid en hoge transparantie in een reeks verschillende apparaten en reproduceren een directe Andreev-spin polariserende microgolftransitie uit het vorige Hoofdstuk. De resultaten van dit Hoofdstuk tonen de haalbaarheid aan van het combineren van hybride circuit kwantumelektrodynamica met geavanceerde materiaalcombinaties en fabricagegeometrieën.

In het laatste experiment, Hoofdstuk 7, gaan we terug naar op InAs/Al gebaseerde juncties. Als basis voor dit Hoofdstuk gebruiken we de resultaten uit Hoofdstuk 5 en werken die de mogelijkheid aantoonden een enkele supergeleidende spin als qubit te manipuleren. In dit experiment plaatsen we twee supergeleidende spin qubits in een enkele SQUID.

Hierdoor kunnen we een sterke longitudinale koppeling tussen hen aantonen over een afstand die veel groter is dan hun golflengte.

De resultaten en methoden die in dit proefschrift zijn ontwikkeld, maken de weg vrij voor verdere verkenning van de ingewikkelde fysica van supergeleidende spins en zetten eerste stappen in de richting van hun gebruik als nieuw platform voor kwantumcomputers.

1

1

Introduction

Ik heb het nog nooit gedaan, dus ik denk dat ik het wel kan.

Famous misquote from Astrid Lindgren's Pippi Longstocking

1

1.1 The search for qubit universalis

The practical goal of doing physics is to figure out a way to accurately describe the world around us. A solely mathematical description is not sufficient, nor is it practical. We want to use the description to predict what will happen if we do something, and preferably we want to know this fast, such that we can test many different variations of inputs and observe the outputs they will generate.

This simulation of various inputs is currently done on computers capable of extremely fast calculations functioning well for most purposes. However, there are some limitations to this approach. A bit more than forty years ago, Richard Feynmann posed a now famous challenge titled: "Simulating Physics with Computers" (Feynman, 1982). He argued that it is impossible to find a computer as we know them, to simulate quantum mechanical systems properly. And since the world around us comprises of those systems, he suggested: "Can you do it with a new kind of computer - a quantum computer?". For example, using bits to store the state of 50 spin 1/2 particles would require 2^{50} numbers, which becomes practically impossible if the number of particles grows beyond this. Thus, it would be interesting if we can make and control quantum bits (qubits), that are the spin 1/2 particles themselves, as computation elements. In this way, the number of required components scales proportionally to the problem size, and the time required for simulation polynomially (Lloyd, 1996). Although this merely guarantees that computation times won't explode indefinitely, figuring out whether it is possible make such a computer in practise, has been a long standing goal for quantum-physicists and engineers.

So, how do we make such a quantum bit, and what do we make it of? This is an open question and also the underlying motivation of the work in this thesis. Given the extreme success in the scaling of lithographically defined semiconductor based electronics of the last decades, we focus on quantum bits that can be defined using existing lithography techniques. Currently, one the widespread variant of these type of quantum bits are those defined in millimeter-sized circuits made of superconducting material (superconducting qubits). Another popular method is to trap single electrons in a tiny semiconducting box on the size less than a millionth of a meter and use their spin as a bit (spin-qubits). Only recently it became possible to make bits this way, for example, the first superconducting qubits were made in 1999 (Nakamura et al., 1999) and also here in Delft in the group of Hans Mooij (Chiorescu et al., 2003). Note that these "bits" could only hold their information stored for about 1-billionth of a second!

Fast forwarding to present day, we currently are in the so-called "noisy intermediate scale quantum computing era" (NISQ) (Preskill, 2018), with, for superconducting qubits, a number around 100-1000 qubits on the same chip, and some of which have been able to keep their information up to a millisecond. This is a remarkable improvement of a factor of one million in twenty years for this type of qubit. Similar to classical bits, error correcting codes can be used to sacrifice qubit numbers for lifetime or operation quality (Shor, 1995).

NISQ systems have reached a point, where with currently known methods, days of the best available supercomputing time is needed to simulate the output of about 20 layers of operations on such devices (AI, 2019), taking about 10 minutes to generate. However, doing truly useful calculations, besides offering a lot of new insights purely from a physics researcher perspective, has remained out of reach (Preskill, 2023).

There are two ways to perform simulation with quantum bits: *analog* and *digital* quan-
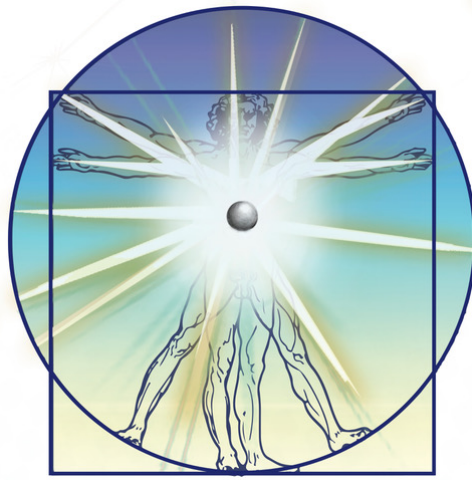
Figure 1.1: **The search for qubit universalis.** Artist impression of the current effort towards finding the qubit-equivalent of homo-universalis, based on the sketch of vitruviusman by Leonardo da Vinci.

tum simulation. The first can be seen as building a well-controlled toy model of some specific system of interest and letting it evolve for some time in order to observe what comes out, similar as using a windtunnel to simulate aerodynamics. It appears that, already now, real-world examples of such simulators exist that can perform practically relevant simulations[1] (Daley et al., 2022).

The second, relies on slicing the evolution of the system into small time steps, where each step can be approximated using error-corrected circuits (Aspuru-Guzik et al., 2005). This has the advantage that an arbitrary system can be simulated, very similar to current computers, but potentially comes at the cost of a large computation overhead.

To provide an example, estimates exist that for calculating the ground state energy of the molecular structure of FeMoCo, a molecule relevant in the Haber-Bosch process for nitrogen fixation, on a digital quantum simulator, can pessimistically cost several millions of physical qubits if the error rate of each qubit is around 0.1% per operation (Lee et al., 2021). This estimate is based on using a specific type of error correcting code (Fowler et al., 2012). The number of required physical qubits for solving such a problem, depends on the qubit quality, hence there is an active search for qubits that are "intrinsically better".

Here not only the time such a bit can retain it's state is relevant, but it should satisfy other important criteria as well regarding addressability, connectivity, scalability and compatibility with error correcting codes (DiVincenzo, 2000; Fowler et al., 2012; Bravyi et al., 2024). Thus, a relevant goal is to find clever tricks, improvements to existing qubit architectures, or new qubit types, to obtain a "qubit universalis" (see Figure 1.1), for example by improving addressability and connectivity without sacrifing qubit lifetime or scalability. One way to address this is to investigate currently unknown physical phenomena that

---

[1]Note that the main current platforms to perform analog quantum simulations have not been mentioned so far, such as trapped ions, neutral atoms in optical lattices and atom arrays with Rydberg lattices (Daley et al., 2022).

1

could potentially aid towards this goal, which is how the contents of this thesis can be seen in practise.

1.2 Thesis outline

In this thesis, we use superconducting microwave circuits as a detector to study Andreev bound states that reside in Josephson junctions between two sections of hybrid semiconductor - superconductor nanowires in presence of magnetic field, spin-orbit coupling and electron-electron interactions. Andreev bound states lie at the heart of the Josephson effect and are the elementary excitations of hybrid semiconductor - superconductors, which have been predicted as building blocks for a topologically protected qubit (Kitaev, 2001; Lutchyn et al., 2010; Oreg et al., 2010) - a key component in the Microsoft led effort towards building more resource efficient scalable quantum computers (Karzig et al., 2017). By applying a magnetic field we allow investigation into the Andreev bound state spin (Lee et al., 2014; van Woerkom et al., 2017).

The use of circuit-quantum electrodynamics (circuit-QED) techniques, benefitting from developments for superconducting qubits (Blais et al., 2004), has led to high-resolution detection of spinless transitions between Andreev states in atomic break junctions (Janvier et al., 2015) and also in hybrid nanowires (Hays et al., 2018). Two exciting experiments were published during the start of this thesis (Tosi et al., 2019; Hays et al., 2020), which showed that the attainable resolution ($< 1\,\mu\text{eV}$) of circuit-QED techniques allowed to distinguish transitions between zero-field spin-split Andreev states in long nanowires with spin-orbit coupling. In parallel, magnetic field compatible circuits (Kroll et al., 2019; Samkharadze et al., 2016) were developed in combination with superconducting "gatemon" qubits that had hybrid semiconducting - superconducting nanowire Josephson junctions (de Lange et al., 2015; Larsen et al., 2015; Luthi et al., 2018; Kringhøj et al., 2021). The combination of these results, amongst others, served as a stepping stone for the chapters described below, aimed at detecting and manipulating spinful Andreev states in superconducting circuits.

In **Chapter 2**, we explain the basics of superconductivity, Andreev bound states, their microwave absorption, and provide a simple picture of their coupling to superconducting circuits. We then move on in **Chapter 3** to explain the methodology and design process of the circuits used in this thesis, as well as various aspects related to fabrication and magnetic field control. The Chapter concludes with an explanation of our data-processing procedure.

In **Chapter 4** we use a superconducting resonator galvanically shunted by a radio-frequency superconducting quantum interference device (rf-SQUID) to inductively measure time domain dynamics of the fermion parity of Andreev bound states in an InAs/Al nanowire Josephson junction. We then show that we can polarize this parity in-situ using a strong microwave drive.

In **Chapter 5**, in the same device, we apply a magnetic field to detect transitions between various spinful Andreev states. We observe transitions involving a spin-flip within a single bound state manifold, as well as transitions involving pairs of singlet and triplet spins and conclude with a measurement of a gate-tunable anomalous Josephson effect. We find that both spin-orbit coupling and electron-electron are important ingredients required to model these devices.

In **Chapter 6**, motivated by recent successes with shadow-wall lithographically defined Josephson junctions in InSb/Al (Badawy et al., 2019; Heedt et al., 2021), we exchange the InAs/Al nanowire Josephson junction for such a device and measure high-transparency ABS over extended gate-ranges. By applying a magnetic field, we reproduce the direct spin-flip transition observed in Chapter 5.

In **Chapter 7** we implement a proposal by Padurariu and Nazarov (2010), and build a circuit to couple two superconducting spin qubits separated by a distance of approximately 25 μm. We find strong longitudinal coupling between the two spin qubits. In this chapter, we use a different device design compared to the preceding Chapters and switch to embed the nanowire SQUID in a transmon qubit[2].

Finally, in **Chapter 8** we discuss highlights of the results of the previous Chapters and provide suggestions for future work.

---

[2]This is motivated by the requirement of achieving strong coupling between the nanowire Josephson junctions, which makes the total SQUID inductance much larger than the preceding Chapters. This in turn would cause the resonator inductance to be dominated by the non-linear inductance of the SQUID loop, effectively making it a transmon.

2

Background

We have a theory of everything only to discover that it has revealed exactly nothing about many things of great importance.

Laughlin and Pines

The process of Andreev reflection and the resulting bound states provide a fundamental microscopic picture of the proximity effect of superconductors and the Josephson effect. It is quite rivetting that after more than 60 years of developments following the original papers by Andreev (1964) and Kulik (1970), their physics is still considered to be state of the art condensed matter research and keeps providing new surprises to those who look at them.

In this Chapter we start with a macroscopic picture of superconductivity in Section 2.1 to describe the basic physics required to understand superconducting circuits in magnetic fields. Later, in Section 2.2 we will switch to a microscopic picture of superconductivity and attempt to illustrate the physics of Andreev bound states in a "realistic" scenario, which includes the presence of multiple transport channels, spin-orbit coupling, magnetic fields and finally touch upon the effect of interactions. The combination of the first three components makes a general analytical description intractable so we provide along the way a microscopic numerical toy model. Unfortunately the inclusion of electron-electron interactions additionally greatly increases computational complexity for numerical methods, so we resolve to a brief overview of the effect of interactions, which can provide important qualitative insights required to explain the measured data in Chapter 5. Finally in Section 2.3 we describe the theory of embedding a Josephson junction in a superconducting circuit.

2.1 Superconductivity

Superconductivity was discovered 1911 by Heike Kamerlink Onnes in Leiden. Later, the discovery of perfect diamagnetism by Meissner and Ochsenfeld (1933), led to the London brothers writing down a phenomenological theory of the electromagnetic properties of superconductors (London et al., 1935) that could account for this observation. In 1950 Ginzberg and Landau developed an intuitive picture of superconductivity for non-homogeneous superconductors (Ginzburg, 2009).   Pippard (1953) then suggested a non-local version of the London equations using the concept of a coherence length ξ in order to explain the strong effects that impurities could have on the extracted penetration depths of electric and magnetic fields according to the London equations. It was only in 1957 that Bardeen Cooper and Schrieffer (Bardeen et al., 1957) managed to write down a successful microscopic theory of superconductivity (BCS theory) of which the key concepts are summarized below following the books by Tinkham (2015), de Gennes (1999) and Annett (2011). [1]

A material reaches a superconducting state when the free-energy of a fraction of the electrons in a small band around the Fermi energy can be reduced significantly by condensing into Cooper pairs. These Cooper pairs are a result of an attractive interaction between two electrons by lattice phonons and cause the key characteristics of a superconductor: zero resistance to current, an expulsion of magnetic fields from the interior of the conductor (the Meissner effect) and an energy gap of low-energy excitations of a window Δ around the Fermi-level, corresponding to the condensation energy gained from pairing up into Cooper pairs. The Cooper pair condensate forms a macroscopic wavefunction that

---

[1]Tinkham and de Gennes are the classic textbooks. Annett deserves a special mention here because it uses SI units instead of the older Gaussian units, making it a bit more accessible for contemporary physicists.

can retain phase-coherence over distances much longer than the normal state electrons in a metal or semiconductor. As such, before BCS theory was invented Ginzberg-Landau theory was able to describe most effects of superconductivity with a single position dependent complex order parameter $\psi = |\Delta|(\vec{r})e^{i\phi(\vec{r})}$, which in the limit of the temperature close to the critical temperature and variations of the order parameter in space being not too fast, can be exactly related to the condensate wavefunction $|\psi(\vec{r})\rangle$ from BCS theory (Gor'kov, 1959).

There are two important length scales that determine the behaviour of superconductors. The first length scale is the coherence length ξ, which can be seen as the correlation length of the attractive interaction, or the size of a typical Cooper pair, and can be heuristically derived from Heisenbergs uncertainty principle in a region of the superconducting gap Δ around the Fermi energy E_F, i.e. $\delta x \delta p = \hbar$, where $E_F - \Delta < p^2/2m < E_F + \Delta$, yielding

$$\xi \sim \delta x \sim \hbar/\delta p \sim \frac{\hbar v_F}{\pi \Delta}, \tag{2.1}$$

where v_F is the Fermi velocity. The coherence length is affected by scattering in the superconductor (Pippard, 1953), and in presence of strong scattering, this so called dirty limit results in a renormalization of $\xi = \sqrt{\xi_0 l_e} < \xi_0$, where l_e is the elastic scattering length.

Another important length scale is the penetration depth λ, which is the length at which magnetic field lines can penetrate the surface of the superconductor, before being cancelled by dissipationless surface currents. The penetration depth can be found by minimizing the free energy corresponding to the kinetic energy of Cooper pairs participating in the surface current and the potential energy of the magnetic field penetrating that surface volume. The result derived by London (de Gennes, 1999) depends on the phenomenological density of superconducting electrons n_s

$$\lambda_L = \sqrt{\frac{m_e}{\mu_0 n_s e^2}}, \tag{2.2}$$

where μ_0 is the Bohr magneton, m_e the electron mass, e the electron charge and n_s depends on temperature, reaching the normal state electron density at $T = 0$. Note that dependent on the material, temperature and thickness λ can be different than the simple expression for λ_L above and it is expected to increase in the dirty limit.

Based on the length scales ξ and λ superconductors can be divided into two classes, those for which $\xi_0 \ll \lambda$ (type 1) and those for which $\xi_0 \gg \lambda$ (type 2). For both superconductors, after a critical field H_c, superconductivity becomes energetically unfavorable and breaks down. Additionally, when a large enough area is exposed to a perpendicular field that is smaller than the critical field, normal domains that allow flux to penetrate will be formed in both types. The difference between the two is that for type 1 superconductors, the surface energy is positive for creating normal domains, while for type 2 superconductors this is negative. This results in a minimization of the number of normal domains in a type 1 superconductor, while the superconducting domains retain the full Meissner effect (see Figure 2.1a). For Type 2 superconductors, the free energy gain by adding a domain wall is negative, thus as many normal domains are created as is possible to minimize the free energy. The smallest possible normal domains in a type 2 superconductor are those
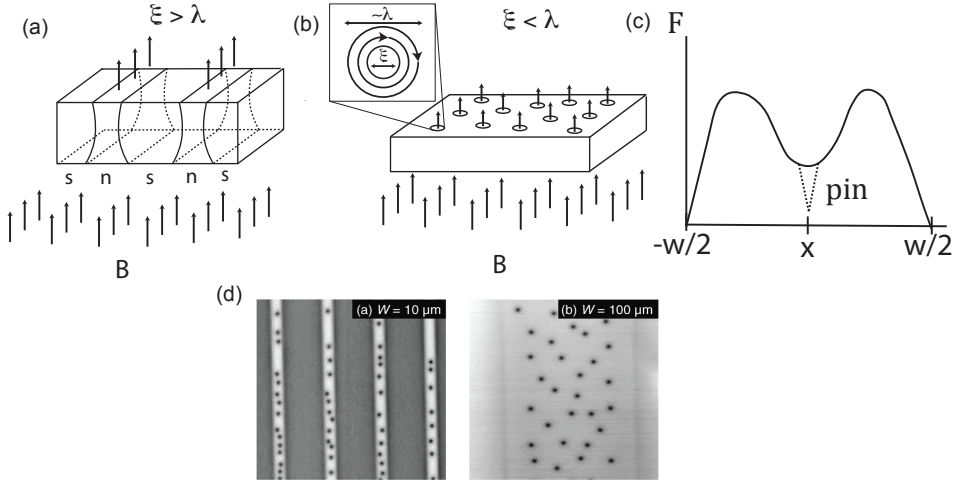
Figure 2.1: **Effect of a perpendicular magnetic field on the two types of superconductors.** (a) Sketch of a Type 1 superconductor where $\xi > \lambda$ and thus the free energy associated with forming a domain wall is positive, minimizing the number of domains. (b) Sketch of a Type 2 superconductor where $\xi < \lambda$, here the energy associated with forming a domain wall is negative and thus as many domain walls as possible are formed resulting in the Abrikosov vortex lattice. Inset shows how supercurrent circulates around a normal vortex core of size $\sim \xi$. (c) Sketch of the free energy landscape of a single vortex in a narrow strip of superconducting wire of width w for an applied magnetic field close to the critical field where a single vortex enters the wire. The dashed line indicates the reduction of free energy if a pinning site is located at the center of the strip x. (d) Illustrative example of real-life vortices in a superconducting wire. Image taken from Ref. (Stan et al., 2004), an experiment where a thin Nb superconducting wire is cooled below T_C under an applied magnetic field, illustrating the creation of vortices measured using scanning Hall probe microscopy.

that allow the minimal amount of one magnetic flux quantum $\Phi_0 = 2 \cdot 10^{-15}$ Wb to penetrate, called vortices (Abrikosov, 1957) because the normal core where the order parameter goes to zero is surrounded by a circulating screening current (Figure 2.1b).

The two superconductors that are used in this work are mainly NbTiN (Type 2) and Al. Al behaves as a type 1 superconductor generally. However, if the thickness of the material is shorter than the bulk coherence length, the coherence length is reduced by surface scattering similar to a superconductor in the dirty limit. Thus, thin film type 1 superconductors can behave as type 2 superconductors, including the possible formation of vortices (Tinkham, 1963; Huebener and Clem, 1974), which were indeed observed in thin aluminum films (Maloney et al., 1972; Song, 2011).

2.1.1 Kinetic inductance

When a film of superconductor becomes thin enough, such that the (superconducting) electron density becomes low, the inductance that comes from the inertia of accelerating Cooper pairs becomes relevant. To see this, let's assume we apply an AC current $I = I_0 \sin(\omega t)$ through a cross section of a volume of area A and length l. This current must be

Material	l_e	ξ	λ	Δ	T_C
NbTiN	~nm	5-10 nm	$\sim 300-400$ nm	1.2-1.5 meV	8-10 K
Al (Bulk)	~μm	1.3 μm	45 nm	180 μeV	1.2 K
Al (~10 nm)	10 nm	~100 nm	>100 nm	250 μeV	1.6 K

2

Table 2.1: The various properties related to superconductivity for the materials used in this thesis. The coherence length quoted for NbTiN is estimated by that observed in NbN and Nb films (Annunziata et al., 2010) and λ estimated in Kroll et al. (2018) for thin NbTiN films as used in this thesis. For bulk Al values are obtained from (de Gennes, 1999), and for thin-film Al λ and ξ are only provided as an estimate. Nevertheless it is expected to increase, while ξ decreases, due to the lower l_e (Tinkham, 2015; López-Núñez et al., 2023). The gap is considered at $T = 0$, with $\Delta(0) = 1.76k_BT_c$ following BCS theory.

carried by a Cooper pair current, such that $I_0 = Aevn_s$ where v is the velocity of the charge carriers and $n_s/2$ is the cooper pair density. These carriers have a total kinetic energy of $E = A \cdot l \cdot n_s \frac{1}{2} m_e v^2$, and thus if the density is lowered, v needs to increase proportionally to keep the same current, but the required energy scales quadratically with v. In other words, in order to generate a fixed current one would need much more energy to accelerate a few charge carriers to high velocity, than many to a low velocity. This increase in the energy stored can be expressed as an inductance by equating the kinetic and inductive energy $A \cdot l \cdot n_s \frac{1}{2} m_e v^2 = \frac{1}{2} L_K I^2$, from which we find (Annunziata et al., 2010)

$$L_K = \frac{m_e l}{e^2 A} \frac{2}{n_s}.$$ (2.3)

Kinetic inductance thus plays a larger role for thin films with low cooper pair density. Typical values that are found in this thesis for 20 nm NbTiN are around 10 pH per square, see Chapter 3.

2.1.2 Vortices

As stated above, vortices arise in type 2 superconductors (Abrikosov, 1957) and can be seen as small tornados of supercurrent which decay exponentially with length scale λ_L away from a normal core of size $\sim \xi$. A schematic is indicated in Figure 2.1b. The total flux penetrating a normal core is the quantized value Φ_0. When an AC current is flowing through the superconductor, vortices feel a Lorentz force of $J \times B$, which induces movement of the core. This provides a complex impedance often described using a two-fluid model (Song, 2011). The real part of the impedance comes from movement of the core of normal electrons, which following the Drude model dissipate energy when moving. The imaginary part of vortices' impedance yields an inductive response.

When embedding superconducting circuits in a magnetic field, the vortex impedance can heavily impact their performance. There are two obvious ways to minimize detrimental effects of vortices. The most straightforward way is to make circuit components that have strong current flowing through them thin, because the required field B_c to nucleate vortices through a square of area A is about a flux quantum, i.e. $\Phi_0 \sim B_c A \sim 2 \, \text{mT} \cdot \text{μm}^2$. Thus by reducing the area per square of a thin conductor to less than a micron, this can be made higher than the typical perpendicular fields applied to the sample during the experiments and thus no vortices can nucleate in those sections. When the area of the supercon-

E	$k_B T$	hf	E_J	I_C	$1/L$
$4\,\mu\text{eV}$	$T = 50\,\text{mK}$	f=1 GHz	1 GHz	2 nA	$(160\,\text{nH})^{-1}$
			$\langle H_A \rangle$	$\dfrac{1}{\varphi_0}\dfrac{d\langle H_A\rangle}{d\varphi}$	$\dfrac{1}{\varphi_0^2}\dfrac{d^2\langle H_A\rangle}{d\varphi^2}$

Table 2.2: Unit conversion for experimentalists. Left side of the double column: three ways to rewrite the same amount of energy in electronvolt, temperature or frequency. Right side: conversion of Josephson energy, Josephson current and Josephson inductance. Each indicated column scales proportionally with the others and φ_0 is the *reduced* flux quantum $\Phi_0/(2\pi)$. Note that L is indicated inversely to indicate that an *increase* in E_J or I_C by a factor of A corresponds to a *decrease* of L by that same factor A.

ducting element cannot be made small, impurities in the material, or artifical pinning sites, can create a free energy minimum for the vortex core to "stick" to shown in Figure 2.1c, thus impeding movement and therefore reducing dissipation. Additionally, sharp corners or edges in the device design can lower the entry barrier of vortices and should thus be avoided in device designs that aim to minimize vortex nucleation (Benfenati et al., 2020).

2.1.3 The Josephson effect

In 1962 (a few years after BCS theory), Brian D. Josephson predicted an effect which was later named after him (Josephson, 1962)[2]. The key thing that he realized was that the phase of the superconducting wavefunction plays a role when two superconductors are in close contact. When they have a different phase, a current between them results from that gradient in phase, and, when a bias voltage is applied over the junction one gets an oscillating phase difference

$$\frac{h}{2e}\frac{d\phi}{dt} = V, \tag{2.4}$$

which can be understood using the Einstein relation between frequency and energy ($\hbar\omega = hd\phi/dt = E = 2eV$), where the factor of 2 comes from the fact that we have a Cooper pair with charge $2e$. Note that the prefactor is equal to the magnetic flux quantum $\Phi_0 = h/2e$.

Relation between Josephson current, inductance and energy

The current flowing through the junction as a function of the phase difference ϕ across the junction can be found semiclassically by noting that the power dissipated is $dE/dt = P = IV$, thus using Equation (2.4) we obtain

$$I = \frac{dE}{dt}\frac{dt}{d\phi}\frac{2e}{h} = \frac{1}{\Phi_0}\frac{dE}{d\phi} = \frac{1}{\varphi_0}\frac{dE}{d\varphi} \tag{2.5}$$

Inductance describes the proportionality between an AC current and voltage $V = LI$, thus using Equation (2.4) again this leads to an expression for the inverse of the inductance

$$L^{-1} = I/V = \frac{1}{\varphi_0^2}\frac{d^2E}{d\varphi^2} \tag{2.6}$$

---

[2]See also Ref. (Anderson, 1970) for an interesting anekdote by Philip. W. Anderson (from the Anderson model) how Josephson found this effect.

These relations are useful especially when replacing E with the expectation value of the energy of a many-body state of interest found by solving a microscopic Hamiltonian H_A of the junction, as discussed later in this chapter. In Table 2.2 we summarize these relations and additionally typical values of units used for fast conversion between energy, temperature, current and inductance, which generally comes in handy when performing experiments. Note that to avoid confusion, for typical long averaged measurements of supercurrent or inductance, for example in DC transport, one should generally think of $\langle H_A \rangle$ as the expectation of the density matrix $\text{Tr}\{H_A \rho\}$, where ρ describes a statistical ensemble of the junction many-body states under a thermal distribution (or non thermal in presence of quasiparticle poisoning!) .

2.2 Andreev reflection and Andreev bound states

In this section I will summarize the key concepts required to understand Andreev states in Section 2.2.1 without lengthy derivations and later in Section 2.2.2 we will explore Andreev states and their microwave susceptibility in more detail using a microscopic numerical model. Excellent prior works exist reviewing Andreev bound states and their properties using a scattering formalism from the Quantronics group in Saclay (Bretheau, 2013; Janvier, 2016; Metzger, 2022) and recently in Yale (Hays, 2021). The problem is there that it is quite difficult to include the effects of multiple occupied bands and magnetic field under a single umbrella as is the case in the experiments of Chapters 5 and 6. In sections Sections 2.2.3 to 2.2.5 we will, using simulations from the model described in Section 2.2.2, illustrate characteristic cases and the microwave absorption spectrum of a short junction, finite length junction with and without spin-orbit coupling and briefly consider the effect of magnetic field. Finally in Section 2.2.6 we will touch upon the effect of interactions in the junction that go beyond the microscopic model presented in Section 2.2.2.

2.2.1 Key concepts

Andreev reflection

Andreev found in 1964 that in an interface between a normal conductor and a superconductor evanescent solutions exist inside the superconductor for quasiparticles with energies below Δ. These solutions allow for charge transport of electrons that have energies below Δ in the normal conductor by reflecting as a hole with opposite energy and momentum and creating a Cooper pair in the superconductor at the Fermi-energy (Andreev, 1964). The phase ϕ_A that the electron gains during reflection as a hole then depends on its energy ϵ and the phase of the superconducting condensate $\phi/2$ according to

$$\varphi_A(\epsilon) = -\arccos\left(\frac{\epsilon}{\Delta}\right) \pm \varphi/2 \tag{2.7}$$

Phase obtained during propagation of the normal region

From Bloch's theorem a quasiparticle wavefunction has the phase $e^{i\vec{k}\cdot\vec{r}}$, where $\vec{r}$ is the position. In a one dimensional system, the phase gained for a weak link of length L in the x-direction is thus $k_x \cdot L$. The wavevector can be related to energy by its dispersion relation, which if linearized near the Fermi energy yields $\epsilon = \frac{d\epsilon}{dk_x}|_{E_F} k_x = \hbar v_F k_x$, where v_F
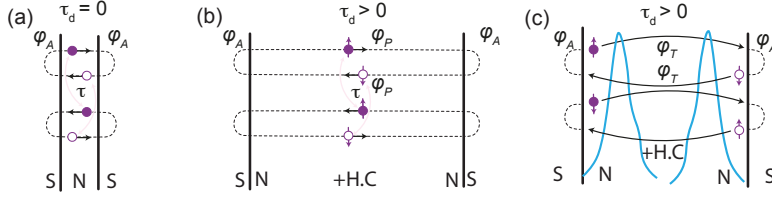
Figure 2.2: **Diagrams of bound states arising from constructive interference involving Andreev reflection.** (a) Short S-N-S junction. An electron can Andreev reflect back as a hole due to the superconducting pairing potential that couples electrons and holes. The energy dependent phase gained by Andreev reflection φ_A for bound states that consist of electron-hole superpositions adds up to 2π, $n \in N$. Also indicated with light arrows is coupling between right and left moving electrons or holes. This can be caused by scattering inside the junction region, due to disorder for example. (b) Diagram of a junction with a length such that there is a signifcant phase gained during propagation φ_P. If the junction is long enough ($L > \xi$), there exist multiple solutions of energy below Δ to Equation (2.9). (c) Schematic of a junction where a quantum dot is instead placed in the normal region and the picture of propagating particles is replaced with a phase gained during tunneling φ_T, further discussed in Section 2.2.6.

is the Fermi velocity. Therefore

$$\varphi_{\text{prop}}(\epsilon) = \frac{\epsilon L}{\hbar v_F} = \frac{\epsilon}{\Delta} \frac{L}{\xi}, \tag{2.8}$$

where in the last equality we used $\xi = \frac{\hbar v_F}{\Delta}$ in the ballistic limit. Thus the phase gained during propagation both scales with the energy of the bound state and the Fermi-velocity.

Andreev bound states

We are now ready to obtain a simple criterion for the existence of Andreev bound states, which can be seen as the superconducting equivalent of a particle in a box. When an electron with energy ϵ traverses a normal section gaining a phase during propagation $\varphi_{\text{prop}}(\epsilon)$, impinges on a superconductor, reflects as a hole gaining phase $\varphi_A(\epsilon)$, traverses the normal section again and subsequently reflects back as an electron, constructive interference can occur if these processes add up to a total phase gain of 2π.

$$2\varphi_A(\epsilon) + 2\varphi_{\text{prop}}(\epsilon) = 2\pi n, \, n \in N \tag{2.9}$$

This yields a transcendental equation for ϵ which can be solved to obtain the bound state energy.

Effect of spin-orbit coupling

Spin-orbit coupling, as its name suggests, couples the spin of a quasiparticle to its orbit (momentum). This can be expected to create a different phase gain during propagation for spin up quasiparticles compared to spin-down quasiparticles, because the Fermi-velocity of propagating quasiparticles becomes spin-dependent (Governale and Zülicke, 2002). The spin-dependent propagation phase thus creates a different interference condition dependent on spin and can lift the spin-degeneracy of ABS (Chtchelkatchev and Nazarov, 2003; Park and Yeyati, 2017)

$$2\varphi_A(\epsilon) + 2\varphi_{\text{prop}}^{\sigma\in\{\uparrow,\downarrow\}}(\epsilon) = 2\pi n, \, n \in N \tag{2.10}$$

Effect of magnetic field

Magnetic field comes into play in two ways. Firstly, it just affects the energy ϵ of the propagating quasiparticles by the spin-dependent Zeeman energy $\epsilon \pm \frac{1}{2} g \mu_B B$, which both affects the propagation phase and reflection phase, and thus again creates a spin-dependent bound state energy following Equation (2.9). Secondly, it creates an orbital effect through the vector potential that acts on the charge of the quasiparticle, resulting in an additional phase and change of effective propagation length, so this would occur even for spinless particles, similar to the origin of the Aharanov-Bohm effect. The effect scales with the total flux threaded through the particle trajectory in real space, so it is often neglected in junctions with small cross sections. This is also the case in this thesis. See for example Zuo et al. (2017) for an experimental and theoretical study using 3-dimensional tight-binding simulations of orbital effects on the critical currents of nanowire Josephson junctions.

2.2.2 Microscopic description of a nanowire Josephson junction

We now continue with a description of a simple two dimensional microscopic model for the nanowire Josephson junctions studied in this thesis, as this can be used to understand most of the core ABS physics. There are three main ingredients in the Hamiltonian of the semiconducting section of the nanowire

$$H = H_0 + H_R + H_Z, \tag{2.11}$$

which represent the following:

The kinetic and potential energy are described by H_0

$$H_{\text{kin}} = \left(\frac{\hbar^2 \vec{k}^2}{2m^*} - E_{\text{F}} - e\phi(\vec{r}) \right) \sigma_0 \tag{2.12}$$

where the potential $\phi(r)$ is spatially dependent and thus represents disorder or potential barriers in the nanowire. E_F is the Fermi energy, or chemical potential. Here m^* is the effective mass, which determines the level spacing of the bands. For InAs and InSb m^* is very small, i.e. $m^*_{\text{InAs}} = 0.023 m_e$, allowing for level spacings on the order of meV.

The Rashba spin-orbit coupling in general takes the form of $\vec{\alpha} \cdot (\vec{\sigma} \times \vec{k})$. Spin-orbit coupling originates from the effective magnetic field that a moving electron feels in its rest frame (from special relativity) while traversing an electric potential induced either by electrostatic gates or the crystal lattice. This can be approximated for a 2-dimensional system to

$$H_R = \alpha_y (k_z \sigma_x - k_x \sigma_z) \tag{2.13}$$

here α denotes the Rashba spin-orbit strength. In InAs/InSb nanowire devices considered in this thesis, this spin-orbit strength is gate tunable and is typically between 5-40 meV nm (Liang and Gao, 2012; Albrecht et al., 2016; van Woerkom et al., 2017; Tosi et al., 2019).

The Zeeman energy describes the inclusion of an externally applied magnetic field $\vec{B}$

$$H_Z = g \mu_B \vec{B} \cdot \vec{\sigma} \tag{2.14}$$

where g is the Landé g-factor which depends on the material and for the semiconductors used in this thesis ranges between $g_{\text{InAs}} = -15$ and $g_{\text{InSb}} = -55$. In the above, σ_i denotes the Pauli matrices acting on the spin degree of freedom.

Superconductivity can be described in the mean-field approximation by the Boguliobov de Gennes Hamiltonian H_{BdG}, given by (Bogoliubov et al., 1959; Tinkham, 2015)

$$
\begin{aligned}
H_{\text{BdG}} &= \begin{pmatrix} H_0 + H_R + H_Z & \tilde{\Delta} \\ \tilde{\Delta}^* & -(H_0 + H_R) + H_Z \end{pmatrix} \\
&= (H_0 + H_R)\tau_z + H_Z\tau_0 + \Delta\cos(\varphi/2)\tau_x + \Delta\sin(\varphi/2)\tau_y
\end{aligned}
\tag{2.15}
$$

where the complex superconducting pairing $\tilde{\Delta} = \Delta\cos(\varphi/2) + i\sin(\varphi/2)$ to account for the phase φ of the condensate wavefunction, mentioned here explicitly for its use in describing Josephson junctions, and τ_i are the Pauli matrices acting on particle-hole space. In the BdG Hamiltonian described above, particles and holes are included explicitly to facilitate diagonalizing the Hamiltonian. This comes at the cost of artificially doubling the number of solutions and should be corrected for later.

For the theory section and the non-interacting simulations in Chapter 5, tight-binding simulations of the Josephson junction were performed using the Kwant package (Groth et al., 2014), and in particular adapting code from Laeven et al. (2020).

Determining the BdG spectrum and many body states
Diagonalization of the BdG Hamiltonian yields the energies $\sum_{i,\sigma} \pm E_{i,\sigma}$ of the Andreev levels (see e.g. Figure 2.4b,e), where the particle hole symmetry enforces a doubling of the spectrum. These fully determine the system behaviour if we assume no interactions are present. The low-energy Hamiltonian can be written as a sum over the Andreev levels to construct the many body states

$$
H = \sum_{i,\sigma} E_{i,\sigma}\left(c_{i,\sigma}^\dagger c_{i,\sigma} - \frac{1}{2}\right)
\tag{2.16}
$$

Where $c_{i,\sigma}^\dagger$ is the creation operator for the diagonalized basis states with spin included explicitly as an index σ. From this we obtain the many-body wavefunctions by "counting" fermionic excitations present (see Figure 2.4c for the case of a single ABS). Zero excitations gives the energy of the many body ground state $|V\rangle$[3] with $E^g = -\frac{1}{2}\sum_{i,\sigma} E_{i,\sigma}$, and which is a product state of the single-particle wavefunctions. The ground state depends on the phase difference over the junction and other parameters, thus this is what carries the supercurrent and the maximum current that this can carry is what is measured in standard current-bias experiments (at exactly 0 temperature).

Excitations from many-body levels
When performing microwave, or tunneling experiments, one needs to consider excitations from the ground state. Following Equation (2.16), in Table 2.3 the different states are

---

[3]Note that we indicate the ground state as the vacuum of ABS excitations to keep the notation clear, but this should not be confused with a vacuum of electrons/holes, see e.g. Refs. (Bretheau, 2013; Datta and Bagwell, 1999) for a deep dive on this topic.

n manifolds	n states	parity	available basis states
1	2	even	$\|V\rangle, \|\uparrow_a\downarrow_a\rangle$
1	2	odd	$\|\uparrow_a\rangle, \|\downarrow_a\rangle$
2	4	odd	$\|\uparrow_a\rangle, \|\downarrow_a\rangle, \|\uparrow_b\rangle, \|\downarrow_b\rangle$
2	6	even	$\|V\rangle, \|\uparrow_a\downarrow_a\rangle, \|\uparrow_b\downarrow_b\rangle,$ $\|\uparrow_a\downarrow_b\rangle, \|\uparrow_b\downarrow_a\rangle, \|\uparrow_a\uparrow_b\rangle, \|\downarrow_a\downarrow_b\rangle$
2	6	even (with e-e interactions)	$\|V\rangle, \|\uparrow_a\downarrow_a\rangle, \|\uparrow_b\downarrow_b\rangle,$ $\frac{1}{\sqrt{2}}(\|\uparrow_a\downarrow_b\rangle + \|\uparrow_b\downarrow_a\rangle),$ $\frac{1}{\sqrt{2}}(\|\uparrow_a\downarrow_b\rangle - \|\uparrow_b\downarrow_a\rangle), \|\uparrow_a\uparrow_b\rangle, \|\downarrow_a\downarrow_b\rangle$
3	12	even	*many*

Table 2.3: Available low-energy Andreev states dependent on the parity, occupation and number of manifolds below the gap. The basis are chosen to illustrate the spin-content explicitly. For a description of the even-parity basis states with e-e interactions, see Chapter 5

shown for the various occupations of the low-energy ABS when considering one or two manifolds present in the junction. Microwave excitations must conserve fermion parity, as photons are bosonic and cannot create fermions, so transitions between states when using microwave drives are only between states that have the same parity of excitations in the ABS. In order to show an overview of the various transitions and basis states for junctions with one or two manifolds a lexicograph is given in Figure 2.3. Note that in Chapter 4 we demonstrate that by exciting quasiparticles to a bath of fermions (the leads) it is actually possible to change the fermion parity of bound states in the junction using microwaves. But this still conserves global fermion parity.

Microwave absorption of Andreev states
In this section we follow the derivation outlined in van Heck et al. (2017) to obtain the microwave response of Andreev bound states given the BdG spectrum. When a microwave signal is applied to the junction this can be seen as generating an AC voltage difference over the junction $V(t) = V_0\cos(\omega t)$ at radial frequency ω. This leads in first order to a time dependent coupling term in the Hamiltonian

$$\delta H(t) = \hat{I}_A V_0/\omega \sin(\omega t) \tag{2.17}$$

Thus, using linear response theory, the microwave absorption is proportional to the squared absolute value of the matrix elements of the current operator $\hat{I}_A$ between initial and final states of the transition, scaled by the occupation of the initial and final states. The frequency dependent admittance of the junction is given by $Y(\omega) = i\chi(\omega)/\omega$, where $\chi(\omega)$ is the fourier transform of the response function that results from Equation (2.17). The real part of the addmittance is proportional to the microwave absorption power, which is what we are interested in and we quote the results below. The set of eigenvalues obtained from diagonalizing $H_{\mathrm{BDG}} + E_m, -E_m$, with corresponding eigenstates $\Psi_m, \mathscr{P}\Psi_m$, where $\mathscr{P}$ denotes the particle-hole operator, can be used to evaluate the current matrix elements[4]

---

[4]We calculate the current operator I_A with kwant by using a $-\sigma_0 \otimes \sigma_z$ on-site matrix that is then filled into the current operator. the current operator is evaluated on a vertical slice in the normal section (e.g the hoppings
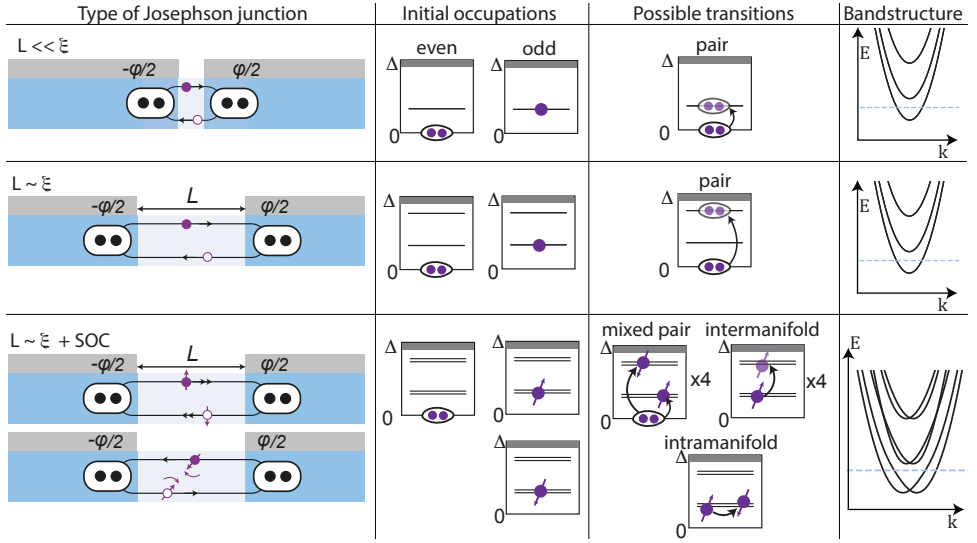
Figure 2.3: **Lexicograph of the types of Josephson junctions and their corresponding Andreev levels and possible transitions**. Top row: Short junction where the junction length L is much smaller than the coherence length ξ. Middle row: Long junction where is on the order of ξ such that another Andreev manifold enters below the gap. Bottom row: Long junction with spin-orbit coupling. Spin now becomes a relevant quantity and the Kramers doublets split at finite phase difference. Due to spin-orbit coupling, the bands for different spins are pushed and thus the group velocity (i.e. the derivative of the band vs k) at the Fermi level ν_f becomes spin-dependent, yielding separate energies for the ABS. Indicated with dashed arrows are (i) Kramers doublet. (ii) Ground state Andreev "Cooper pair" (iii) continuum density of states.

$j_{n,m} = \langle \Psi_n | I_A | \Psi_m \rangle$. The diagonal elements give the contribution to the supercurrent of a single ABS level. The off-diagonal elements are those that determine the possible microwave transitions. For pair transitions, consisting of breaking a Cooper pair and exciting two ABS levels, i.e. the even parity spectrum, the result is

$$\mathrm{Re}\{Y_e(\omega)\} = \frac{\pi}{\omega} \sum_{n \geq m} |j_{n,\mathscr{P}m}|^2 \delta(\omega - (E_m + E_n)) \tag{2.18}$$

where $j_{n,\mathscr{P}m}$ is defined as $\langle \Psi_n | I_A \mathscr{P} | \Psi_m \rangle$, the energy eigenvalues are ordered and the Dirac-delta function only selects frequencies that correspond to breaking a Cooper pair and excite the two occupied levels n,m. For single-particle transitions, where a quasiparticle already in the junction is excited to a higher state, i.e. the odd parity spectrum, the result is

$$\mathrm{Re}\{Y_o(\omega)\} = \frac{\pi}{\omega} \sum_{n \geq m} |j_{n,m}|^2 \delta(\omega - (E_m - E_n)) \tag{2.19}$$

where here the Dirac-delta function only selects frequencies that equal the difference between energies of level n,m. If we include a finite temperature using Fermi factors, to account for finite populations of excited states, this results in the total response

$$Re\{Y(\omega)\} = \mathrm{Re}\{Y_e(\omega)\}[1 - f(E_m) - f(E_n)] + \mathrm{Re}\{Y_o(\omega)\}[f(E_m) - f(E_n)] \tag{2.20}$$

between two columns of sites).

where the Fermi-Dirac function at finite temperature T is defined as

$$f(E) = \frac{1}{e^{(E-\mu)/k_B T} - 1} \tag{2.21}$$

and the delta function $\delta(\omega)$ is replaced with a finite with Lorentzian function to emulate finite linewidths of the transitions as is the case in any real experiment.

2
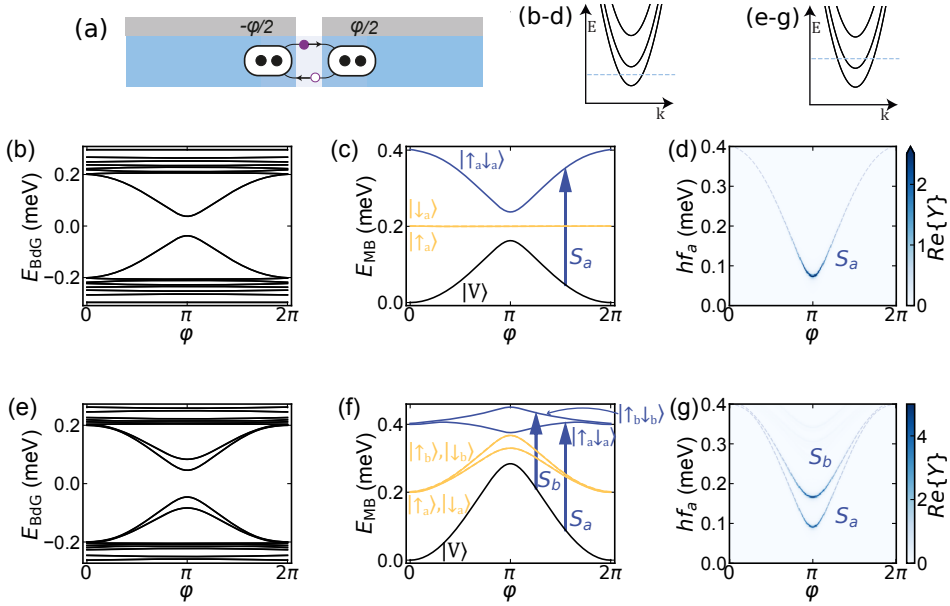
Figure 2.4: **Simulated short ($L = 5\,\text{nm}$) Josephson junction spectrum, many body states and excitation spectrum.** (a) (b-d) A single ABS manifold corresponding to the lowest subband, labeled a, is present inside gap. (e-g) A second subband is occupied, thus a second ABS manifold, labeled b becomes visible inside the gap. (b,e) The BdG spectrum (limited to 32 states). (c,f) Many body levels (see (2.16)), corresponding to the ground state $|V\rangle$, the degenerate excited odd parity states $|\uparrow_i\rangle$, $|\downarrow_i\rangle$ and the excited states $|\uparrow_i\downarrow_i\rangle$ where $i \in \{a,b\}$ labels the manifold corresponding to the two subbands. The coloring of the states corresponds to the number of quasiparticle excitations above the ground state present in each state ranging from 0 (black), 1 (orange) to 2 (blue), the minimum energy of $|V\rangle$ is subtracted in the many body spectra (d,g) Excitation spectrum(see (2.20)) where the energy of the pair transitions S_a, S_b are shown.

2.2.3 Short junctions

In the short junction approximation $L \ll \xi$, the length of the normal section is neglected resulting in $\phi_{\text{prop}} = 0$, thus only ϕ_A plays a role. The solution to this including a barrier that mimics disorder in the junction was calculated analytically (Beenakker, 1991)

$$E_A = \pm\Delta \sqrt{1 - \tau \sin(\phi/2)^2} \tag{2.22}$$

where $\tau \in \{0, 1\}$ is a measure of the barrier strength in the model. In Figure 2.4 an example is shown of a numerical simulation of Equation (2.15) for a 5 nm wide junction. The energies

resulting from diagonalization of the BdG Hamiltonian are shown in Equation (2.15)(a) and the many-body state energies inEquation (2.15)(b). For the many-body states, the ground state disperses with phase and thus carries a current. The odd-parity states $|\uparrow\rangle$ $|\downarrow\rangle$ are degenerate here and do not disperse, thus these carry no supercurrent. This "blockade" of supercurrent was clearly observed in the first time-resolved circuit-QED experiments that probed Andreev states in hybrid nanowires and atomic break junctions (Janvier et al., 2015; Hays et al., 2018).

Multiple transverse modes
We now consider a situations where a second transverse channel is occupied. This can be seen as a generalization of Equation (2.22) for a single channel in Landauers picture of conduction channels, each with their own effective transparancy τ_i (see Figure 2.4 (e-g)). It is interesting to note that in this case, the odd-parity states $|\uparrow_a\rangle$, $|\downarrow_a\rangle$ of the lowest manifold (manifold a) still have the dispersion of the second manifold b and thus carry a supercurrent, because only that manifold is "blocked".

Chemical potential dependence of ABS spectrum
In experiments performed in this thesis, the electrostatic gate voltage is often swept to tune the density of ABS. This can be seen as changing the chemical potential of the nanowire, and thus allowing tuning of the number of ABS in the junction. It is informative to look at the junction spectrum at $\varphi = 0$ and $\varphi = \pi$. If the junction is short and ballistic, the behaviour is rather trivial, all states at $\varphi = 0$ stick to the gap edge and at $\varphi = \pi$ come down as soon as the chemical potential is high enough for the Andreev approximation to hold, i.e. no normal reflection at the N-S interface (see Figure 2.5a).

When the junction is short and disordered, as is the case in most experiments, (see Figure 2.5b), the transmission τ fluctuates with chemical potential dependend on the disorder potential, thus the ABS at $\varphi = \pi$ fluctuate at finite energy dependend on the ratio of μ and the disorder potential strength. At $\varphi = 0$ the ABS still stick to the gap edge.

Finally, in presence of a double barrier potential at each N-S interface (see Figure 2.5c), resonant behaviour can occur as discussed below.

Effects of confinement in the junction region
A feature that is often observed in realistic experiments on nanowire junctions is that the Andreev bound state energy at $\varphi = 0$ does not reach the gap Δ, and the gate dependence shows resonant behaviour. This is experimentally often dubbed "dotty" behaviour, as the quasi-periodic[5] resonant structure resembles that of the Coulomb diamonds in the conductance through resonant levels in a quantum dot (see Figure 2.5c for an example simulation including disorder and a double barrier potential). Beenakker and van Houten (1992) calculated the modifications to the bound state energy for the case of having two barriers at the sides of the junction (representing a quantum dot with negligable charging energy). Generally, the modifications have to found by solving a transcendental equation dependent on the resonant level energy ϵ_g, and tunneling rates through the double barriers

---

[5]Note that in actual nanowire quantum dots oscillations are not perfectly periodic. A metallic island with charging energy and zero level spacing has perfect periodicity, but as soon as the level spacing becomes sizable, it is not periodic anymore. The spacing involves both energy scales and additionally particle-in-a-box levels have increasing spacing with chemical potential.
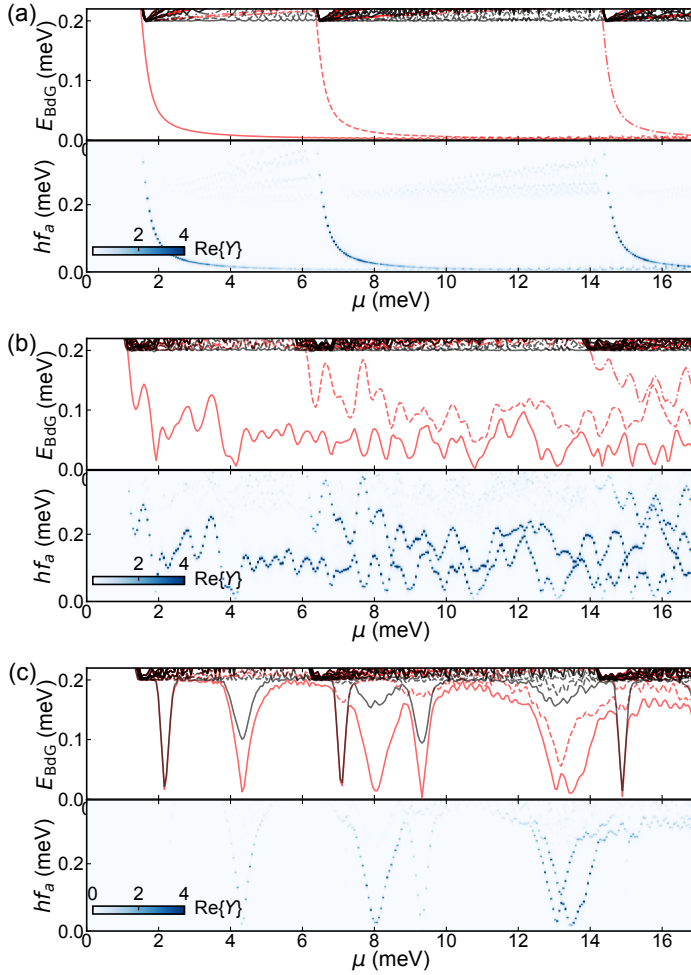
Figure 2.5: **Chemical potential dependence of ABS spectra for three characteristic potentials**. Top panels show the positive BdG eigenenergies for $\varphi = 0$ (black) and $\varphi = \pi$ (red) versus chemical potential μ. Bottom panels show the microwave absorption spectrum ((see (2.20))), where f_a denotes the frequency of the applied tone. (a) A ballistic junction with no disorder potential. (b) More realistic junction with 8meV random on-site disorder. The phase-dependence data from Figure 2.4 are taken close to the first (around 1meV) and second (around 8meV) subband entry, with these disorder settings. (c) Junction with a strong confinement by a 20meV double barrier potential. This creates Fabry-Perot like resonances and the ABS can peel off from the gap at $\varphi = 0$ even in a short junction, as described in the Beenakker van Houten model.

Γ_1, Γ_2 (Beenakker and van Houten, 1992), however for some limits closed form expressions can be found. For example in the case of equal tunneling rates through the left and right barriers $\Gamma_1 = \Gamma_2 = \Gamma$, we obtain

$$E_A = \pm \frac{\Delta}{1 + \Delta/\Gamma} \sqrt{1 - \tilde{\tau} \sin^2(\phi/2)} \tag{2.23}$$

where $\tilde{\tau}$ becomes additionally dependent on the resonant level energy (the distance from being on resonance) and the tunneling rates. The effect of confinement can be seen as a reduced coupling to the superconductor, hence the effective superconducting pairing $\Delta^* = \frac{\Delta}{1+\Delta/\Gamma}$ that the ABS "sees" is reduced. In practise, these states can thus be modeled simply using the earlier Beenakker formula (Equation (2.22)), but with a renormalized gap. An important consideration is that for this behaviour to occur, only strong confinement is necessary, no charging energy. The addition of (weak) charging energy to the solutions of Andreev states is a topic of ongoing research and is further discussed in Section 2.2.6 and Chapter 5 and recent experiments (Matute-Cañadas et al., 2022; Fatemi et al., 2022; Bargerbos et al., 2022).

Also in the recent works focusing on creating artificial Kitaev chains using two quantum dots coupled with a superconducting section from our lab (Wang et al., 2022; Dvir et al., 2023), these kind of confined ABS have been seen very clearly at $\varphi = 0$ and utilized to couple neighbouring dots with a superconducting flavour at an energy of choice tuned by using electrostatic gates to modify the chemical potential, and thus the distance to the gap edge.

2.2.4 Consequences of finite junction length
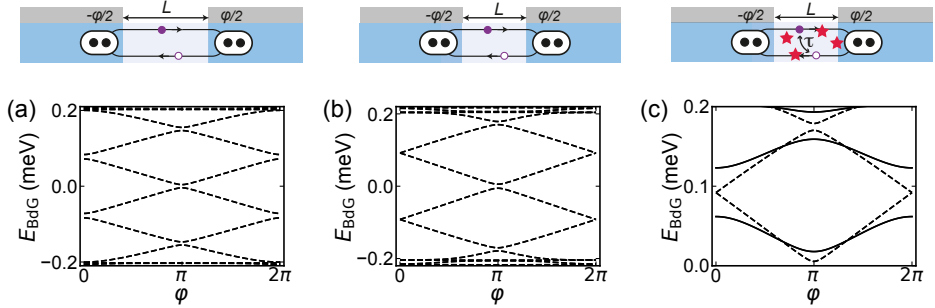
Figure 2.6: **Consequences of finite junction length for a single occupied subband in the nanowire.** (a) BdG spectrum of a ballistic junction close to the first subband entry, where $L > \xi$. Multiple (spin-degenerate) ABS appear with spacing of approximately $E_T < \Delta$. (b) Lower ratio of L/ξ than in (a), by increasing the chemical potential to change the effective junction L/ξ length via $v_F(\mu)$. (c) Zoom in of positive Andreev levels with (solid lines) and without (dashed lines) random on-site disorder. Disorder opens up gaps at the crossings near $\varphi = 0$ and $\varphi = \pi$ because it couples left and right moving orbits. Note that this is an especially symmetric case, and for a general disorder realization the size of the gaps at $\varphi = 0, \pi$ does not have to be equal.

For junctions where the traversal time is sufficiently long, i.e. $L \gg \xi$, and the phase coherence in the normal section is sufficiently large, higher harmonics can arise similar to a particle in a box. By combining Equations (2.7) and (2.8) into Equation (2.9) the following transcendental equation for the ABS energies in a ballistic long junction is obtained (Kulik, 1970)

$$2\arccos\left(\frac{\epsilon}{\Delta}\right) + \left(\frac{L\epsilon}{\xi\Delta}\right) \pm \phi = 2\pi n \qquad (2.24)$$

where $n \in Z$ and ϕ is the phase difference over the junction. The first term relates to

the phase obtained from the evanescent part of the quasiparticle wavefunction that enters the superconductor ϕ_A which includes the phase difference of the superconducting condensates ϕ that is picked up. The second term comes from the phase gained during propagation ϕ_{prop} by the electrons and holes that are propagating. The phase during propagation for energies below the superconducting gap Δ can become more than 2π resulting in the existence of mutliple solutions to Equation (2.9). The dispersion of each Andreev level is then no longer given by Δ (as in the short junction case) but in the long junction limit by the Thouless energy[6] $E_T = \pi\hbar v_F/L$, which can be seen from Equation (2.24).

So, if $E_T < \Delta$ we get *per* conduction channel *multiple* ABS manifolds below the gap Δ, with the number of manifolds roughly equal to Δ/E_T, because multiple solutions exist to Equation (2.24). This "stacking" of ABS for the lowest subband in a nanowire is shown in Figure 2.6(a), (b) for a simulation of a 1 µm long junction with two different effective coherence lengths set by the chemical potential.

Finite transparancy

A finite transparancy can again be modeled effectively by including a potential barrier in the normal region, now at a position x_0 (due to the finite junction length). The resulting small modifications to the transcental equation above was calculated by Bagwell (1992)

$$2\arccos\left(\frac{\epsilon}{\Delta}\right) + \left(\frac{L\epsilon}{\xi\Delta}\right) \pm \alpha = 2\pi n \qquad (2.25)$$

where the effective phase gained α is defined by $\cos(\alpha) = \tau\cos(\phi) + (1-\tau)\cos\left(\frac{(L-2x_0)\epsilon}{\xi\Delta}\right)$, with again τ being the transmission probability through the barrier. A few things to note here are: as the barrier is moved away from the center the transparancy decreases, additionally, the expression reduces to the expression for a single conduction channel in the short junction limit of $L \to 0$ and to Equation (2.24) for $\tau \to 1$. The barrier couples right and left movers, so the resulting spectra can also be interpreted as having an avoided crossing between states that were right and left moving states without the barrier present in the ballistic case.

An example of finite transparancy induced by disorder in the nanowire is shown in Figure 2.6(c) [solid lines].

Effects of spin-orbit coupling

In short junctions, if no magnetic field is applied, spin-orbit effects on the ABS spectrum are minimized and the ABS energies remain degenerate [7]. In general, a finite dwell time τ_d in the junction, either due to confinement or finite junction length, can cause the ABS levels to spin-split in energy (Chtchelkatchev and Nazarov, 2003; Béri et al., 2008; Padurariu and Nazarov, 2010; Reynoso et al., 2012).

The specific application of determining the microwave spectrum of a long Josephson junction in a few-band nanowire with Rashba spin-orbit coupling was treated in Park and Yeyati (2017) and recently signatures were experimentally detected in Tosi et al. (2019);

---

[6]This is generally defined in mesoscopic physics as the energy required for a propagating particle to gain a π phase-shift during its trajectory.

[7]A derivation of the degeneracy based on the scattering matrix approach is given in (Chtchelkatchev and Nazarov, 2003; Béri et al., 2008)
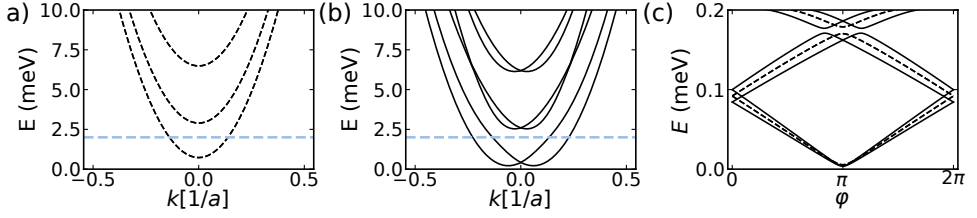
Figure 2.7: Effect of Rashba spin-orbit coupling on the bandstructure and on the long-junction spectrum. (a) Band structure without SOC. The chemical potential is indicated with dashed blue line. (b) bandstructure with Rashba SOC. The second subband interacts with the lowest and changes the slope of the lowest band spin-dependently, causing the splitting of ABS energies shown in (c). (c) Positive BdG energies of the ABS in a ballistic junction without (dashed line) and with spin-orbit coupling, keeping other parameters fixed. Note that the crossing between the upper two manifolds is still avoided, possibly because the chemical potential was set near a subband entry, where the Andreev approximation does not fully hold, alternatively a small residual scattering can be induced in simulations because of the finite length of the leads (set here to 3000 nm) that cause normal reflection at the boundary.

Hays et al. (2020). To understand the origin of the spin-splitting, we consider the case where the lowest subband is occupied (Figure 2.7(a)), spin-orbit coupling couples higher subbands spin-dependently to the lowest band (Figure 2.7(b)) and therefore alter the curvature of it. This subsequently creates a spin-dependence of the Fermi-velocity (Governale and Zülicke, 2002), and thus can create a spin-dependent propagation-phase and constructive interference condition for the ABS energies (Equation (2.10)). Alternatively, this can be rewritten to result in an effective spin-dependent coherence length $\xi(v_F)$, which alters the transcendental equation for constructive interference (Equation (2.25)) of a long junction to (Tosi et al., 2019)

$$\tau \cos((\lambda_1 - \lambda_2)\epsilon/\Delta \mp \phi) + (1-\tau)\cos((\lambda_1 + \lambda_2)\epsilon/\Delta x_0) = \cos(2\arccos\epsilon/\Delta - (\lambda_1 + \lambda_2)\epsilon/\Delta),$$
(2.26)

where $\lambda_i = L/\xi_i = \frac{L\Delta}{\hbar v_i}$ is a phenomenological parameter that illustrates the effect of a spin-dependent Fermi-velocity (not to be confused with the London penetration depth λ_L). The ABS spectrum thus breaks spin-degeneracy, with a strength that depends on φ as shown in Figure 2.7(c). This reduces to Equation (2.25) if $\lambda_1 = \lambda_2$ and can be interpreted as now having a spin-dependent $\phi^\sigma_{\text{prop}}$ as discussed above if $\lambda_1 \neq \lambda_2$. However, note that spin is no longer a good quantum number, as it is coupled to the orbital degree of freedom.

Microwave transition spectra of long junctions with SOC

We now have developed all ingredients to investigate a "canonical" realistic example of microwave transition spectra for a long junction with spin-orbit coupling, such as found in InAs nanowire Josephson junctions. We focus on the lowest two manifolds illustrated in Figure 2.8a, which is simulated using the parameters from Figure 2.7(c), with an added random onsite disorder to simulate scattering (see Figure 2.8(a)). The disorder causes the right and left moving states to couple, again opening gaps around $\varphi = \pi, 0$.

The many body states for the two lowest manifolds are indicated in Figure 2.8b, which are separated into odd or even parity by yellow or blue color shades respectively. An
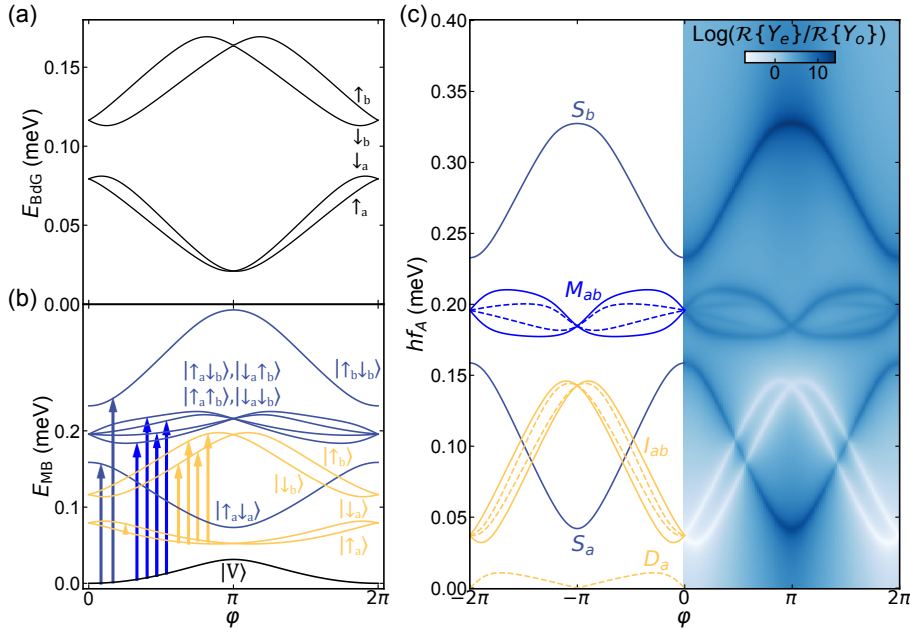
Figure 2.8: **BdG eigenenergies, many body states and microwave transition spectrum of a long junction with spin-orbit coupling and disorder.** (a) BdG eigenenergies of the lowest two junction states. (b) Many-body levels corresponding to the states indicated. The coloring corresponds to the number of quasiparticle excitations above the ground state present in each state ranging from 0 (black), 1 (orange) to 2 (blue). (c) Microwave transition spectrum (see Eqs.2.18, 2.19). The transitions correspond to those indicated with the arrows in (b). Dashed lines indicate transitions that involve a spin-flip, which are less visible in the absorption spectrum on the right hand side. $\Delta = 0.2\,\text{meV}$, $L = 1000\,\text{nm}$, $W = 120\,\text{nm}$, $\alpha = 60\,\text{meV nm}$, $\mu = 2.9\,\text{meV}$.

important distinction with the short junction scenario is that the dispersion of the ABS many body states, and thus the supercurrent carried by them, now depends on spin.

We can again calculate the full microwave absorption spectrum using the current-operator matrix elements (limiting the spectrum up to the third ABS manifold, i.e. neglecting states in the continuum), following the description in section Section 2.2.2 at a temperature of 250 mK to emulate a finite population of the lowest ABS manifold. This spectrum is shown in Figure 2.8(c) on the right hand side, while the left side highlights the various transitions extracted by simply subtracting the ABS energies.

Starting from the even parity ($n = 0, 2$) ground state $|V\rangle$, several transitions are possible (indicated with blue arrows in panel b and shown in panel c with the corresponding label). We observe the singlet transition to the lowest manifold S_a, indicated in blue, the dispersion of this transition is very similar to the short junction case, but with a maximum frequency much lower than the gap Δ because of the finite junction length limits it to E_T. Additionally it is possible to drive singlet pair transitions to the second manifold S_b which has an opposite dispersion as S_a.

In the $n = 1$ excitation odd-parity subspace, i.e. a quasiparticle is trapped in the junction, the available many body states are limited to those shaded yellow in Figure 2.8b.

Intermanifold microwave transitions I_{ab} are then possible between manifold a and b, starting from one of the low energy odd-parity states $|\uparrow_a\rangle, |\downarrow_a\rangle$ in manifold a to the final states $|\uparrow_b\rangle, |\downarrow_b\rangle$ of manifold b (yellow arrows in panel b). This gives characteristic bundles of four transitions (shown in panel c). The transitions that require a spin-flip are indicated with dashed lines as they have a smaller matrix element, visible in the accompanying absorption spectrum. A direct spin-flip within a manifold $D_a : |\downarrow_a\rangle \to |\uparrow_a\rangle$ is also enabled by spin-orbit coupling, but the matrix element is generally small at low magnetic field (dashed orange line near zero in Figure 2.8c).

Additionally, in the even-parity $(n = 0, 2)$ subspace, new types of even-parity transitions appear. We find sets of four even-parity mixed pair transitions to two different manifolds. These are labeled M_{ab} and denote transitions from $|V\rangle$ to the basis spanned by the states $\{|\uparrow_a\downarrow_b\rangle, |\downarrow_a\downarrow_b\rangle, |\uparrow_a\uparrow_b\rangle, |\downarrow_a\uparrow_b\rangle\}$.

An interesting observable feature is that transitions that require a spin-flip are generally much less visible compared to those that do not require a spin-flip. This is also pointed out in measurements of the applied micrwowave drive power dependence of the visibility intermanifold transitions in Hays et al. (2020), although the visibility depens also on the exact chemical potential setting and the way transitions are driven as discussed in Section 2.2.5.

Transitions in presence of a third manifold

In general, there are often more than two manifolds present in the junction, either due to multiple transverse modes as shown in Figure 2.4 or due to higher harmonics from a finite length junction as shown in Figure 2.8. To exemplify the consequences of more manifold, the same simulated spectrum as in Figure 2.8 including the previously neglected third manifold is shown in Figure 2.9. In Figure 2.9b, the additional transitions are indicated that arise besides those shown in Figure 2.8b. Qualitatively, one new type transition that is visible in the absorption spectrum is the intermanifold transition I_{bc} starting from an excited quasiparticle in manifold b. Although these are possible in real devices at the 250 mK temperature used in the simulation to emulate a higher effective quasiparticle population, the short lifetime ($\sim \mu s$) of these states would generally make the quasiparticle relax to manifold a or recombine with another quasiparticle to the ground state. Qualitatively it is already clear that the spectrum becomes crowded quite fast with increasing numbers of manifolds considered, lovingly described as the "beautiful mess" by Hays (2021), but perhaps better described by "Andreev spaghetti soup".

Transitions to the continuum

So far, transitions involving the continuum have been neglected in the above spectra. The reasoning behind this is that the final states of the continuum are extremely short-lived, which subsequently makes pair transitions to the continuum states hard to observe in reality. However, there are cases where the continuum can play a significant role in the microwave spectra. This is the case for transitions that end up exciting *a single* quasiparticle to the continuum, because as this quasiparticle quickly diffuses away, the result is a clearly observable (incoherent) change of junction parity. These kind of transitions were seen in switching current measurements under microwave irradiation at frequencies that result in exciting a quasiparticle to the continuum (Bretheau et al., 2013b). Several theory
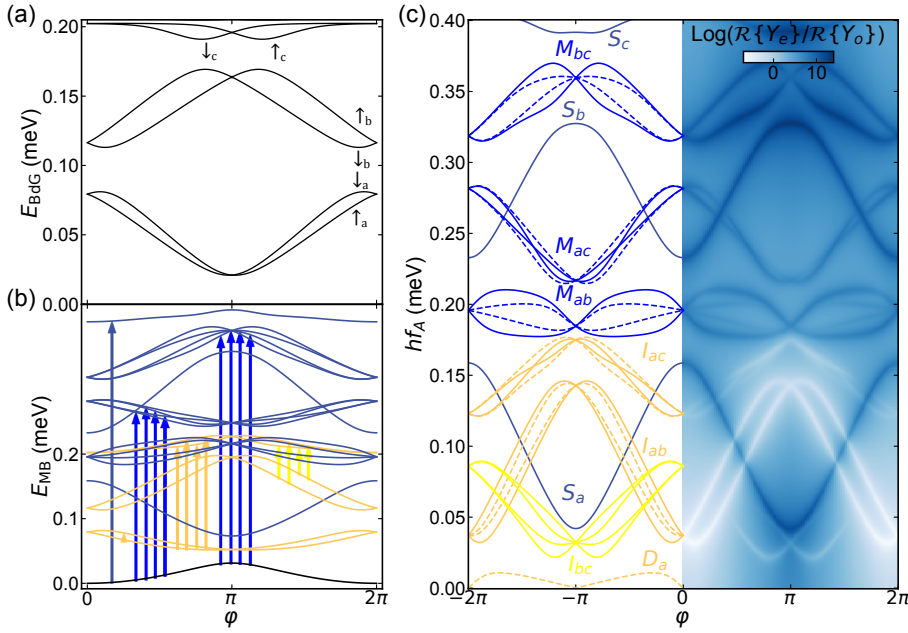
Figure 2.9: **Microwave transition spectrum of a long junction with spin-orbit coupling and disorder with a third manifold.** (a) BdG eigenenergies of the lowest three junction states. (b) Many-body levels corresponding to the states indicated. The coloring corresponds to the number of quasiparticle excitations above the ground state present in each state ranging from 0 (black), 1 (orange) to 2 (blue). (c) Microwave transition spectrum (see Eqs.2.18, 2.19). The transitions correspond to those indicated with the arrows in (b), where only the transitions are drawn that are not shown in Figure 2.8. Dashed lines indicate transitions that involve a spin-flip, which are less visible in the absorption spectrum on the right hand side. $\Delta = 0.2\,\text{meV}$, $L = 1000\,\text{nm}$, $W = 120\,\text{nm}$, $\alpha = 60\,\text{meV nm}$, $\mu = 2.9\,\text{meV}$

studies have investigated mechanisms for microwave induced parity changes following this experiment (Riwar et al., 2014; Riwar, 2015; Klees et al., 2017; Olivares et al., 2014).

In Chapter 4 we report on the observation of parity changes due to microwave irradiation in a circuit-QED setup, unexpectedly, also when we drive transitions that do not involve continuum states directly. An explanation is proposed in the follow-up theoretical work from Ackermann et al. (2023). Interestingly, we can, dependent on the type of transition driven, both trap and detrap a quasiparticle in the junction with a pulse much faster than the quasiparticle switching time, allowing for a dynamical way to initialize ABS parity.

Effect of magnetic field on band structure

First, we consider effect of the magnetic field on the bandstructure. In principle, a magnetic field splits the spin-degenerate bands as shown in the top left panel of Figure 2.10 linearly. However, spin-orbit coupling (top right panel) defines a competing quantization axis of spin, coupled to the direction of momentum. Thus in presence of both spin-orbit coupling and externally applied magnetic field, magnetic field generally opens up a gap
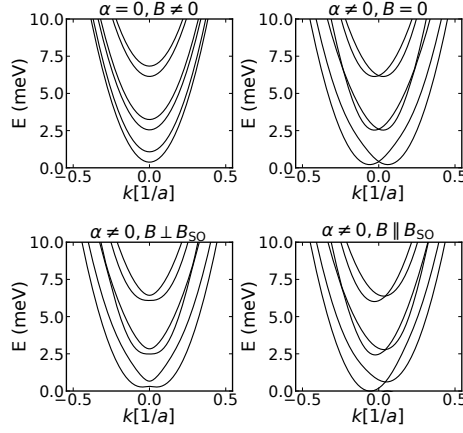
Figure 2.10: Changes to the bandstructure due to an applied magnetic field. From top left to bottom right: Only applied magnetic field, only SOC on, SOC on together with applied magnetic field perpendicular to the effective magnetic field seen by propagting modes due to SOC and lastly SOC on with applied magnetic field perpendicular to the spin-orbit field.

when not aligned with the effective magnetic field seen by the propagating modes due to SOC (bottom right panel). If the magnetic field direction is along the effective spin-orbit field, the band-structure is tilted instead and no avoided crossings appear because there still exists a common quantization axis for spin.

Because the band structure plays an important role in the shape of the interband spin-flip transitions, the dispersion of these transitions could provide insight in the effective spin-orbit coupling direction as proposed in Tosi et al. (2019).

2.2.5 Effect of magnetic field on the ABS spectrum

We now describe the effect of magnetic field on an isolated ABS manifold, in presence of spin-orbit coupling. The main effect of magnetic field is to cause a linear Zeeman splitting of the manifold. In Figure 2.11 we illustrate this. To first order, or for low magnetic field, the magnetic field causes a linear Zeeman splitting. Denoting the manifold energies by $E_{a,\uparrow}$, $E_{a,\downarrow}$, the splitting of the Kramers doublet is as follows

$$E_{a,\uparrow/\downarrow}(B) = E_a \pm \frac{1}{2} g_a^* \mu_B B, \tag{2.27}$$

here μ_B is the Bohr Magneton and g_a^* is the effective g-factor of the manifold, which is generally smaller or equal than the bare g-factor of the semiconductor, which will be clarified in more detail below. The effect of splitting is schematically indicated in Figure 2.11b for small fields.

To capture the effect of spin-orbit coupling, we proceed with an example of a short ($L/\xi \leq 1$) junction in presence of magnetic field parallel to the wire and perpendicular to the spin polarization axis for the Rashba spin-orbit term considered so far(see Equation (2.13)). The theory for this case is described in detail in van Heck et al. (2017). Here we highlight the main consequences relevant for the experiments in this thesis using the

2
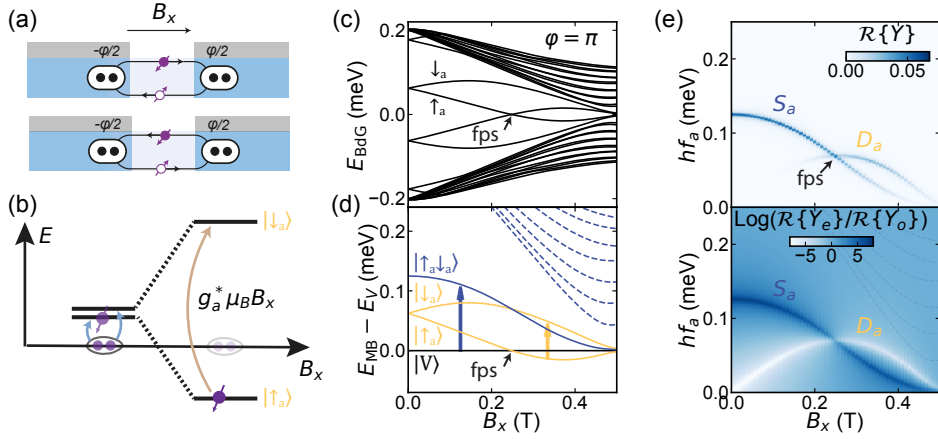
Figure 2.11: **Effect of magnetic field on an isolated ABS in presence of spin-orbit coupling.** (a) A magnetic field is applied parallel to the propagation direction, and thus approximately perpendicular to the magnetic field generated by the Rashba spin-orbit coupling. (b) Schematic of the effect of magnetic field on an isolated ABS manifold. A degenerate level at low field is split linearly by the Zeeman energy with an effective g-factor $g_a < g$ set by the chemical potential and spin-orbit coupling. When one of the spin-species crosses zero energy the ground state changes parity. (c) Example simulation of BdG eigenenergies of a L=300 nm JJ at low chemical potential such that only the lowest subband is occupied in presence of spin-orbit coupling at $\varphi = \pi$. The low-chemical potential and finite length allow a second manifold close to the gap edge to come in. However, we ignore this level as it merges with the continuum at finite magnetic field, so the spectra and many body levels are only plotted for the lowest manifold. (d) Many-body states associated with the BdG eigenenergies shown in (c), where the energy of the ground state $|V\rangle$ at zero field is subtracted for all fields. (see Equation (2.16)) (e) Associated microwave absorption spectrum (see Equation (2.20)) plotted both in linear and log scale at T=250 mK. Parameters are $\Delta = 0.2$ meV, $L = 300$ nm, $W = 80$ nm, $\alpha = 20$ meV nm, $\mu = 2.5$ meV, $g = 15$.

same microscopic model used so far in this Chapter. A representative example spectrum is shown in Figure 2.11c for fixed phase difference $\varphi = \pi$. For $\varphi = \pi$, at $B = 0$, the manifold is degenerate, even in presence of spin-orbit coupling as visible in the phase dispersion shown earlier Figure 2.7. At low fields the two eigenenergies corresponding to the states $|\uparrow_a\rangle, |\downarrow_a\rangle$ split linearly. The Zeeman term competes with spin-orbit interaction, hybridizing spin and orbital number, and thus spin is no longer a good quantum number (we do still keep the same notation for convenience). At large enough field the dispersion becomes quadratic due to the coupling with higher energy states of the continuum induced by the Rashba spin-orbit coupling. Without spin-orbit present, these states would simply cross since they would have opposite spin.

Fermion parity switches: from singlet to doublet ground state
At large enough magnetic field, one of the spin-split eigenenergies can cross the Fermi level (indicated with the black arrow in Figure 2.11c). At this point, the ground state becomes that which has a single quasiparticle trapped in the junction (see the schematic in Figure 2.11b). Hence this is called a *fermion parity switch* (fps), because the parity of the number of fermions in the junction ground state changes[8]. This is a quantum phase

---

[8]Note that the transition is only a change of *ground state* parity, because if the transition is swept fast, the junction will remain in the initial parity state unless a quasiparticle enters or leaves the ABS by a poisoning or

transition from a ground state with singlet spin-character to a doublet ground state, thus it is also often called a *singlet to doublet transition*. A related phenomenon is the so called *0-π transition*, where the supercurrent reverses sign (van Dam et al., 2006), because the energy minimum of the phase dispersion of the ground state is at $\varphi = \pi$ instead of 0. Often a singlet-doublet transition is also a 0-π transition, but not necessarily, as it depends on the dispersion of the odd-parity many body state. Even weak interactions can give a π shifted contribution to the dispersion of the continuum for the odd parity many body state, thus making a parity switch also a 0-π shift (Kurilovich et al., 2021). However, for a short junction without spin-orbit coupling and interactions, when a quasiparticle enters the junction at zero field, the supercurrent in that manifold is blocked and the odd parity state is dispersionless (see section Section 2.2.3), thus having no 0-π transition. Magnetic field then is able to cause a 0-π transition, but this is generally at higher field than the singlet-doublet transition at $\varphi = \pi$ (Yokoyama et al., 2013).

The ground state parity switch can also be seen from the many body state energies, shown in Figure 2.11d relative to the zero field ground state $|V\rangle$, where it becomes clear that after the parity switch $|\downarrow_a\rangle$ is the new ground state.

Towards a directly driven superconducting spin(orbit)-qubit
Another important consequence of a magnetic field perpendicular to the spin-orbit field is that the matrix element of spin-flip transitions increases, both between manifolds and within a manifold (Park and Yeyati, 2017) [9]. Together with an increase in population of the $|\downarrow_a\rangle$ after the parity switch, this enables direct driving of the Andreev spin-flip D_a : $|\downarrow_a\rangle \rightarrow |\uparrow_a\rangle$, as visible in the microwave absorption of Figure 2.11e. However, note that the matrix element calculated using the current operator in our model is generally still much smaller than the pair-transition by a factor of $10-100$ (van Heck et al., 2017). Therefore the simulation settings in Figure 2.11 were chosen at a point close to the band bottom, such that the low lying ABS manifold was only slightly dispersing, and both transitions were equally visible in the absorption spectrum.

Experiments focusing on transitions involving a spin-flip, either in strongly coupled junctions (Chapters 5 and 6, Tosi et al. (2019); Hays et al. (2020, 2021)), or in quantum dot junctions (Chapter 7, Bargerbos et al. (2023a); Pita-Vidal et al. (2023a)), generally observed for some gate-settings strongly visible spin-flip transitions. This points towards mechanisms other than the current-operator considered in the model as the dominating driving mechanism such as voltage modulation of chemical potential, barriers, g-factors or EDSR which is currently an active topic of research (Hays, 2021; Metzger, 2022; Pita-Vidal et al., 2023a).

Effective g-factor of ABS manifolds
As described by the start of this section, the *g*-factor of the Andreev manifold is not necessarily equal to the bare g-factor of the semiconductor. Generally in hybrid systems, dependent on the wavefunction weight in the superconductor and semiconductor, the *g*-factor lies between that of the superconductor, which for Al is 2, and -15 (-55) for InAs (InSb) (Winkler et al., 2019). For ABS in a junction with spin-orbit coupling, the effective

---

 pair breaking event.
[9]see also the supplementary information of Chapter 5

g-factor depends on phase-difference, the bound state transparancy and chemical potential as well. For a short junction this was analytically calculated in van Heck et al. (2017). In this work, a few trends can be seen: the effective g-factor *decreases* with increasing chemical potential (i.e. the distance to the band bottom), as the effective spin-polarization due to Rashba spin-orbit *increases* with the Fermi-velocity. For the transparency dependence of the bound state two regimes can be identified. At low chemical potential such that $\mu \ll m\alpha^2$ the g-factor scales inversely with transparency, while for the opposite limit $\mu \gg m\alpha^2$, the effective g-factor scales with increasing transparancy.

This has several consequences. First, the ABS transparency is highly tunable with gates in presence of microscopic disorder, thus the effective g-factor is expected to vary with gate, as observed in Chapter 5. Second, the effective g-factor of different manifolds is expected to differ from one and another.

Additional effects of magnetic field

A detailed treatment of more manifolds in magnetic field and topological phase-transitions is beyond the scope of this introductory theory and many existing works treat the effect of magnetic field on the ABS spectrum theoretically (Cheng and Lutchyn, 2012; Väyrynen et al., 2015; Peng et al., 2016; van Heck et al., 2017; Cayao et al., 2018; Zuo et al., 2017; Murthy et al., 2020). Here I summarize some of the features that are relevant for the data in our work.

- Chapter 4 describes the presence of at least two ABS manifolds (either due to mutliple conduction channels, or due to higher harmonics from a long junction), spin-orbit coupling allows *driving of mixed pair transitions to parallel spin final states* that can be seen as splitting a Cooper pair and exciting two Andreev levels in different manifolds with similar spin direction. This implies a coupling of these states to the ground state, thus inducing local triplet pairing in the junction ground state. This local triplet pairing can be seen as the hybrid equivalent of the search for triplet supercurrent in junctions made of magnetic structures (Khaire et al., 2010; Robinson et al., 2010; Sprungmann et al., 2010; Linder and Robinson, 2015) and metals with spin-orbit coupling (Jeon et al., 2020; Cai et al., 2021; Yang et al., 2021; Ahmad et al., 2022). The triplet Cooper pairs carry a net spin in the junction, which can be relevant for spintronics applications– given the relaxation time of the spin in the leads is sufficiently long. Additionally, this opens up *even parity Andreev spin qubits*, i.e. manipulating the spin of Cooper pairs, coherently. However, it remains to be seen if the ground state can be tuned into a spin-triplet state, as this was not yet shown in our work in Chapter 5.

- When several conduction channels are populated, and in presence of spin-orbit coupling, or orbital effect of the magnetic field, the ground state can have a free energy minimum at a phase difference *other than* $\varphi = 0$. This is called the *anomalous Josephson effect* and implies in general that a DC supercurrent is flowing through the junction without an applied phase difference (Krive et al., 2004; Zazunov et al., 2009; Brunetti et al., 2013; Reynoso et al., 2012; Yokoyama et al., 2014, 2013; Bergeret and Tokatly, 2015; Campagnano et al., 2015). In Chapter 5 we observe this effect directly in the microwave spectrum.

- For the type of hybrid superconducting-semiconducting nanowires studied in this thesis, under specific requirements of disorder (Das Sarma and Pan, 2021), the competition of spin-orbit coupling and the Zeeman effect induced by a parallel magnetic field is predicted lead to a bulk triplet pairing (Lutchyn et al., 2010; Oreg et al., 2010; Alicea, 2010; Potter and Lee, 2011), and the associated *topological phase* with Majorana zero modes (Kitaev, 2001; Ivanov, 2001; Read and Green, 2000). The current phase relation then becomes 4π-periodic in the adiabatic limit[10], because after a 2π phase evolution the ground state parity changes and only after a 4π rotation the junction is back to the original state. Signatures of this effect in the ABS (microwave) spectrum are discussed extensively in Refs. van Heck et al. (2017); Peng et al. (2016); Cayao et al. (2018); Väyrynen et al. (2015); Cayao et al. (2018).

2.2.6 Effects of electron-electron interactions

So far we have neglected electron-electron ($e-e$) interactions present in the junction. The considered case so far has been one where the superconducting leads are strongly coupled to the junction region, and most charging effects are screened, thus neglecting charging effects seems to be a reasonable assumption. For the case of weak coupling between the leads and the normal region, such that effectively a quantum dot forms between the superconductor, it is well known that interactions play a strong role (Anderson, 1961; De Franceschi et al., 2010).

A quantum dot weakly coupled to superconducting leads

We consider a junction where the normal region is only weakly coupled to the superconductor, for example by electrostatically defining tunnel barriers using gate electrodes in a nanowire junction (as done in Chapter 7). Here, the model used so far is no longer applicable as the charging energy U becomes an important energy scale. For example, for a

---

[10]ignoring quasiparticle number changing effects by interaction with the environment.
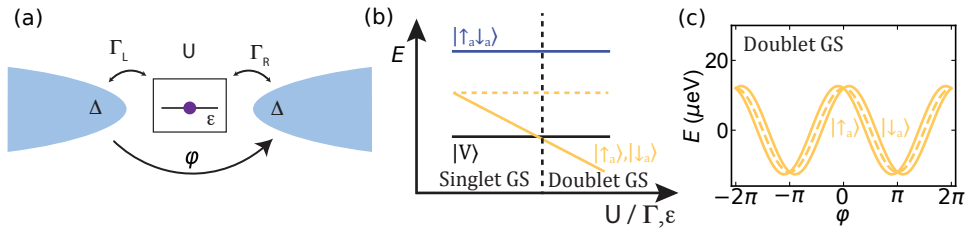
Figure 2.12: **Summary of the effect of interactions for a quantum dot weakly coupled to superconducting leads.** (a) Representation of the single impurity Anderson model with superconducting leads and relevant parameters. A single degenerate level at energy ϵ is coupled with tunneling rates Γ_L, Γ_R to two superconducting leads with gap Δ and phase difference φ. (b) Sketch of the effect of interaction strength U on the low lying singlet and doublet states of the junction according to the Anderson model in the limit $\Delta \to \infty$ relative to $|V\rangle$. (c) Effect of spin-orbit coupling on the doublet states following the phenomenological model of Equation (2.29) described in Padurariu and Nazarov (2010), in the regime where $U \gg \Gamma, \epsilon$ and the doublet is the ground state. This type of dispersion is observed in Chapter 7. Parameters used were those found in typical experiments (Pita-Vidal et al. (2023a), Chapter 7) $E_{SO} = 1\,\text{GHz}, E_0 = 3\,\text{GHz}$ and $E_Z = 0$.

quantum dot with a large level-spacing such that only a single level is relevant, charging energy can be written as a term of the form

$$H_c = U n_\uparrow n_\downarrow, \tag{2.28}$$

where $n_\sigma = d_\sigma^\dagger d_\sigma$ and $d_\sigma^\dagger$ is the creation operator for an electron in the dot with spin σ. Thus, U represents the energy cost of adding an additional electron after one is already present due to Coulomb interaction. The consequence of such a term is that it is in general no longer possible to solve the BdG equation for the single-particle energies and add the energy of occupied levels together to obtain the many-body states as we did before.

A well-known model for a quantum-dot Josepshon junction is generally given by the extension of a single impurity Anderson model (Anderson, 1961) coupled to superconducting leads (Glazman and Matveev, 1994, 1989). A detailed derivation of such a model and its solutions is beyond the scope of this work, but I refer the interested reader to a recent introductory chapter written by my colleague (Bargerbos, 2023), review articles (De Franceschi et al., 2010; Martín-Rodero and Levy Yeyati, 2011; Meden, 2019) and references therein.

The solutions to the extended Anderson model can be parameterized with a few characteristic parameters shown in Figure 2.12a. Namely, the charging energy U, tunneling rates to the left and right lead Γ_L, Γ_R, energy of the spin-degenerate level ϵ, superconducting gap Δ in the leads and phase difference φ between the superconducting condensate on the left and right side. The solution to this system is generally not analytically tractable. Only in certain limits, such as the "atomic limit" $\Delta \rightarrow \infty$ analytic where BCS-like solutions exist for the bound state energies (Meng et al., 2009) The main effect of interactions in the Anderson model that I wish to highlight here is a predicted phase-transition boundary between a singlet ground state and doublet ground state as U becomes larger than both the tunneling rates Γ_L, Γ_R and the detuning of the level from the Fermi-level ϵ, which arises from the competition between charging energy and superconducting pairing(Figure 2.12b). Finally, note that the dispersion of the ABS found using the Anderson model with $U \rightarrow 0$ reduces to that of a resonant level described by Beenakker and van Houten (1992).

From Figure 2.12b can be seen that the doublet ground state is predicted to be degenerate in the Anderson model. It turns out that it is possible to obtain similar spin-split dispersions for the doublet states in the weakly coupled regime of small Γ and large U as was shown earlier for the strongly coupled case of a finite length junction without charging energy(Figures 2.7 to 2.9). This behaviour was observed experimentally in our lab a recent work Bargerbos et al. (2023a) for $U \sim 10\Delta$. Similar to the strongly coupled case these effects appear when considering multiple orbitals and spin-orbit coupling. Analogous to spin-dependent Fermi-velocities causing the propagation phase and thus the Andreev bound state energy to become spin-dependent (Equation (2.9)), now the effect is captured by effective spin-dependent tunneling rates $\Gamma_L^{\uparrow,\downarrow}, \Gamma_R^{\uparrow,\downarrow}$. Including multiple orbitals and spin-orbit coupling with interactions, and without considering explicit limiting cases for $\Delta, \Gamma_{L,R}$, makes the model not analytically solvable, thus in Bargerbos et al. (2023a) numerical renormalization group methods were used to model the data. However, an effective model proposed by Padurariu and Nazarov (2010), turns out to accurately predict

the doublet state phase dispersion

$$H = E_0 \cos(\varphi) - E_{SO} \sin(\varphi)\vec{n}\cdot\vec{\sigma} + \frac{\vec{E}_Z}{2}\vec{\sigma}. \tag{2.29}$$

Here $\vec{n}$ denotes the direction of the spin-orbit field, which for a quantum dot can in general point in an arbirtrary direction dependent on the disorder potential and gate voltage (Han et al. (2023); Pita-Vidal et al. (2023a), Chapter 7), $\vec{\sigma}$ the spin operator, and E_0 and E_{SO} are energies of which the magnitude depends on spin-independent and spin-dependent tunneling respectively and E_Z describes the effect of magnetic field. The simple Equation (2.29) fully describes the energy phase-relation of a superconducting spin embedded in a quantum dot (see Figure 2.12c), where the quantum dot adds the advantage of stabilizing the odd-parity doublet state as the ground state (since quasiparticle poisoning events become much less energetically favorable with increasing U). This is employed in Pita-Vidal et al. (2023a), Chapter 7 to built a superconducting spin qubit without the constant uncontrollable parity switches that we observe in Chapters 4 and 5 and were present in the first superconducting spin-qubit implementations Hays et al. (2020, 2021).

Interactions in the strongly coupled regime
Now one might wonder, are interactions relevant in the strongly coupled regime ($\Gamma, \Delta > U$), where U is mostly screened away? It turns out that even a small U can have a non-negligable effect on the ABS spectra and the microwave response (Kurilovich et al., 2021; Fatemi et al., 2022; Matute-Cañadas et al., 2022). For pair transitions to multiple manifolds, even small interactions compared to the gap can cause significant corrections to the many-body ABS energies as presented earlier in this section, in the form of singlet-triplet splitting at zero field (Padurariu and Nazarov, 2012; Matute-Cañadas et al., 2022). Additionally, interactions cause a particle-number dependent energy shift of the odd states relative to the even-parity states as shown for a single level in Figure 2.12b, complicating fitting of the spectra without considering interactions. In Chapter 5 we study the effect of interactions as a perturbation the ABS excitations and measure the evolution of triplet ABS excitations in magnetic field. This can be seen as an equivalent to how interactions create singlet-triplet splittings in multi-orbital quantum dots (Kouwenhoven et al., 2001). Here the interaction manifests as an effective exchange interaction $-JS^2$ where S is the total spin of the two excitations similar to what was predicted for an isolated mesoscopic grain (Kurland et al., 2000). We refer the interested reader to Chapter 5 for more details.

2.3 Embedding Josephson junctions in a superconducting circuit

The use of superconducting resonators to perform readout of some system of interest is based on techniques stemming from quantum optics, namely cavity quantum electro-dynamics(cQED) (Walls and Milburn, 2008) aiming at increasing the naturally extremly weak interaction between ligth and matter. A cavity (resonator) is used to increase the electric field strength locally and increase interaction with the dipole moment of atomic transitions. In circuit-QED, the cavity is implemented by a superconducting resonator and often the atom is replaced with a superconducting circuit, where the capacitively shunted cooper pair box qubit (transmon) is a famous example (Blais et al., 2004; Koch et al., 2007). For transmon qubits the coupling is capacitive, however, probing Andreev bound states in a Josephson junction naturally requires an inductive coupling instead, more akin to flux-qubits. These can be seen as the dual of charge qubits like the Cooper pair box and arose around the same time (Chiorescu et al., 2003). The essential ingredients for describing the inductive coupling of superconducting circuits to ABS will be explained in this section.

2.3.1 A Resonator galvanically coupled to a Josephson junction

A lumped-element model of a typical resonant circuit is shown in Figure 2.13a, consisting of a capacitance C_r and inductance L_r to ground. The circuit acts as a harmonic oscillator with a fundamental resonance frequency $\omega_r = \sqrt{1/L_r C_r}$, which can be described the single mode Hamiltonian H_R

$$H_R = \hbar \omega_r \left(\hat{a}^\dagger \hat{a} + \frac{1}{2} \right) \tag{2.30}$$

where $\omega_R/2\pi$ is the resonator mode frequency.

In order to utilize the resonator to probe the properties of the nanowire Josephson junction as done in Chapters 4 to 6, we embed the nanowire Josepshon junction in a rf-SQUID and place it in series with the inductance of the resonator as shown in Figure 2.13b. Initial experiments focusing on circuit-QED probing of Andreev bound states coupled via placing the SQUID loop close to a current antinode (where the magnetic field fluctuations are largest) of a distributed element resonator, creating a mutual inductance between the loop and resonator (Janvier et al., 2015; Hays et al., 2018; Tosi et al., 2019). Here we use a direct galvanic connection between the resonator and SQUID loop in combination with high kinetic inductance material instead, which has the advantage that the coupling does not depend on the loop size. This allows to make the effective area of the loop ~ 3 orders of magnitude smaller compared to earlier works (Tosi et al., 2019; Hays et al., 2018, 2020, 2021), which reduces flux noise in a large magnetic field. As explained in the following, the resulting coupling between the resonator mode and the degrees of freedom of the junction can still be written as a mutual inductance term.

The degree of freedom belonging to the Andreev states in the junction are described by $H_A(\phi)$, where ϕ is the superconducting phase difference between the leads. This phase difference is further perturbed by a small AC flux coming from the resonator mode (Hays et al., 2020; Bretheau, 2013), such that the total Hamiltonian is given by

$$H = H_R + H_A(\phi + p\hat{\phi}_{zpf}) \tag{2.31}$$
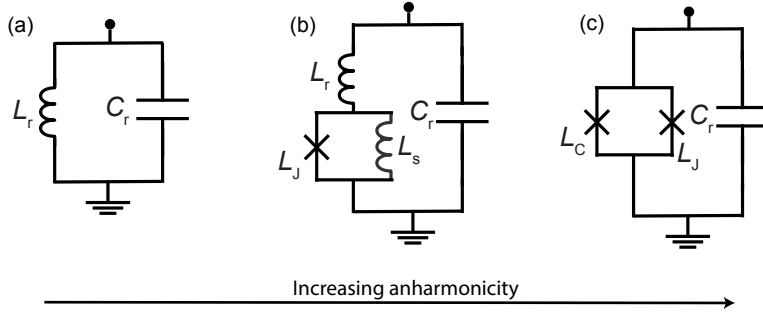
Figure 2.13: Diagrams of superconducting (an)harmonic oscillator circuits used to investigate the nanowire Josephson junctions in this thesis ordered by increasing anharmonicity and sensitivity of the resonance frequency to the junciton inductance L_j from left to right. (a) Harmonic oscillator circuit consisting of a linear capacitance and inductance. (b) Same LC circuit, but with an rf-SQUID put in series with the inductance of the resonator, used in Chapters 4 to 6 for probing the Andreev spectrum. (c) Transmon circuit where the non-linear inductance of the Josephson junctions determines all of the inductance of the LC oscillator, making it an anharmonic oscillator. This was used in Chapter 7 to enable stronger coupling of the resonance frequency to the inductance of the nanowire Josephson junction. There, to facilitate readout in presence of the increased anharmonicity, the circuit in (c) was coupled capacitively to an additional readout resonator as shown in (a).

where ϕ is fixed by the external magnetic flux and $p\hat{\phi}_{zpf} = p\frac{\Phi_{zpf}}{\phi_0}(\hat{a}+\hat{a}^\dagger)$. In this expression, p is the fraction of the resonator mode voltage that drops across the junction. The participation ratio can be approximated by $p \approx \frac{L_s}{L_s+L_R}$ in the limit $L_j \gg L_s$. The zero-point fluctuation of the mode $\Phi_{zpf} = \sqrt{\frac{\hbar Z_R}{2}}$ is set by the total resonator impedance $Z_R = \sqrt{\frac{L}{C}}$ (Vool and Devoret, 2017). Using a second order Taylor expansion around ϕ, the Hamiltonian can be written as

$$H \approx \hbar\omega_R\left(\hat{a}^\dagger\hat{a}+1/2\right) + H_A(\phi) + \frac{\partial H_A}{\partial\phi}(\phi)\frac{p\phi_{zpf}}{\phi_0}\left(\hat{a}+\hat{a}^\dagger\right)$$
$$+ \frac{1}{2}\frac{\partial^2 H_A}{\partial\phi^2}(\phi)\frac{p^2\phi_{zpf}^2}{\phi_0^2}\left(\hat{a}+\hat{a}^\dagger\right)^2$$

(2.32)

Additionally, the rotating wave approximation yields [11]

$$H = \left(\hbar\omega_R + \frac{\partial^2 H_A}{\partial\phi^2}\frac{p^2\phi_{zpf}^2}{\phi_0^2}\right)\left(\hat{a}^\dagger\hat{a}+1/2\right)$$
$$+ H_A + \frac{\partial H_A}{\partial\phi}\frac{p\phi_{zpf}}{\phi_0}\left(\hat{a}+\hat{a}^\dagger\right)$$
$$= \left(\hbar\omega_R + \hat{L}_A^{-1}p^2\phi_{zpf}^2\right)\left(\hat{a}^\dagger\hat{a}+1/2\right)$$
$$+ H_A + \hat{I}_A p\phi_{zpf}\left(\hat{a}+\hat{a}^\dagger\right)$$

(2.33)

---

[11]dropping fast rotating terms involving 2 resonator photons $\hat{a}^\dagger\hat{a}^\dagger$, $\hat{a}\hat{a}$ and making use of $[\hat{a},\hat{a}^\dagger]=1$

where we dropped the explicit dependence on ϕ and in the last line we used the definition of the inverse inductance operator $\hat{L}_A^{-1} = \frac{1}{\phi_0^2} \frac{\partial^2 H_A}{\partial \phi^2}$ and the current operator $\hat{I}_A = \frac{1}{\phi_0} \frac{\partial H_A}{\partial \phi}$. From this we can see two contributions to the resonator frequency.

One inductive part from the second order term: $\hbar \chi_2 \approx \langle \hat{L}_A^{-1} \rangle \, p^2 \phi_{zpf}^2$ due to the effective inductance of the Andreev states. This shift is the same as you would get when you consider the junction as a classical inductor with inverse inductance given by $\langle \hat{L}_A^{-1} \rangle$. Recently in our lab, radio-frequency measurements of quantum capacitance $C_q \sim \left(\frac{d^2 H}{dq^2} \right)^{-1}$ (de Jong et al., 2019), where q is the charge, have led to fast high-fidelity readout of quantum dots. Thus, for radio-frequency readout of Josephson junctions, the readout of quantum inductance can be seen as the dual of quantum capacitance as charge is the dual of phase. A good summary of this viewpoint can be found in Park et al. (2020).

One other contribution to the resonator frequency shift comes from the first order coupling term $\hat{I}_A \, p \, \phi_{zpf} \left(\hat{a} + \hat{a}^\dagger \right)$ [12]. As shown in Section 2.3.2, the current operator corresponding to a single Andreev level is generally not diagonal in the basis of energy eigenstates, and contains an off-diagnal σ_x term (Zazunov et al., 2005; Metzger et al., 2021), where σ_i denote the Pauli matrices for the two-level system spanned by the Andreev states under consideration. This term leads to a typical dispersive shift of the resonator frequency as discussed below for the simplest pair transition example.

In the design of the shunt inductance for the SQUID there are two practical constraints:

- The shunt inductance L_s must be much smaller than the resonator inductance L_r to keep the resonator sufficiently linear. This ensures that the resonator frequency remains fixed up to a reasonable average photon-number occupation used for readout.

- The shunt inductance must be small enough to ensure a linear relation between the applied flux through the loop and the resulting phase drop over the junction. The calculation for this geometry is provided in Chapter 5.

2.3.2 Short junction expression for resonator-junction coupling

We now discuss how the current and inductance operators would look like for the general expression of Equation (2.33) in the simplest case where H_A consists of a single manifold in the short junction limit as described by Beenakker (1991). The microwave transition under consideration is the pair transition, where a cooper pair is broken and two degenerate ABS levels are excited (shown schematically in the upper row of Figure 2.3).

Assuming a single transparent ABS doublet, the current operator can be written as (Zazunov et al., 2003, 2005; Bretheau, 2013):

$$\hat{I}_A (\phi) = I_A \left(\sigma_z + \sqrt{1-\tau} \tan(\phi/2) \sigma_x \right) \tag{2.34}$$

---

[12]Note that the term $\hat{I}_A \, p \, \phi_{zpf} \left(\hat{a} + \hat{a}^\dagger \right)$ is simply the product of current and voltage drop over the junction, which could have been written down directly as well as the coupling term, i.e. $H_c = I_A V_{RMS}/\omega_r$. This term is a bit more intuitive at it is clear that this has units of energy and shows how the voltage induced by the resonator drive a current through the JJ. However, it is nice to see that the Taylor expansion results in the same term if only expanded up to first order.

where and $I_A = \frac{\Delta^*}{4\phi_0} \frac{\tau \sin(\phi)}{\sqrt{1-\tau \sin^2(\phi/2)}}$ is the expected supercurrent for a single transparent chan-
nel, and σ_i indicate the Pauli matrices for the two-level system spanned by the even parity
subspace. The inductance operator is given by

$$\hat{L}_A^{-1}(\phi) = L_A^{-1}(\phi)\left(\sigma_z - \frac{2\sqrt{1-\tau}\sin(\phi)}{\tau + (2-\tau)\cos(\phi)}\sigma_y\right), \tag{2.35}$$

with $L_A^{-1} = \frac{I_A}{\varphi_0} \frac{\tau + (2-\tau)\cos(\phi)}{2\sin(\phi)}$.

Combining Eqs. (2.33) and (2.34) we obtain an effective coupling strength to first order
$\hbar g = p\phi_{\text{zpf}} I_A \sqrt{1-\tau} \tan(\phi/2)$, which yields a dispersive shift $\chi_{\text{disp}} = \frac{g^2}{(\omega_A - \omega_r)}$. The inductive
shift is given by combing Eqs. (2.35) and (2.33) yielding $\chi_{\text{ind}} = p^2 \phi_{\text{zpf}}^2 L_A^{-1}/\hbar$, which be-
comes the dominant contribution away from $\phi = \pi$ for highly transparent ABS. The total
resonator shift δf is obtained by summing the dispersive and inductive shift

$$2\pi\delta f(\phi) = \chi_{\text{disp}}(\phi) + \chi_{\text{ind}}(\phi). \tag{2.36}$$

In Figure 6.14 we plot the resulting dispersive and inductive shift and their sum, these
are used to fit the data in Chapter 6. For more complex situations, involving longer junc-
tions and spin-orbit coupling, i.e. multiple ABS manifolds and odd-parity states, the total
shift is the sum of all invidual shifts caused by each possible transition between available
ABS levels. Recently, Metzger et al. (2021) beautifully mapped out how each of the possible
transitions contribute to the total resonator frequency shift, without a magnetic field and
e-e interaction present. Additionally, in presence of interactions Kurilovich et al. (2021)
show that the continuum, which is often neglected, also plays a non-negligable role in
the total shift. Although at the time of writing of this thesis, no explicit works aimed at
calculating the expected resonator shifts in magnetic fields exist, examples do exist that
discuss the linear microwave response (the first order term) in presence of magnetic field,
e.g. van Heck et al. (2017); Peng et al. (2016) for short junctions and Väyrynen et al. (2015)
for longer junctions.

2.3.3 Embbeding the nanowire Josephson junction in a transmon
For the experiments of Chapter 7 we embedded the nanowire Josephson junction into a
transmon circuit as shown in Figure 2.13c. This can be seen as the limit where $p \to 1$
and thus the "resonator" inductance is dominated by the non-linear inductance of the
junction and the oscillator becomes anharmonic. This allows for stronger sensitivity of
the resonance frequency of the transmon to the states in the junction, which is useful to
detect spin-splitting and ground state properties. Additionally, by coupling an additional
(linear) readout resonator to the transmon, the sensitivity can be tuned in situ by moving
the transmon frequency either closer or further away from the resonator, this additional
tuning knob was exploited with success in the recent works from our group (Bargerbos
et al., 2022, 2023a; Pita-Vidal et al., 2023a).

The description of the transmon becomes somewhat different compared to the descrip-
tion of the coupling between the harmonic oscillator and the junction. So far, we have
considered the phase difference over the Josephson junction as a classical variable. In a

transmon circuit, the phase-fluctutations are no longer small and thus, the macroscopic phase difference over the JJ is no longer a good quantum number and we have to replace it with a quantum operator. The typical Hamiltonian for a transmon circuit is given by (Koch et al., 2007)

$$H_T = 4E_C\hat{n}^2 + H_J(\hat{\phi}) \tag{2.37}$$

Where $E_C = \frac{2e^2}{C_\Sigma}$ is the charging energy of the island and C_Σ the total island capacitance. For a tunneling junction, or a nanowire junction opened with a gate into the many channel regime we obtain to first order:

$$H_J = -E_J \cos\left(\hat{\phi}\right) \tag{2.38}$$

The anharmonicity α of the transmon is approximately $\alpha = -E_C$ and the charge dispersion scales as $e^{-\sqrt{8E_J/E_C}}$. To illustrate some numbers, for Chapter 7 we use $E_C/h = 200\,\mathrm{MHz}$ ($C_\Sigma = 100\,\mathrm{fF}$) and $E_J/h \sim 6 - 20\,\mathrm{GHz}$, which is tunable with the gate voltage underneath the nanowire. Thus we have $E_J/E_C \geq 30$.

In our experiments SQUID loop in Figure 2.13 contains two junctions, thus the total Hamiltonian is given by

$$H_T = 4E_C\hat{n}^2 + H_J(\hat{\phi}) + H_A(\hat{\phi} - \phi_E) \tag{2.39}$$

where $\phi_E = 2\pi\Phi_E/\Phi_0$, if the Josephson junction is a quantum dot as used in Bargerbos et al. (2022, 2023a); Pita-Vidal et al. (2023a) and Chapter 7, $H_A(\phi) = E_J^I \cos(\phi) + E_J^\sigma \sigma_z \sin(\phi)$ (as discussed in Section 2.2.6), where E_J^I denotes the spin-independent contribution, E_J^σ the spin-dependent contribution and σ_z refers to the spin degree of freedom of the Andreev spin. In Chapter 7, we describe the extension of this circuit for creating strong spin-spin coupling. There we embed two Andreev spin qubits in the SQUID by adding another junction in paralllel as proposed by Padurariu and Nazarov (2010).

3

Experimental methods

Beter één vogel in de hand, dan tien in de lucht...

Dutch proverb

3.1 Superconducting chip design

In this thesis, we use superconducting circuits to probe physics with radio-frequency (RF) microwave signals. The advantage of using superconducting circuits as a tool to probe condensed matter is that it allows to design for high sensitivity to the device under test and high energy resolution spectroscopy. This unfortunately comes with a drawback: the circuit design becomes non-trivial. Thus, the lead time to go from an experimental idea towards actually starting the fabrication is often much longer compared to using conventional DC-transport techniques. Additionally, all time spent on optimizing and designing the circuit is time not spent on studying the underlying physics. For this purpose, we have tried to optimize the workflow in our team to allow for the least possible time lost in the design and fabrication[1], which is summarized in Fig. 3.1.
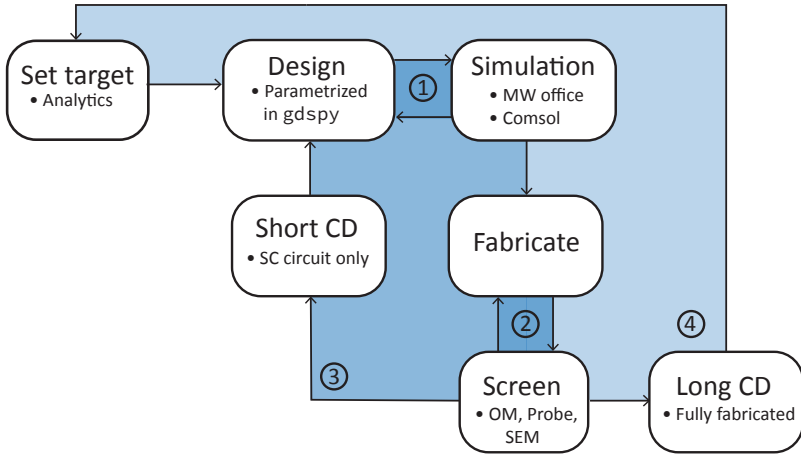
Figure 3.1: **Device creation process.** Each block describes a process performed, with arrows indicating the next step. At some points, arrows point towards steps that have already been performed and create feedback loops (same shade background) that describe iterative processes. The numbers indicate the smallest enclosing feedback loop. For example, loop 1 is the iterative process where the output of the design is simulated and subsequently modified to converge towards the target parameters. Detailed explanation for the steps and acronyms can be found in the main text.

The first step of every project is to *set the target*. Next to the wish-list of on-chip components, this consists of analytical calculations of desired couplings and frequencies and how that translates to physical capacitances, inductances and size. This is followed by coding up the chip *design*, which is done in Python using the gdspy package. The design step results in a .gds file, which is a standard integrated circuit (IC) fabrication file type and consists of layers of 2-dimensional patterns that each represent an e-beam lithography patterning step. The design philosophy here is, that by defining the chip design in Python, each chip element can be parameterized and thus quickly adapted when needed, without requiring a complete overhaul of all other parts of the design. This requires initially more

---

[1]Unfortunately this is still in general a considerable fraction of the total time spent in a project and improvements the flow are definitely welcome and recommended.

effort on the design side compared to using graphical drawing software such as AutoCAD (which used to be the standard in our group), but saves a lot of time in the following iteration steps. A second advantage is that one has programmatic access to the geometry, allowing estimations of the total inductance of a resonator instantly when changing the design.

We then perform *simulation* of the circuit layer in Comsol for calculating capacitances and in Microwave Office (MWO) for obtaining resonator frequencies and coupling quality factors. Here we tried to automate as much as possible by making the design code output an inverted version of the superconducting circuit layers and include only a small ground-plane region around each resonator to limit the simulation time. Microwave Office uses a finite element simulation of the microwave response with a 2.5-dimensional method of moments solver, which can efficiently combine layers, i.e. dielectrics, that do not vary in the x-y plane with circuit layers that do vary. This is especially suited for IC design simulation. The simulations often result in design changes, as indicated by loop 1 in Fig. 3.1. For the Microwave Office simulations to be accurate, the dielectric constant of the Si substrate, $\epsilon_r = 11.7$, and the kinetic inductance per square, around $10\,\mathrm{pH}/\square$ for a 20 nm thick NbTiN film , are added as material settings.

When the simulations indicate that the couplings, quality factors and resonance frequencies are as desired we continue towards the *fabrication* of the chips, of which the precise steps are described in section 3.2. During the fabrication, each step and the final result is *screened* using for instance optical microscopy (OM), probing of the sheet resistance of the NbTiN film and scanning electron microscopocy (SEM) to get accurate doses for the sub-micrometer wide features such as the inductors and gates. The screening at each fabrication step can provide early warning signs that a step failed and the fabrication should start over, indicated with loop 2 in Fig. 3.1. To increase the yield when faced with many required fabrication steps, we often fabricate in a pyramid-scheme where we start out in the first step with several dies with many chips each (as there is often no additional time cost associated with doing a single step on many chips). Subsequent steps are then performed only on a selection of the devices such that when a step inevitably fails the chips that are one step behind can be used and the fabrication can be continued. The hope is that, at the last step, we are left with at least one working device, without having to start the whole pyramid anew.

When a design is new and untested, we generally first perform the fabrication steps involving only the superconducting circuit patterning, which is then loaded in either a quick-test fridge[2] or (if available) the dilution refrigerator for a *short cooldown (CD)*. This only takes a few days of loading and cooling down and can already show whether the circuit is behaving as designed and the resonators are "alive". As this is unfortunately often not the case, feedback loop 3 indicates going back to the design phase and updating the circuit design before running this test again. This step also serves as the best feedback on what kinetic inductance we should use in the simulations to target resonator frequencies, as this can vary typically by approximately $10 - 20\%$ for 20 nm NbTiN films, dependent

---

[2]Often we use the Heliox, a dipstick kindly made available to us from the neighbouring superconducting qubit group of L. DiCarlo. This dipstick includes a sorb with He^{-3} and can reach 300 mK, which is well below the 9 K critical temperature of NbTiN films. Additionally, below 1 K we generally don't see the internal quality factors of the resonators decrease so this can also test how well the resonator design in combination with the fabrication stack performs.

on whether it is a newly deposited film and location on the wafer. If this step succeeds, it dramatically increases the certainty that when you claim you need time in the dilution refrigerator (and ask your coworkers to deposit nanowires for you), you can actually use it to measure a working device! Finally, the last and the longest loop, number 4, indicates that after a *long cooldown (CD)*, we still find features in the circuits that can be improved in next design generations or in designs of other group members. This serves more as a "collective memory" of the group. Examples of these elements include optimization of the gateline filter order, resonator shapes and geometry, hole-patterning areas, and asymmetric input ports for the feedline.

3.1.1 Description of superconducting circuit elements

In this section we give an overview of the typical elements used in our superconducting circuits, accompanied when relevant with simulations.
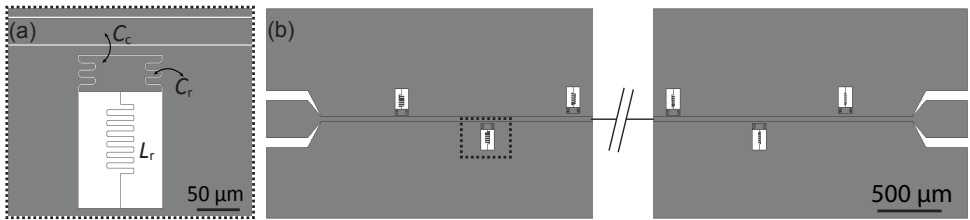
Figure 3.2: **Feedline with multiple devices coupled to it for transmission readout.** (a) Zoom in of example lumped element resonator that is capacitively coupled to the feedline (dashed box in (b)). The capacitance of the resonator is implemented using an in-plane capacitance to ground C_r and to the feedline C_c. The capacitor plate is connected to ground via an thin meandering strip of NbTiN that has a high kinetic inductance L_r forming the LC resonance circuit. (b) Left and right sides of a full (7 mm-long) chip with in total 9 resonators (3 not shown) coupled to it, which was fabricated for a resonator test run.

The feedline

All our devices start with a *feedline*, this is an impedance-matched coplanar waveguide that has an input and output port (see Ref. Pozar (2012) for an introduction to distributed element microwave components). Since the characteristic impedance of commercially available coaxial cables is 50 Ω, we match the printed-circuit board lines (see section 3.3.2) and the on-chip waveguides to have 50 Ω characteristic impedance as well. This is done to minimize reflections that arise from impedance mismatches, and thus allow most of the signal that we send to our device to arrive there. Additionally, due to interference, a not-well matched configuration can have standing waves which appear as resonances, or large (periodic) peaks/dips in the transmitted signal through your system[3].

Although, in principle, a feedline is not needed —one can simply bond from the PCB to a resonator directly, as is often done— we generally employ it because it allows us to use one input/output line with multiple coupled devices[4]. The number varies gener-

---

[3] The appearance of spurious dips/peaks in the transmitted signal through a set of lines is often used as an indication that there is some issue with a cable and for the trained eye the shape or frequency of the dip(s) can tell a lot about what the precise issue is!

[4] We generally call one resonator a device, as it then either incorporates the nanowire as part of the inductance (Chapters 4 to 6), or a transmon coupled to it, which contains the nanowire SQUID loop (Chapter 7).

ally between 2 and 8 depending on the size of each device and other required input lines. This allows us to increase the chances of obtaining a working device in a single cooldown. When using nanowires or other semiconducting elements, the yield is generally not as high as for "pure" superconducting circuits. Additionally, having (limited) statistics about the reproducibility of the physics observed by measuring multiple devices is another benefit of this approach.
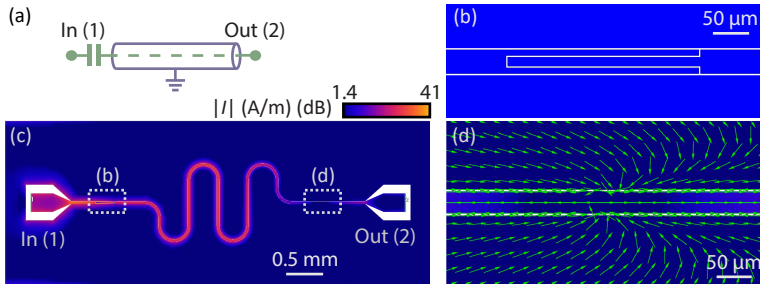
Figure 3.3: **Feedline input capacitor design and simulation of the current distribution.** (a) Circuit diagram of a coplanar-waveguide transmission line with a capacitor at its input port. (b) Design of the input capacitor, where blue denotes the NbTiN regions. (c) Current magnitude yielded by a microwave simulation performed with Microwave Office. A current node forms at a distance of approximately $l = \lambda/2$ away from the capacitor, where λ denotes the wavelength at the intended resonator frequency. (d) Enlargement of the region where the current node forms. The green arrows indicate the current direction at each point.

We later added an *input capacitor* to the feedline (see Fig. 3.3). One of the disadvantages of measuring in transmission with symmetric input and output ports, is that you always lose around 50% of the input photons that go out through the input port after reflecting of the resonator under investigation (Girvin, 2014). This reduces the signal-to-noise ratio by a factor of two. For simple characterization experiments this is not really an issue (generally one can increase the readout power to compensate). However, when interested in single-shot measurements, or photon-number sensitive measurements, the factor of two can save a lot of time! Thus, in Chapter 7 , we use an input port that is weakly coupled to the feedline. From a quantum optics point of view, the feedline can then be seen as having one very transparent mirror (to the output line) and one very reflective mirror. Thus, for an attenuation of roughly 20 dB, 99% of all photons that enter the feedline, exit through the output line. Besides the above-mentioned advantage, this brings some complications with it as well. The length of the feedline now becomes relevant, as standing waves will form as we now impose a boundary condition at the input capacitor (see Fig. 3.3(c)). Thus, dependent on the resonance frequency of the resonator that is coupled, it should be placed at a voltage anti-node, as the capacitive coupling is reduced otherwise and the resonance lineshape becomes very asymmetric. This effect is similar to if one would have a very badly impedance-matched feedline, see for example Khalil et al. (2012) for a mathematical description of this effect. Additionally, the required input power for the same amount of microwave power at the resonator rises by about 20 dB.

The resonators

Throughout this thesis we use lumped element resonators, consisting of a coplanar capacitance to ground C_r, coupling capacitance to the feedline C_c and inductance L_r set by the kinetic inductance of a thin line to ground (see Fig. 3.2). All of these elements are patterned in a single step in the NbTiN film. The resonator that we designed specifically for the ABS spectroscopy measurements is a continuation of the design used in Pita-Vidal et al. (2020) and shown with detailed SEM images in Chapters 4 and 6.[5]

We now discuss a few considerations that led to the design and choice of these resonators shown in(Figure 3.2a). We use lumped element resonators with thin wires of NbTiN as inductors (Samkharadze et al., 2016; Pita-Vidal et al., 2020). The main goal was to make them magnetic field compatible, for this reason they were made out of thin-film NbTiN, where we choose 20 nm thick films, and 300 nm wide inductors to balance magnetic field compatibility, with fabrication tolerances for frequency targeting.

Some advantages for our applications to highlight over the more "standard" coplanar waveguide resonators, which can also be made field-compatible (Kroll et al., 2019) are: The higher harmonics only arrive at higher frequencies at the self-resonance of the inductor. For the resonators in Chapter 5 we estimated it to be around 28 GHz for a resonator with $f_r \sim 4.8$ GHz. Additionally, the required perpendicular field for creating vortices near the inductors depends on the width of the inductor. Thus, they are more stable in perpendicular fields, requiring less precise magnetic field alignment in field sweeps.

For ease of design, the capacitor was made such that you could fairly independently vary C_c and C_r by placing it closer or further away from the feedline, or change the distance between the ground plane and the capacitor. In a single chip, we generally fixed the capacitance and varied the inductor length only, to change the resonator frequencies. This would make sure that all resonators move equally up or down in case of misestimate of the inductance. Generally there were global shifts of around ~ 500 MHz due to variations in the kinetic inductance in the films.

The inductor also allowed for simple targeting of the coupling between the nanowire SQUID and resonator as discussed in Section 2.3.1, by turning the participation ratio $p = \frac{L_s}{L_r+L_s}$ of the shunt inductance L_s of the total resonator inductance into a simple fraction of shunt arm length versus resonator inductor length.

For Chapter 7 we used a newer iteration of these resonator designs that was optimized and designed by another member of our lab (Feldstein Bofill, 2022).

The electrostatic gates and filters

One of the main advantages of using semiconducting components is that they allow the electron density, and thus their conductivity or inductance, to be tuned by applying an electrostatic voltage with a metal gate. However, incorporating those in superconducting circuits should be done with some care, as they can act as a loss channels for microwave

---

[5]The microwave simulations, design and testing of these resonators took quite some work in the early stages of this PhD and is described extensively in the master and bachelor theses of the former students that I had the pleasure of working with on the projects. Sebastiaan Roelofs thesis (Roelofs, 2019), contains an extensive tutorial on how to use Microwave office for beginners and part of the design simulations for Chapters 5, 4. Arjen vaartjes' thesis (Vaartjes, 2020) contains more design simulations and resonator targeting results for Chapters 5 and 4. Finally, the thesis of Pepijn Rot (Rot, 2022) contains simulations performed for Chapter 6, including detailed simulations of our first iteration of thin-film flux lines used for Chapter 7.
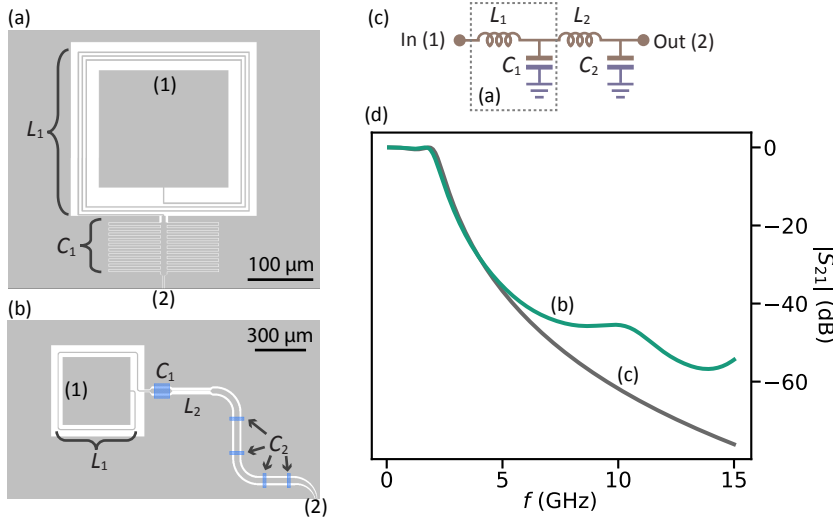
Figure 3.4: **Low-pass filters for the gate lines.** (a) First order low-pass on-chip LC filter, a design which was followed up by (b). (b) Design of a fourth-order Chebyshev filter, which is simulated using the indicated microwave ports, labeled as (1) and (2), at each end of the gate line section. (c) Circuit diagram of a fourth-order LCLC Chebyshev filter, composed of inductances $L_1 = 5.21$ nH and $L_2 = 6.13$ nH and capacitances $C_1 = 2.45$ pF and $C_2 = 2.08$ pF. Equivalent diagram of (a) is indicated with the grey dashed box (with other inductance / capacitance). (d) Simulated transmission from the input to the output port, as a function of frequency, f. The grey and green lines correspond to the circuit in (c) and to the simulation in (b), respectively.

photons. For the gates used in our devices, we generally add an on-chip low-pass LC filter that attenuates strongly at the resonance frequency of the resonator that contains the nanowire with gates . For Chapters 5, 6 and 7 we use a coplanar filter similar to that in Mi et al. (2017a), with a spiral inductor and an interdigitated capacitor (see Fig. 3.4(a)). Later, to increase the filtering strength, we moved in Chapter 7 to an improved higher order filter design where we replaced the interdigitated capacitor by parallel plate capacitors inspired by Harvey-Collard et al. (2020). We realized that we could implement the parallel-plate capacitors without an additional fabrication step because they were made at the same time as the overpasses that we already made to connect the ground plane around the gate lines (see section 3.2).

Note that the length of the gate line from the bondpad to the device can also act as a resonator. We thus tried to make this section as short as possible to keep the self-resonance frequency, where a standing wave can form inside the element, as high as possible and covered the distance from the PCB to the gate bondpads with long bond wires. Finally, if space allows it, we recommend making the bondpads for the gates large (200×200 μm) to prevent shorting your device by a misbond at the final step of device preparation[6], and facilitate rebonding the device if ever necessary.

---

[6]or find out the hard way like we did

Figure 3.5: **Scanning electron micrographs of various chip elements.** (a) Large NbTiN bridge overpass over a gate line to connect the ground plane on each side. These structures are also used as parallel plate capacitors for the filter desi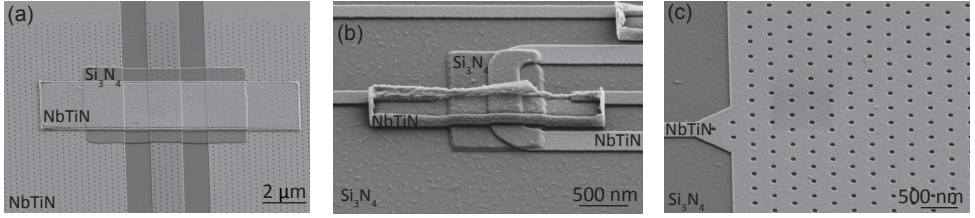gn of the gate. (b) Example of a smaller overpass to connect a gate line across a SQUID loop. (c) Part of the capacitor plate of the resonator, which is patterned with ~ 80 nm diameter vortex trapping holes in a triangular lattice.

Drive lines

In Chapter 7 we use one of the gate lines for driving spin-flip transitions, thus here we cannot apply the low-pass filtering and we directly connect it to a $50\,\Omega$ coplanar waveguide.

In this case, as opposed to the DC gate lines, we put the bondpads as close to the edge of the chip as possible to minimize the bond length and with it impedance mismatches, similar to the feedline bondpads and how it is typically done in larger superconducting qubit devices (see for instance Krinner et al. (2022)).

In Chapters 4 to 6 we utilize a single transmission line to drive four on-chip devices in order to save input lines. The coupling is then facilitated with additional capacitive coupling elements for each resonator to the drive line.

On-chip overpasses

Our standard fabrication recipe involves both a dielectric (for the gates) and a NbTiN deposition (for the contacts) step after having defined the base circuit layer. We thus use these existing steps to define bridges that connect the ground plane around the DC-lines. Since these bridges have only a ~ 28 nm layer separating the two NbTiN layers, we do not use them to connect the ground plane across the feedlines and drivelines as they would drastically change the impedance of these elements. In superconducting circuits, air-bridges are typically used in a final fabrication step, which have vacuum instead of dielectric with thus a much smaller dielectric constant Stavenga et al. (2023).

Prevention of flux jumps

An important element of the chip design is the patterning of holes in the whole chip to minimize detrimental effects of vortices. Although it is customary in the field of circuit-QED to pattern the ground plane with large holes to facilitate flux to penetrate the large area of superconductor (even the Earth magnetic field of around 40 μT is relevant there due to the large area) without inducing vortices, we additionally pattern small holes in a large area around the resonator and inside capacitors (Kroll et al., 2019) to trap vortices that are unavoidibly present in the film when exposed to magnetic fields of several hundred mT(see section 2.1.2) .

The flux bias line

For the device in Chapters 7, 6 , we use on-chip flux-bias lines to control the flux through the SQUID loops. The SQUID loops that we use are generally small, on the order of several tens of μm^2. Additionally, the flux line is fabricated in the $\sim 20\,nm$ thick base layer of NbTiN. Hence, we needed to make sure that the line can sustain enough supercurrent to allow the current that generates several flux quanta to pass through. Additionally, for compatibility with future experiments, we wanted to allow for the ability of fast-flux pulsing up to $\sim 1\,GHz$. The flux-line was therefore designed in large part as a $50\,\Omega$ coplanar waveguide similar to the feedline and driveline, which is shorted to ground near the loop that is flux-biased.

From measurements of the critical current in the flux lines, we found that we could apply maximally between around $3\,mA$ of on-chip current before the thinnest section of the flux line on-chip turned normal. Additionally, we found that the line kept around 50% of its critical current up to $1.5\,T$. In order to still be able to drive several flux quanta, the flux line needed to be placed close to the loop (as $B \propto 1/r$, with r being the distance from the flux line). To mitigate losses through the flux line, which we found to be significant in an earlier design iteration (see Chapter 6), we implemented an on-chip low-pass LC-filter similar to the gate lines. The difference is now that we could not use the thin inductors to keep the critical current maximal. We therefore implemented the filter using solely a parallel-plate capacitor, which combined with the existing inductance of the transmission line gave the filter response shown in Fig. 3.6.
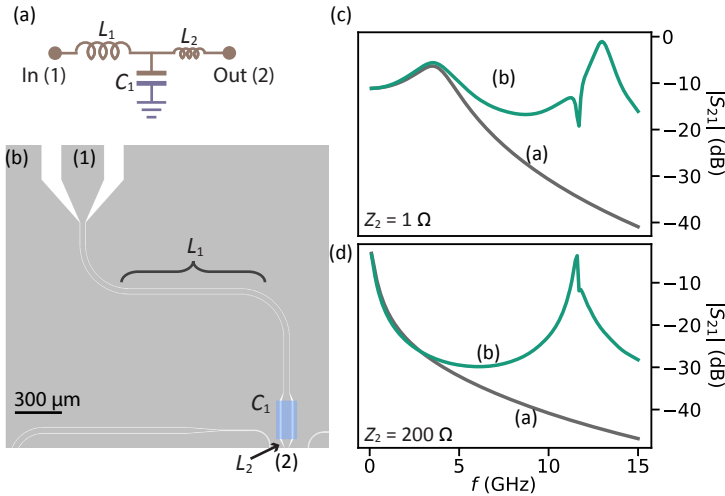
Figure 3.6: **Flux-bias line with a low-pass LC-filter.** (a) Circuit diagram of an LC filter, composed of an inductance $L_1 = 1\,nH$ and a capacitance $C_1 = 22\,pF$. An extra inductor segment, with inductance $L_2 = 0.08\,nH$ is included at the end of the filter to account for the non-idealities of the real implementation of the flux line. (b) Schematic of the simulated part of the flux line including the input and output microwave ports, labeled as 1 and 2, at each of its ends. (c) and (d) Simulated transmission from the input to the output port, as a function of frequency. The grey lines correspond to the circuit in (a) and the green lines correspond to the circuit in (b). The impedance of the input port is $50\,\Omega$ in both cases, while the impedance of the output port is $1\,\Omega$ in (c) and $200\,\Omega$ in (d).

3.1.2 COMSOL to calculate capacitance matrices

Besides simulations in Microwave Office, we often additionally use Comsol following the approach outlined in Ref. friedel (2017), to simulate coupling capacitances between resonator and feedline, resonator and transmon and between either the resonator or transmon to all other gate- and or drive-lines to check whether they are small enough to prevent leakage. An example of the simulation performed on the device used in Chapter 7 is shown in Fig. 3.7.
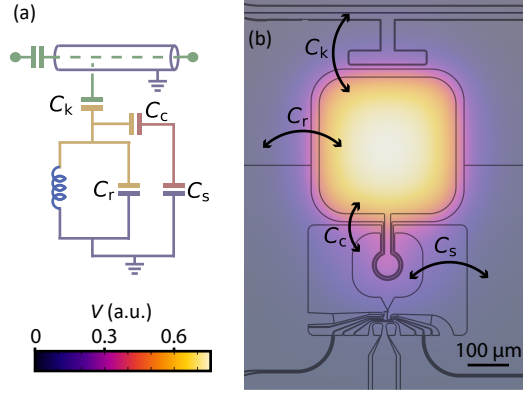
Figure 3.7: **Capacitance simulations.** (a) Circuit model of a feedline (with inner conductor in green) capacitively coupled to a resonator island (yellow) which is in turn capacitively coupled to a transmon island (red). Ground is indicated in purple. (b) Result of an electrostatics simulation performed with Comsol showing the potential, V, distribution when a certain charge is applied to the resonator island. This simulation is used to estimate the capacitance between each pair of elements.

3.2 Standard nanofabrication for InAs devices

The fabrication process for the InAs/Al nanowire-based devices employed in the experimental sections of this thesis initiates with the preparation of a complete 4-inch wafer. Over this wafer, a layer of NbTiN is deposited before the wafer is diced into smaller chips. As opposed to individual chip preparation, this method allows for higher homogeneity of the film properties across different devices and for more accurate targeting of the kinetic inductance for each device.

Most of the nanofabrication steps undergone by our hybrid devices are visually summarized in Fig. 3.8 and detailed in the following sections.

3.2.1 Wafer preparation

The wafer preparation steps prior to dicing are shown in Fig. 3.8(a)-(e). We use high resistivity silicon substrates coated with low-pressure chemical vapor deposited (LPCVD) SiN_x[7]. We generally found that the LPCVD SiN_x was not limiting resonator internal quality factors compared to subsequent fabrication steps, but allowed for higher gate-voltages before significant leakage currents appeared as opposed to for example high-resitivity sil-

---

[7]The SiN_x was deposited by Paolo M. Sberna at the Else Kooi Laboratory of the TU Delft.
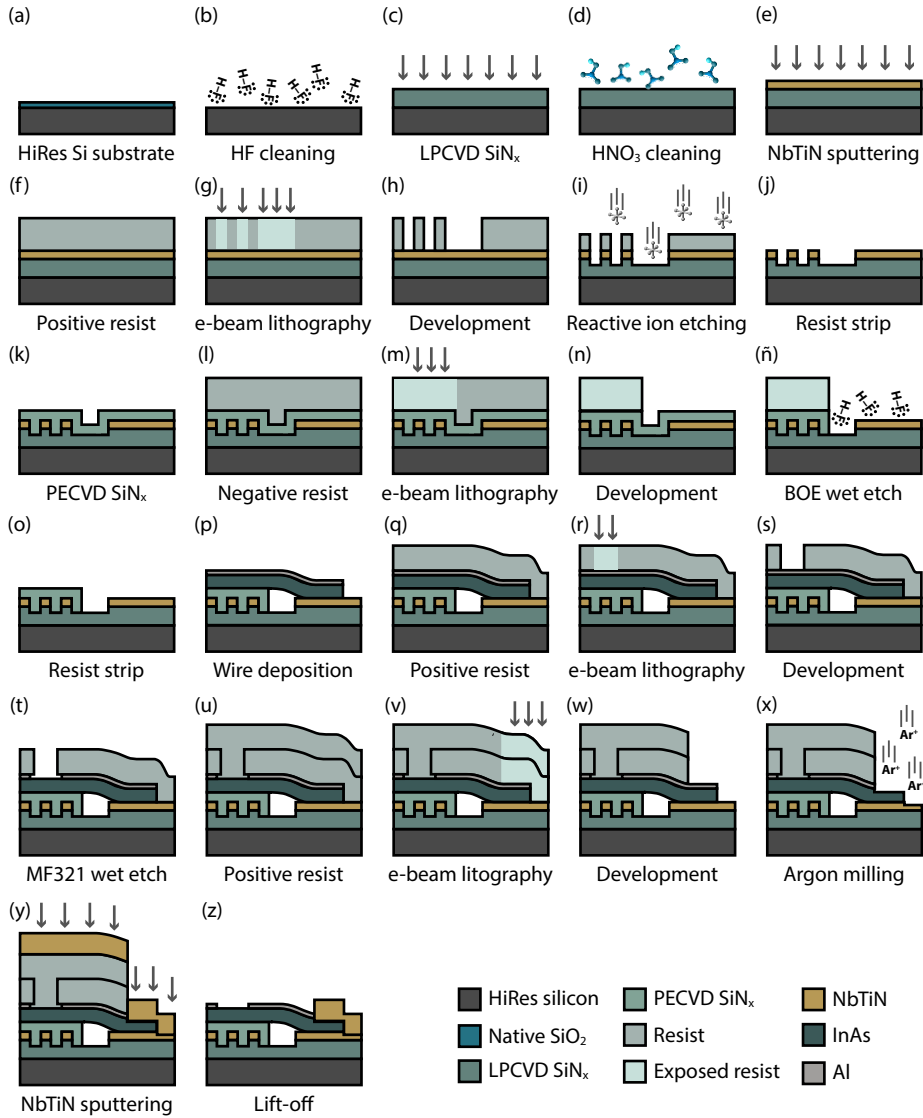
Figure 3.8: Nanofabrication steps. Diagrams showing the cross-section view after each of the nanofabrication steps undergone to fabricate a device, starting from a substrate (a) and ending with the depositing the nanowire contacts (z). The marker step and the two dicing steps —one between (e) and (f) and the other after (z)— are not shown.

icon without the SiN$_x$ layer (Splitthoff et al., 2022). Prior to the deposition of NbTiN, the substrate is cleaned with fuming nitric acid.

Subsequently, a thin film of NbTiN is sputtered onto the entire 4-inch wafer, with the film thickness determined by the targeted kinetic inductance of the film. Opting for a

thinner film results in a higher kinetic inductance and higher field compatibility. However, excessively thin films can lead to a larger variation of the kinetic inductance across the wafer, hindering accurate kinetic inductance targeting To strike a balance, we choose a film thickness of approximately 20 nm for the experiments requiring a modest kinetic inductance in the range of 10 to 15 pH/$\square$.
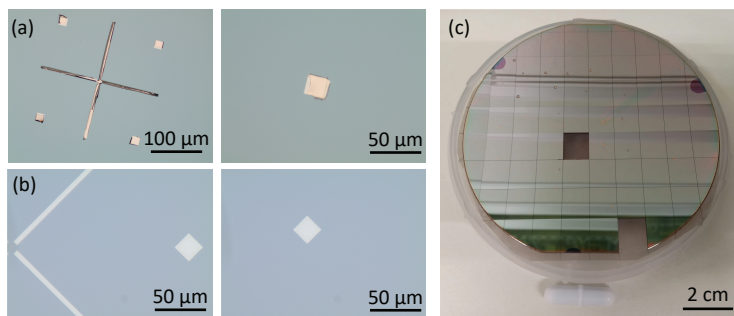
Figure 3.9: **Wafer preparation.** (a) Optical microscope images of ill-defined platinum markers obtained by performing a single evaporation step. (b) Optical microscope images of well-defined platinum markers obtained by performing three subsequent evaporation steps with cooldown times in between. (c) Photograph of a 4-inch wafer covered by dicing resist and diced onto smaller chips.

In a subsequent step, not shown in Fig. 3.8, we pattern markers across the entire wafer. The markers have a size of $20 \times 20 \ \mu m^2$ and are used for alignment at the various e-beam lithography steps. When choosing the marker material, various aspects, such as fabrication ease, contrast under the electron beam and compatibility with subsequent nanofabrication steps, must be taken into consideration. One efficient option fabrication-wise would be to define negative-tone[8] markers together with the initial NbTiN dry etching step (see next section). However, given the typically small thickness of our NbTiN layers, this approach could lead to reduced contrast under the e-beam, hampering subsequent alignment steps. Moreover, the patterning of the base etching layer for the different devices presented in this thesis involves several layers that are written with different beams. Such layers must be aligned with each other, which requires alignment markers to be present before performing this first patterning step. An alternative approach, which we used for Chapters 5, 4 , is using positive-tone gold markers with high enough thickness, on the order of 100 nm. Gold markers offer nanofabrication benefits, as they can be deposited at multiple evaporators of the Kavli Nanolab and are very easy to lift off. Moreover, the high gold atomic number translates into enhanced e-beam contrast, thanks to an increased backscattered signal. However, due to potential cross-contamination issues with other materials, gold is prohibited within certain deposition and etching cleanroom systems. In particular, it is not allowed in the reactive ion etching system used for Chapter 7 For these Chapters, we explored different alternative materials. One such option which also has a large atomic number, thus leading to high e-beam contrast, is platinum (Pt). We often found that thin films of platinum showed a high surface roughness when deposited on 4-inch wafers, resulting in ill-defined markers. Fig. 3.9(a) and (b) show Pt

---

[8]Negative-tone and positive-tone markers respectively appear darker and brighter than the surrounding material.

markers obtained from two different depositions. Despite both Pt evaporation processes using identical parameters, the Pt markers in the first deposition exhibit lift-off imperfections, absent in the second deposition. The only differences lay in that, for the markers in Fig. 3.9(a), the deposition was done over a complete 4-inch wafer and in a continuous manner, while, for those in Fig. 3.9(b), it was performed over half of a 4-inch wafer and in three subsequent deposition steps with 20 min cooldown intervals between them. We hypothesize that the imperfections found in the first deposition may be attributed to either high tensile stress on the films Afshar et al. (2010) or inadequate thermalization during metal evaporation. To avoid the complications found for Pt marker fabrication, for 6 and 7 we instead converged to using palladium (Pd) markers. Pd markers have proven simple to fabricate in a reproducible way, show enough e-beam contrast, and are compatible with most nanofabrication tools.

After marker deposition and lift-off, the wafer is coated with dicing resist and diced onto smaller chips of approximately 1×1 mm^2, as shown in Fig. 3.9(c). Subsequently, the chips are reserved and used to fabricate the different devices. The dicing resist is left on each of the chips, serving as a protective layer. The chips are then stored in a cleanroom space until further processing, a period typically spanning from a few days to several months after the wafer's initial preparation.

3.2.2 Substrate preparation prior to nanowire deposition

For each individual chip, we maximize the number of nanofabrication steps that are performed before depositing the Al/InAs nanowires. This is done to mitigate potential detrimental effects on the nanowire, which could arise from the different nanofabrication steps. Such effects can be due to factors such as electrostatic discharge, mechanical stress during e-beam resist application and lift-off, or elevated processing temperatures leading to diffusion of the aluminium shell onto the InAs nanowire core. The steps performed prior to nanowire deposition are schematically depicted in Fig. 3.8(f)-(o) and involve the definition of the NbTiN circuitry by dry etching and the subsequent deposition of the bottom gate dielectric.

The processing of an individual chip begins by removing the dicing resist using an organic solvent (not shown in Fig. 3.8). Following this, we define all of the NbTiN base layer structures using electron beam lithography. To enhance precision in regions with finer structures, such as gates and narrow inductors, we use an electron beam with a low current and a small spot size. For the coarser structures are instead patterned with an electron beam with a higher current and larger spot size, thus reducing the exposition time. Strategically adjusting the current and spot size of the electron beams across different layers results in significant reductions in overall writing time, from multiple hours down to approximately 10 to 20 minutes.

During the base layer definition step, we also pattern holes in the superconducting layer Kroll et al. (2019). The holes configuration, while always distributed in a honeycomb lattice, varies depending on the region of the device and on their function. For the regions of the ground plane near any microwave circuitry structures, as well as for the capacitive transmon and resonator pads and the inner conductor of the feedline and drive lines, we use small holes. These holes serve as pinning sites for magnetic vortices and their specific geometry varies among chapters, with diameters ranging from 70 to 100 nm and inter-hole

distances spanning 320 to 550 nm. This minimizes the disruption to the transmon and resonator capacitance, as well as to the impedance of the feedline and drive lines, values which we simulate without accounting for vortex pinning sites. For the wide ground plane regions which are far away from the main structures, we instead use larger holes with a squared shape to allow for magnetic field penetration and reduce the amount of ground plane surface that is exposed to it. These bigger holes have an edge length of 500 nm and an inter-hole spacing between 1.5 and 2.2 μm depending on the chapter, to reduce the total writing time.
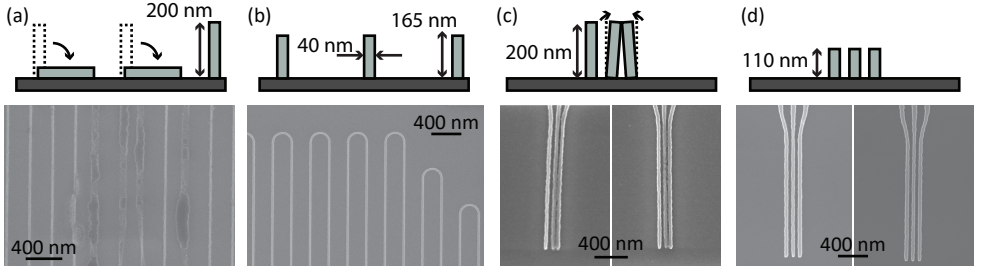
Figure 3.10: **Fine structures optimization.** (a), (b) Scanning electron micrographs (SEMs) of the typical inductors after NbTiN etch for two different resist thicknesses: 200 nm and 165 nm, respectively. (c), (d) SEMs of quantum dot junction bottom gates after NbTiN etch for two different resist thicknesses: 200 nm and 110 nm, respectively. The top panels show schematics of the device cross-section after resist development in each case.

Finally, during the e-beam patterning of the base layer we consider different aspects to enhance the definition accuracy of the fine structures. Apart from using a small-sized beam with a precisely calibrated dose, we use proximity effect correction (PEC) in the vicinity of narrow gates and inductors. Additionally, for certain devices, we develop using the critical point drying (CPD) method to ensure a more gentle process. Moreover, we found that using too thick resist can lead to undesired outcomes, as exemplified in Fig. 3.10. When we employ a 200 nm-thick e-beam resist layer (Fig. 3.10(a)), the resist often collapses due to its high aspect ratio after development, resulting in poorly defined inductor shapes. Using instead a resist layer of 165 nm leads to more reproducible and well-defined structures (Fig. 3.10(b)). In Chapter 7 we pattern 40 nm-wide gates spaced roughly 40 nm apart. A 200 nm-thick resist layer often leads to two neighboring gates shorting due to the resist's high aspect ratio, as shown in Fig. 3.10(c). Using 110 nm-thick resist instead leads to better defined gates (Fig. 3.10(d)). Note that the minimum resist thickness that can be used is in each case determined by the duration of the NbTiN etching step (Fig. 3.8(i)), during which the resist is etched at a rate of approximately 1.8 nm/s. This constrains the thickness to be at least 100 nm for Chapter 7.

For all experiments performed in this thesis, we use a SiN_x layer of approximately 28 nm as the gate dielectric. This dielectric film is first epitaxially grown over the entire chip using plasma-enhanced chemical vapor deposition (PECVD)(see Fig. 3.8(k)). It is subsequently etched so that it only remains over specific regions (see Fig. 3.8(l-o)).

3.2.3 Nanowire-specific steps

The nanowire-related nanofabrication steps, schematically depicted in Fig. 3.8(p)-(z), include the nanowire deposition process, the junction etching and the establishment of electrical contact between the nanowire and the underlying circuitry. Optical images of the device chip before and after each of these steps are shown in Fig. 3.11. The InAs nanowires used in this thesis are grown with the vapor-liquid-solid (VLS) method and have a length of approximately 10 µm. They have a hexagonal cross-section and are covered by epitaxially grown aluminum on two of their facets Krogstrup et al. (2015).

The transfer from the growth chip to the device chip is performed under an optical microscope using a commercially available tungsten needle attached to a micromanipulator[9]. During the design and fabrication of the device chip, different aspects can be considered to streamline the nanowire deposition process. As the deposition can be performed with an accuracy of approximately 1 µm in the longitudinal direction, maintaining a short distance between contact pads (7 µm or less) facilitates comfortable nanowire placement. Similarly, wider contact pads result in a broader deposition area, with 2 µm providing adequate space for comfortable nanowire deposition.
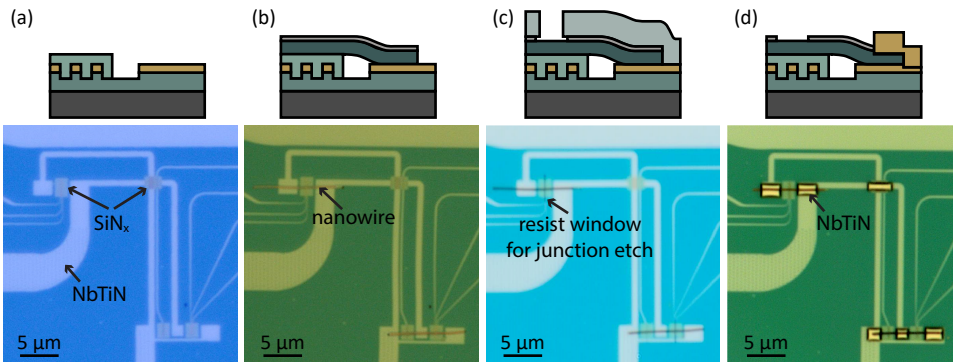
Figure 3.11: **Nanowire-specific nanofabrication steps.** Optical microscope images of the nanowire area. (a) Right after dielectric etch and before nanowire deposition (Fig. 3.8(o)). (b) Right after nanowire deposition (Fig. 3.8(p)). (c) Right after junction etch (Fig. 3.8(t)). (d) Right after contact lift-off (Fig. 3.8(z)). The top panels show schematics of the device cross-section at each step.

Following the nanowire deposition, the junctions are defined by etching away the aluminium on a nanowire section on top of the pre-patterned gates The resist mask used for selectively wet-etching of these aluminium segments can be seen in Fig. 3.11(c). After etching, the e-beam resist that covers the nanowires is not removed, to prevent potential nanowire displacement on the chip surface. Instead, a new layer of resist is applied (Fig. 3.8(u)) and used to pattern the contacts that galvanically connect the nanowire to the underlying circuitry.

The contact fabrication process entails the removal of surface oxides through argon milling (Fig. 3.8(x)), followed by sputtering a 120 nm-thick layer of NbTiN (Fig. 3.8(y)). These two processes are also used to define NbTiN structures in other chip areas, as needed

---

[9]For Chapter 6 the deposition is performed by N. van Loo and, for all other chapters, it is performed by Lukas J. Splitthoff.

depending on the device. Finally, in Chapter 7 this step is also used to fabricate the top capacitor plate of the flux line low-pass filter and, as shown in Fig. 3.11(d), the loop twist overjump.

3.2.4 Postfab and final device checks

The final fabrication steps prior to loading the device into the cryogenic refrigerator, which are not included in Fig. 3.8, comprise dicing, probing and wire-bonding the device to the printed circuit board (PCB).

The chips are diced to match the size of the PCB sample area (see Sec. 3.3.2 for PCB details),which is 6×6 mm^2 . To prevent damage to the nanowires due to electrostatic discharge during dicing, the process is only initiated when the dicing water resistivity drops below 1 Ω.

Subsequently, the room temperature resistance of different circuit elements is determined by probing the device using tungsten needles, as shown in Fig. 3.12(a). Measuring the resistance between the resonator island and the ground plane facilitates estimating the resonator inductance and in turn its resonance frequency. A similar estimate can be obtained by probing the resistance between input and output feedline ports for the devices without an input capacitor. Similarly, the resistance between the transmon island and ground provides information about the quality of the nanowire contacts. For working devices as those in Chapter 7, resistance measurements ranging from 20 to 200 kΩ are typically observed between the transmon island and ground. Additionally, the resistance between chip lines and ground is probed to identify potential short circuits.
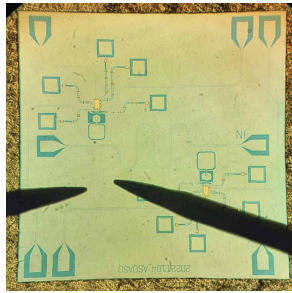
Figure 3.12: **Optical image of a diced chip being probed at the probing station prior to wire-bonding.**

Finally, the chip is mounted onto the printed circuit board and wire-bonded to it using aluminum bonds. We include short bonds along the chip edge that connect the ground plane of the chip to that of the PCB. In addition to establishing a homogeneous ground connection, these bonds serve as a path for heat dissipation away from the chip during cool-down. For each device, the radio-frequency (RF) lines design is realized to position their bonding pads in close proximity to corresponding bonding pads on the PCB. This configuration enables the use of wire bonds that are as short as possible, minimizing the potential for undesirable RF signal reflections resulting from impedance mismatches, as the longer wire-bonds have a large inductance (see Fig. 3.13(a) and (b)). This consideration, however, does not apply to the direct current (DC) lines, whose on-chip length is

instead minimized to prevent unwanted line self-resonance. Consequently, the wire bonds arriving at the DC lines' bond pads are relatively longer (see Fig. 3.13(a) and (b)).

Finally, we incorporate on-chip bonds that interconnect different ground plane regions. Such bonds prevent the formation of unwanted resonance modes and result in a more uniform ground reference across the chip, resulting in higher internal quality factors of the resonators. An extreme example of a case where we initially had only a single on-chip bond on a chip with four resonators (we hoped this minimized the flux jumps discussed below), is visible in Fig. 3.13 ((a), black curve in (c)). We then later warmed up the device and added extra on-chip bonds, as shown in panel (b), red curve in (c). This made the internal quality factors increase significantly, and even some resonators that earlier were so shallow (meaning lossy) that they were only visible when sweeping the gate and subtracting the background, now became visible. Note that the middle two resonators had lower internal quality factors even after rebonding due to being overcoupled to on-chip flux lines, which was not related to the bonding.
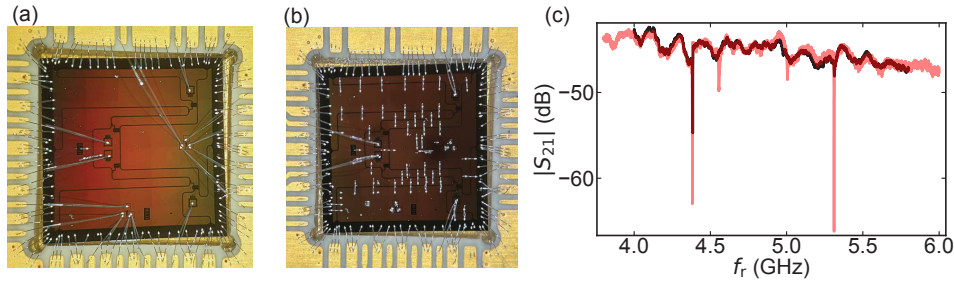
Figure 3.13: **Comparison of spectra with and without on-chip bonds.** (a) Optical microscope image of a chip with four resonators (one of the devices used in Chapter 6) , with only a single on-chip bond. The ground plane was simply-connected on-chip because the resonators are encircled with ground strips. (b) Optical microscope image of the same device after warming up and adding many on-chip bonds. (c) Microwave response through the feedline for the cooldown of the bond configuration of panel a (black), and panel b (red), illustrating the increase in internal quality factor after adding on-chip bonds. The curve without on-chip bonds is offset by 25 dB to account for attenuation and cable changes at the room-temperature equipment between the cooldowns.

3.2.5 Specifics for nanofabrication of InSb-based devices

Although we focused on the InAs/Al with etched Josephson junctions so far, in Section 6.2 we describe the differences in fabrication used to create circuit-qed devices containing InSb/Al nanowires with shadow-wall defined Josephson junctions.

3.3 Experimental setup

3.3.1 Cryogenic setup

The experiments presented in this thesis are performed at temperatures of a few tens of mK to suppress thermal excitations, and they involve magnetic fields on the order of 1 T. To achieve these conditions, all experiments are performed using cryogenic dilution refrigerators equipped with vector magnets. An exception is made for fast resonator characterization at zero field, performed while iterating the chip designs, which are carried out

using an Oxford Instruments Heliox system, a sorption-based ^{3}He insert. In particular, for Chapters 5, 4 we use a Bluefors XLD refrigerator, nicknamed "QT3". For part of the measurements in Chapter 6 we use a custom made Leiden cryogenics refrigerator, nicknamed "B3". Finally, for Chapter 7 and part of the measurements of Chapter 6 we use a Triton 300 refrigerator, nicknamed "K1".
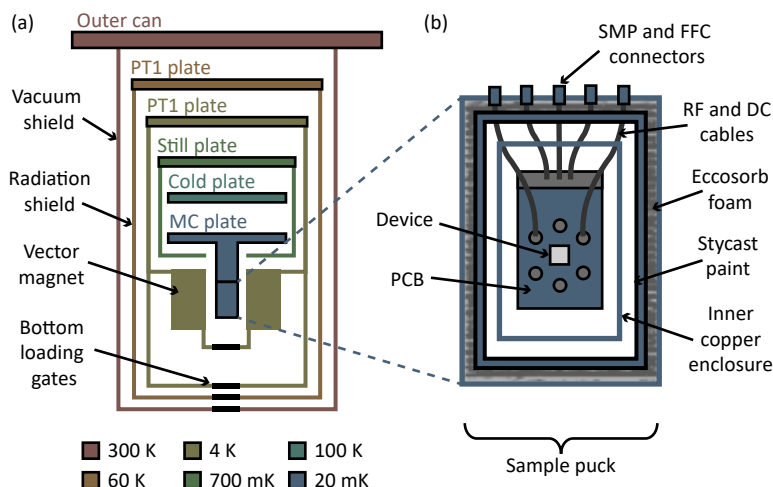
Figure 3.14: **Dilution fridge and sample puck.** (a) Diagram of a dilution refrigerator. Different colors denote different temperature stages. The shields prevent radiation from the outer temperature stages towards the inner ones. The puck (blue rectangle, enlarged in (b)) is thermally anchored to the lowest temperature stage and placed at the center of the vector magnet. The loading gates at the bottom of the fridge (black rectangles) permit inserting the puck into the fridge while keeping the fridge cold and under vacuum. (b) Puck formed by an outer can and various copper enclosure boxes which shield against radiation. The gap between the outer can and the outer enclosure box is filled with Eccosorb foam, which absorbs stray microwave radiation. The outer enclosure box is moreover pained on both sides with a mixture of silicon carbide grains, Stycast and carbon powder Bargerbos (2023).

A simplified schematic of a Triton 300 system is shown in Fig. 3.14. The inside of the fridge is maintained under high vacuum and separated by the exterior by the outer shield shown in red. Within it, multiple layers of inner shields, each thermally anchored to a different temperature stage, prevent radiation towards the interior of the fridge. The fridge is equipped with a multi-axis vector magnet capable of reaching magnetic fields up to 6 T in the vertical direction and up to 1 T in the horizontal plane. This magnet is thermally anchored to the PT1 plate, which is kept at around 4 K, thus maintaining the superconducting state of the magnet coils. The sample is situated within a cylindrical enclosure known as the puck. The puck is situated at the center of the magnet but is thermally anchored to the lowest temperature stage, referred to as the mixing chamber (MC). The MC can reach a base temperature of 10 to 20 mK.

A bottom-loading mechanism enables sample exchange while maintaining the system's low temperature[10] and vacuum conditions Batey et al. (2014). The bottom-loading

---

[10]Note that, during sample exchange, the system is not at base temperature. As the ^{4}He/^{3}He mixture has to be collected during sample exchange, the MC temperature raises to a few Kelvin before and during the sample

gates, depicted in black in Fig. 3.14(a), open when pushed upward by the exchange mechanism and allow passage of the puck from the outside to the inside of the fridge, and vice-versa. When the puck is pressed onto the MC stage, its lines are connected to those inside the fridge.
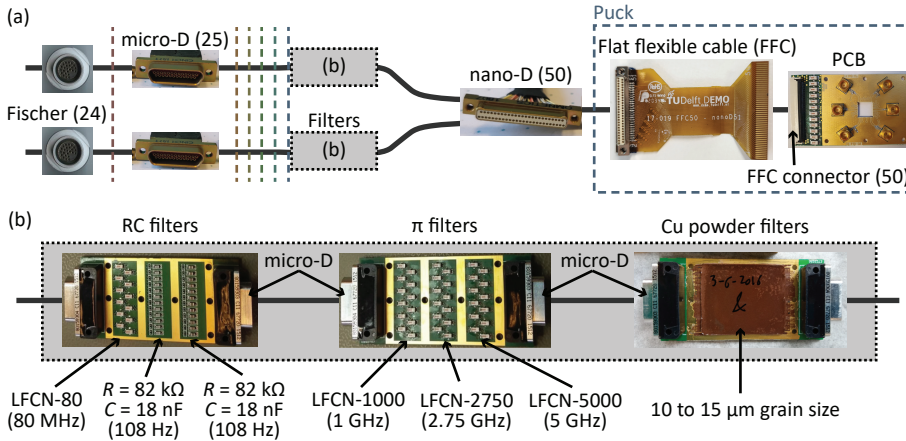
Figure 3.15: **DC cryogenic wiring and filtering.** (a) DC wiring from the top of the fridge (left) to the bottom of the fridge (right). The dashed lines indicate the different temperature stages, with the same legend as in Fig. 3.14. (b) Photographs of the three subsequent filter boards placed on the mixing chamber. The frequencies in the labels denote the 3 dB point of each filter.

The refrigerators used in this thesis are equipped with both radio-frequency (RF) and direct-current (DC) lines. The precise attenuation, filtering and amplification of each RF line differ based on its intended function, as detailed in the supplementary section of each of the experimental chapters (Krinner et al., 2019). A schematic of the DC lines is shown in Fig. 3.15.

The DC lines, totaling 48 in number, are connected to the room-temperature DC electronics outside of the fridge via two separate Fischer cables, each containing 24 lines. At the higher temperature stages within the fridge, these lines are divided into two distinct bundles of 24 lines each. Successive sections of these bundles are interconnected at each temperature stage using micro-D (Ohmnetics) connectors. In the mixing chamber stage, each line passes through a series of low-pass filters (see Fig. 3.15(b)). Each filter board is thermally anchored to the MC through a large surface to enable efficient heat dissipation[11]. Upon entry into the puck, the two bundles merge into a single group, soldered to a nano-D (Ohmnetics) connector. Within the puck itself, a nano-D to flat flexible cable (FFC)[12] adapter directly connects the DC lines to the printed circuit board (PCB). On the PCB, each DC line features an additional low-pass filter, as discussed in Sec. 3.3.2. On the

---

[11] The design of these filter boards was carried out by Maja Cassidy and Rogier van de Berg from DEMO, the electronics shop of TU Delft.

[12] Although similar flexible cables are commercially available, the FFCs used in this thesis were designed in-house and tailored to fit the particular needs of the experiments conducted in this thesis. This was done by Jason Mensingh and by Kees Esser from DEMO, the electronics shop of the TU Delft.

exchange process. Right after inserting the new sample, the system temperature reaches a few tens of Kelvin due to the extra heat load.

PCB, 16 of the lines are directly routed to the sample and 4 other lines are combined with RF lines via bias tees (see Fig. 3.16(d)). The remaining 24 lines are shorted to ground and remain unused in the configuration.

3.3.2 Hybrid printed circuit board details

Throughout this thesis, we used hybrid DC-RF printed circuit boards to route the DC and RF signals from the fridge lines to the chip. We detail the design used for Chapters 6 and 7.[13]. The latest version of this hybrid PCB design from our lab at the time of writing[14], is presented in Fig. 3.16. The hybrid PCB has a total thickness of 705 μm and it is composed of four copper layers separated by insulating layers of different materials and thicknesses, as indicated in Fig. 3.16(b). The board is gold-plated to prevent oxidation of the outer copper layers. Throughout the board, through-hole ground vias (indicated by black circles in Fig. 3.16(e-h) uniformly interconnect the ground reference of all layers. The sample area, with a squared shape, is situated in the central part of the board and is surrounded by bonding pads that permit bonding the chip to different DC and RF PCB lines.

The 48 fridge DC lines from the fridge reach the board through an FFC connector (see Fig. 3.16(c)). To prevent problems derived from electrostatic discharge during loading and unloading the puck from the fridge, two copies of the FFC connector are placed on the front and back of the PCB, shorted to each other. This arrangement ensures that all lines remain grounded when a shorting strip is connected to one of the FFC connectors while the other one becomes connected or disconnected from the fridge. Among the 48 fridge DC lines, only 20 are used; the rest are shorted to ground. Each of the 20 lines is filtered on the PCB with a low-pass π-filter with a cutoff frequency of 80 MHz. These π-filters are arranged as a capacitance to ground, followed by an inductor, and then another capacitance to ground, resembling the shape of the Greek letter π. Twelve of the π-filters are situated on the top part of the board (visible in Fig. 3.16(a) and (c)). The remaining eight are instead placed on the bottom part (see filter pads in Fig. 3.16(h)). Following the filters, all DC lines are connected to the third layer of the PCB. For the DC lines that come from the top of the PCB, this connection is established via blind vias, while, for the ones that come from the bottom, it is done via through-hole vias, as indicated in Fig. 3.16(b). All DC lines are then routed on the third layer until reaching the sample area, as shown in Fig. 3.16(g). Subsequently, additional blind vias bring the DC lines up to the top PCB layer, where they reach the bond pads situated at the edge of the sample area. All blind vias are machined by Fineline using the back-drilling technique. This method involves a first step where a complete through-hole via is fabricated. Such through-hole via is subsequently selectively drilled to a precise depth using a drill tool with a diameter larger than that of the hole of the original via (see Fig. 3.16(b)). This procedure prevents undesirable antenna and cross-talk effects that could be caused by the unconnected vias parts or stubs, enhancing

---

[13]Note that, for the earlier Chapters 5 and 4, we used a different enclosure and hybrid DC-RF PCB with the Bluefors XLD refrigerator. This was an In sealed CuBe box filled with ecosorb, obtained from collaborators in Copenhagen. For the resonator characterization measurements performed at the Heliox, we instead used simpler only-RF PCBs with a circular shape and formed by just two copper layers separated by a single dielectric layer.

[14]This design, adapted by Kees Esser to accommodate a greater number of DC lines and larger chip sizes, is an extension of Maja Cassidy's original concept, and incorporates elements from a variation by Angela Kou. The boards are machined by Fineline.
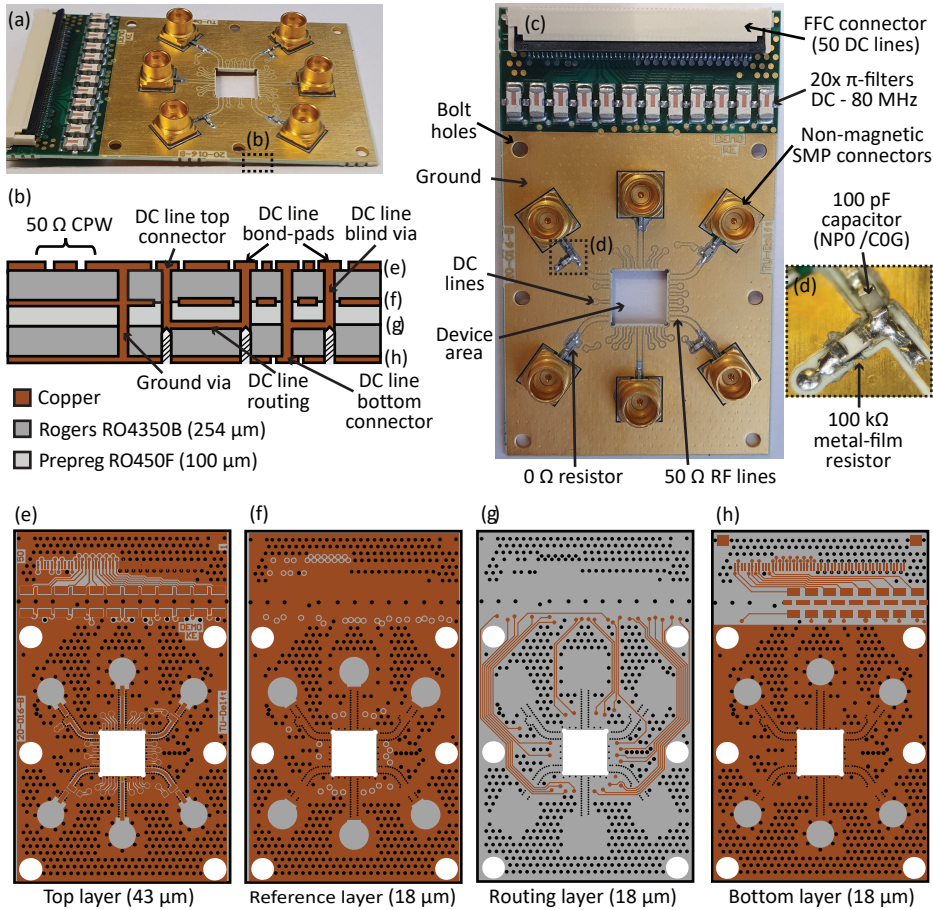
Figure 3.16: **Printed circuit board (PCB) design.** (a) Photograph of the hybrid PCB from an angle. The cross-section is enlarged in (b). (b) Diagram of the PCB cross-section (not to scale) showing four copper layers separated by three insulating layers. Through-hole vias connect all four copper layers together. Blind vias connect only the three topmost layers. Not shown is the gold-plating layer which covers all exposed metallic surfaces. (c) Top view of the PCB showing the different components assembled on the top layer. (d) Enlargement of the bias tee, composed of a resistor and a capacitor. (e-h) Diagrams of each of the four layers.

overall signal integrity.

The RF signals instead reach the board through six non-magnetic Rosenberger sub-miniature push-on (SMP) connectors, serving as both entry and exit points. From there, the RF lines are routed through the surface of the board until the edge of the sample area. The surface RF lines are implemented with conductor-backed coplanar waveguide (CPW) transmission lines with a $50\,\Omega$ impedance and use the second layer as the bottom ground reference layer (see Fig. 3.16(f)). Out of the six RF lines, two are directly routed to the edge of the sample area and are used as input and output lines for transmission measurements. The remaining four RF lines incorporate pads with 0402 footprint, allow-

ing versatile component integration based on the specific experimental requirements. For instance, in Chapter 7, one of the RF lines is purposed as a flux line by connecting a $0\,\Omega$ surface-mounted device (SMD) resistor to it. Another RF line is instead used as a drive line through an electrostatic gate. To combine the DC and RF components of the signal, we mount a bias tee on the line, as shown in Fig. 3.16(d). On the DC part of the bias tee, we connect a $100\,\mathrm{k\Omega}$ SMD resistor of the thin-film type (Panasonic ERA-2AEB104X), while on the RF part, we connect a $100\,\mathrm{pF}$ SMD multilayer ceramic capacitor (MLCC) of type NPO (Kemet C0402C101J5GACTU). These components result in an RC time constant of $10\,\mu\mathrm{s}$, equivalent to a cutoff frequency of $16\,\mathrm{kHz}$.

3.3.3 Details on magnetic field control

One of the key "new" parameters swept in the experiments presented in this thesis, when compared to other experiments with superconducting circuits, is the global magnetic field. Thus, naturally, we spent some time optimizing the setting of this field. All devices that are shown in this thesis are cooled down in dilution refrigerators with a commercial 6-1-1 axis vector magnet. These magnets are generally made by three independent superconducting coils (cooled by thermal anchoring to the $4\,\mathrm{K}$ stage). Each coil is controlled with its own current source. Typically the coil constants of the 1 T axes are around 60 A/T and these of the 6 T axes are 12-16 A/T. Thus for using the full field range one needs a large 100 A rated current source, which is output by commercially available sources that are delivered with the magnets (in our case from mercuryIPS (see Fig. 3.17(b)) and American Magnetics Inc.). Due to the large operation range, the minimum step size of these sources is generally quite large, for example, the American Magnetics Inc. current source has a quoted programming accuracy of 50 mA and a stability of 25 mA, which corresponds to about 1 mT and 0.5 mT resolution and stability respectively (in reality the resolution and stability are much better). For the mercuryIPS the quoted stability is $\pm 2\,\mathrm{mA}$ ($33\,\mu\mathrm{T}$) and minimum step size is 0.15 mA ($2\,\mu\mathrm{T}$).
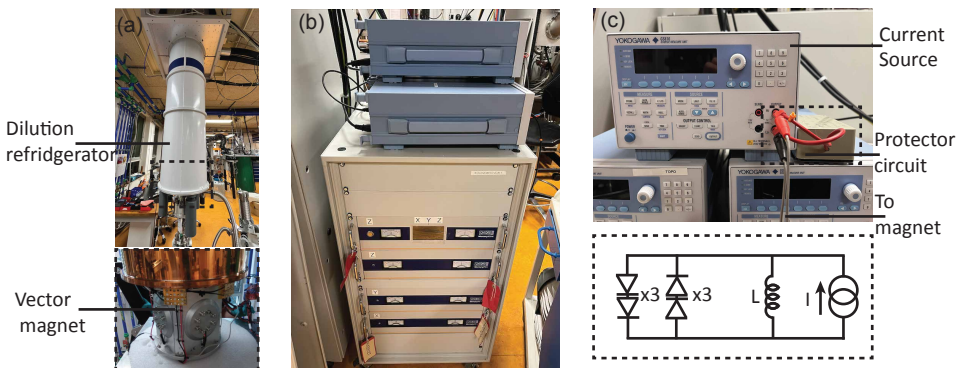
Figure 3.17: **Triton dilution refrigerator with a 6T-1T-1T vector magnet and current sources used for magnetic field control.** (a) Top panel: Triton dilution refrigerator with all shields installed and bottom loader. Bottom panel: 6-1-1 T vector magnet attached to the still shield. The probe is loaded via the bottom loader in the bore of the magnet. (b) Large (bottom) and small (top) current sources used to control the magnets. (c) Zoom in on the Yokogawa GS610 current source used for fine-stepped field control connected to the magnet leads, together with a diode protection box wired in parallel as shown in the wiring diagram (bottom panel).

Since for flux control we only apply fields of a few millitesla, we used smaller current sources to control these axes. For example, if one has a $10\,\mu m^2$ area SQUID loop, the field required to thread one flux quantum is approximately $200\,\mu T$ ($12\,mA$). The current sources used were Yokogawa GS200(GS210), rated up to $200\,mA$, and the GS610 source measure unit, rated up to $3\,A$ with minimum current step size of $1\,\mu A$ for $< 200\,mA$, $10\,\mu A$ for $< 3\,A$ (see Fig. 3.17(c)). During an in-house stability test by Raymond (our electronics expert), we found the output current to drift during setting it at $1\,A$ for about one hour (no temperature control applied) by approximately $60\,\mu A$ ($1\,\mu T$).

The larger current sources supplied with the magnets have built-in quench protection. To protect the Yokogawa current sources in case of a sudden quench of the magnet, which is not rated for such large inductive loads, we built a small box[15] (see Fig. 3.17c) containing two antiparallel rows of several Schottky diodes in series that all together can be added in parallel with the magnet current loop. The main functionality is that when a large voltage develops —a rapid change in current during a quench generates a voltage proportional to the inductance of the magnet which is several Henry— it allows current to flow through the diodes such that the voltage stops increasing, but when the voltage is low, no current should flow (otherwise the magnet field setting might be affected). The choice of diodes thus was aimed at having a negligible current at the operation voltages, while being able to handle the full $3\,A$ current in case of a quench. In Fig. 3.17(d) the current is written given a certain voltage drop. At $5\,V$ the maximum current of $3\,A$ is reached, which is well below the maximum allowed voltage of the GS610, rated up to $12\,V$.

Loop design considerations for proper flux control

We found that even after circuit optimizations with holes and thin components, small out-of-plane fields of several tens of μT could still cause both large and small flux jumps through the superconducting SQUID loops, hindering the use of flux as a controlled parameter in our initial experiments. However, we found that the suspension of the nanowire with a superconducting shell on the gate and dielectric creates a small vertical loop with typically an area of around $0.3\,\mu m^2$ for $28\,nm$ SiN_x of gate-dielectric. With this design, it is then possible to use a magnetic field parallel to the chip plane for flux biasing with a period of several mT per flux quantum. This has the advantage that the total exposed area of superconducting film to flux becomes proportional to the thickness (tens of nanometers) of the NbTiN film instead of the width of the chip (several millimeters), greatly *reducing* the observed flux jumps (see fig .. for a direct comparison between flux biasing with out of plane or in-plane field). Various sketches of possible loop designs are shown in Fig. 3.18, with the loop area exposed to out-of-plane and in-plane fields shown in the accompanying diagrams. Interestingly it would be possible to design a SQUID that has no loop in the vertical direction at all, as shown in Fig. 3.18)(c), which could allow for compact circuits, or loops with small footprint.

In Chapterss 5, 6 and 4 we use a gradiometric design (see Fig. 3.18b). In this design, the total flux is proportional to the area difference between the two loops. By designing the areas to be equal (up to the accuracy of the nanowire placement), one can become nearly insensitive to a global out-of-plane magnetic field. One of the advantages of this design is that each of the individual loops can still be large, simplifying the design of large

---

[15]Without labor costs, the box total cost was about €2,50, a small price to pay for an insurance policy.
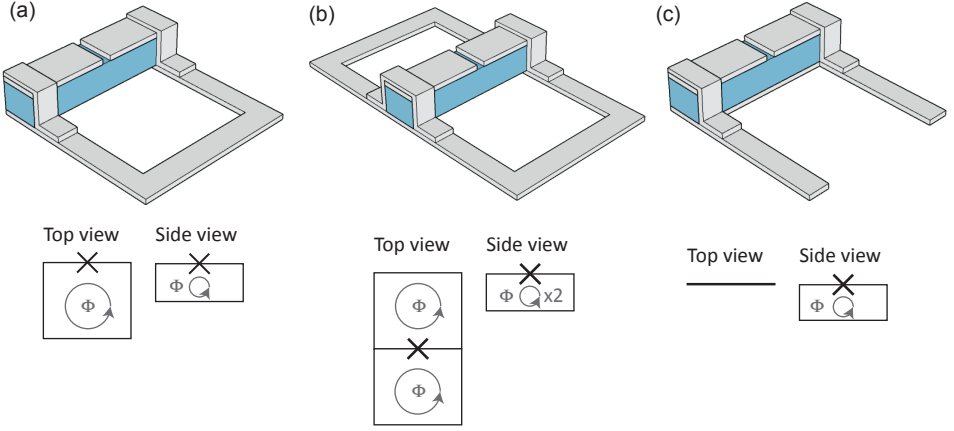
Figure 3.18: **Schematic of vertical loop superconducting quantum interference devices for parallel field flux biasing.** (a) RF-SQUID with a single loop and Josephson junction. The suspension of the junction allows flux biasing using either a parallel or a perpendicular field. (b) Gradiometric RF-SQUID design, which cancels perpendicular flux and amplifies parallel flux by a factor of two. (c) Vertical RF-SQUID loop solely defined by the elevated nanowire. See de Lange and Wesdorp (2023) for more details. A fourth iteration of a loop design is given in 7 , where the loop is twisted (Pita-Vidal et al.).

shunt-inductances or allowing the use of on-chip flux lines in combination with a global magnet, as we do in Chapter 7

Flux jumps due to on-chip wirebonds
Even while using the in-plane magnetic field for flux control, flux jumps can still occur. We found that the presence of on-chip wire bonds can lead to undesired flux jumps when sweeping the B_y component of the magnetic field (parallel to the chip plane and perpendicular to the nanowires). This phenomenon is attributed to the wire bonds having a cross-sectional area in the B_y direction, as the ones shown in Fig. 3.19(d). As, at zero magnetic fields and cold temperatures, these wire bonds are superconducting, an applied B_y field produces a circulating supercurrent that passes through them and through the chip plane. This circulating supercurrent in turn generates an out-of-plane field that affects the flux through the device loop. As the magnitude of B_y is swept, spurious currents are produced in the loop that contains the bond wire, resulting in unwanted flux jumps on the device.

Throughout this thesis, different strategies are used to mitigate such undesired effect. For chip 1 in Chapter 6, the flux jumps are observed in the absence of a magnetic field. To circumvent them, we apply 10 mT and turn the bond wires normal. In this way, supercurrents can not circulate through the bond wire, resolving the issue (see Fig.6.11 in Chapter 6). This is however not a general solution, as in general we need to measure the flux dependence of devices also in the absence of a magnetic field. In Chapter 7 we

However, when the on-chip bonds are instead arranged parallel to the B_y direction (as those in Fig. 3.19(c)), we find that the frequency of flux jumps is substantially reduced.
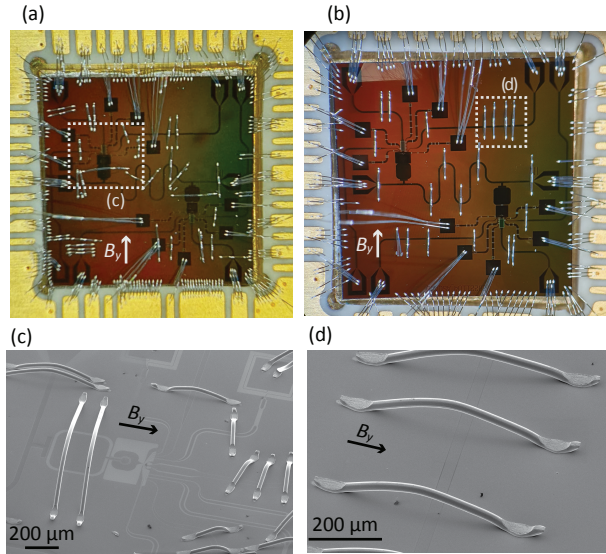
Figure 3.19: **Field-aligned wire-bonding.** (a) Optical microscope image of a chip bonded with an on-chip bond configuration that results in multiple flux jumps when sweeping the B_y on-chip component of the magnetic field. This bonding configuration includes multiple bonds with a y cross-section underneath on-chip bonds that are in the region nearby the nanowire region. (b) Similar to (a) but for an almost identical device for which the on-chip bonds are instead made along the y direction. The length of the side of the chip is 6 mm. (c)-(d) Scanning electron micrographs (SEM) showing enlargements of different wire-bonds. These images correspond to a device almost identical but different from the ones shown in (a)-(b). (c) shows wire bonds with a y cross-section placed over the resonator. (d) show wire bonds without a y cross-section that connected the pieces of ground plane on both sides of the feedline and drive line, respectively.

Alignment of the chip with respect to the magnet axes

In general, there exists a slight misalignment of the sample in the PCB with respect to the magnet axes (typically of a few degrees). In the case of large applied fields, or strong sensitivity to small fields in one of the field directions, the misalignment should be corrected for. Our general approach for this is to apply a 3-dimensional coordinate transformation that corrects this misalignment. For this purpose, we denote the original coordinate vector of the magnetic field by B_e, where e stands for Cartesian coordinates (e.g the x, y, z system of the vector magnet that is used). In principle, there are many general transformations possible, but some are easier to find experimentally than others. It can be proven, that with three rotations around at least two different axes, any general 3-dimensional transformation can be performed (Euler angles). The rotation matrices around a single axis are given by

$$R^z(\phi) = \begin{pmatrix} \cos(\phi) & -\sin(\phi) & 0 \\ \sin(\phi) & \cos(\phi) & 0 \\ 0 & 0 & 1 \end{pmatrix} \quad R^x(\phi) = \begin{pmatrix} 1 & 0 & 0 \\ 0 & \cos(\phi) & -\sin(\phi) \\ 0 & \sin(\phi) & \cos(\phi) \end{pmatrix}$$

$$R^y(\phi) = \begin{pmatrix} \cos(\phi) & 0 & \sin(\phi) \\ 0 & 1 & 0 \\ -\sin(\phi) & 0 & \cos(\phi) \end{pmatrix}. \tag{3.1}$$

We use intrinsic rotations around 3 different axes. The original field vector then is transformed $B_e \to B_u \to B_v \to B_w$, where the subscript denotes the new coordinate system of the B-vector after each rotation. B_w is thus the chip coordinate system. We aim to find the rotation angles α, β and γ such that $B_w \to B_e$ via

$$B_w = R^x(\gamma)B_v = R^x(\gamma)R^y(\beta)B_u = R^x(\gamma)R^y(\beta)R^z(\alpha)B_e$$

With this sequence, after the first two rotations one can get the x and y axes aligned with the chip plane (which are most important for flux control). With a third rotation, one can align the in-plane nanowire axis[16] with the z-axis of our coordinate system (so we can apply a truly "parallel field" to the nanowire). Note that from a linear algebra viewpoint this boils down to having to find the coordinate transformations $A_{i \to j}$ to go from basis i to j. The first transformation $A_{e \to u}$ is given by

$$B_u = A_{e \to u}B_e = R^z(\alpha)B_e$$

where B_e and R^z are expressed in the Cartesian coordinates e.

We find the angles of rotation using the following procedure. Generally, the devices are more sensitive to a perpendicular field than to other field directions. Thus, we can detect when the "true" out-of-plane field is 0. So we can obtain α by sweeping x_e for various y_e and determining for each y_e set for which $x_e(y_e)$, $x_u = 0$. We can then perform a linear fit to obtain the slope a^{yx} and we can calculate the first rotation angle by

$$\alpha = \tan^{-1}(1/a^{yx})$$

Then we continue

$$B_v = A_{u \to v}B_u = R^y(\beta)B_u$$

So if we express the new sweep in the rotated coordinates using α then from $x_v = 0$ (perpendicular field out of chip plane) versus $z_u(= z_e)$, $x_u(\neq x_e)$.

$$\beta = \tan^{-1}(-1/a^{zx})$$

where a is the slope of $z_u(x_u|x_v = 0)$

Finally, we should be able to find the in-plane rotation of the NW by minimizing the flux change due to z_v.

$$B_w = A_{v \to w}B_w = R^x(\gamma)B_v$$

Again if we express the new sweep in the rotated coordinates using β, α then from $y_w = 0$ (perpendicular field in chip plane) versus z_v, y_v

$$\gamma = \tan^{-1}(1/a^{zy})$$

---

[16]Dependent on the placement accuracy of the nanowires the degree of misalignment can vary quite a bit from device to device.

where a_{zy} is the slope of $z_v(y_v|y_w = 0)$. Note that in all cases, there can be an offset from zero by field coming from other sources (like circulating currents on chip) so by fitting linear functions $a_i j + b$ we account for this. Note, additionally, that using intrinsic rotations is preferred, because it allows to perform the next angle measurement in the new coordinate system of the previous one, without worrying about corrections to other axes. However, if the angles are small enough, extrinsic and intrinsic rotations yield the same result.

3.3.4 Measurement and data processing

As has become the standard in experimental condensed matter physics, we use *Python* to code up measurement scripts, analysis and plotting. In general, our approach to taking data can be summarized in the following statements:

1. A measurement should contain sufficient metadata, such that a person who did not do the measurement can still figure out what all instrument settings were.

2. It should be clear what measurements came before and after each measurement.

3. The intention of the experimenter for taking the measurement should be retrievable.

To adhere to the first item, we use *qcodes* as our measurement framework. For each instrument in the setup, *qcodes* generates a *snapshot* of its settings that is saved along with each dataset. We extend this by creating so-called virtual instruments, which are simply used to store some additional state of interest during our experiment in the snapshot. For example, we have a class (instrument) that is called *Magnet3D* and saves all the settings of the alignment angles used (see the alignment paragraph in section 3.3.3) and has additional functions that allow one to sweep various coordinates in the rotated frame of the chip. In general, the principle is that, if you feel like it is important to write down a certain value in your lab notebook, it is probably worth it to make an instrument for it. This both saves you time from having to write it down, and it makes sure that you can be certain of the actual value that is set, without relying on your memory. This can also be a digital twin of your device for example, which stores the bare resonance frequency of the resonator, transmon frequency, flux periodicity of the loop, etc.

To adhere to the second point, *qcodes* stores the data in a *sqlite* database that contains timestamps and incrementing IDs. Together with the *plottr* software package, one can easily inspect the data in chronological order, and do some rudimentary plotting, with a graphical user interface to quickly get an overview of what data is where.

The third point is then covered by making annotations in the lab notebook, for which we use *OneNote*. The idea is here, that because all data is saved in the *qcodes snapshot* one should never have to write down a setting or value in the lab notebook, because it can be extracted directly from the data itself. Thus, *OneNote* is reserved to write down the interpretation and motivation behind the datasets, together with plots of the results.

Data processing for a manuscript

We now describe the typical procedure we follow when a collection of data appears complete enough to make a manuscript. Recently, a large effort from the university has been directed towards promoting *open science*, and especially towards *open data*. Here, open data
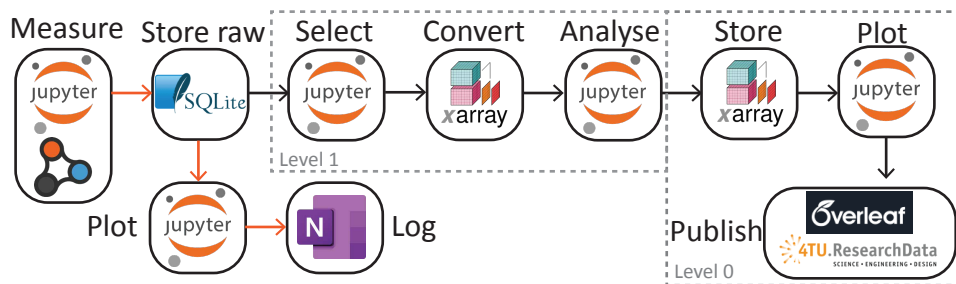
Figure 3.20: **Data processing pipeline.** Two routes are illustrated, with icons representing the specific software or package used for the step. A fast route to go from measurements to logging the data in the lab notebook during day-to-day work (in orange), and a longer route that prepares a selection of the data for publication. Grey boxes indicate which steps need to be included in order to reach the open data standards as defined in Ref. Akhmerov and Steele (2019).

basically means that anyone should be able to find the raw data underlying the manuscript, reproduce the figures, inspect the analysis line-by-line of code, and, of course, allow them to perform their own analysis on the data. All this should be possible on their own hardware, with ideally similar effort as opening and reading the manuscript pdf. More formally, the following *open data* levels are suggested Akhmerov and Steele (2019):

1. Level 0: Publication of the processed data files as plotted in the figures in the paper.

2. Level 1: Publication of the raw data, as recorded by our computers, along with software and processing scripts that derive the plotted data from the raw data

We have generally adhered to level 1 using the steps shown in Fig. 3.20. First, we select the data of interest and convert it (without processing) to a more generally accessible format .netcdf using the *xarray* package. The advantage here is that access to variables in arrays is done by the variable name, such that the analysis code that follows it becomes much more readable. The selected data is then analysed using a combination of custom-written functions (usually shared within the team with *git* version control) and open-source libraries. The results of this analysis are then stored again using xarray or *pickle* for unsupported formats. Finally, the processed data is plotted (without additional processing) using Python and input in the manuscript.

4

Dynamical polarization of the fermion parity in a nanowire Josephson junction

Josephson junctions in InAs nanowires proximitized with an Al shell can host gate-tunable Andreev bound states. Depending on the bound state occupation, the fermion parity of the junction can be even or odd. Coherent control of Andreev bound states has recently been achieved within each parity sector, but it is impeded by incoherent parity switches due to excess quasiparticles in the superconducting environment. Here, we show that we can polarize the fermion parity dynamically using microwave pulses by embedding the junction in a superconducting LC resonator. We demonstrate polarization up to $94\% \pm 1\%$ ($89\% \pm 1\%$) for the even (odd) parity as verified by single shot parity-readout. Finally, we apply this scheme to probe the flux-dependent transition spectrum of the even or odd parity sector selectively, without any post-processing or heralding.

4.1 Introduction

Josephson junctions (JJs) play an essential role in the field of circuit quantum electro-dynamics (cQED) (Blais et al., 2004), providing the non-linearity required for quantum-limited amplification and quantum information processing (Devoret and Schoelkopf, 2013; Roy and Devoret, 2016; Wendin, 2017; Kjaergaard et al., 2020). Microscopically, the Joseph-son current is carried by Andreev bound states (ABS) (Kulik, 1970; Beenakker, 1991). Recent advances in hybrid circuits with JJs consisting of superconducting atomic break junctions (Bretheau et al., 2013a; Bretheau, 2013; Janvier et al., 2015) or superconductor - semi-conductor - superconductor weak links (de Lange et al., 2015; Larsen et al., 2015; Casparis et al., 2018; Pita-Vidal et al., 2020) have opened up exciting research avenues due to the presence of few, transparent, tunable ABS.

ABS are fermionic states occurring in Kramers degenerate doublets (Beenakker, 1991). Their energy depends on the phase difference across the JJ, and the degeneracy can be lifted in the presence of spin-orbit coupling (Chtchelkatchev and Nazarov, 2003) or magnetic field. Each doublet can be occupied by zero or two, or one quasiparticle (QP), giving rise to even and odd parity sectors. Theoretical proposals have investigated both sectors as qubit degrees of freedom (Zazunov et al., 2003; Despósito and Levy Yeyati, 2001; Chtchelkatchev and Nazarov, 2003; Padurariu and Nazarov, 2010), relying on conservation of fermion parity. These "Andreev qubits" combine the beneficial small size of semiconductor qubits with strong (spin) state-dependent supercurrents allowing fast, high-fidelity, microwave based readout and manipulation similar to superconducting qubits (Hays et al., 2021; Janvier et al., 2015; Hays et al., 2018).

A difficulty is that superconducting circuits contain a non-equilibrium population of QPs (Glazman and Catelani, 2021; Aumentado et al., 2004; Lenander et al., 2011; Sun et al., 2012; Ristè et al., 2013; Wenner et al., 2013; Pop et al., 2014; Vool et al., 2014; Wang et al., 2014; Riwar et al., 2016; Serniak et al., 2018; Uilhoorn et al., 2021), which can enter the junction and "poison" the ABS on timescales of $\approx 100\,\mu s$ (Zgirski et al., 2011; Hays et al., 2018; Janvier et al., 2015). Despite this, recent experiments have demonstrated remarkable control over the ABS dynamics using microwave drives. Refs. (Janvier et al., 2015; Hays et al., 2018) were able to demonstrate coherent manipulation in the even parity manifold, while Refs. (Tosi et al., 2019; Hays et al., 2020, 2021) focused on the odd manifold and coherently controlled a trapped QP and its spin. In both cases poisoning events must be monitored to operate in the intended parity sector.

So far, the strategy to control the ABS parity has been to engineer the free energy landscape via electrostatic (van Dam et al., 2006; De Franceschi et al., 2010) or flux (Zgirski et al., 2011) tuning to make the QP trapping and de-trapping equilibrium rates strongly unbalanced. Applications like Andreev qubits (Zazunov et al., 2003; Despósito and Levy Yeyati, 2001; Chtchelkatchev and Nazarov, 2003; Padurariu and Nazarov, 2010; Park and Yeyati, 2017; Janvier et al., 2015; Hays et al., 2018, 2021) or Majorana detection (Prada et al., 2020) for topological qubits (Karzig et al., 2017) require to dynamically set the parity without changing gate or flux settings - e.g. using a microwave drive. While microwave photons are only allowed to drive transitions that preserve parity, they should be able to polarize the fermion parity of a JJ by exciting one QP into the continuum of states above the superconducting gap in the leads (Chtchelkatchev and Nazarov, 2003; Riwar et al., 2014; Klees et al., 2017; Olivares et al., 2014; Riwar, 2015). However, so far microwaves have
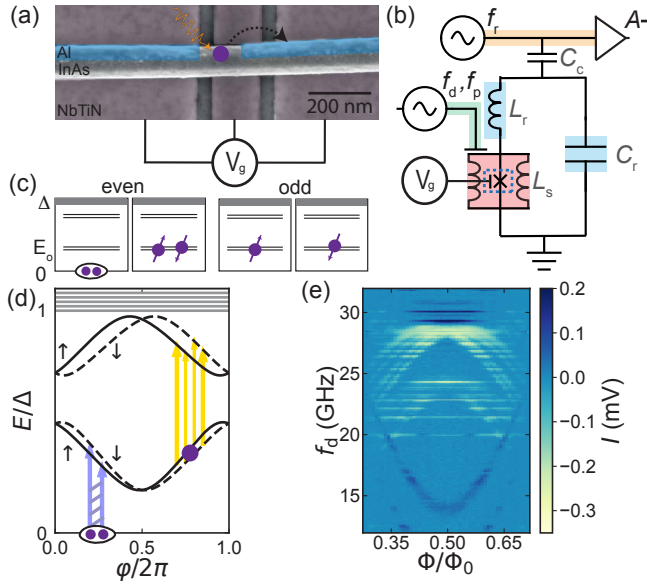
Figure 4.1: **(a)** False-colored scanning electron micrograph of the InAs/Al nanowire JJ formed by etching a $\approx 150\,$nm section of the Al shell, and sketch of the detrapping of a QP (purple circle) from an ABS by microwave irradiation (yellow arrow). ABS arise in the semiconducting junction due to constructive interference from consecutive Andreev reflection into the Al leads (Hays et al., 2018, 2020; Tosi et al., 2019). **(b)** Setup schematic. Two parallel inductances shunt the gate-tunable junction (blue dotted box) and form a gradiometric RF-SQUID (red). For dispersive readout of the ABS spectrum, we integrate the SQUID into an LC resonator (blue) capacitively coupled to a transmission line (orange) and probed with a near-resonant tone at frequency $f_r \approx 4.823\,$GHz. A second transmission line (green) allows direct driving of ABS transitions via microwave tones (f_d, f_p). **(c)** Schematic energy levels of ABS inside the superconducting gap Δ and the lowest doublet occupation configurations for even and odd junction parity. **(d)** Energy diagram (Tosi et al., 2019) of levels shown in (c) versus phase bias $\varphi = 2\pi\Phi/\Phi_0$ applied via an external flux Φ. Also indicated are parity-conserving transitions starting from the odd or even parity occupation of the lowest ABS doublet, with colors matching the parity of transitions shown in (e). Blue connected arrows denote transition within the even parity sector starting from the ground state, yellow arrows denote transitions within the odd sector starting with one of the lower levels occupied by a QP. **(e)** Measured spectrum containing the transitions indicated in (d), starting from odd (yellow) or even (dark blue) parity. Note that spectral copies of the transitions likely are visible due to multi-photon processes involving the cavity photons at $f_d \pm f_r$ (Section 4.8; cf. footnote 3). Colorbar indicates real part (I) of the complex amplitude A of the transmitted tone at f_r (Section 4.8).

only been observed to increase the rate of QP escape (Levenson-Falk et al., 2014; Farmer et al., 2021; Hays et al., 2021) or trapping (Bretheau et al., 2013b) from the junction, while deterministic polarization towards either parity has not yet been demonstrated.

In this Chapter, we demonstrate dynamical polarization of the fermion parity of ABS in a nanowire JJ using only microwave control. We first demonstrate single shot readout of the ABS parity. We then show that we can polarize the ABS into either parity depending on the frequency and power of a second pumping tone. Using a two-state rate model, we infer that the pumping tone can change the transition rate from even to odd parity, or vice versa, by more than an order of magnitude. Finally, we show that we can deterministically polarize the ABS parity over a wide range of flux by pumping at a flux-dependent

frequency, as confirmed by parity-selective spectroscopy without post-selection or heralding.

We focus on the microwave transition spectrum of ABS confined to an InAs nanowire JJ embedded in a radio-frequency superconducting quantum interference device (RF SQUID) [Figure 4.1(a)] (Clarke and Braginski, 2004) acting as a variable series inductance in an LC resonator tank circuit [Figure 4.1(b)] (Section 4.8). For driving ABS transitions we include a separate transmission line that induces an AC voltage difference across the junction. The number of ABS levels is controlled by applying a voltage V_g to the bottom gates (Doh, 2005; van Woerkom et al., 2017; Goffman et al., 2017). In order to have a consistent dataset, we keep the gate fixed at $V_g = 0.6248$ V (Section 4.8).

At this particular V_g, ABS transitions are visible using two-tone spectroscopy [Figure 4.1(e)] in the flux range between $0.3\Phi_0$ and $0.7\Phi_0$, where $\Phi_0 = h/2e$. Due to QP poisoning, the parity of the ABS fluctuates during the measurement (Hays et al., 2018; Janvier et al., 2015; Zgirski et al., 2011). Thus, the measured spectrum [Figure 4.1(e)] is the combination of two sets of transitions with an initial state of either even or odd parity. In Figure 4.1(c) we depict a schematic (Section 4.8) of the relevant ABS levels for this particular V_g. The lowest doublet consists of two spin-dependent fermionic levels (energies $E_o^\uparrow, E_o^\downarrow$) that can either be occupied by a QP or not (van Heck et al., 2017). The occurrence of odd-parity transitions [yellow lines in Figure 4.1(e)] requires the presence of another doublet at higher energies, as generally expected in finite-length weak links or in the presence of multiple transport channels. The ABS levels are spin-split at zero field and finite phase drop φ, because spin-orbit coupling induces a spin- and momentum-dependent phase shift gained while traversing the weak link (Governale and Zülicke, 2002; Park and Yeyati, 2017; Hays et al., 2020; Tosi et al., 2019), as depicted in Figure 4.1(d) (Tosi et al. (2019), Section 4.8). Colored arrows indicate transitions visible in Figure 4.1(e) with initial odd (yellow) or even (blue) parity.

4.2 Parity selective spectroscopy

Without a driving tone, the junction switches between two parity-dependent ground states corresponding to the lowest-energy ABS doublet being empty or occupied by a single QP [1]. We first demonstrate parity readout by doing pulsed spectroscopy conditioned on the outcome of a stronger measurement pulse [Figure 4.2(a)] [2]. Readout for both the parity and the spectroscopy pulse is performed with a 20 μs near-resonant pulse which is short compared to the parity lifetime (∼ 0.5 ms) at $f_r \approx 4.823$ GHz that traverses the readout line and interacts with the resonator. From the resulting complex transmitted amplitude $A = I + iQ$ we time-integrate the real (I) and imaginary part (Q). The inductive coupling of the ABS to the resonator causes a state-dependent dispersive frequency shift of the resonator (Hays et al., 2018; Janvier et al., 2015; Metzger et al., 2021). The I, Q-values of the parity measurement

---

[1]Configurations with one or more QPs trapped in higher ABS doublets are also possible, to which our parity readout is not sensitive. However, when QPs are trapped in these configurations, they presumably relax to their parity-dependent ground state on timescales much faster than the measured switching time of ∼ 0.5 ms that we report in Figure 4.3(f). This is supported by recent works on similar nanowires (Hays et al., 2020, 2018), which reported 13 μs for the even excited state, or 3 μs for the odd excited state.

[2]For clarity, in Figure 4.2(a) we indicate each pulse combination with a colored card and a symbol representing the type of operation, so it can be easily compared with the pulse sequences of Figure 4.3(b), Figure 4.4(a).
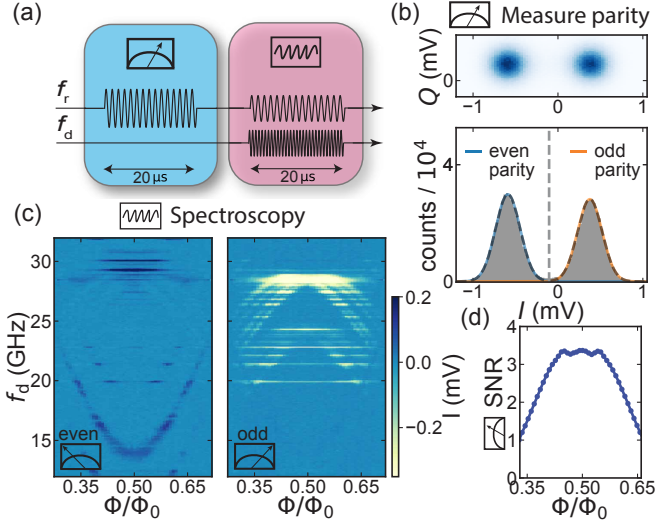
Figure 4.2: Spectroscopy conditioned on the result of an initial single shot parity readout. **(a)** Pulse sequence. We first measure the initial junction parity with a strong $20\,\mu s$ readout pulse at frequency f_r (blue card) and subsequently perform a spectroscopy pulse (red card) consisting of using a weaker $20\,\mu s$ pulse at f_r at the same time as a pulse at variable f_d on the drive line. **(b)** Top - 2D Histogram of rotated parity measurement outcomes at $\Phi = 0.44\Phi_0$ in the I-Q plane. Bottom - histogram of the projection to the I-axis (grey bars) fitted to a double Gaussian distribution (dashed black line). Blue (orange) lines show single Gaussians using the previously fitted parameters indicating even (odd) initial parity. Dashed grey line indicates the threshold used for parity selection. **(c)** Post-processed spectroscopy results of the second pulse conditioned on the initial parity, i.e the first measurement being left or right from the threshold indicated in (b). Post-selection separates the data based on initial parity [cf. Figure 4.1(e), where the same data is shown without post-processing]. **(d)** Signal to noise ratio (SNR) of the parity measurement.

are thus distributed in two Gaussian sets corresponding to the two parities [Figure 4.2(b)]. We fit a double Gaussian distribution to the projection towards the I-axis (black line) from which we extract the even (p_e) and odd (p_e) populations of the ABS (Section 4.8). We then post-select the second pulse data conditioned on the measured I in the first pulse being left or right from a Φ-dependent threshold [grey line in Figure 4.2(b)] (Section 4.8). This allows us to verify that the parity measurement outcomes belong to the even (odd) parity sector by comparing the resulting two-tone spectra of Figure 4.2(c) to Figure 4.1(e). Finally, we quantify the ability to select on parity by investigating the signal to noise ratio (SNR) of the parity measurement [Figure 4.2(d)] (Section 4.8). The SNR changes with Φ, reflecting the strong flux dependence of the dispersive shifts of the resonator corresponding to different transitions (Janvier, 2016; Metzger et al., 2021).
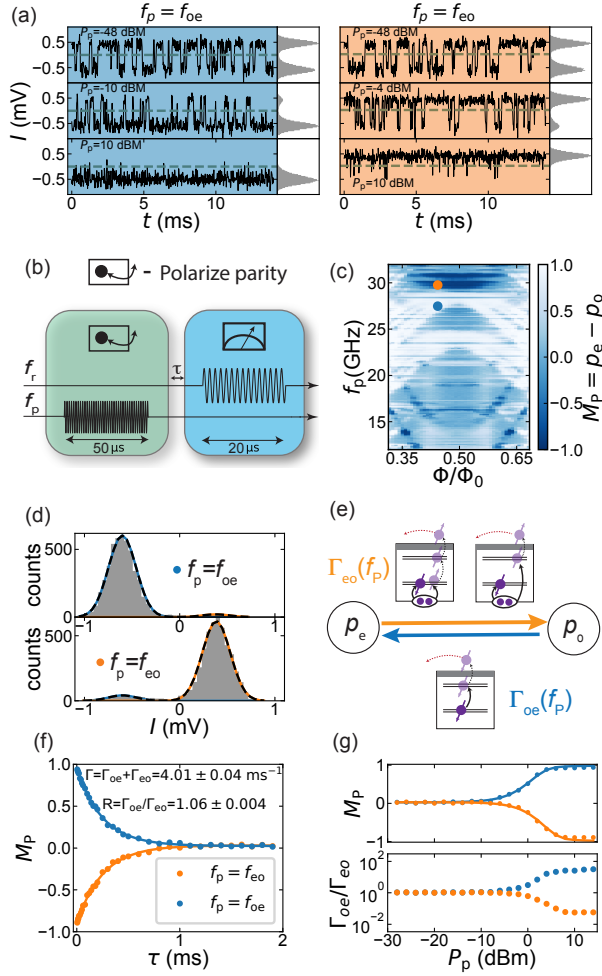
Figure 4.3: Dynamical polarization of the junction parity via microwave pumping. **(a)** Continuous parity monitoring (20 µs integration time, 15 ms trace), while applying a second tone resonant with one of the odd ($f_{oe} = 27.48\,\text{GHz}$) or even ($f_{eo} = 29.72\,\text{GHz}$) parity transitions at low, medium and strong drive power. Grey histograms show all measured points in the 2 s trace. **(b)** Pulse scheme used to verify the polarization for panels (c-g). A 50 µs polarization pulse (Section 4.8) at frequency f_p (green card) is followed after a delay τ by the same parity measurement used in Figure 4.2 (blue card). **(c)** Flux-dependent map of measured parity polarization M_P versus f_p used for the first pulse, where +1 (-1) indicates complete polarization to even (odd) parity. **(d)** Histograms of I-values of the parity measurement after polarization (P_p=14 dBm, $\tau = 4$ µs) to even (odd) parity via pumping at $f_p = f_{oe}$ ($f_p = f_{eo}$). Flux and f_p set-points are indicated by same colored dots in (c). **(e)** Phenomenological two state rate model used to describe the parity dynamics and polarization process. Dependent on f_p, either the trapping rate Γ_{eo} or de-trapping rate Γ_{oe} increases from its equilibrium value. Sketches of possible processes that increase the rates are shown. Full black arrows indicate the driven transitions, smaller arrows sketch a QP subsequently exiting the junction changing the final state parity and blocking the pumping process. **(f)** Decay time experiment. First we polarize (P_p=14 dBm) the junction into even (blue dots) or odd (orange dots) parity and then vary τ before the parity measurement. Numbers indicate equilibrium parity switching rates Γ_{oe}, Γ_{eo} extracted from an average of fits (solid lines) of the rate model for different f_p (Section 4.8). **(g)** Pump power dependence of M_P for extracting $R = \Gamma_{oe}/\Gamma_{eo}$ with $\tau = 4$ µs. Error bars in (f, g) are smaller than the markers.

4.3 Dynamical polarization of the junction parity using a microwave drive

In the absence of drive, repeated parity measurements yield a near 50-50 split between even and odd [Figure 4.2(b)], as reflected by the telegraph noise measured under continuous readout of the cavity at f_r [Figure 4.3(a, top)]. A second drive tone at a frequency f_p comparable to the ABS transition frequency changes this balance [Figure 4.3(a, middle)], with the effect increasing at stronger pumping powers P_p [Figure 4.3(a, bottom)]. In order to rule out a direct effect on the parity readout by the strong drive, we continue with a pulsed experiment [Figure 4.3(b)]. We send a pulse at f_p to polarize the parity, followed by a parity measurement (same as in Figure 4.2) on the final state. A delay $\tau = 4\,\mu s$ is inserted between pulses to make sure the resonator is not populated by the polarization pulse. We also expect the delay to allow ABS excitations to decay to their parity-dependent ground state before the readout.

To map out the frequency and flux dependence of the parity polarization, we perform a similar pulse sequence at high P_p versus Φ and f_p [Figure 4.3(c)]. We quantify the polarization $M_P = p_e - p_o$ via the parity population imbalance at the end of the sequence. For some f_p the effect is to almost completely suppress one of the two measurements outcomes, indicating that at the end of the pulse the ABS are initialized in a given parity [Figure 4.3(d)]. For instance, at $\Phi = 0.44\,\Phi_0$ we reach $M_P = 0.94 \pm 0.01$ for pumping on an odd parity transition ($f_p = 27.48\,\text{GHz}$) and $M_P = -0.89 \pm 0.01$ for pumping on an even parity transition ($f_p = 29.72\,\text{GHz}$). Note that the resulting parity is opposite to the parity of the pumped transition.

We interpret the polarization to result from the effect of the drive on the parity transition rates. To quantify this, we use a phenomenological model involving two rates Γ_{oe} (for QP de-trapping) and Γ_{eo} (for QP trapping) at which the junction switches between even and odd ground states [Figure 4.3(e)] (Section 4.8). We can estimate Γ_{oe} and Γ_{eo} by varying the delay τ between the drive and measurement pulse at the optimal drive frequencies that initialize the parity [Figure 4.3(f)]. In the absence of the drive, two rates are comparable: on average, $R = \Gamma_{oe}/\Gamma_{eo} = 1.06$ and $\Gamma = \Gamma_{oe} + \Gamma_{eo} = 4.01 \pm 0.04\,\text{ms}^{-1}$ (Section 4.8). The rates are independent of f_p or P_p used for polarization before the measurement, indicating that when the pump is off, they go back to their equilibrium value on timescales faster than the measurement time and delay used.

To investigate the effect of the drive power on the transition rates, we perform the same pulse sequence as in Figure 4.3(b), keeping $\tau = 4\,\mu s$ but varying P_p. From the power dependence of M_P we extract R versus power [Figure 4.3(g)], by assuming that we have reached a new steady state at the end of the pump tone (Section 4.8). We see that the rates become strongly imbalanced, reaching $R = 32 \pm 9$ ($R^{-1} = 17 \pm 2$) for pumping at f_{oe} (f_{eo}). From Fermi's golden rule, a single photon process would result in a linear increase of the rates with power. However, a phenomenological fit [solid lines in Figure 4.3(g)] indicates an exponent larger than one (Section 4.8). We therefore suspect multi-photon processes are at play.

The single-photon threshold frequencies expected for trapping and de-trapping are $\Delta + \min\{E_o^\uparrow, E_o^\downarrow\}$ and $\Delta - E_o^{\uparrow,\downarrow}$ (Riwar et al., 2014; Klees et al., 2017; Olivares et al., 2014; Riwar, 2015), respectively, corresponding to the breaking of a pair into one QP in the continuum

and one in the ABS, and to the excitation of a trapped QP in the continuum. However, we observe polarization at drive frequencies lower than these thresholds: Γ_{eo} increases already by driving at a frequency $E_o^{\uparrow} + E_o^{\downarrow}$, while Γ_{oe} increases when driving resonant with any odd-parity transition [3]. We suspect that the combination of a crowded spectrum - from the multiband-nature of our wire and other modes in the circuit (Olivares et al., 2014) - together with a strong drive allows ladder-like multi-photon processes [sketches in Figure 4.3(e)], as suggested in earlier experiments (Hays et al., 2021; Levenson-Falk et al., 2014). A recent theory work proposed a possible explanation for the parity polarization via a bath-induced coupling of the higher ABS doublet to the continuum (Ackermann et al., 2023).

4.4 Deterministic initialization of the junction parity

To demonstrate the effectiveness of the parity control, we perform parity-selective two-tone spectroscopy without post-selection or heralding. We deterministically initialize the parity of the junction before each spectroscopic measurement via the pumping scheme demonstrated in Figure 4.3 followed by a spectroscopy measurement [Figure 4.4(a)]. As indicated in Figure 4.4(b), at each Φ we adjust the pumping frequency to initialize in the even state to the optimum value experimentally determined in Figure 4.3(c), while a constant pumping frequency of 22.76 GHz is adequate to initialize the odd state at all Φ (Section 4.8). In Figure 4.4(c) the result is shown for even (odd) initialization on the left (right). The similarity with the post-selected results of Figure 4.2 provides conclusive evidence for the deterministic parity polarization.

---

[3]Note that we also see peaks in the polarization at transitions $f_{\text{even,odd}} \pm f_{\text{r}}$ due to multiphoton processes involving the cavity. This could be explained by the fact that a weak readout tone was on during the pumping for Figure 4.3(c) (Section 4.8). Additionally, the copy of the odd-parity transition bundle (also visible in Fig. 2) could be due to the presence of a third ABS doublet in the junction.
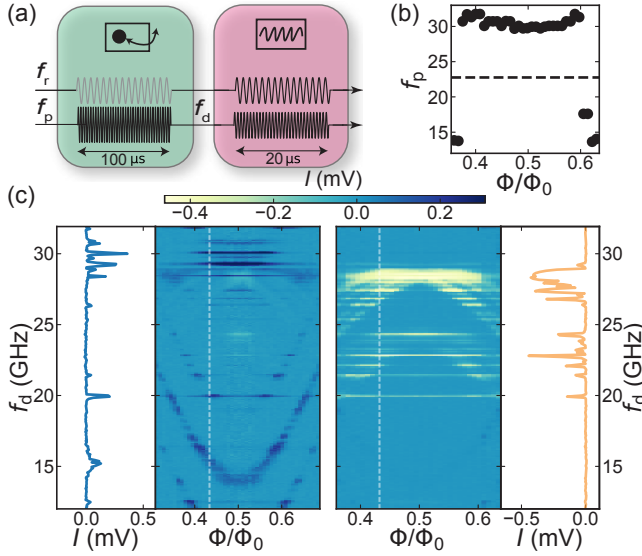
Figure 4.4: Deterministic parity initialization verified by spectroscopy for a range of flux values. **(a)** Pulse sequence. We initialize the parity using a flux-dependent f_p for 100 µs together with a low power tone at f_r (green card). This is followed after 5 µs by a spectroscopy pulse of 20 µs similar to Figure 4.2.(a), but without any post-selection or heralding (red card). **(b)** Pump frequency f_p used to increase Γ_{eo} (dots) and Γ_{oe} (dashed line). **(c)** Result of the second spectroscopy pulse after initializing into even (left panel) or odd parity (right panel). Linecuts at $\Phi = 0.43\Phi_0$ demonstrate the disappearance of odd (even) transitions after initialization in even (odd) parity.

4.5 Summary and conclusion

In summary, we demonstrated deterministic polarization of the fermion parity in a nanowire Josephson junction using microwave drives. For pumping towards even parity the maximal polarization is limited by parity switches during the measurement pulse (Section 4.8). This mechanism is not sufficient to account for the higher residual infidelity when polarizing to odd parity, which we suspect is due to a finite pumping rate towards the even sector during the polarization pulse. These results enable fast initialization of ABS parity and thus provide a new tool for studying parity switching processes, highly relevant for Andreev (Hays et al., 2021; Janvier et al., 2015; Hays et al., 2018) and topological (Karzig et al., 2017) qubits.

4.6 Acknowledgments

4.7 Data availability

Raw data and analysis scripts for all presented figures are available online at `https://doi.org/10.4121/17876240.v1`

4.8 Supplementary information

4.8.1 Methods

Author contributions

JJW, AV, LJS, MPV contributed to sample fabrication and inspection. JJW, LG, AV contributed to the data acquisition and analysis with input from GdL, BvH, AB, MPV. JJW, LG, AV, wrote the manuscript with comments and input from GdL, BvH, AB, LJS, MPV. Nanowires were grown by PK. Project was supervised by GdL, BvH.

Fabrication

The whole circuit [Figure 4.5] is patterned in a sputtered 22 nm thick NbTiN film with a kinetic inductance of around 11 pH/square using SF6/O2 reactive ion etching. Subsequently, 28 nm of Si_3N_4 is deposited using plasma-enhanced chemical vapor deposition (PECVD) at 300 ˚C and patterned using a 3 minute 20:1 BOE (HF) dip with surfactant, serving both as a bottom gate-dielectric and as isolation for 75 nm sputtered NbTiN bridges connecting the separated ground plane around the gate lines. The hexagonal nanowire has a diameter of ≈ 80 nm and is epitaxially covered (Chang et al., 2015) on 2 facets by a 6 nm Al shell [Figure 4.1(a)]. It is transfered using a nanomanipulator on top of a NbTiN gate structure separated by Si_3N_4 dielectric. The ≈ 150 nm junction is etched with a 55 second MF321 (alkaline) etching step. Finally the nanowires are contacted by 150 nm of sputtered NbTiN after 3 min of in-situ AR-milling at 50W.

Circuit design

The circuit shown in Figure 4.1(b) consists of a lumped element readout resonator with a resonance frequency $f_c = 4.823$ GHz ($L_r \approx 21$ nH, $L_s \approx 0.7$ nH, $C_r \approx 47$ fF), which is over-coupled to a 50 Ω transmission line. A chosen $C_c \approx 4$ fF results in a coupling quality factor $Q_c = 1.7 \cdot 10^3$. The coupling and internal quality factor $Q_i = 15 \cdot 10^3$ are extracted using the model in (Khalil et al., 2012) for a fit at average intra-cavity photon number $\langle n_{ph} \rangle \approx 1800$ (Bruno et al., 2015) as shown in Figure 4.6 (a fit at $\langle n_{ph} \rangle \approx 17$ gave similar results). Typical coupling to the ABS was designed to be $g/h = I_s \frac{L_s}{L_s + L_r} \sqrt{\frac{\hbar Z_{Lc}}{2}} \approx 250$ MHz at $\varphi = \pi$ using a single channel ABS model (Zazunov et al., 2003) with $I_s \approx 10$ nA. Note that the actual coupling strength depends on flux and I_s, which also depends on V_g. We set Φ using a magnetic field with a vector magnet applied perpendicular to the nanowire but in plane with the NbTiN film, to reduce flux jumps. The effective loop area then consists of twice the area A under the nanowire between the contacts due to the gradiometric design (see Figure 3.18). The field corresponding to one flux period is 3.65 mT ($A = 0.28 \mu m^2$). By choosing $L_s \ll L_j$, we ensure that the phase drop φ over the junction is proportional to the external flux threading the loop $\varphi = 2\pi\Phi/\Phi_0$ (Clarke and Braginski, 2004).
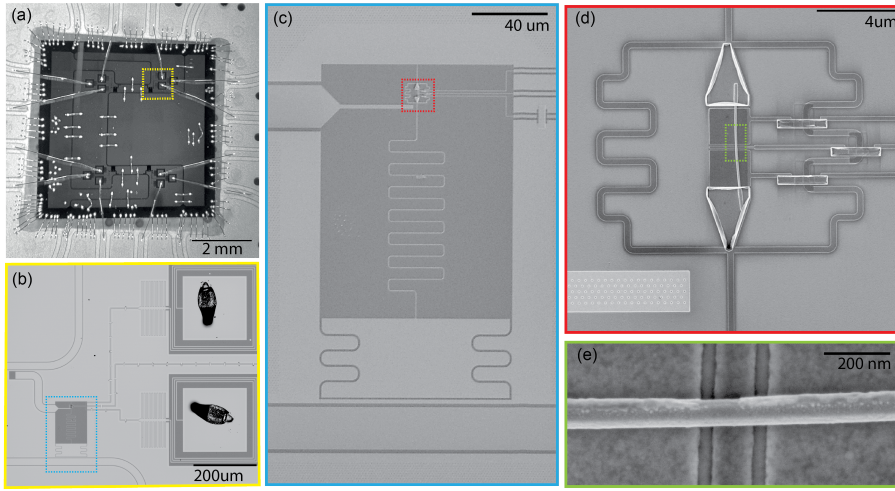
Figure 4.5: Additional images of the measured device. (a, b) The chip contains four devices of which one was fully functional and studied in this work. Readout was performed for all devices via a single transmission line. A second transmission line is coupled to all devices via coupling elements acting as an effective capacitance to the device. This allows using a single line to drive multiple devices. The gate lines had on-chip LC filters to reduce high frequency noise (Mi et al., 2017b). (c-e) Additional scanning electron micrographs of the device described in Figure 4.1. In a 21 μm radious around the resonator, as well as in the capacitor plate, transmission-lines and drive-line, 80 nm diameter round vortex pinning sites were patterned to reduce flux jumps and vortex induced losses when applying magnetic fields (Kroll et al., 2019). Furthermore the ground plane was patterned with 500 nm square holes to trap residual flux.

Wiring diagram

A wiring diagram is shown in Figure 4.7. A R&S ZNB 20 VNA was combined with a standard homodyne detection circuit using a splitter. A Zurich instrument high frequency lockin amplifier (UHFLI) both generated and demodulated a microwave tone between 500 MHz and 600 MHZ using the same internal oscillator. This signal was upconverted by mixing it with the RF output of a R&S SRS 100A microwave source set to a fixed frequency of 4237.11 MHz resonant with the frequency of another resonator on the chip to minimize LO leakage. After traveling through the fridge, the signal was amplified at 4K using a LNF 4-8 GHz HEMT amplifier as well as by two amplifiers at room temperature. This was then downconverted by mixing with the LO output of the SRS100A microwave source and demodulated in the UHFLI to obtain the I,Q values shown in the main text. All RF instruments were synced using a 10MHz rubydium reference.

Pulse sequences were generated on both a Tektronic AWG 5208 and the internal AWG of the UHFLI and were both set to a clock frequency of 1.8 GHz. The UHFLI AWG was set to a sampling frequency of 225MHz. The Tektronic AWG send pulses (square) on 2 channels:

1. A first long pulse gated UHFLI data streaming -allowing for a low duty-cycle measurement to circumvent ethernet bandwidth problems when streaming at a UHFLI sampling rate of ≈1 MHZ. The same pulse triggered the UHFLI internal AWG to start.
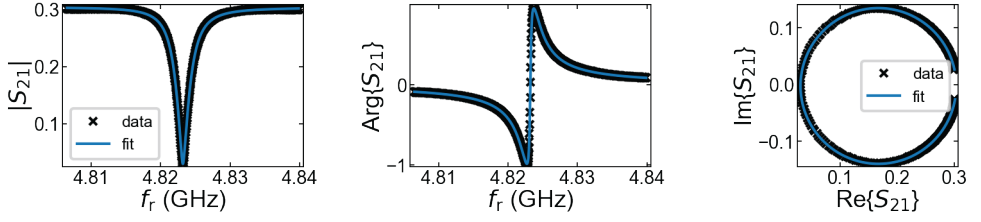
Figure 4.6: Measurement and fit of resonance of the readout resonator shown in Figure 4.5.

2. A second pulse controlled the R&S SMR drive pulse-modulation used to pump parity.

The UHFLI internal AWG also send two pulse sequences:

1. The first sequence amplitude modulated the internal oscillator output of the UHFLI

2. the second sequence was send to the pulse-modulation input of the Agilent E8267D microwave source used for the spectroscopy drive.

The roughly 150 ns delay due to activation of pulse modulation and fridge traveling time were calibrated out using the internal scope function of the UHFLI. Readout amplitudes A quoted in this work correspond to $A = V_{pp}/1.5\text{V}$ of the carrier sine wave at f_r used for readout pulses.
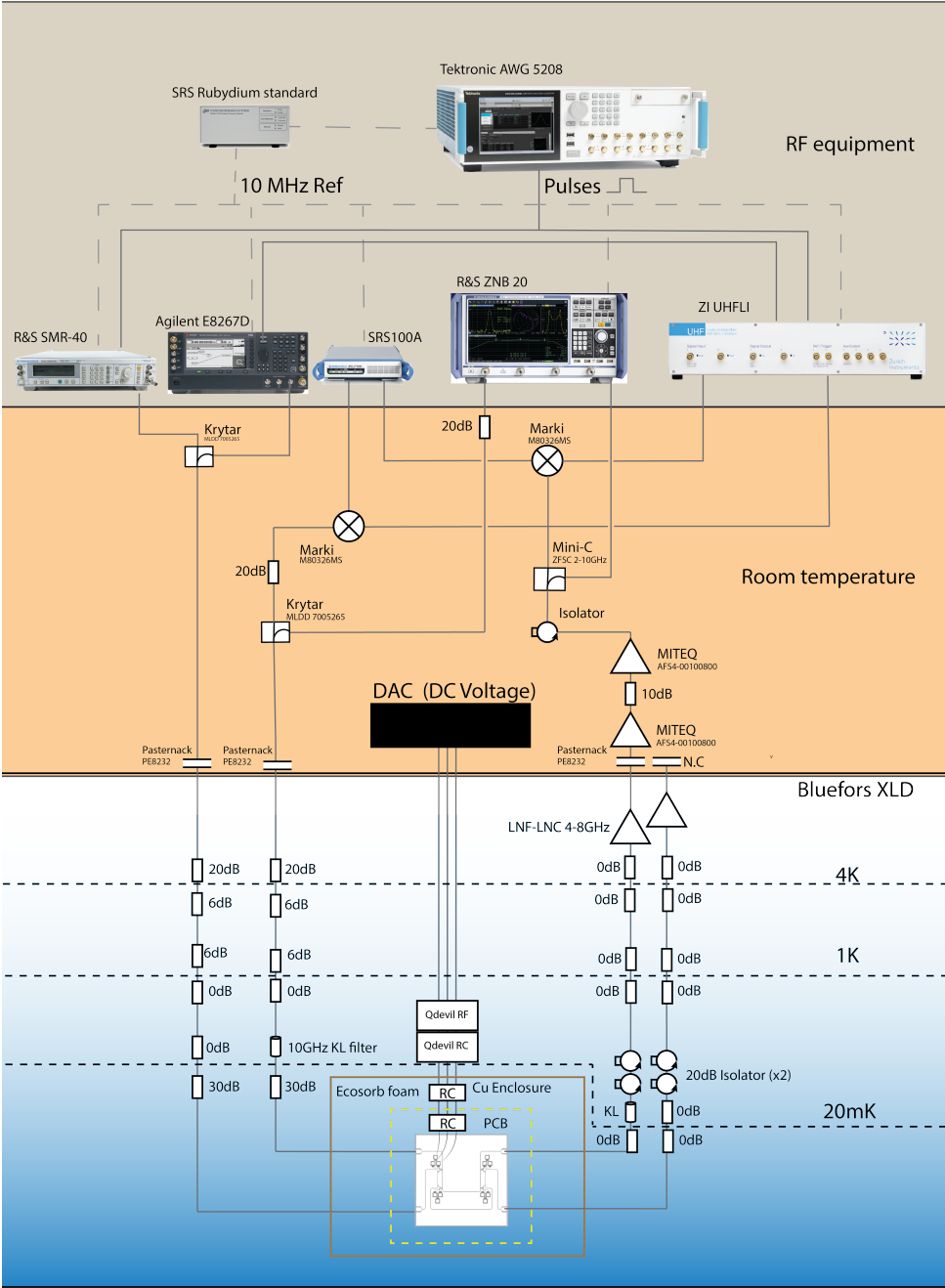
Figure 4.7: Full wiring diagram of the experiment.

Measurement methods

For all two tone spectroscopy data in the paper, we determined the optimal readout point by fitting a simple Lorentzian to $|S_{21}|$ [Figure 4.6 (a)] by taking a frequency dependence for each Φ value. We then took the readout point to be at the minimum of this fitted Lorentzian. We found fitting a single Lorentzian worked even in the case of a split resonator from the dispersive shift of the even state close to $\Phi = 0.5\Phi_0$. This resulted in measuring in the middle between the even/odd shifted resonator, allowing for both even and odd parity readout.

Gate operation point

In Figure 4.6(a) we show an RF version of a typical pinch-off trace of the supercurrent. Here we monitor the magnitude of the transmitted signal, which is a proxy for a change in resonance frequency f_c of the resonator. At $0.5\Phi_0$ as shown here, f_c goes up when the magnitude of the supercurrent increases - or similarly the inductance decreases. The trace shows mesoscopic oscillations as often seen in these systems (Doh, 2005), but nevertheless has an increasing trend with V_g. We stay close to pinch-off such that we stay in the few-mode regime as shown in a two tone trace at $\Phi = 0.6\Phi_0$ [Figure 4.6(c)]. The gate dependence of odd and even states show a clear opposite trend (Tosi et al., 2019), since when the transparency of ABS decreases, the interband odd transitions go down in frequency while the even transitions go up. As described in the main text, for all data taken in the main text figures we kept the gate voltage fixed at $V_g = 0.6248$ V during the three weeks of data taking for this experiment in order to have a consistent dataset. V_g was chosen to minimize overlap between even and odd parity transitions in the spectrum. The lowest available transition was taken to be far away from the resonator to prevent non-linearities in the cavity at high n_{ph} and facilitate parity readout. We expect the polarization to be possible also at other gate voltages where ABS transitions are available. However, since we suspect the polarization is caused by ladder-like processes, it might be that the polarization becomes harder (easier) when the spectrum is less (more) crowded.
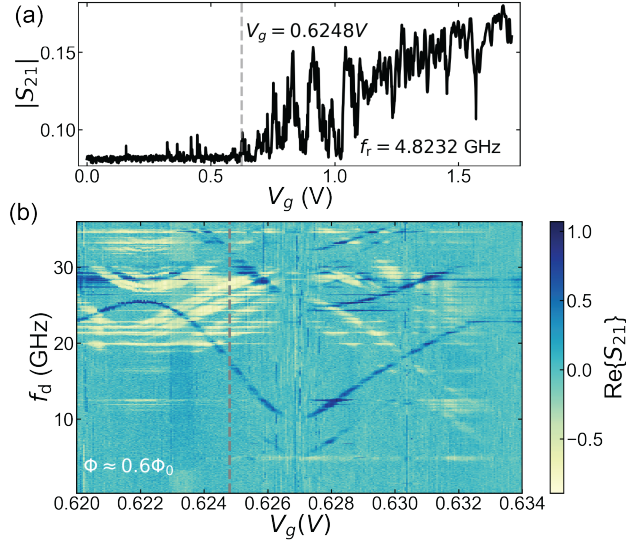
Figure 4.8: (a) Pinch-off trace, monitoring the magnitude $|S_{21}|$ of the transmitted signal at fixed frequency indicated versus applied gate voltage. Also indicated is the operating point $V_g = 0.6248\,$V for all other data taken. (b) Two tone trace taken at $\Phi \approx 0.6\Phi_0$ showing the ABS dispersion versus a small gate range. Grey dashed line indicate again the operating point.

4.8.2 Data analysis and additional information

In general, for all figures, the measured I-Q values during a parity or spectroscopy pulse pulse give two Gaussian distributed sets of outcomes in the I-Q plane [see e.g. Figure 4.2(b)]. These are rotated to maximize the variance in the I-quadrature. Subsequently they are projected towards I for each Φ separately, since the readout frequency is Φ dependent. For 2D measured spectra(c.f Fig 1., Fig 2, Fig 4.) we also subtracted a flux-dependent background - the median of I of all f_d for each Φ - to compensate for the change in $f_r(\Phi)$.

Parity selective spectroscopy - Figure 4.1, Figure 4.2
We now describe the analysis steps used to create the results of Figure 4.1.(e) and Figure 4.2. For the spectroscopy data of Figure 4.1, we used the average of all shots of the measured data in the spectroscopy pulse for Figure 4.2 - e.g without any post-selection. For the pulse sequence used in Figure 4.2 (a), we first sent a 20 μs readout pulse at frequency f_r ($A = 0.05$), followed by a 20 μs two-tone spectroscopy sequence, i.e reading out at f_r ($A = 0.025$) while driving at f_d ($P_d = 10\,$dBm). To empty the cavity between parity measurement and spectroscopy, we inserted a 5 μs wait time. Note that the drive power is sufficient to also induce parity pumping (see Figure 4.13) in addition to exciting the transition directly. We found this to increase the contrast in the spectrum. The sequence was repeated every 1.2 ms for each shot, in order to make sure the junction returned to its equilibrium state. This also made sure any parity pumping in the spectroscopy did not affect the subsequent shot. From the total line attenuation and adding $\approx 6\,$dB loss due to the skin-effect and insertion losses, we estimate average photon number in the resonator

during parity readout to be $\langle n_{\text{ph}} \rangle \approx 44$ ($P_{\text{in}} = -118$ dBm) and $\langle n_{\text{ph}} \rangle \approx 11$ ($P_{\text{in}} = -124$ dBm) during the spectroscopy pulse (Bruno et al., 2015).

For the parity readout pulse, the rotated 1D histograms of I are fitted to a double Gaussian distribution (black line in Figure 4.2) of the form $c(x) = a_1 / \sqrt{2\pi\sigma_1^2} \exp(-(x - \bar{x}_1)^2/2\sigma_1^2) + a_2 / \sqrt{2\pi\sigma_2^2} \exp(-(x - \bar{x}_2)^2/2\sigma_2^2)$. For each Φ we determined a selection threshold $I_T(\Phi) = \left(F^{-1}(0.4) + F^{-1}(0.6) \right)/2$ where F^{-1} denotes the inverse function of the cumulative normalized histogram of measured I values. The threshold for $\Phi = 0.44\Phi_0$ is indicated in Figure 4.2(b). We then post-select the data of the second pulse conditioned on having $I < I_T$ ($I > I_T$) in the first pulse, keeping all data. Note that it is possible to improve the accuracy of the selection if we selected further away from the threshold, keeping less data. We define the signal-to-noise ratio as SNR $= |\bar{x}_e - \bar{x}_o|/2\sigma$ (de Jong et al., 2019). Here, $\bar{x}_e(\bar{x}_o)$ is the mean of the fitted Gaussian belonging to the even (odd) parity and σ the standard deviation, which is kept fixed to the values found in [Figure 4.2(b)] and kept the same for both Gaussians. Note that for $0.46\Phi_0 < \Phi < 0.54\Phi_0$ we see a slight deviation from the fit, reducing the validity of the SNR estimate, possibly due to a small readout-induced excited population. Letting σ free as a fit parameter then results in a maximally 8% reduction in the extracted SNR. Extracting R versus Φ from the fitted amplitudes resulted in a ≈ 0.1 variation in R over the flux range.

Pulsed polarization measurements - Figure 4.3

We now describe the procedure used to obtain the data in Figure 4.3(d-g) using the pulse sequence of Figure 4.3(b). For this data, we varied the pump power P_{p} for four pump frequencies f_{p}. This was repeated for each delay time τ. An additional 1 ms of waiting time was introduced after the two-pulse sequence to get back to equilibrium before the next sequence. For each f_{p}, we do a double Gaussian fit to the rotated I histograms of the 2nd pulse measurement shots for all P_{p} together to obtain a single σ and two means x_1, x_2. We then keep the means and the single σ fixed for each τ. Measuring each τ versus power took about 30 minutes so we allowed for a small variation in the mean of the Gaussians due to slow drift in the setup. We fit a_1 and a_2 for each P_{p}. We then obtain the populations by normalizing $p_{\text{o}} = \frac{a_1}{a_1 + a_2}, p_{\text{e}} = \frac{a_2}{a_1 + a_2}$. Uncertainties in M_{P} and R follow from propagating the error in the fit uncertainties of a_1, a_2.

The pump-frequency map of Figure 4.3 (c) was analysed similarly as described above, but keeping σ fixed at all fluxes. By inspection of the fits and the residuals χ^2, for some drive frequencies the fit residuals were very large (e.g. the data did no longer match a double Gaussian), resulting in horizontal lines in the plot. These we attribute to circuit resonances affecting the readout when excited with the drive tone. As stated in the main text, the second pulse (parity readout) was the same used for Figure 4.2, Figure 4.3(d-g). However, for the pumping pulse, next to a tone at f_{p}, a second weak tone at $f_{\text{r}}(A = 0.02)$ was present (see in Figure 4.9), which we expected to help the pumping (see discussion in Section 4.8.7). The wait time after each shot was reduced to 200 μs in order to save measurement time for the large 2D map, which is also the case for Figure 4.4.
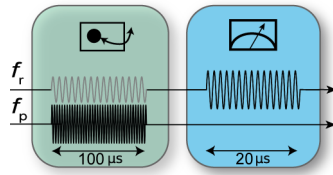
Figure 4.9: Pulse sequence used in Figure 4.3(c)

Deterministic parity initialization spectroscopy - Figure 4.4

For this dataset we used Figure 4.3 to estimate the best pumping frequency for the polarization emperically for $f_{\mathrm{eo}}(\Phi)$, by looking where $M_{\mathrm{P}}(\Phi, f_{\mathrm{p}})$ was maximal. We then applied the pulse sequence described in Figure 4.4, for the even and odd initialization separately. Note that for $f_{\mathrm{oe}}(\Phi)$ we pumped at a fixed frequency $f_{\mathrm{oe}} = 22.76$ GHz, because the crowded spectrum of odd transitions there gave a finite pumping rate over the whole required flux range.

4.8.3 Comparison of measured spectrum to theory
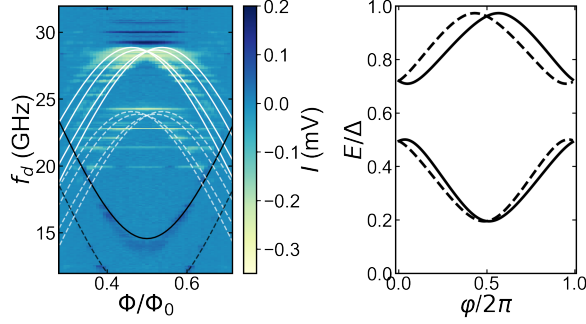
Figure 4.10: Fit of the ABS spectrum with to a single barrier model (Tosi et al., 2019) used to construct the energy levels of Figure 4.1(d). (a) Black and white solid lines indicate the fitted even and odd transitions and dashed lines are copies, displaced by -f_r (4.82 GHz) that are visible in the data due to a finite $\langle n_{ph} \rangle$ in the cavity during spectroscopy. The optimal single barrier model parameters are: Δ=37.1 GHz, λ_1=1.37, λ_2=1.82, τ=0.76, x_r=0.68. (b) Corresponding spin-down (solid) and spin-up (dashed) Andreev levels also shown in Figure 4.1(d)

We applied the phenomenological model described in Tosi et al. (2019); Park and Yeyati (2017) to fit a pair of even and odd transitions simultaneously. This model considers a junction with 2 sub-bands in presence of spin-orbit coupling. Only the lowest sub-band is occupied, and the lowest levels gain a spin-dependent Fermi-velocity v_{Fj} due to spin-orbit interaction with the higher band. The resulting ABS energy spectrum is used in Figure 4.1(d) to illustrate the two types of transitions.

Even and odd transitions were extracted from the spectrum by thresholding I. The fit was performed by first mapping the theoretical lines to 2D by assigning an artificial 0.2GHz wide step-function, and applying a Gaussian filter over both theory and extracted data. Finally the resulting 2D arrays are compared. The extracted model parameters are: Δ=37.1 GHz, λ_1=1.37, λ_2=1.82, τ=0.76, x_r=0.68. Here, Δ is the superconducting gap; λ_j is the ratio of the effective junction length L and the ballistic coherence length, $\lambda_j = L/\xi = L\Delta/(\hbar v_{Fj})$, τ is the transmission probability of a single scatterer located at x_r used to model a finite normal reflection probability due to elastic scattering in the junction. We refer the reader to Refs (Park and Yeyati, 2017; Tosi et al., 2019) for further details about the parameters.

We are hesitant to relate these parameters to microscopic properties of the junction, because the fit was very sensitive to the initial guess and the model assumes only a single occupied sub-band, while in gate sweeps we generally see multiple ABS present (c.f Figure 4.6), which can significantly distort the extracted fit parameters. However, the model shows qualitatively good agreement with the shape of the transitions shown in the data, clearly demonstrating the parity nature of the two transitions which is what is important for the conclusions drawn in this work.

4.8.4 Rate equations and additional fits

The simple rate model illustrated in Figure 4.3 (e) is given by

$$\dot{p}_{\mathrm{e}} = \Gamma_{\mathrm{oe}} p_{\mathrm{o}} - \Gamma_{\mathrm{eo}} p_{\mathrm{e}}$$
$$\dot{p}_{\mathrm{o}} = \Gamma_{\mathrm{eo}} p_{\mathrm{e}} - \Gamma_{\mathrm{oe}} p_{\mathrm{o}} \tag{4.1}$$

The general solution for a given population $p_{\mathrm{e}}(0)$ and $p_{\mathrm{o}}(0)$ at $t = 0$ is given by

$$p_{\mathrm{e}}(t) = p_{\mathrm{e}}(0) + \frac{\Gamma_{\mathrm{oe}} p_{\mathrm{o}}(0) - \Gamma_{\mathrm{eo}} p_{\mathrm{e}}(0)}{\Gamma} \left(1 - \Gamma e^{-\Gamma t}\right)$$

where $\Gamma = \Gamma_{\mathrm{oe}} + \Gamma_{\mathrm{eo}}$ and $p_{\mathrm{o}}(0) = 1 - p_{\mathrm{e}}(0)$. Note that we are under the (simplified) assumption that we don't have population in the excited states of each parity branch. We denote the populations in both spin-split levels with p_{o}, since we do not resolve spin in our measurement.

Fit of equilibrium rates
We fit the data from Figure 4.3 (f) to the above model in order to extract Γ, R when the drive is off. This is done by setting $t = 0$ at the end of the drive pulse and then evolving the undriven rate model for a time τ in Equation (4.1) (adding 10 μs to compensate for decay during the measurement pulse). In Figure 4.11 we show the fit results for the two frequencies used in Figure 4.3 (f) of the main text, as well as for two additional pumping frequencies on which we performed the same experiment.

Using the equilibrium values for Γ and R, we can infer that the residual infidelity of the parity pumping towards even of Figure 4.3(d) is limited by the decay back to equilibrium during the wait time τ and the measurement pulse. This is because evolving the equilibrium rates starting from a fully pumped $M_{\mathrm{P}} = 1$ for the duration of the delay and of half the measurement pulse width (14 μs) would give $M_{\mathrm{P}} = 0.946$ (the full 24 μs would give $M_{\mathrm{P}} = 0.91$). The same explanation is not enough to explain the residual depolarization when pumping towards odd parity. This could be due to a finite power dependent pumping towards even at those frequencies, for example due to higher order odd transitions $\pm f_{\mathrm{r}}$ occurring at high powers, since the odd spectrum is more crowded in general.

Fit of power dependence of pumping
In an attempt to shed light on the order of the processes involved during pumping, we now consider a modification to Equation (4.1) by assuming $\Gamma_{\mathrm{oe}}, \Gamma_{\mathrm{eo}}$ are changed during the pumping pulse. We adopt the following phenomenological model to account for a power-dependence of the transition rates

$$\begin{cases} \text{if } f_{\mathrm{p}} = f_{\mathrm{oe}}, \ \Gamma_{\mathrm{oe}} = \Gamma_{\mathrm{oe}}^{\mathrm{Eq}} + kP_{\mathrm{p}}^{x}, & \Gamma_{\mathrm{eo}} = \Gamma_{\mathrm{eo}}^{\mathrm{Eq}} \\ \text{if } f_{\mathrm{p}} = f_{\mathrm{eo}}, \ \Gamma_{\mathrm{oe}} = \Gamma_{\mathrm{oe}}^{\mathrm{Eq}} & \Gamma_{\mathrm{eo}} = \Gamma_{\mathrm{eo}}^{\mathrm{Eq}} + kP_{\mathrm{p}}^{x} \end{cases} \tag{4.2}$$

Here, P_p is the applied pumping drive power at de-trapping (trapping) frequency f_{oe} (f_{eo}) and k, x are fitting parameters that may depend on the pump frequency. Here, k is a measure of the frequency response of the circuit and tranmission lines at f_{p} from the microwave source to the sample, which is assumed constant versus pump power. The

extracted x gives information on the order of the process involved during the pumping. In accordance with Fermi's golden rule, a single photon process would result in $x = 1$. $\Gamma_{oe}^{Eq}, \Gamma_{eo}^{Eq}$ represent the equilibrium rates extracted in Figure 4.11. To reduce the amount of fit parameters, we assume that pumping on an even (odd) transition at f_{eo} (f_{oe}) only changes Γ_{eo} (Γ_{oe}).

For each power, we evolved the rate model with one of the rates made power-dependent for the duration of the pump pulse, followed by evolving the un-driven model for the wait time τ and half the measurement pulse length. We apply this procedure to fit the power dependence at four f_p with k and x as free fit parameters [Figure 4.12]. The average of the best fit results of x for the four different f_p is $x = 1.4 \pm 0.1$.

The extracted value of k varied with f_p, because k represents the absolute power as a function of frequency that arrives at the sample. Therefore, k depends on the frequency response of the setup plus on-chip lines, which is not easily known from an independent measurement at frequencies outside the amplifier bandwidth. Since k, x had a large correlation coefficient in the fit, in Figure 4.12 we display additional fits keeping x fixed at the values indicated and fitting only k. The fact that $x = 1$ doesn't fit well points towards a multiphoton nature of the polarization processes, also suggested for de-trapping in Hays et al. (2021). Care has to be taken for extraction of x at high powers, since from the analysis of continuously readout traces in Section 4.8.8 we found that eventually both rates start increasing, which violates one of the simplifying assumptions of the model in Equation (4.2).

Extraction of R

By assuming the system is in equilibrium at the end of the pump pulse, we can solve Equation (4.1) directly: $R = 1/p_o - 1$. This is used in Figure 4.3 (g) to extract the power dependence of R. This gives a conservative estimate of R, because a steady state is not reached for a pump pulse length of 50 μs. Furthermore we neglected decay during τ and measurement time which also reduces the extracted R. Note that we could have also gotten R as a function of power from fitting Equation (4.2), which would slightly increase the estimates shown in the main text.
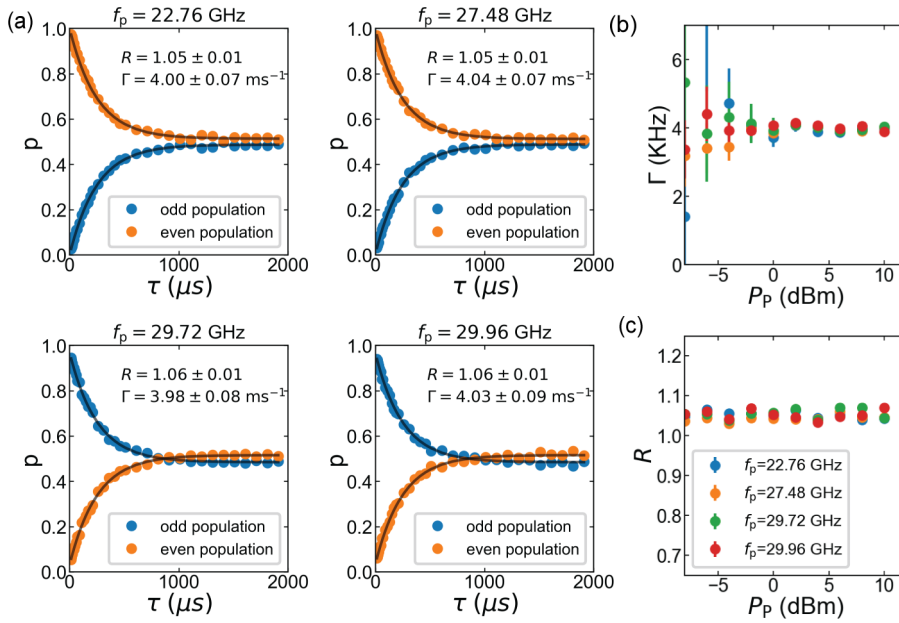
Figure 4.11: (a) Fits of the population decay shown after pumping at different f_p in the main text, and two additional datasets used to extract R, Γ. (b, c) extracted ratios R and Γ from the delay time fits of (a) versus P_p, at lower pump powers the contrast goes down and the fits become more inaccurate. The fact that R stays constant vs P_p indicates that there is no drive induced long time scale process (longer than $4\mu s$ governing the parity imbalance (e.g a non-equilibrium QP population that remains after turning the pump off).

4
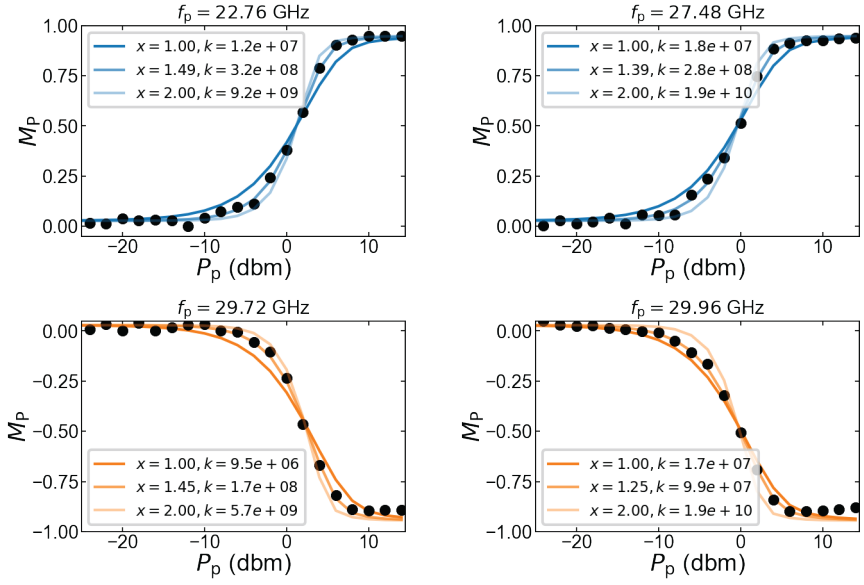
Figure 4.12: Power dependence at the same f_p as in Figure 4.11 with fits using Equation (4.2) with both x, k as free parameters. Two additional fits are shown keeping x fixed to 1,2 and fitting only k.

4.8.5 Effect of pump pulse length on the polarization

In Figure 4.13 we show how the polarization depends on the length of the pumping pulse τ_p and pump power at the same pump frequencies and flux value used in the main text Figure 4.3 and Figure 4.12. At high P_p we reach $M_\mathrm{P} > \pm0.9$ already after 5 μs which could be beneficial for state-initialization protocols with high repetition rates.

In the bottom panel Figure 4.13 we show results of the rate equation model Equation (4.2) for varying pump lengths τ_p keeping all parameters fixed to those obtained in the fit of the 50 μs pulse in Figure 4.12. This is done both at f_oe and f_eo. The agreement with the model for most τ_p indicates that transient effects (a time dependent R after the drive is turned on) become relevant at $\tau_\mathrm{p} < 5$ μs, where the steady state rate equation starts deviating from the data.
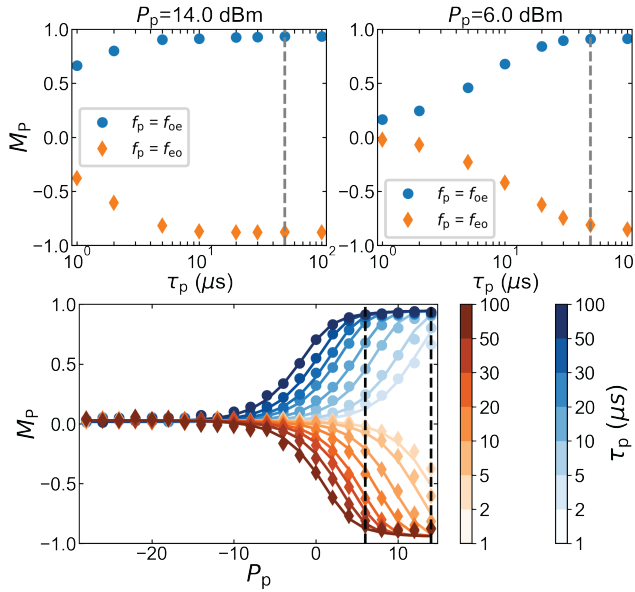
Figure 4.13: Pump length dependence of the polarization. Top panels show dependence of M_P on the length of the pumping pulse τ_p for two pump powers P_p (black dashed lines in bottom panel). Grey dashed line indicates $\tau_p = 50$ μs, which is used in Figure 4.3. Bottom panel indicates polarization power dependence for each τ_p (markers). Solid lines are evaluations of the driven rate model keeping all fit parameters fixed to the values obtained in Figure 4.12 (for $\tau_p = 50$ μs) and only varying τ_p according to the experimental setting. Used pump frequencies and pulse scheme were the same f_p as used in Figure 4.3 in the main text.

4.8.6 Parity population after readout pulse at f_r

We performed a calibration experiment to make sure that the parity measurement does not influence the populations, and therefore M_p, at the readout amplitude used for Figs. 2 and 3. We first apply an initial 20 µs readout pulse at a flux-dependent f_r (using the fitting protocol described in Section 4.8.1) with variable amplitude A_1, simulating the parity readout used in the rest of this work. Then, after waiting 5 µs to reset the cavity, this is followed by another 20 µs pulse at f_r at low amplitude $A_2 = 0.02$ to measure the resulting parity populations. This was repeated for multiple flux values Φ.

Figure 4.14: Effect of parity readout on the parity population. (a) Pulse scheme. A first 20 µs variable amplitude parity readout pulse is sent in, followed after waiting 5 µs by another low power 20 µs parity readout pulse. (b) Population difference (odd p_o, minus even p_e) induced by the initial parity measurement resonant with the cavity 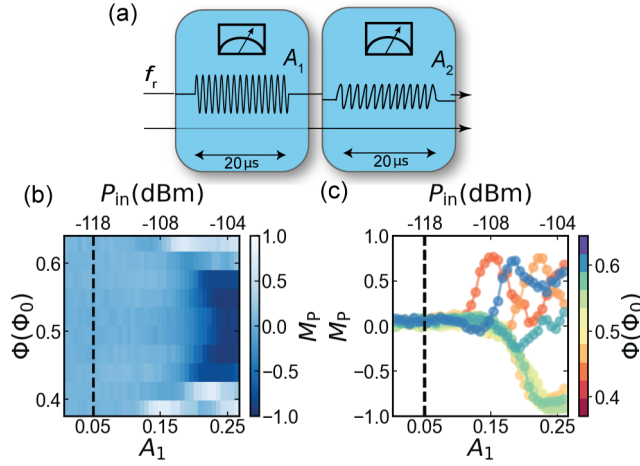frequency f_0 versus flux and parity pulse amplitude A_1 as measured by the second low power readout pulse ($A_2 = 0.02$). The black dashed line indicates the amplitude used for the parity readout ($A_1 = 0.05$) of the parity readout pulse in the rest of the paper. This is well below the values where the parity starts being pumped by a cavity tone alone. (c) Line-cuts at different Φ (indicated in colorbar) versus A_1. For reference, an estimate of $LP_{in} = V_{rms}^2/Z$, with $Z = 50\,\Omega$ and $V_{rms} = \frac{A_1}{2\sqrt{2}} \cdot 1.5\,V$, at the input of the chip is given on the top axis. Here the attenuation L includes line attenuation, known conversion losses and an additional estimated 6dB loss from the skin-effect and other sources. See Figure 4.7. In the region of the oscillations at high A_1 the response of the cavity (when inspecting the first pulse I-Q outcomes) becomes highly non-linear which makes a clear interpretation challenging.

After rotation we fit a double Gaussian to a combined histogram of the rotated I values of the 5 lowest A_1 (to obtain more counts and a better fit) at $\Phi = 0.535\Phi_0$ where we had the largest SNR. Secondly, keeping $\sigma_1, \sigma_2 = \sigma$ fixed to $\sigma = (\sigma_1 + \sigma_2)/2 \; \forall \; \Phi$, we fitted for each Φ the means x_1, x_2 of again the 5 lowest A_1 combined. Then finally keeping all $x_1, x_2, \sigma_1, \sigma_2$ fixed to the values obtained for each Φ we fitted the amplitudes a_1, a_2 for each Φ, A_1 value. Note that by inspection of the fits we discarded the data at $\Phi < 0.37\Phi_0$ and $\Phi > 0.62\Phi_0$ since there the SNR was too low to do a proper double Gaussian fit.

The result of the second pulse parity measurement is shown in Figure 4.14. At the amplitude $A_1 = 0.05$ used for the parity measurements of the main text, the populations are not affected by the parity measurement itself. However, at higher readout power, the

parity can be pumped by the readout tone alone, as also found in previous works (Janvier, 2016). Note that the pump direction due to photons in the cavity switches sign around $0.43\Phi_0$ and $0.57\Phi_0$, pumping towards even instead of odd parity. This feature is not fully understood: it could be related to the change of ABS transition frequencies with flux relative to other resonances coupled to the cavity, or to multi-photon transitions involving the cavity (Olivares et al., 2014).

4.8.7 Readout power dependence of pulsed pumping process

The pumping sequence of Figure 4.4 and Figure 4.3(c) had a weak ($A_1 = 0.02$) cavity tone on during the pumping, since we assumed that would facilitate multi-photon transitions towards the continuum. We investigate the effect of pumping parity when a second tone at f_r is present in Figure 4.15. The pulse sequence of Figure 4.9 was used. We then varied the amplitude of the first pulse tone at f_r as well as P_p. In Figure 4.14 we already found that a readout tone can polarize the parity by itself, where the polarization direction depends on the applied phase bias. The results of Figure 4.15 show that indeed for lower pump powers a weak cavity tone helps the pumping process (in both directions). However, at strong pump power the highest polarization is actually achieved for $A_1 = 0$ in both pump directions. A possible explanation could be that with increasing $\langle n_{ph} \rangle$ in the cavity the total Γ increases (as seen in Figure 4.18), reducing R effectively. A general trend of pumping towards even parity with A_1 is also visible.
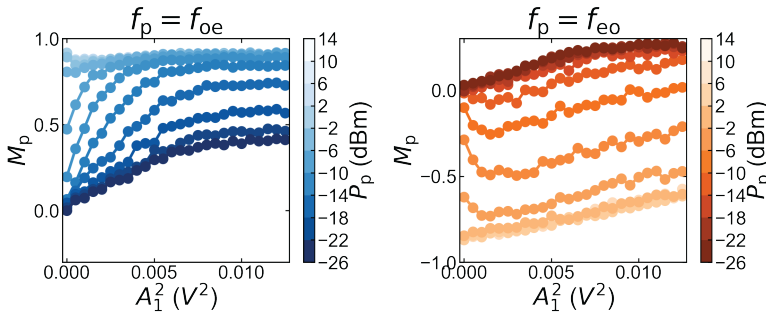
Figure 4.15: Pump versus readout power dependence of the pumping pulse at $\Phi = 0.44\Phi_0$. The pulse sequence of Figure 4.9 was used. Depicted is M_p versus squared readout amplitude A_1 of the tone at f_r and P_p of the tone at f_p for $f_p = f_{oe} = 27.48$ GHz (left graph) and $f_{eo} = 29.72$ GHz (right graph) for different P_p as indicated on the colorbar.

4.8.8 Continuous readout during pumping

As an alternative verification of the parity pumping process, we perform experiments with continuous driving and readout of the ABS (two traces shown in Figure 4.3 (a)), similar to e.g. Janvier et al. (2015); Hays et al. (2018). Opposed to the pulsed experiments described before, we now send a continuous microwave tone at fixed frequency and power to readout and drive line, respectively, and record traces of 2 s for various combinations of drive frequency f_d, drive power P_d and readout amplitude A_{ro}. The experiments were performed at the same f_p and a flux $\Phi = 0.46$ close to the pulsed experiments in order to
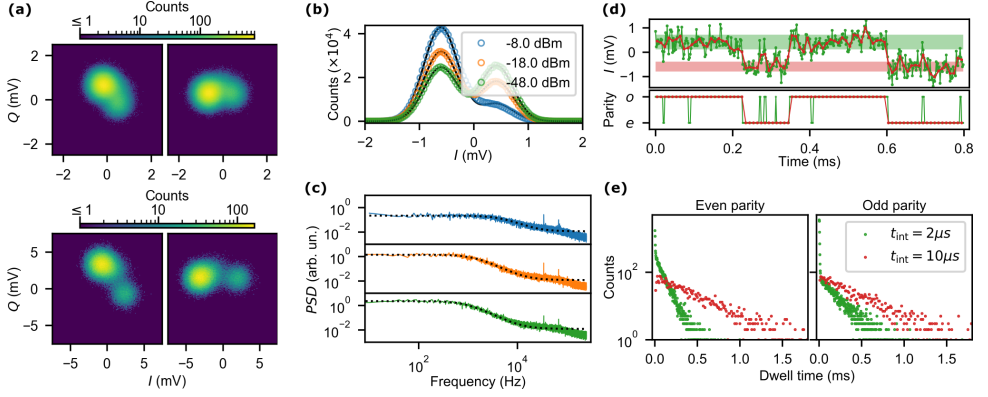
Figure 4.16: Analysis procedure for driven parity switching traces. **(a)** 2D histogram of the raw (left) and rotated (right) measured data in the *IQ* plane to project parity information solely into the *I* quadrature. The top panel shows the original data with $t_{int} = 2\,\mu s$, while the bottom panel shows the data obtained by summing five consecutive points. **(b)** Histogram of the *I* quadrature of rotated raw measurement data (points) and fit of a double Gaussian distribution (solid black line) for three different drive tone powers. At high drive power the amplitude of one Gaussian decreases, indicating the decreasing presence of the associated junction parity. **(c)** Power spectral density of the projection to the *I* quadrature of the rotated time resolved data (colored lines, legend of panel (c) applies) and fit of a Lorentzian (dashed line) yielding a characteristic transition rate (Machlup, 1954). **(d)** Time resolved *I* quadrature projection of the rotated data (top) and corresponding state assigned using a two-point filter (Vool et al., 2014). Green (red) points indicate the data for $2\,\mu s$ ($10\,\mu s$) integration time. Shaded areas indicate $\pm 1\sigma$. **(f)** Histogram of dwell times in the even and odd parity for $2\,\mu s$ (green) and $10\,\mu s$ (red) integration time. In the distributions should be identical and single exponential for both integration times assuming sufficient SNR, and a purely Poissonian switching process. We attribute the double exponential distribution for short integration time to a finite overlap between the two Gaussians, i.e. too low SNR.

pump on the same transitions. After down-conversion and demodulation we integrate the signal for $2\,\mu s$ per point and store 10^6 points per trace. Given the relatively slow equilibrium parity switching rates, we sum five consecutive points from the original raw data to increase separation between the two clusters of points, i.e. increase SNR, while sacrificing time resolution with an effective integration time of $t_{int} = 10\,\mu s$ [see top vs. bottom panel of Figure 4.16(a)]. We rotate the time series of points in the *IQ* plane such that we achieve maximum contrast in the *I* quadrature[cf. right panels of Figure 4.16(a)]. Following this we fit again a double Gaussian distribution to a histogram of the *I* values of the rotated data.

To extract the characteristic transition rates between even and odd parity we obtain the power spectral density (PSD) of the time series $I(t)$ extracted from the rotated complex data by fast-Fourier transformation [cf. Fig.4.16(c)]. To reduce the noise in the PSD, we take the original 2×10^5 samples long time trace and reshape it into 20 non-overlapping segments of equal length, finally we average the 20 PSD obtained from the individual segments (Bartlett, 1948). We fit the averaged PSD of a random telegraph switching process with two characteristic rates $\Gamma = \Gamma_{oe} + \Gamma_{eo}$ (Machlup, 1954) $PSD(\omega) = a\,4\Gamma/\left(\Gamma^2 + \omega^2\right) + c$, where c accounts for constant background noise. By assuming a two state rate equation model in steady state, we are finally able to extract the individual parity switching rates from the fitted values of $\Gamma = \Gamma_{oe} + \Gamma_{eo}$ and the fitted Gaussian amplitudes $a_1/a_2 = \Gamma_{oe}/\Gamma_{eo}$.

To check the underlying assumption of the analysis outlined above, namely uncor-related parity switching events, we also analyze the recorded $I(t)$ directly in the time domain by applying a two-point filter (Vool et al., 2014). Figure 4.16 (d) illustrates the raw recorded time traces for 2 µs integration time for a drive power of −48 dBm in green, with the green shaded area indicating $\pm 1\sigma$ of the Gaussian histogram of all data points [cf. Figure 4.16 (b)]. Red data points indicate the average of 5 consecutive raw points similar to Figure 4.16(a). The lower panel of Figure 4.16(d) shows the parity assigned by the two point filter in the color corresponding to the data on which it is based. If a Poisson pro-cess governs the parity switches the histogram of the dwell times in even and odd parity should show an exponential distribution. Note, however, that non-Poissonian quasiparti-cle processes have been observed (Vool et al., 2014) and could in principle also be present in the device investigated in this paper. Figure 4.16(e) shows typical histograms of the dwell times in even and odd parity extracted from the state assignment by the two-point filter for 2 (green) and 10 µs (red) integration time. For short integration time, we observe a large excess count of short dwell times. We attribute this to be an artifact of the limited SNR. By increasing the integration time, and consequently also SNR, the excess counts of short dwell times vanish and we recover exponential distributions of the dwell times in even and odd parity as expected for Poissonian processes.

By fitting an exponential distribution to the dwell time histograms we extract the char-acteristic transition rates for even and odd parity directly from the time series. We observe good agreement between PSD and two-point filter method for low drive powers and rates that are much slower than $1/t_{\text{int}}$. However, for increasingly fast transition rates the corre-sponding histogram of dwell times has a rapidly decreasing number of points making the fit of the exponential distribution unreliable. For consistency, we therefore use the PSD method for all analysis presented in the following sections.

4.8.9 Power dependence of transition rates

Similarly to the analysis of the pulsed measurements in Figure 4.3, we extract parity switch-ing rates as a function of drive power. The top row of Figure 4.17 shows the transition rates between even (orange) and odd (blue) parity for the four different driving frequen-cies as a function of drive tone power. The markers indicate the rates obtained following the PSD approach (cf. Section 4.8.8) using $t_{\text{int}} = 10$ µs. A light-gray dashed line indicates $1/t_{\text{int}}$ to show where the extracted rate becomes comparable to the time resolution of the measurement, and the sum of both rates is indicated by a dark grey dashed line. We fit the obtained rates ($\Gamma_{\text{oe}}, \Gamma_{\text{eo}}$) using a generic model

$$\Gamma(P) = \Gamma_0 + k P^x, \tag{4.3}$$

where the power P is given in Watt. The top row of Figure 4.17 shows the rates together with the best fit curves.

Different exponents for the different driving frequencies, and onsets of the rate change could be either due to the underlying physical process, or a due to the frequency depen-dent transmission of the drive line. For high drive powers, the transition rates surpass the time resolution $\approx 1/t_{\text{int}}$, and the observed flattening is likely an artifact of this fact. We show the ratio $R = \Gamma_{\text{oe}}/\Gamma_{\text{eo}}$ in the middle row of Figure 4.17, and observe a power depen-dent change in the ratio up to a factor ≈ 10. Finally, the bottom row indicates the mean

value of the two Gaussians forming the double Gaussian distribution of the measurement results in the *IQ*-plane. As can be seen, the Gaussian indicating the parity we are dynamically polarizing to stays constant, while the mean position of the parity polarized away from moves towards the former. Additionally, we observe a decrease proportional to R in the pumped parity Gaussian's amplitude. Finally, due to the increased transition rates between the two parities, the Gaussian we are polarizing away smears out and gradually merges into the Gaussian indicating the dynamically polarized parity. For $f_p = 22.76\,\text{GHz}$ we see an opposite trend compared to Figure 4.12 (Γ_{eo} increases first while Figure 4.12 shows an increase of Γ_{oe}). We attribute this to the $0.02\Phi_0$ difference in flux setting causing a move off resonance with the odd transition. This is not the case for the other f_p (see Figure 4.3(c) for the mapping).

Figure 4.18 shows the power dependence of transition rates between even and odd parity driving on resonance with the lowest available even transition $f_d = 17.5\,\text{GHz}, \Phi = 0.60$, for three different readout amplitudes A_{ro} applied at f_r. Note that, compared to driving a higher frequency even transition [cf. Figure 4.17], the fitted exponent is lower here, while the onset of pumping starts ~20 dB higher. Since the drive frequency we are using here is lower, we would expect a higher order process, which is consistent with the larger power needed for the onset of pumping, but inconsistent with the smaller fitted exponent. Increasing the readout amplitude by about a factor of two results in ∼ 3 times larger switching rate from even to odd parity (orange dots). We hypothesize this is due to effective parity pumping by the readout tone [cf. Figure 4.14].

For all three readout amplitudes, the ratio between the parity transition rates follows a similar trend (see middle plot in last column of Figure 4.18), and decreases by about an order of magnitude. For even higher powers R increases again until the rate extraction becomes uncertain due to $\Gamma \sim 1/t_{int}$. Similar to the bottom row of Figure 4.17, the bottom row of Figure 4.18 shows the means of both Gaussians, which constitute the double Gaussian distribution indicating the two parities. For drive powers $> 0\,\text{dB}$ the Gaussian associated with even parity moves towards the constant mean of the odd parity Gaussian.

In summary, the continuously measured traces support the conclusions as presented with the pulsed experiments. Here we can obtain both rates separately when the drive is on. This shows that with stronger readout amplitude as well as with strong drive power, both rates increase. However, the analysis does not capture excited ABS populations which are present (the driven blob starts spreading outward in Figure 4.16). At high drive powers possible distortions of the readout signal due to the strong drive tone come into play as well. This is why we applied a pulsed scheme that avoids these caveats to support the main conclusions of this work. Future work could include excited populations in the model for the jump traces, which we did not attempt here because the short coherence times relative to our SNR did not allow for a clear separation of the excited populations from their parity ground state.

4
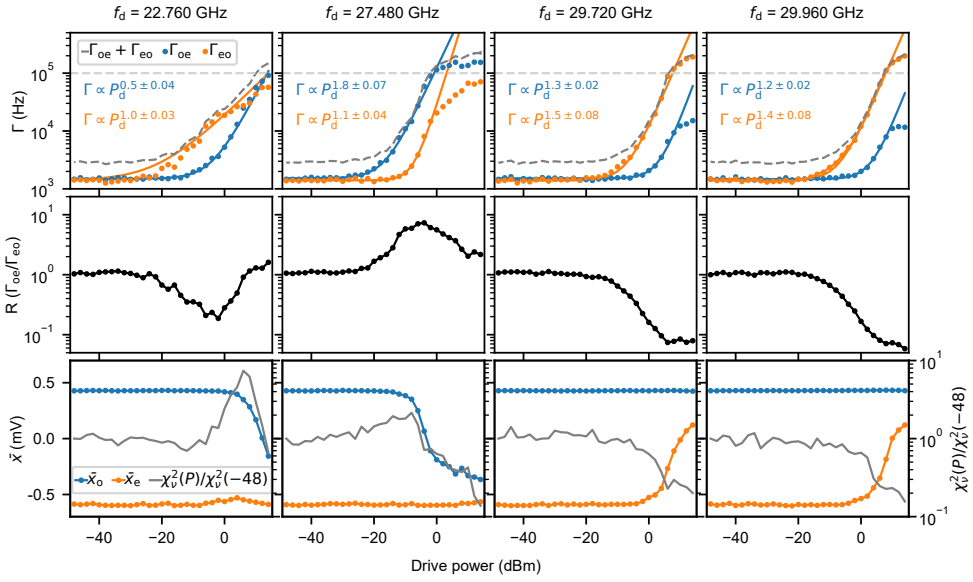
Figure 4.17: Parity switching rates as a function of drive power at frequencies indicated at $\Phi = 0.46\Phi_0$. **Top** Parity transition rates as a function of drive power (blue, orange marker), and sum of both rates (grey dashed line). Colored lines are fits of the corresponding data to Eqn. 4.3 with fitted exponents given in the respective panels. The horizontal grey dashed line indicates $1/t_{int}$, roughly the maximum resolvable transition rate. **Middle** Ratio of Γ_{eo}/Γ_{oe} as a function of drive power. **Bottom** Means of the two Gaussian distributions indicating even (orange) and odd (blue) parity. As the transition rate approaches $1/t_{int}$ the mean of the Gaussian associated with the pumped parity moves towards the other one, and the normalized reduced χ^2 (grey line, right y-axis) deviates strongly, indicating that the goodness of fit decreases due to approaching the limit of the experimental time resolution.
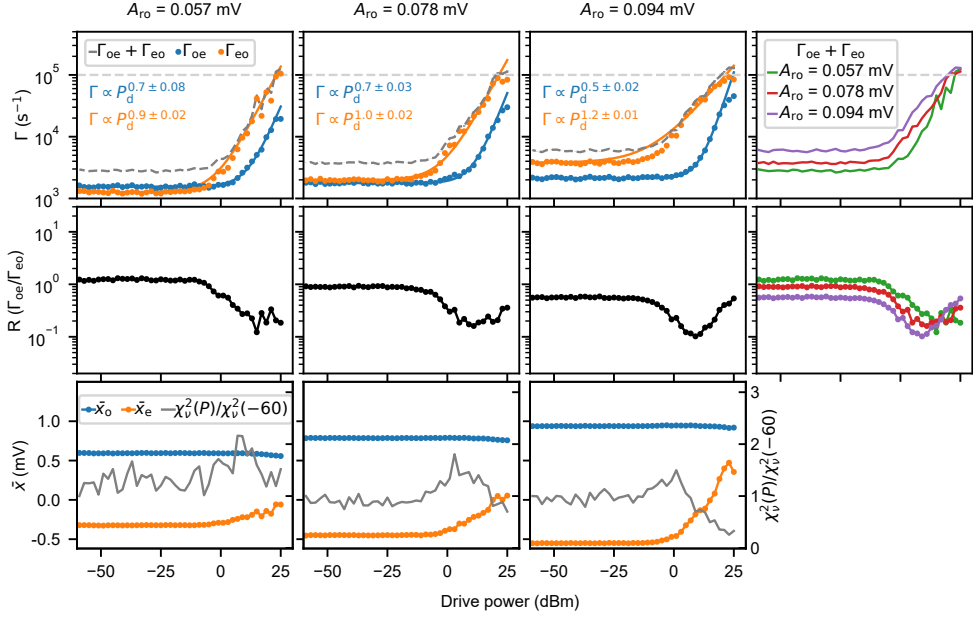
Figure 4.18: Parity switching rate as a function of drive power at $f_d = 17.5\,\text{GHz}$ resonant with the lowest available even pair transition for three different readout powers. Note that there was 6 dB less attenuation on the drive line compared to the drive-power axes of all previously presented data. **Top** Parity transition rates as a function of drive power (blue, orange markers), and sum of both rates (grey dashed line). Colored lines are fits of the corresponding data to Equation (4.3) with fitted exponents given in the respective panels. The horizontal grey dashed line indicates $1/t_{\text{int}}$, the maximum resolvable transition rate. The right most panel compares the total rates as a function of drive power for the different readout amplitudes and indicates an increase of the rates with increasing readout power. **Middle** R as a function of drive power. The right most panel compares the drive power dependend ratios for the three different readout amplitudes (same legend as in the top row applies). **Bottom** Means of the two Gaussian distributions indicating even (orange) and odd (blue) parity. As the transition rate approaches $1/t_{\text{int}}$ the mean of the Gaussian associated with the pumped parity moves towards the other one, and the normalized reduced χ^2 (grey line, right y-axis) deviates, indicating that the goodness of fit decreases due to approaching the limit of the experimental time resolution.

5

Microwave spectroscopy of interacting Andreev spins

Andreev bound states are fermionic states localized in weak links between superconductors which can be occupied with spinful quasiparticles. Microwave experiments using superconducting circuits with InAs/Al nanowire Josephson junctions have recently enabled probing and coherent manipulation of Andreev states but have remained limited to zero or small magnetic fields. Here we use a flux-tunable superconducting circuit compatible in magnetic fields up to 1 T to perform spectroscopy of spin-polarized Andreev states up to ∼ 250 mT, beyond which the spectrum becomes gapless. We identify singlet and triplet states of two quasiparticles occupying different Andreev states through their dispersion in magnetic field. These states are split by exchange interaction and couple via spin-orbit coupling, analogously to two-electron states in quantum dots. We also show that the magnetic field allows to drive a direct spin-flip transition of a single quasiparticle trapped in the junction. Finally, we measure a gate- and field-dependent anomalous phase shift of the Andreev spectrum, of magnitude up to ∼ 0.7π. Our observations demonstrate new ways to manipulate Andreev states in a magnetic field and reveal spin-polarized triplet states that carry supercurrent.

5.1 Introduction

Experimental results in recent years have advanced our understanding of the Josephson effect in terms of Andreev bound states (ABS) (Kulik, 1970; Beenakker, 1991; Klapwijk, 2004). When two superconductors (S) are separated by a normal (N) material, the transport of Cooper pairs between them is mediated by Andreev reflections at the N-S interfaces. The consequent formation of current-carrying, discrete Andreev states in SNS junctions can be observed with microwave spectroscopy (Bretheau et al. (2013a); Janvier et al. (2015); Bretheau et al. (2013b); van Woerkom et al. (2017); Hays et al. (2018); Tosi et al. (2019); Hays et al. (2020, 2021); Metzger et al. (2021); Fatemi et al. (2022); Matute-Cañadas et al. (2022), Chapter 4) .

In *s*-wave superconductors, which preserve time-reversal symmetry, Cooper pairs are formed with opposite spins in singlet states with zero total spin. On the other hand, in semiconductors with strong spin-orbit coupling that are proximitized by an *s*-wave super-conductor (Gor'kov and Rashba, 2001; Reeg and Maslov, 2015), a parallel magnetic field can induce a triplet *p*-wave component in the superconducting pairing due to the competition of the spin-orbit interaction and the Zeeman effect (Lutchyn et al., 2010; Oreg et al., 2010; Alicea, 2010; Potter and Lee, 2011). Such triplet pairing is of fundamental interest, in part because it is a key ingredient to create topological superconducting phases with Majorana zero modes (Read and Green, 2000; Ivanov, 2001; Kitaev, 2001).

The consequences of triplet pairing on the Josephson effect have been widely investigated theoretically and include the occurrence of the anomalous Josephson effect and of spin-polarized supercurrents (Krive et al., 2004; Buzdin, 2005; Reynoso et al., 2008; Yokoyama et al., 2014; Konschelle et al., 2015). The experimental detection has, however, proven more challenging. Early signatures of triplet supercurrent have been reported in Josephson junctions with magnetic materials (Khaire et al., 2010; Robinson et al., 2010; Sprungmann et al., 2010; Linder and Robinson, 2015) and more recently in experiments making use of materials with spin-orbit coupling to induce spin-mixing (Jeon et al., 2020; Cai et al., 2021; Yang et al., 2021; Ahmad et al., 2022). In hybrid semiconductor-superconductor systems, a precursor of triplet pairing stems from the observation of the anomalous Josephson effect in InAs/Al nanowires (Szombati et al., 2016; Strambini et al., 2020) and in 2-dimensional electron gases (2DEGs) (Mayer et al., 2020). Additionally, there are indications of triplet pairing from microwave susceptibility measurements of resonators made out of InAs/Al 2DEGs (Phan et al., 2022) and from spin-polarized crossed Andreev reflection in InSb/Al nanowires (Wang et al., 2022). Evidence of spin-polarized triplet pairs based on microwave absorption and their associated supercurrent has, however, been elusive.

Embedding nanowire Josephson junctions in microwave superconducting circuits allows for probing of individual Andreev states with a remarkable energy resolution of $\sim 100\,\mathrm{MHz}$ (i.e. $\sim 0.4\,\mu\mathrm{eV}$) (Hays et al., 2018, 2020, 2021; Tosi et al., 2019; Metzger et al., 2021; Matute-Cañadas et al., 2022; Fatemi et al., 2022) and with potential spin-sensitivity (Tosi et al., 2019; Hays et al., 2020, 2021; Metzger et al., 2021). Thus, such circuits provide an excellent platform to study the (spin) properties of Andreev bound states. In fact, microwave spectroscopy has already revealed that spin-orbit coupling (Tosi et al., 2019; Hays et al., 2020) and electron-electron interactions (Matute-Cañadas et al., 2022; Fatemi et al., 2022) are crucial ingredients that determine the many-body Andreev spectrum of hybrid

nanowire Josephson junctions. However, so far, such experiments using superconducting circuits have been limited to zero or small magnetic fields.

In this work, we demonstrate measurements of the Andreev spectra of an InAs/Al nanowire Josephson junction embedded in a superconducting circuit with magnetic fields up to ~ 250 mT. The magnetic field dependence of the microwave absorption spectrum shows clear signatures of excitepd Andreev levels in a triplet state. The spectrum can be well understood based on a minimal model which includes spin-orbit coupling, the Zeeman effect, and ferromagnetic exchange interaction between Andreev bound states, originating from electron-electron interactions in the junction. A particularly interesting feature of the data is the presence of a singlet-triplet avoided crossing. Due to quasiparticle poisoning (Glazman and Catelani, 2021), the microwave absorption spectra also reveal transitions between odd-parity states, which were recently used to realize Andreev spin qubits (Hays et al., 2021). Here, we detect the direct driving of the spin-flip transition of an Andreev bound state, activated by the magnetic field. Finally, at high fields we observe a gate-tunable anomalous Josephson effect and resolve the individual contributions of Andreev bound states to the anomalous phase shift. In the next Section, we kick-off the presentation of our results by discussing the experimental setup and the ingredients that made these measurements possible.

5.2 Field compatible design and operation

Previous microwave experiments probing Andreev states with superconducting circuits have traditionally used thick (150 nm) coplanar-waveguides (Tosi et al., 2019; Janvier et al., 2015; Metzger et al., 2021; Matute-Cañadas et al., 2022) or coplanar stripline resonators (Hays et al., 2018, 2020, 2021; Fatemi et al., 2022). Here we use thin-film (20 nm) lumped-element resonators due to their proven resilience to parallel fields shown earlier in fluxonium devices (Pita-Vidal et al., 2020). Additionally, the second harmonic of the resonator is expected to be at higher frequencies (28.5 GHz, see Section 5.8.1) relative to the lowest mode compared to a coplanar geometry of equal fundamental frequency. This helps with spectroscopic measurements at frequencies up to the superconducting gap $\Delta \approx 44$ GHz.

We fabricate multiple resonators on a chip, one of which is shown in Figure 5.1(a). The resonator is coupled to a common feedline that is used for microwave readout. The lumped-element resonator, with resonance frequency f_0 = 4.823 GHz, consists of a capacitor ($C_r \approx 47$ fF) that is connected to the ground plane via an inductor ($L_r \approx 22$ nH). The inductance is dominated by the kinetic inductance of the thin-film NbTiN (Annunziata et al., 2010). The inductor has a width of 300 nm, such that the required perpendicular field for vortex generation corresponding to one magnetic flux quantum through 300^2 nm^2 is > 20 mT in locations where the current is strongest. This is well above perpendicular fields expected due to misalignment when using a vector magnet. We patterned vortex traps with a diameter of 80 nm within a 8 μm radius in the capacitor and surrounding ground planes with a 200 nm gap from structure edges to prevent flux jumps due to moving vortices (Kroll et al., 2019) [1]. The inductor is connected to ground via a gradiometric radio-frequency superconducting quantum interference device (RF-SQUID) [Figure 5.1(b)] (Pita-

---

[1]We found that holes closer spaced to the edges of structures reduced the flux jumps significantly, compared to a 1 μm spacing used in Kroll et al. (2019)
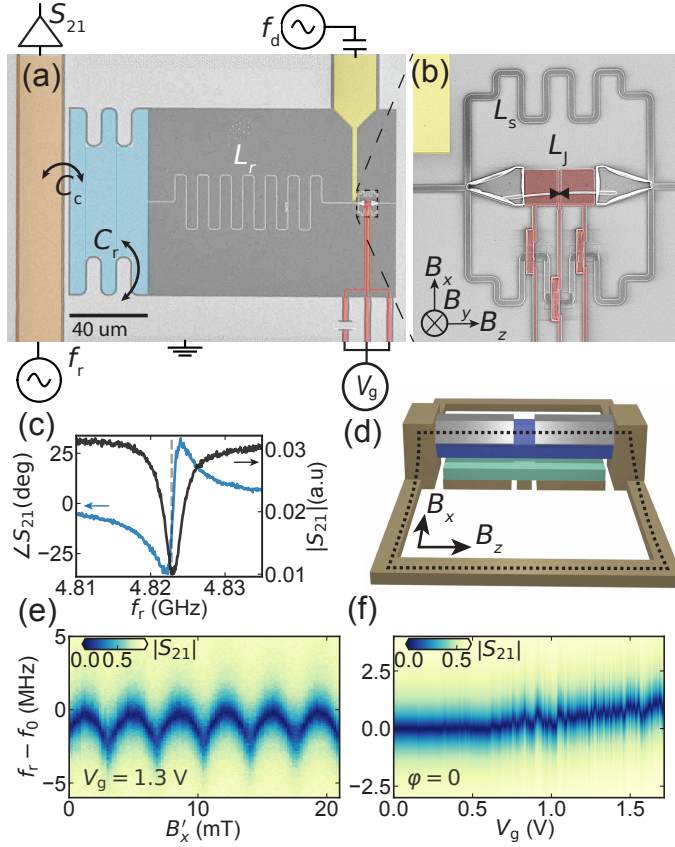
Figure 5.1: Field compatible circuit design and operation principle. **(a)** Device image and circuit schematic. A lumped element resonator is capacitively coupled (C_c) to a transmission line (orange). The resonator consists of a capacitor (blue) with capacitance C_r to ground (light grey), and inductor (L_r, white) connected to ground via a gradiometric RF-SQUID that modulates the total inductance. **(b)** The SQUID consists of two loops of inductance L_s that shunt a nanowire Josephson junction with gate-tunable Josephson inductance L_J. A drive-line (yellow) is used for spectroscopy at frequency f_d. The gradiometric design reduces sensitivity to perpendicular field B_y and the shunt-inductance determine the coupling strength to Andreev bound states in the junction. The magnetic field coordinate system aligned to the nanowire and used throughout the text is indicated. **(c)** Amplitude and phase response of the resonator when the junction is pinched-off. **(d)** 3D sketch of the SQUID loop. An InAs nanowire (blue) with Al shell (silver) and a 144 nm junction (Chapter 4) is suspended on gate dielectric (teal) above bottom gates (gold). By applying an in-plane field B_x, we can thread a flux through a vertically defined loop (dashed dots). **(e)** SQUID oscillations when applying B'_x. **(f)** Gate dependence of the junction without applying flux. f_0 increases as the critical current (inductance) of the junction increases (decreases).

Vidal et al., 2020), which consists of a nanowire Josephson junction shunted on two sides by an inductance ($L_s \approx 0.7$ nH) forming two nearly equal sized loops. We define a Josephson junction by selectively etching away a 144 nm section in a ∼ 6 nm thick aluminum shell that covers two facets of a hexagonal InAs nanowire of ∼ 80 nm diameter (Chang et al., 2015). The nanowire is placed on bottom gates defined in the NbTiN layer, which are covered with a 28 nm Si_3N_4 dielectric before nanowire placement. To each resonator,

we add capacitive coupling to an additional transmission line to drive transitions in the junction and perform spectroscopy.

The specific gradiometric loop design [Figure 5.1(b, d)] was optimized to allow for flux-biased measurements in high magnetic field. The phase difference over the junction $\varphi = 2\pi\Phi/\Phi_0$ can be tuned by applying a flux Φ through the SQUID, where $\Phi_0 = h/2e$ is the magnetic flux quantum. In a gradiometric geometry, the two loops create opposite circulating currents through the nanowire Josephson junction under applied flux by out of plane field B_y (see Section 5.8.2). The effective loop area is therefore proportional to the area difference between the loops, which here is determined by the inaccuracy of the nanowire placement with respect to center axis of the two loops ($\sim 300\,\text{nm}$). The resulting effective loop area ($\approx 0.77\,\mu\text{m}^2, \Phi_0 \sim 2.6\,\text{mT}$) is much smaller than the individual patterned loop areas ($\approx 50\,\mu\text{m}^2$) and those used in previous works ($> 1000\,\mu\text{m}^2$) that did not measure Andreev spectra in substantial magnetic fields (Hays et al., 2018, 2020, 2021; Tosi et al., 2019). A small effective loop is desired to render the SQUID insensitive to flux from out-of-plane field (B_y), reducing flux noise in presence of strong external fields. The gradiometric design also allows for picking a shunt inductance L_s – which determines the coupling strength to the Josephson junction – nearly independent of the loop size, which makes for easier design and fabrication.

Additionally, our device design exploits the nanowire placement for optimal flux tuning. That is, by placing the nanowire on top of the bottom gates, we lift the nanowire and thus elevate part of the loop vertically in the z-y plane [Figure 5.1(d)]. This allows flux biasing the SQUID with an in-plane field B_x parallel to the rest of the superconducting circuit. Since the magnetic field B_x induces currents flowing in the same direction through the nanowire Josephson junction, the effective flux is proportional to twice the out-of-plane loop area ($A = 0.28\,\mu\text{m}^2, \Phi_0 \sim 3.65\,\text{mT}$). This is shown by in the measured SQUID oscillations on the device over a range of 20 mT [Figure 5.1(e)]. Due to the thin-film NbTiN, the area of superconducting film that is exposed to parallel field B_x is much smaller compared to the area exposed to perpendicular field B_y. This is essential for flux biasing without flux jumps (see Figure 5.9 for a comparison between tuning with B_x and B_y), because vortex nucleation and circulating currents are proportional to the total area of superconducting film exposed to magnetic field (Benfenati et al., 2020; Tinkham, 2015).

Throughout this work we define $\vec{B}$ as the magnetic field aligned to the chip-plane and with z along the nanowire axis [Figure 5.1(d)] and $\vec{B}'$ as the magnetic field direction output by each of the coils of the used vector magnet (see Section 5.8.3 for the alignment procedure). We operationally define Φ as $\Phi = B_x'/3.65\,\text{mT} + c$ where c is an offset added to compensate for fluxoids trapped in the outer loop, flux due to the B_x'-component of applied B_z and a small residual ($\sim 0.05\Phi_0$, see Section 5.8.4).

We operate the devices by sending a near resonant probe tone at frequency f_r through the feedline and monitoring the transmitted complex scattering parameter S_{21} using a vector network analyser. Out of the four resonators we focus on the only one in which the junction showed considerable gate response ($f_0 = 4.823\,\text{GHz}$). At $f_r = f_0$ there is a dip in the magnitude $|S_{21}|$ and a $\sim 60°$ shift in the phase $\angle S_{21}$ [Figure 5.1(c)]. The Josephson junction then acts as a gate- and flux-tunable inductor L_J [Figure 5.1(b)] that changes f_0

via

$$f_0 = \frac{1}{2\pi \sqrt{\left(L_{\mathrm{r}} + L_{\mathrm{squid}}\right) C}}$$

where $L_{\mathrm{squid}}^{-1} = L_{\mathrm{J}}^{-1} + 2L_{\mathrm{s}}^{-1}$. Thus, by monitoring changes in f_0 we get access to L_{J}, which is related to the Andreev bound state energies and their occupation (Zazunov et al., 2003; Bretheau, 2013; Park et al., 2020). As we increase the gate voltage V_{g} on the bottom gates, we observe a trend that more current carrying channels start to conduct in the junction, which decreases L_{J} and increases f_0 [Figure 5.1(f)]. The smaller modulations on top of the general trend can be attributed to mesoscopic fluctuations of the transparency of individual Andreev states (Doh, 2005; Goffman et al., 2017). As shown later, we use this to tune the Andreev energies over a large range within small mV gate ranges. From the change in inductance at $\varphi = 0$ between the junction being in an open configuration ($V_{\mathrm{g}} = 1.68\,\mathrm{V}$) and pinched-off ($V_{\mathrm{g}} = 0\,\mathrm{V}$, $L_{\mathrm{J}} = \infty$), we estimate $L_{\mathrm{J}} = 38\,\mathrm{nH}$ at $V_{\mathrm{g}} = 1.68\,\mathrm{V}$, resulting in an estimate for the maximal critical current $I_{\mathrm{c}} \approx \varphi_0/L_{\mathrm{J}} = 8.5\,\mathrm{nA}$. In general, the Andreev states induce a state-dependent frequency shift (Metzger et al., 2021) which generates changes in $\angle S_{21}$ monitored at f_{r}. This allows us to perform spectroscopy by sweeping a drive tone f_{d} via the drive line, which results in changes in $\angle S_{21}$ when f_{d} is equal to an energy difference between Andreev levels of the same parity.

5.3 Andreev bound state spectrum

In a nanowire Josephson junction, Andreev states arise due to constructive interference after consecutive Andreev reflections from the hybrid superconducting leads (Kulik, 1970; Beenakker, 1991) [Figure 5.2(a)]. The energy of an Andreev state depends on an energy-dependent phase gained while Andreev reflection occurs, as well as a phase gained while traversing the junction. In the presence of time-reversal symmetry, which holds at $\varphi = 0$ or $\varphi = \pi$ when the magnetic field is zero, the Andreev energies are two-fold degenerate because of Kramers' theorem. The number of Kramers doublets (manifolds) present below the gap depends on the number of the occupied sub-bands in the leads, and on the length of the junction. In what follows, we restrict our attention to the two lowest manifolds of Andreev levels, labeled a and b [2].

Recent works have highlighted the importance of both spin-orbit interaction (Park and Yeyati (2017); Hays et al. (2020); Tosi et al. (2019), Chapter 4) and electron-electron interaction (Matute-Cañadas et al., 2022; Fatemi et al., 2022) to understand the Andreev spectrum of nanowire Josephson junctions. While Andreev bound states are spin-degenerate at all phases in the absence of spin-orbit interaction, the latter may lift the degeneracy away from $\varphi = 0$ and $\varphi = \pi$. This occurs in junctions of finite length such that a phase shift accumulated due to a spin-dependent Fermi velocity becomes relevant (Governale and Zülicke, 2002; Chtchelkatchev and Nazarov, 2003; Krive et al., 2004; Béri et al., 2008; Yokoyama et al., 2013, 2014; Konschelle et al., 2016; Park and Yeyati, 2017), see Figure 5.2(b). The typical phase dispersion of the resulting spin-split manifolds is illustrated in Figure 5.2(c). As inferred in Refs. (Matute-Cañadas et al., 2022; Kurland et al., 2000), electron-electron

---

[2]Note that the labels can refer either to manifolds that originate from the same transverse sub-band, due to finite-length effects, or to orbitals from different transverse sub-bands
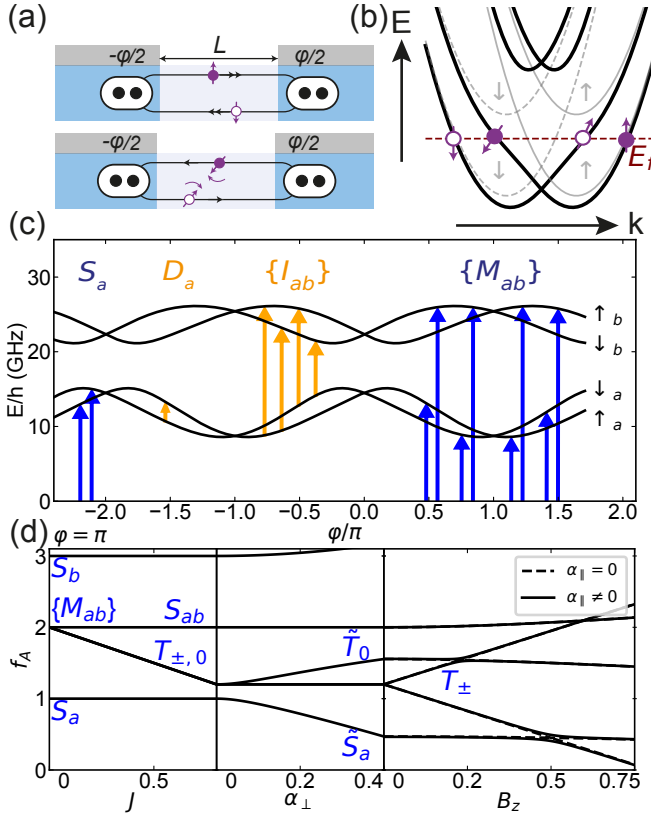
Figure 5.2: Hybrid nanowire Josephson junction hosting spin-split Andreev bound states at zero field. **(a)** Schematic of two Andreev reflection processes in the nanowire junction. Spin-orbit induced sub-band hybridization rotates the spins of the bottom Andreev states and lowers the Fermi velocity (v_F). Note that the time reversed processes are also possible (not shown), and that the Andreev states are generally superpositions of these four Andreev reflection processes. **(b)** Electron band structure indicating hybridized sub-bands due to spin orbit interaction. The anti-crossings lead to a rotated spin of the inner Andreev mode and a spin-dependent v_F. **(c)** Phase dependence of two low lying spinful Andreev manifolds (a,b) in the non-interacting picture (Tosi et al., 2019). Arrows denote possible parity conserving microwave transitions. Pairs of blue arrows indicate even-parity transitions starting from the ground state. Yellow arrows indicate transitions starting from one of the two lowest levels occupied with a quasiparticle. **(d)** Evolution of even parity transitions at phase difference $\varphi = \pi$ using Eq. (5.1), illustrating the effect of exchange interaction J, spin-orbit interaction and Zeeman energy using $\alpha_\parallel < J < \Delta$, which resembles the experiment. J splits the four mixed states $\{M_{ab}\}$ into a singlet S_{ab} and three triplet transitions $\{T\} = \{T_0, T_+, T_-\}$. Spin-orbit interaction hybridizes T_0 and S_a, moving the now hybridized $\tilde{T}_0$ up and $\tilde{S}_a$ down in energy. Finally, a magnetic field splits $T_\pm$.

interaction manifests itself via a ferromagnetic exchange interaction $-J\vec{S}^2$ between two quasiparticles in a state of total spin $\vec{S}$, each occupying a different manifold.

We now present a minimal model that captures the combined effect of spin-orbit interaction, exchange energy and the Zeeman effect of an external magnetic field on the two manifolds, restricting our attention to the case $\varphi = \pi$. To do so it is convenient to consider the Andreev states $\{|\downarrow_a\rangle, |\uparrow_a\rangle, |\downarrow_b\rangle, |\uparrow_b\rangle\}$ belonging to the a or b manifold and with spin up

or down with respect to the z-axis, running parallel to the nanowire. Denoting with $\gamma_{i\sigma}^{\dagger}$ the operator which creates a quasiparticle with spin σ in the $i = a, b$ manifold, the model Hamiltonian is:

$$
\begin{aligned}
H = \quad & \sum_{i,\sigma} \left(E_i + \sigma g_i^* B_z \right) \gamma_{i\sigma}^{\dagger} \gamma_{i\sigma} - J/2 \vec{S}^2 \\
& + \sum_{\sigma} i\bar{\sigma} \alpha_{\perp} \gamma_{a\sigma}^{\dagger} \gamma_{b\sigma} + i\alpha_{\parallel} \gamma_{a\bar{\sigma}}^{\dagger} \gamma_{b\sigma} + \text{h.c.}.
\end{aligned} \tag{5.1}
$$

Here, E_i is the energy of the Andreev manifold in the absence of spin-orbit interaction; B_z is the parallel magnetic field and g_i^* is an effective g-factor which can depend on the manifold; $\vec{S} = \frac{1}{2} \sum_{i,\sigma,\sigma'} \gamma_{i\sigma}^{\dagger} (\vec{\sigma})_{\sigma,\sigma'} \gamma_{i\sigma'}$ is the total spin, where $\vec{\sigma}$ is the vector of Pauli matrices; and finally, $i\alpha_{\parallel}$ and $i\alpha_{\perp}$ are the matrix elements of the spin-orbit interaction described with a 2D Rashba model, respectively in the direction parallel and perpendicular to the nanowire. More details about each term are given in Section 5.11.2.

Within this minimal model, it is straightforward to find the single-particle and two-particle energy levels, which determine the transitions measured in spectroscopy. In particular, the simultaneous occupation of the junction by two quasiparticles results in six possible states. These are two singlet same-manifold states $|S_a\rangle = |\uparrow_a \downarrow_a\rangle$ and $|S_b\rangle = |\uparrow_b \downarrow_b\rangle$ as well as four states corresponding to a mixed occupation of the two manifolds. For the latter, it is natural to pick the basis of simultaneous eigenstates of $\vec{S}^2$ and S_z. These are the singlet $|S_{ab}\rangle = (|\uparrow_a \downarrow_b\rangle - |\downarrow_a \uparrow_b\rangle)/\sqrt{2}$ and the triplet states $|T_0\rangle = (|\uparrow_a \downarrow_b\rangle + |\downarrow_a \uparrow_b\rangle)/\sqrt{2}$, $|T_+\rangle = |\uparrow_a \uparrow_b\rangle$, and $|T_-\rangle = |\downarrow_a \downarrow_b\rangle$. Note that without exchange interaction, a more natural basis of mixed states would be $\{|T_-\rangle, |\uparrow_a \downarrow_b\rangle, |\downarrow_a \uparrow_b\rangle, |T_+\rangle\}$. Also, note that spin-orbit interaction breaks spin-rotation symmetry by hybridizing spin and spatial degrees of freedom. Therefore, in its presence, spin is in general not a good quantum number, and the singlet and triplet states hybridize. Nevertheless, for many parameter regimes the eigenstates of Eq. (5.1) are well approximated by the singlet or triplet states, with expectation values of the spin close to zero and one. With this in mind, in the rest of the manuscript we will for simplicity keep referring to singlet, doublet and triplet states, except in cases where spin-orbit effects change this simple picture appreciably.

In microwave spectroscopy, we only have access to transitions between many-body states of the same fermion parity. In Figure 5.2(c) we label the possible transitions in both even and odd parity sectors. In the even parity sector, we only consider transition from the ground state of the junction $|0\rangle$, with no quasiparticle excitations. There are therefore six possible transitions (pairs of blue arrows, the transition to $|S_b\rangle$ is not shown), which we will denote by their final state. The lowest energy transition is the singlet pair transition S_a from $|0\rangle$ to $|\uparrow_a \downarrow_a\rangle$. The four transitions that involve breaking a Cooper pair and splitting over the two different manifolds a and b will be globally denoted as $\{M_{ab}\}$ [blue arrows on the right side of Figure 5.2(c)]. Note that these four transitions are degenerate in the absence of spin-orbit interaction and exchange interaction.

In the odd parity sector, we denote the lowest doublet intra-manifold transitions as $D_a : |\uparrow_a\rangle \leftrightarrow |\downarrow_a\rangle$. This is a direct spin-flip of a quasiparticle occupying the lowest Andreev manifold [left yellow arrow in Figure 5.2(c)]. Furthermore, we denote the set of four inter-manifold transitions of a single quasiparticle from $\{|\uparrow_a\rangle, |\downarrow_a\rangle\}$ to $\{|\uparrow_b\rangle, |\downarrow_b\rangle\}$ as $\{I_{ab}\}$ [set of yellow arrows in Figure 5.2(c)]. In the data presented in Section IV, we find signatures of

more manifolds present at higher energies, due to additional inter-manifold transitions, i.e. $\{I_{ac}\}, \{I_{ad}\}$. However, because the even parity transitions corresponding to those manifolds are at frequencies outside the measurement range at zero magnetic field and only appear at higher fields, we restrict the modeling and data analysis to the lowest two manifolds a, b.

In Figure 5.2(d) we sketch the resulting modifications to the two-particle spectrum as predicted by the model of Eq. (5.1). The exchange interaction lowers the energy of the triplet states and, in doing so, partially lifts the degeneracy between the singlet transition and triplet transitions [Figure 5.2(d) - left panel]. The role of spin-orbit interaction is different: it breaks the spin-rotation symmetry and lifts the degeneracy of single-particle states away from the time-reversal invariant points $\varphi = 0, \pi$. The combination of spin-orbit interaction and exchange interaction can completely lift the degeneracy of the triplet states even at $\varphi = 0, \pi$ (Matute-Cañadas et al., 2022). In the minimal model, this occurs partially, by hybridizing $|T_0\rangle$ and $|S_a\rangle$. We will denote the transitions to the hybridized states $|\tilde{T}_0\rangle$ and $|\tilde{S}_a\rangle$ by $\tilde{T}_0$ and $\tilde{S}_a$ respectively [Figure 5.2(d) - middle panel]. The remaining degeneracy within the manifold of two-particle states, that of the triplet states $|T_\pm\rangle$, is lifted by the external magnetic field via the Zeeman effect [Figure 5.2(d) - right panel].
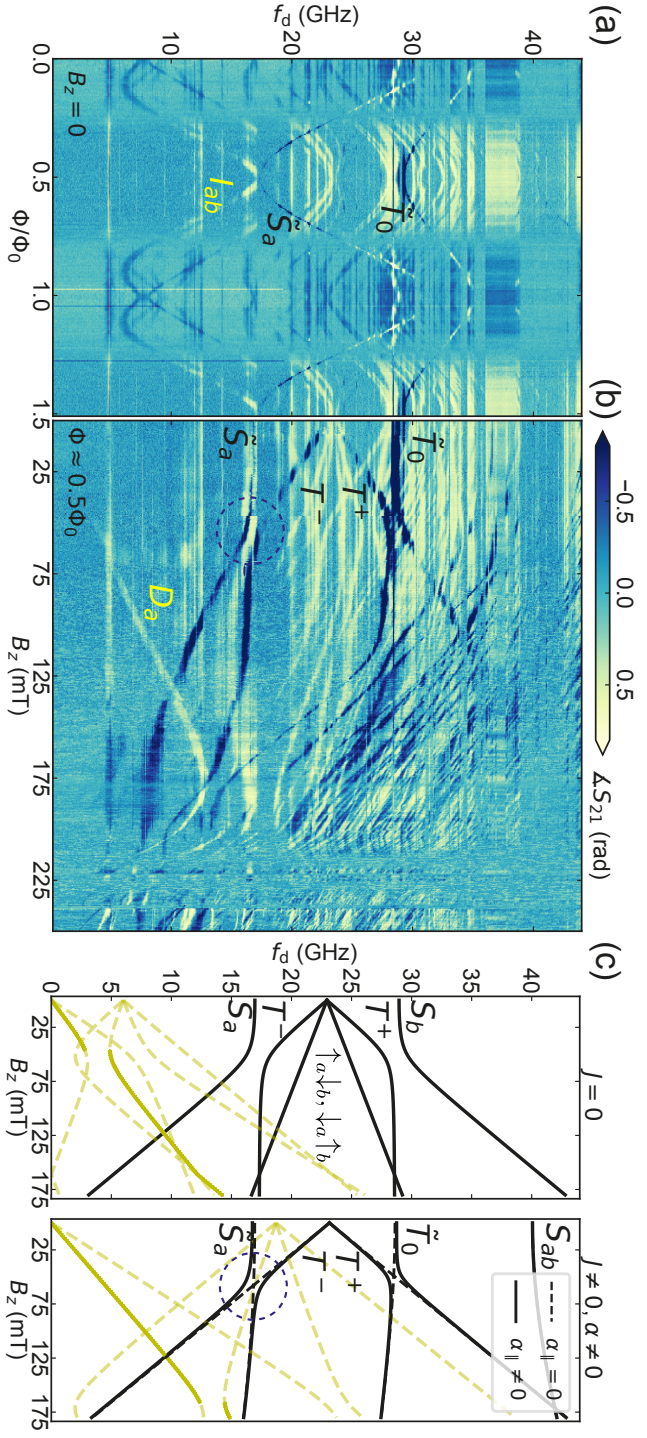
5

Figure 5.3: Spectroscopy of singlet, doublet and triplet Andreev states versus flux and magnetic field. **(a)** Measured spectrum at zero field versus flux Φ at $V_g = 625$ mV. **(b)** Evolution of Andreev transition spectrum in an aligned parallel magnetic field starting from the right side of (a) (Φ ≈ Φ$_0$/2). At low fields, the transitions disperse linearly with B_z and we can distinguish transitions to singlet, doublet and triplet Andreev states as indicated. At higher fields, a plethora of Andreev transitions move downwards until the low-energy spectrum becomes very crowded and visibility low. Note that Φ ≈ Φ$_0$/2 holds only for $B_z < 160$ mT after which Φ changes non-linearly with B_z. **(c)** Fit to minimal theoretical model at φ = π including α and exchange interaction J (see Section V). Black lines indicate even-parity transitions with types indicated. Also indicated are the inter-band I_{ab} (yellow dashed lines), the lowest doublet spin-flip transition D_a (yellow full line) and D_b (yellow dashed line starting from the same point) which is not visible in the data (see discussion the main text Section V). Left plot indicates a best fit when assuming $J = 0$ and the top even transition excitations a second sub-band S_b. When $J = 0$, two more transitions (S_{ab},T_0) should appear that are not in the data and I_{ab} should appear at low frequency. Right plot is best fit with $J = 17$ GHz, $\alpha_\perp = 4.8$ GHz. Here the even-parity transitions and I_{ab} match the data (see Figure 5.29 for lines on top of the data). Note that $\alpha \neq 0$ hybridizes the singlet S_a and triplet T_0 denoted as $\tilde{S}_a$, $\tilde{T}_0$ respectively. The avoided crossing between T_- and $\tilde{S}_a$ only occurs in presence of a spin-orbit component $\alpha_\parallel$ along the wire.

5

5.4 Andreev spectroscopy: singlet, doublet and triplet transitions

With the theory developed, we now continue with the measurement results. We first measure the junction spectrum at zero magnetic field versus applied flux Φ [Figure 5.3(a)]. The gate is set to $V_g = 625\,\text{mV}$, where we have a few Andreev transitions present and the spectrum is dominated by the lowest two manifolds (see Figure 5.10 for additional gate dependence). Due to the presence of quasiparticle poisoning, the junction fluctuates between the even parity ground state $|0\rangle$ with no Andreev level occupied, and, when a quasiparticle has entered the junction due to a poisoning event, one of the odd parity doublet states $|\uparrow_a\rangle$, $|\downarrow_a\rangle$. In a related work performed on the same junction, we measured typical poisoning times of $\approx 0.5\,\text{ms}$ (Chapter 4), much smaller than the integration time per point $\sim 100\,\text{ms}$: thus, the measured spectra are an average of those resulting from initial states with and without a quasiparticle. Odd and even parity transitions can be distinguished by their opposite sign in the dispersive frequency shift induced on the resonator (Metzger et al., 2021) and characteristic dispersion. For instance, the phase response near $\Phi = \Phi_0/2$ is negative (blue) for even parity and positive (yellow) for odd parity.

We first establish that we detect the same types of transitions as in recent experimental works (Tosi et al., 2019; Hays et al., 2020). These are the even-parity transition with parabolic dispersion around 16 GHz at $\Phi = \Phi_0/2$, and the transitions starting from the poisoned doublet state, I_{ab}, with the characteristic "spider-like" shape due to the spin-orbit splitting of the Andreev levels in manifolds a, b. Note that the lowest bundle is associated with $\{I_{ab}\}$ and higher bundles likely correspond to transitions from manifold a to higher manifolds $c, d, \dots$ present in the junction at higher energies. We investigate the splitting of the $\{I_{ac}\}$ transitions due to B_x and B_z in Figure 5.12. A symmetric splitting due to B_z and asymmetric splitting due to B_x was used in Tosi et al. (2019) to infer that the direction of the effective magnetic field generated by spin-orbit interaction was in-plane and perpendicular to their full-shell nanowire. Here, we do not observe such a clear differentiation between symmetric and asymmetric splitting. This leads us to suspect that the effective spin-orbit field is not parallel to B_x, which is consistent with recent findings indicating that, in partial-shell wires, the spin-orbit direction depends strongly on the direction of the local electric field in the wire, which in turns depends on the position and number of Al facets and gate geometry (Bommer et al., 2019; de Moor et al., 2018).

Furthermore, we see a second even-parity transition dispersing in a similar way as the first, but at higher frequency, with a minimum around 30 GHz. The identification of the final states in the even transitions visible at zero field is resolved later in this Section on the basis of the magnetic field dependence. The horizontal bands visible in Figure 5.3(a,b), mostly at higher frequencies, are attributed to resonances in the drive line and connected circuit, resulting in a frequency-dependent driving strength.

Next, we measure a parallel field dependence of the Andreev spectrum, while keeping the gate fixed [Figure 5.3](b), in order to investigate the spin texture of the excited states. By aligning the magnetic field, we keep the phase drop over the junction fixed at $\varphi \approx \pi$ (see Section 5.8.3 for the alignment procedure) and polarize the spins with B_z [see Figure 5.1(d)]. A rich spectrum emerges, with several notable features in both the even and odd transitions.

We start by describing the even-parity spectrum observed in Figure 5.3(b). Based on the phase-response at $\Phi \approx \Phi_0/2$ in Figure 5.3(a) and known dispersion from earlier works (Bretheau et al., 2013a; Janvier et al., 2015; van Woerkom et al., 2017; Hays et al., 2018; Matute-Cañadas et al., 2022), we can distinguish even-parity transitions as spectral lines with a negative (blue) response. The even transitions observed at 16 GHz and 31 GHz at $B_z = 0$ remain approximately constant at low fields, as expected from a transition to a final state with a small spin polarization, thus essentially insensitive to the Zeeman effect. We also observe two even-parity transitions that disperse linearly in field in opposite direction starting at approximately 24 GHz. We thus infer that the final states reached by these transitions are sensitive to the Zeeman effect and must therefore have some degree of spin polarization along the field direction. The fact that they originate from nearly the same frequency as the bundle of four odd-parity transitions I_{ac} at $\Phi \approx \Phi_0/2$ (visible in Figure 5.3a at ~ 23 GHz) , is a coincidence and depends on the specific V_g set point. Notably, they also display an avoided crossing with the non-dispersing even transitions at $B_z \approx 50$ mT, confirming that these transitions are of equal parity.

In order to label the even-parity transitions correctly, we first attempt to fit the main features of the spectrum to our model of Eq. (5.1) without assuming electron-electron interactions. For this, we assume the even transition at 16 GHz in Figure 5.3(a,b) is S_a while the one at 31 GHz is due to a second Andreev manifold, i.e. the pair transition S_b. We then perform a best fit to the extracted transition frequencies at $B_z = 0$, while imposing a constraint that $J = 0$. While such a fit is possible, this choice of parameters also predicts the presence of two additional spectral lines corresponding to the mixed final states without exchange interaction $\sim |\uparrow_a\downarrow_b\rangle, |\downarrow_a\uparrow_b\rangle$. These even-parity states disperse with the difference of the effective g-factors of the two manifolds and should thus appear as two additional lines with a negative (blue) phase response, which are not observed in the field-dependent data. We have investigated, using a standard non-interacting tight-binding model for the nanowire Josephson junction, whether the absence of these transitions could be explained on the basis of a selection rule, i.e. vanishing matrix elements (see Section 5.11.1). We have indeed found cases where transitions to $|\uparrow_a\downarrow_b\rangle$ and $|\downarrow_a\uparrow_b\rangle$ have vanishingly small matrix elements at $\varphi = \pi$. However, even in these cases, the non-interacting model predicts them to be typically more visible than T_+ and T_- at phase differences away from $\varphi = \pi$. The latter fact can be understood on the basis that, unlike $|T_+\rangle$ and $|T_-\rangle$, the final states $|\uparrow_a\downarrow_b\rangle$ and $|\downarrow_a\uparrow_b\rangle$ do not require a spin-flip and thus should be more easily observable at small magnetic fields. Overall, this picture is inconsistent with additional measurements of the phase-dependence of these states at finite magnetic field (see Figures 5.13 and 5.14), where we did not observe the additional transitions.

Having thus disfavored a scenario based on the absence of interactions between Andreev states, we proceed by analyzing the consequence of setting $J \neq 0$ in Eq. (5.1). Only in presence of both a finite spin-orbit interaction $\alpha_\perp, \alpha_\parallel \neq 0$ and $J \neq 0$ we can reproduce the spectrum produced by the lowest two manifolds a, b for small magnetic fields, as seen in the data [Figure 5.3(c) - right panel]. From the fit of the data positions at zero field, we find $J = 17$ GHz and $\alpha_\perp = 4.2$ GHz (see Figure 5.29 for lines on top of the data). The extracted exchange is comparable to estimated values of the effective charging energy of the normal region in a similar device ($\sim 0.1\Delta$) (Matute-Cañadas et al., 2022), and thus singlet-doublet ground state phase transitions are not expected. This is different to the situation reported

in (Fatemi et al., 2022) ($\sim\Delta$), or when a quantum dot is gate-defined in the junction, such as in Bargerbos et al. (2022) where the interaction is estimated to be $\sim 10\Delta$. With these parameters, the two even transitions that do not disperse in field in Fig. 5.3 are identified with the hybridized states $\tilde{S}_a$ and $\tilde{T}_0$, motivating the ordering of transitions displayed in Figure 5.2(d). Note that the fit simultaneously takes into account and matches the position of the odd-parity inter-manifold transitions I_{ab} (yellow dashed lines) at zero field, visible in Figure 5.3(a) but only occasionally and feebly in Figure 5.3(b). I_{ab} is more visible at other flux values shown in the phase-dependence at finite B_z in Figure 5.13. The reason why the I_{ac} transitions starting at $\sim 23\,\text{GHz}$ in Figure 5.3(b) are more visible at $\Phi_0/2$ compared to I_{ab} is presently unclear.

The effective g-factors of the Andreev manifolds are not varied in the fit, but fixed to values extracted separately, as discussed in the next Section. From the fit, together with the wire diameter, we can estimate a lower bound on the Rashba spin-orbit strength α_R of $\alpha_R \geq 2\,\text{meV nm}$ (see Section 5.11.2). This is on the lower side of typical values of 5-40 meV nm found in literature for InAs nanowires (Liang and Gao, 2012; Albrecht et al., 2016; van Woerkom et al., 2017; Tosi et al., 2019). Finally, the avoided crossings between T_- and $\tilde{S}_a$, circled in Figure 5.3 and between T_+ and $\tilde{T}_0$ are only reproduced by the model if we include a finite parallel spin-orbit component $\alpha_\parallel$, set to 1 GHz for visibility. The extracted size of the T_-, $\tilde{S}_a$ crossing from the data, approximated by half the frequency difference of the transitions in the center of the crossing, is $\approx 0.5\,\text{GHz}$. Overall, the observation of the triplet transitions T_-, $\tilde{T}_0$, T_+, in finite magnetic field, together with the fact that they have a strong phase-dispersion (see Figure 5.13), implies that part of the supercurrent flowing in the junction is carried by spin-polarized triplet pairs. From the slope of the transition T_- versus phase at $B_z = 95\,\text{mT}$, we can estimate a change in current of approximately 2.3 nA with respect to the supercurrent flowing when the junction is in the ground state (see Figure 5.15). This is a measure of the supercurrent carried by the spin-polarized pair.

At higher fields we observe a strong downward trend of the transition frequencies. We suspect that this is dominated by the orbital effect of the magnetic field in the nanowire (Zuo et al., 2017), since the 6 nm aluminum shell has a much higher critical field exceeding 1 T (Chang et al., 2015). In Section 5.9.5, we investigate the presence of a revival of the Andreev spectrum in fields up to 1T, motivated by observations of a plasma mode revival on similar nanowires in a transmon geometry (Kringhøj et al., 2021; Uilhoorn et al., 2021) and supercurrent revival (Zuo et al., 2017) due to interference effects, but we do not find it. The presence of a revival would open up the path towards detection of signatures in the microwave response of a topological phase transition in presence of multiple Andreev manifolds (Väyrynen et al., 2015), manifesting as the fractional Josephson effect (Fu and Kane, 2009; Lutchyn et al., 2010).

5.5 Directly driven Andreev spin-flip

So far we have mostly considered the even-parity part of the spectrum of Figure 5.3(b). However, when the junction initially is in one of the doublet states due to QP-poisoning, we can distinguish a linearly upwards dispersing transition D_a with a positive (yellow) phase response [Figure 5.3(b)] at finite field. We attribute this to a directly driven spin-flip between the spin-up $|\uparrow_a\rangle$ and spin-down $|\downarrow_a\rangle$ levels of the lowest Andreev manifold [Fig-

ure 5.3 (c)].

From the slope of D_a we can extract an effective g-factor $g_a^* = 5.3$ of the lowest manifold. The triplet transitions T_+ and T_- should disperse in field with the half sum of the effective g-factors of the two manifolds: $g^* = \pm 1/2(g_a^* + g_b^*) = 7.8$. Thus, we infer that the higher doublet has a higher effective g-factor of $g_b^* = 10.3$. These values are used for the fit to the theory model presented in [Figure 5.3(c)] and are consistent with hybridized states where the g-factor should be between $|g_{Al}| \approx 2$ and $|g_{InAs}| \approx 15$. On the other hand, $\tilde{T}_0$ and S_{ab} disperse weakly in field. We attribute this to a competition between the exchange and the difference in Zeeman energy of each manifold. By solving the model without spin-orbit interaction, the eigenenergies of $|T_0\rangle$ and $|S_{ab}\rangle$ result in $E_a + E_b - J/2 \pm \sqrt{(J/2)^2 + (\mu_B B_z)^2 (g_a^* - g_b^*)^2}$ which is linear in B_z when $B_z \gg J$ and quadratic in B_z when $B_z \ll J$. Thus for large fields their dispersion converges to that of the non-interacting states $|\uparrow_a \downarrow_b\rangle, |\downarrow_a \uparrow_b\rangle$. A possible cause of the large difference in the g-factors of the Andreev manifolds is that, the Fermi velocity of the first sub-band is higher than that of the second sub-band, due to the larger distance from the band bottom. Therefore the effective spin-orbit strength is higher for the first sub-band (van Heck et al., 2017), reducing g_a^* more than g_b^*.

We note that we do not observe the intra-doublet transition D_b of the higher doublet, which would have a larger slope due to the higher g-factor. This can be explained by the fact that the initial state of this transition is too short-lived: any quasiparticle occupying the higher manifold quickly decays into the lowest manifold. A comparison of the measured parity lifetimes $\sim 0.5\,\mathrm{ms}$ that we recently reported for this device (Chapter 4), to measured lifetimes $\sim 4\,\mu s$ of an excited quasiparticle in the higher manifold in InAs/Al nanowires (Hays et al., 2020), supports this.

So far, we have exclusively inferred the observation of a direct Andreev spin-flip transition D_a from data at $\Phi \approx \Phi_0/2$. In order to provide additional evidence supporting this observation, we now explore the phase dispersion of D_a [Figure 5.4]. To facilitate this, we exploit the gate-tunability of the nanowire Josephson junction to move to a nearby gate setting $V_g = 628\,\mathrm{mV}$ where the lowest manifold has a high transparency and thus D_a is energetically separated from the rest of the spectrum (see Figure 5.10 for the gate dependence at $B_z = 0\,\mathrm{T}$). In Figure 5.4(a) we show the evolution of the phase dispersion when increasing B_z. At $B_z = 0$, we only see the singlet transition S_a. When we increase B_z, we observe both S_a and the odd-parity spin-flip doublet D_a as indicated in the diagram of Figure 5.4(b). As the dispersive shift in presence of resonator crossings in general can switch sign (Metzger et al., 2021), which would change their color in Figure 5.3, we have confirmed the odd-parity nature by performing parity-selective spectroscopy (Chapter 4) at $B_z = 100\,\mathrm{mT}$ in Figure 5.17. As expected, the phase dispersion of S_a stays constant at small fields since it is spin-singlet or hybridized with T_0, while D_a moves up in frequency linearly [Figure 5.4(c)] with $g_a^* \approx 6.5$. Note that g_a^* differs from the previous gate-setting (see also Figure 5.24).

The lack of D_a at zero field can be explained by two possible causes. At $B_z = 0$, the steady state population of $|\uparrow_a\rangle$ and $|\downarrow_a\rangle$ could be nearly equal due to the near-degeneracy in energy, reducing signal when driving D_a. Additionally, the matrix element to drive D_a is expected to vanish at zero field (van Heck et al. (2017) Section 5.11.1), which is why recent works on coherent manipulation of an Andreev spin qubit (Hays et al., 2021) were forced to utilize Raman transitions to be able to achieve population transfer. Additionally,
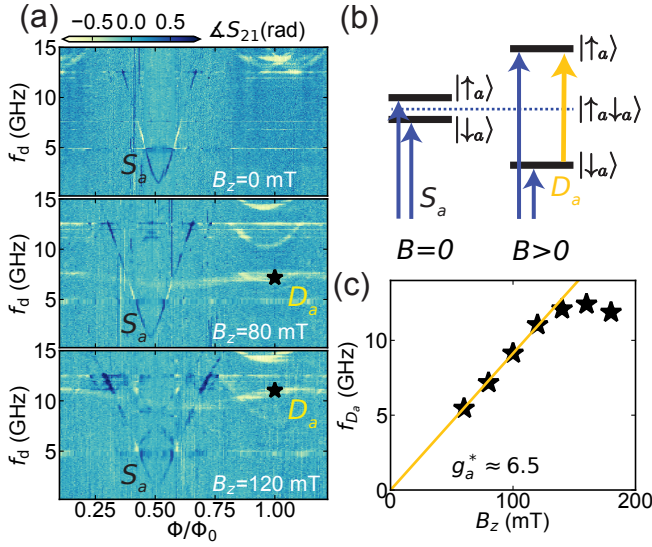
Figure 5.4: Phase dependence of the singlet S_a and directly driven spin-flip doublet D_a transition in the lowest Andreev manifold at finite magnetic field. **(a)** Measured low energy transition spectra at $V_g = 628\,\text{mV}$ for increasing magnetic fields where the transparency of the lowest Andreev state is at a local maximum. The spin-flip doublet transition is visible at $B_z > 50\,\text{mT}$. **(b)** Schematic of the two transitions at zero and finite field. A magnetic field induces a finite matrix element to allow observation of the $D_a : |\uparrow_a\rangle \leftrightarrow |\downarrow_a\rangle$ transition in the spectrum. **(c)** Extracted doublet transition frequency versus phase at $\Phi = \Phi_0/2$ indicated by stars in (a) . The transition evolves linearly versus field until spin-orbit interaction causes the lowest Andreev level to interact with higher levels that come down with B_z bringing down the transition frequency.

recent observations of D_a at zero field (Metzger et al., 2021) indeed observed a vanishing of the transition around $\varphi = \pi$. A finite magnetic field in combination with spin-orbit coupling increases the matrix element, thus facilitating direct driving of this transition at $B > 0$ [thicker yellow line in Figure 5.4(b)]. The field also favors the occupation of $|\uparrow_a\rangle$, possibly increasing the population difference and therefore the strength of the signal.

Although S_a has a large dispersion, D_a only has a small phase dispersion ($\approx 2\,\text{GHz}$). This is consistent with expectations, since the dispersion is only caused by the effective spin-orbit splitting of the Andreev levels (Park and Yeyati, 2017). Finally, note that the minimum of D_a is not aligned with S_a. Using tight-binding simulations of a similar scenario (see Figure 5.28), we found that a possible explanation could be due to a component of the effective spin orbit field B_{SO} parallel to B_z consistent with the earlier mentioned field-dependence of the interband odd-parity transitions. The observation of the spin-flip transition in a magnetic field opens up the path towards directly driven superconducting spin qubits (Chtchelkatchev and Nazarov, 2003; Padurariu and Nazarov, 2010) and allows tuning the qubit frequency over a wide range of frequency depending on the field strength.
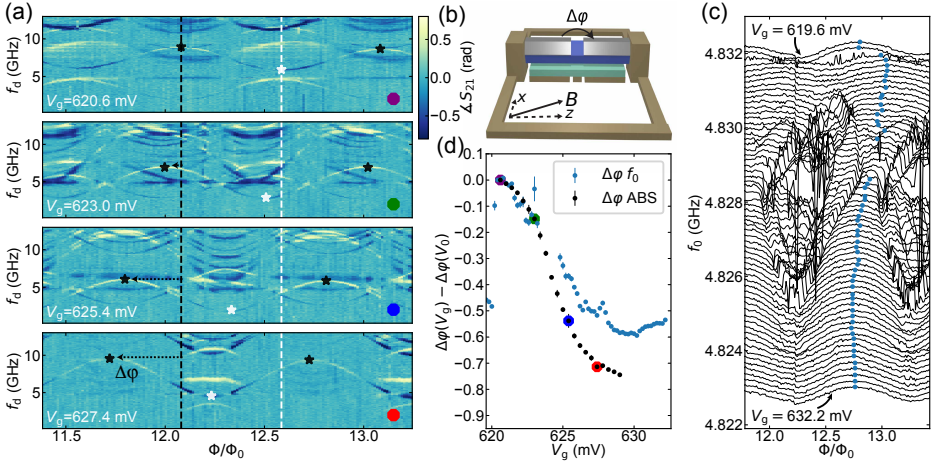
Figure 5.5: Gate-dependent anomalous Josephson effect of both individual Andreev transitions and aggregate supercurrent in presence of finite magnetic field: $B_z = 220\,\mathrm{mT}$ and $B_x = 45\,\mathrm{mT}$. **(a)** In the two-tone spectra, we follow a transition shifting to the left with increasing gate voltage. We suspect this is an odd-parity transition (see Section 5.10.2 for the identification and comparison of even and odd-parity phase shifts). Dashed vertical lines indicate the positions of the maximum (black) and minimum (white) of the reference gate voltage. **(b)** Diagram of the SQUID loop with B indicating the direction of the field. **(c)** SQUID oscillations in the resonator frequency in the same field and gate settings as the spectra in (a). They undergo a leftward phase shift with an increasing gate voltage. The blue dots indicate the positions of the maxima for each V_g. The distortion of the lines in the middle region are caused by avoided crossings between Andreev state transitions frequencies and the resonator when the transparancy of the junction is high. **(d)** Phase shift extracted from the two-tone excitation spectra (colored markers indicate the corresponding panel in (a)) with respect to a reference gate voltage $V_0 = 620.6\,\mathrm{mV}$. Additionally the phase shift $\Delta\varphi\,f_0$ extracted from resonator SQUID oscillations (c) are shown.

5.6 Gate-dependent anomalous Josephson effect at finite fields

In Figure 5.3(b) we have shown the field evolution at fixed phase difference. The entire phase dispersion is also of interest, because of the possible presence of the anomalous Josephson effect (AJE) (Krive et al., 2004; Zazunov et al., 2009; Brunetti et al., 2013; Reynoso et al., 2012; Yokoyama et al., 2014, 2013; Bergeret and Tokatly, 2015; Campagnano et al., 2015). To investigate its occurrence, we measured finite-field spectra at different gate voltages, several of which are shown in Figure 5.5(a) (see Section 5.10 and the data-repository for all data). We track the minima and maxima of this transition, indicated with the white and black stars respectively. As we increase the gate voltage, the transition starts to shift horizontally to the left, demonstrating the phase shift in the spectrum. Both even and odd-parity transitions (offset with a nearly π-phase) exhibit a shift.

In Figure 5.5(d) we show the extracted shift of the maxima for all measured spectra versus gate, resulting in a continuously gate-tunable relative shift up to $\Delta\varphi = 0.72\pi$ at $V_g = 629\,\mathrm{mV}$ with respect to the reference phase at $V_0 = 620.6\,\mathrm{mV}$. For these measurements, the magnetic field is set to $B_z = 220\,\mathrm{mT}$ and we add a perpendicular component $B_x = 45\,\mathrm{mT}$ (equivalent to $\Phi = 12.3\Phi_0$) [Figure 5.5(b)]. The perpendicular component is added to reduce

flux-jumps due to zero-field crossings. Additionally we expected the AJE to be stronger in presence of a perpendicular field component (Yokoyama et al., 2013; Szombati et al., 2016). The choice of field was limited in the B_x direction by the maximum output of the current source. Beyond $B_z = 220\,\text{mT}$, we lost visibility in the two-tone spectra.

In essence, the AJE occurs because coupling between different Andreev levels pushes their minima away from $\varphi = 0$ (Yokoyama et al., 2014, 2013). The minimum of the ground state energy, which is a sum over all the Andreev energies, then also shifts away from $\varphi = 0$ and the junction will assume a phase difference that minimizes the ground state energy at $\varphi = \varphi_0$, or, if a phase difference is imposed externally in a loop geometry, a finite current will flow at zero external flux through the loop.

For the AJE to occur, breaking of time-reversal symmetry is a necessary but not sufficient condition. Additional spatial or spin-rotation symmetries need to be broken depending on the setup (Liu and Chan, 2010; Rasmussen et al., 2016; Assouline et al., 2019). A Zeeman field breaks time-reversal symmetry and spatial symmetries can be broken by spin-orbit interaction in presence of a non-symmetric potential (Campagnano et al., 2015) or multiple sub-bands (Yokoyama et al., 2014). In our system we are clearly in a regime with multiple occupied sub-bands [Figure 5.3] evident by the many Andreev transitions visible at higher fields. Due to the asymmetry of the gates with respect to the junction (see device images in Chapter 4) we would not expect a symmetric potential. Thus we expect to see the AJE. In recent experiments demonstrating the AJE, measurements of the DC supercurrent (Szombati et al., 2016; Assouline et al., 2019; Mayer et al., 2020; Strambini et al., 2020), or of the ground state Josephson energy (Pita-Vidal et al., 2020), were used to probe the anomalous phase shift caused by the summed contributions of all Andreev levels. In Figure 5.5(a) we add to this by showing the underlying microscopic origin of the anomalous supercurrent: the phase shifts of Andreev transitions, which imply shifts of the individual Andreev levels, and which we can measure directly in magnetic fields strong enough to produce this effect.

To compare with supercurrent measurements, we also measure the SQUID oscillations in the resonator in the same gate-regime [Figure 5.5(c)]. The blue datapoints in Figure 5.5(d) correspond to the maxima in the single tone (ST) resonator traces in Figure 5.5 (c). The frequency shift of the resonator f_0 originates from the dispersive coupling with the junction in the ground state, and so it is a measure of the phase shift of the ground state current-phase relation of the junction. Since the total φ_0 results from contributions of different channels, which may lead to cancellation if these channels have different phase shifts (see Section 5.10.3 for a larger frequency range than Figure 5.5(a) illustrating the different shifts per Andreev state), it is not surprising that the phase shift in f_0 is smaller than the phase shift of the individual lowest Andreev states in Figure 5.5(d).

A gate-induced phase shift can have other explanations different than the AJE, and we now discuss measures we took to rule those out. When sweeping the large vector magnet, flux can be trapped or de-trapped on-chip or drift over time, which can cause unwanted phase shifts. To rule out flux drift, we measured the 3D map in the spectra of Figure 5.5(a) by sweeping f_d for each V_g before stepping flux. This ensures that the change in phase is caused by V_g. Alternatively, a change in total supercurrent can change the phase-drop over the junction when the shunt-inductance is large due to a non-linear relation between Φ and φ. In Section 5.8.2 we estimate that we should be in a linear regime

for the given L_s and typical I_c. Also, we measured data at lower field strengths and we saw no anomalous shift at $B = 0$. To exclude a trivial origin of the observed phase shift by a gate-induced change in effective loop size, we have also kept track of the difference between two maxima in the two-tone spectra as an estimate of the total period. We saw no clear correlation with the phase shift. Fluctuations of the period were around $\Delta\Phi = 6\,\text{m}\Phi_0$. This can at most account for a phase shift of $\Delta\varphi = 0.14\pi$, much smaller than what we report here. To further investigate the cause of the gate-dependence of the AJE we performed a series of parallel field sweeps versus gate in Section 5.10.6. Here by inspecting the D_a transition where it was visible, we extracted g_a^* as a function of V_g which is correlated with the size of the phase shift. This would indicate the AJE scales with the effective Zeeman energy of the lowest Andreev manifold. We have also performed measurements of the AJE with the field vector reversed, both for the SQUID oscillations and the spectroscopy. Here we observe a reversal of the phase shift as expected (see Section 5.10.4). We thus conclude that the observed phase shift [Figure 5.5] is indeed due the AJE and not due to the alternative causes mentioned above.

5.7 Conclusions

In this work, we have performed microwave spectroscopy of Andreev bound states in a nanowire Josephson junction in a magnetic field, using a field-compatible superconducting resonator. By aligning the magnetic field parallel to the nanowire, we have investigated the field dependence of the many-body spectrum at fixed phase difference over the junction ($\varphi = \pi$), for both even and odd fermion parity. In the even parity sector, we distinguished singlet and triplet-like Andreev states, hybridized by spin-orbit interaction and split by exchange interaction. In the odd parity, at finite field, we observed the direct doublet spin-flip transition in the lowest Andreev manifold. At fields larger than $B_z = 170\,\text{mT}$, we found a strong gate-tunable anomalous Josephson effect in the many-body spectrum, currently of interest due to its envisioned application in spintronics (Linder and Robinson, 2015). Our findings confirm that both spin-orbit interaction and electron-electron interactions are important to understand Andreev spectra in InAs/Al Josephson junctions.

The observed hybridization of triplet and singlet Andreev transitions is consistent with predictions that in a finite magnetic field, the induced superconducting pairing in the semiconducting nanowire is a mixture of singlet and triplet components (Lutchyn et al., 2010; Oreg et al., 2010). However, our measurements probe states localized at the Josephson junction, which depend on both local and bulk properties, and we cannot exclude that spin-orbit interaction is only active in the junction, but not in the leads. Thus, our measurements should be complemented with methods that can single out the bulk properties of the nanowire (Rosdahl et al., 2018; Phan et al., 2022; Splitthoff et al., 2022).

It remains an open question to explore the dependence of the Andreev spectra on the electron density, in both the proximitized leads and in the junction itself, which is of importance for topological superconductivity. Signatures of topological phase diagrams could be observable in microwave spectroscopy (Väyrynen et al., 2015; Peng et al., 2016; Murthy et al., 2020) due to the onset of the fractional Josephson effect, but it seems crucial to extend available theory to understand the effect of interactions and g-factor renormalization. To prevent the closing of the spectral gap due to orbital interference, it would be interesting to perform these measurements in devices with a lower density of states. This

could be aided by another choice of material, e.g. InSb, which has a lower effective mass and smaller band-offset with Al (Winkler et al., 2019) compared to InAs.

Spectroscopy of Andreev states using superconducting circuitry allow the combination of spectroscopic measurements with high time-resolution, allowing e.g. parity-selective spectroscopy as we have shown recently at zero field (Chapter 4). In future, when combined with on-chip flux control and parametric amplification readily available in the superconducting circuit community, this combination should allow for fast measurements of the phase-periodicity of individual Andreev levels in timescales of GHz to MHz. This type of measurement could provide a more controlled way towards the detection of the fractional Josephson effect, not hindered by the presence of QP-poisoning (Lutchyn et al., 2010) or Landau-Zener effects (Laroche et al., 2019).

Additionally, the observation of the spin-flip transition as well as a singlet-triplet avoided crossing can provide new ways to manipulate Andreev (spin) qubits (Janvier et al., 2015; Hays et al., 2018, 2020, 2021), that exploit an external field. In particular, the direct spin-flip transition activated by the magnetic field makes it possible to circumvent the need to use used Raman techiques (Hays et al., 2021) involving a second bound state in order to manipulate the spin of an Andreev state (Park and Yeyati, 2017). Furthermore, the singlet-triplet avoided crossing is particularly interesting as it opens up the possibility to manipulate Andreev pairs in analogy with singlet-triplet qubits in semiconducting quantum dots (Burkard et al., 2023; Padurariu and Nazarov, 2012).

5.8 Methods

The sample is fabricated using the methods described in Chapter 4. Since this is the same device as used in Chapter 4, we refer to the supplementary information there for detailed device images, a fit of the resonator quality factor at zero field and targeted coupling strength to the Andreev bound states (ABS) and measurement methods. Similar to Chapter 4, we subtract in 2D spectra a median background for each x-coordinate, to compensate for a change in readout frequency with the swept gate, flux or magnetic field. A wiring diagram of the setup is shown in Figure 5.6. Measurements were performed at a temperature of $\approx 20\,\text{mK}$ in a Bluefors XLD dilution refrigerator. A magnetic field is applied using a 6-1-1 Tesla vector magnet thermally anchored at the 4K stage. The Z-axis (6 T) is controlled with a large AMI430 current source (60 A max). For the X and Y axis we used smaller Yokogawa GS210 (200 mA max) and GS610 (3 A max) sources respectively in order to get finer flux control and more precise alignment with the out-of-plane (Y) field. This limited the maximum field to $\sim 45\,\text{mT}$ (3 mT) in the X (Y) direction.

5.8.1 Resonator frequency targeting

We targeted the resonator frequencies using simulations in AWR Microwave office, that uses the method of moments to solve quasi-3D geometries. The simulation consists of a stack of materials infinite in the z-plane and finite in the x-y plane. The stack consisted of $500\,\mu\text{m}$ silicon with a dielectric constant of $\epsilon_r = 11.7\epsilon_0$, where ϵ_0 is the vacuum permittivity, followed by a metal with the circuit design, and finally a layer of vacuum. To emulate the kinetic inductance of the metal, we simulated kinetic inductance as a fixed inductance per square in the thin-film approximation. The kinetic inductance per square was estimated
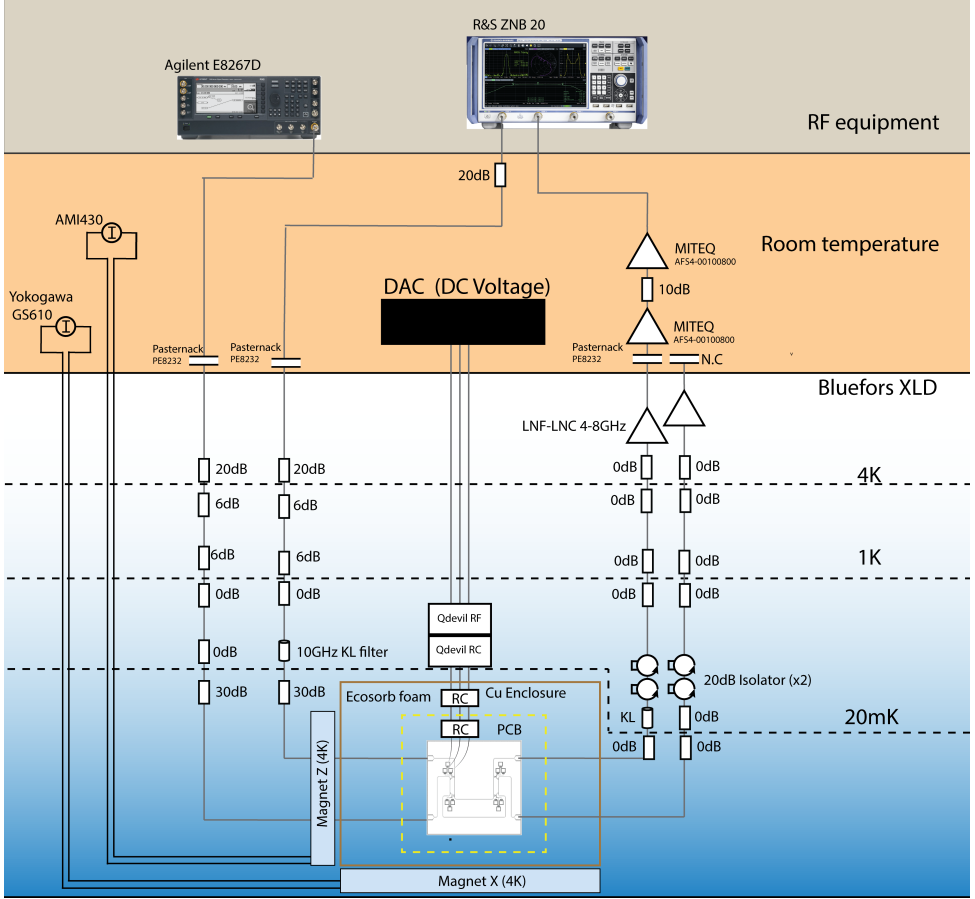
Figure 5.6: Wiring diagram of the experimental setup.

from normal state resistance measurements of the feedline using a dirty superconductor approximation (Annunziata et al., 2010). We found a normal state sheet resistance of the NbTiN film $R_\square = 87\,\Omega$ and used a critical temperature $T_c = 10.6\,$K found in similar devices to obtain an estimate of $L_{k/\square} = 11.3\,$pH. Using these simulations, we reproduced the fundamental mode of the resonator at $4.82\,$GHz when using $L_{k/\square} = 14.5\,$pH. Using the same settings, the first higher harmonic was found to be the self-resonance of the inductor at $28.5\,$GHz, making the lumped-element resonators very suitable for spectroscopy in the frequency range of interest.

5.8.2 Linearity of flux-phase in gradiometric SQUID

To verify that we can measure the un-distorted phase dispersion of ABS, we model the phase difference over the junction φ as a function of the externally applied magnetic flux Φ. The relation should be linear and limits the maximum allowed shunt-inductance in the SQUID loop design. We use a procedure that calculates $\varphi(\Phi)$ assuming a sinusoidal current

phase relation (CPR) with typical critical current strength as this remains approximately valid in the case of a few channel-wire with a modified CPR.
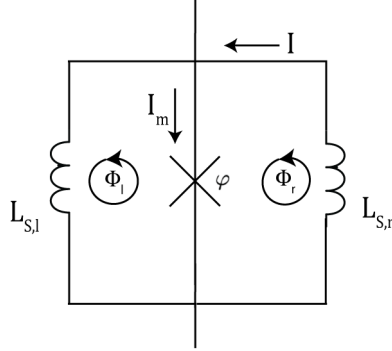

Figure 5.7: Sketch of the gradiometer SQUID (top view)

We begin by a change of variables from the current flowing through the left loop I_l and right loop I_r to the total outer loop current I and the middle branch current I_m.

$$I_r = I + \frac{1}{2}I_m \tag{5.2}$$

$$I_l = I - \frac{1}{2}I_m \tag{5.3}$$

The first step is to quantize the flux in the loops. See e.g. Plantenberg (2007) and Clarke and Braginski (2004) Sections 2.3 and 2.1.

$$\frac{2\pi}{\phi_0}\left[\phi_r - L_r I_r + M I_l\right] + \varphi = 2\pi n_r \tag{5.4}$$

$$\frac{2\pi}{\phi_0}\left[\phi_l - L_l I_l + M I_r\right] - \varphi = 2\pi n_l \tag{5.5}$$

Here, ϕ_0 is the flux quantum, ϕ_r, ϕ_l the externally applied flux in each of the sub-loops. L_r, L_l correspond to the total inductance, kinetic and geometric, in the right loop and left loop respectively and I_r, I_l are the currents inside each of the loops. M is the mutual inductance between the loops.

Adding Eq. (5.4) and Eq. (5.5) gives a condition for the total loop flux $\phi_E = \phi_l + \phi_r$ while the middle branch drops out

$$\phi_r + \phi_l - \phi_w = (n_r + n_l)\phi_0 \tag{5.6}$$

with $\phi_w = I(L_r + L_l - 2M) - I_m\left(\frac{L_l - L_r}{2}\right)$ the total flux coming from the current in the big loop. Taking the difference of the loop equations results in an expression for the JJ phase difference φ as a function of external fluxes

$$\frac{\pi}{\phi_0}\left[\phi_r - \phi_l + I(L_l - L_r) - I_m\left(\frac{L_r + L_l}{2} + M\right)\right] + \varphi = \pi(n_r - n_l) \tag{5.7}$$

Replacing the current in the big loop I using the sum of the flux quantization equations and combining that into the difference of the flux quantization equations results in an expression for φ which only depends on itself, the CPR $I_{\mathrm{m}}(\varphi)$ and known factors

$$\varphi + I_{\mathrm{m}}(\varphi)\frac{\pi}{\phi_0}\left[\frac{(L_{\mathrm{l}}-L_{\mathrm{r}})^2}{2(L_{\mathrm{r}}+L_{\mathrm{l}}-2M)} - \frac{1}{2}(L_{\mathrm{r}}+L_{\mathrm{l}})-M\right] =$$

$$\pi(n_{\mathrm{r}}-n_{\mathrm{l}}) - \frac{\pi}{\phi_0}(\phi_{\mathrm{r}}-\phi_{\mathrm{l}}) - \frac{\pi}{\phi_0}\frac{L_{\mathrm{l}}-L_{\mathrm{r}}}{L_{\mathrm{r}}+L_{\mathrm{l}}-2M}(\phi_0(n_{\mathrm{r}}+n_{\mathrm{l}})-\phi_{\mathrm{r}}-\phi_{\mathrm{l}})$$

(5.8)

We can solve this equation numerically assuming a sinusoidal CPR $I_{\mathrm{m}}(\varphi)=\sin\varphi$ and get the phase drop over the junction as a function of applied external field as a result. Using the above model, for a critical current $I_{\mathrm{c}}=10\,\mathrm{nA}$ and the inductances specified in the circuit, we have investigated the relation and remain well in the linear regime. Non-linearities start appearing at $I_{\mathrm{c}}\sim100\,\mathrm{nA}$, much bigger than what we estimate the nanowire to have based on the change in f_0 of the resonator (see discussion near Figure 5.1).
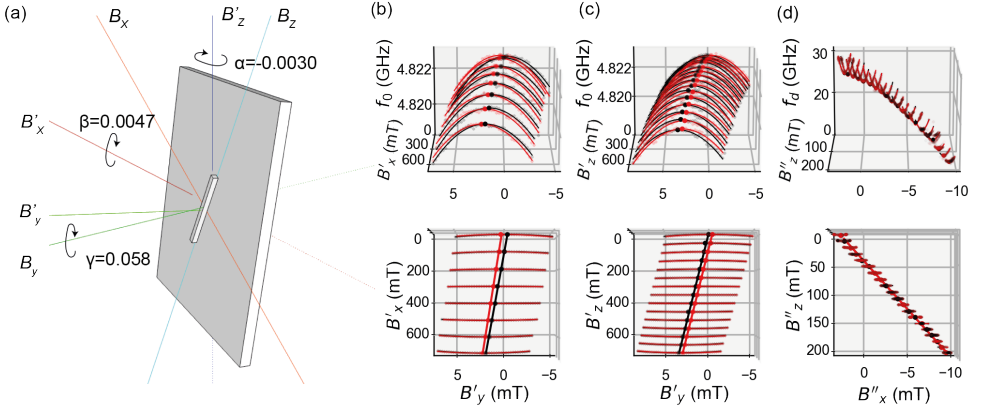
5.8.3 Magnetic field alignment procedure

Figure 5.8: **Magnetic field alignment. (a)** α and β define the chip rotation and γ describes the rotation of the nanowire on the chip plane. The rotation angles are exaggerated for clarity. **(b)** α alignment (front and top view). The maxima of the resonance frequency parabolas indicate a zero B_y component. Black and red lines, indicating forward and backward sweeps, show a slight hysteresis. The slope of the linear fits through the maxima determine the rotation angle around the z-axis: $\alpha=-0.0030\pm0.0002$. **(c)** Determination of the rotation angle around the x-axis, $\beta=0.0047\pm0.00006$ **(d)** Here, minima of an even ABS transition in two-tone spectroscopy are used to determine the nanowire angle γ. Linear fits give $\gamma=0.058\pm0.0002$. The minimas are extracted by the procedure described in appendix 5.10.1. Note that the hysteresis in the magnet and on-chip trapped flux due to circulating currents and vortices cause a larger effective uncertainty than quoted here based on the fit uncertainty alone.

Here we explain the alignment of the magnetic field with the nanowire coordinate system. We denote the raw field vector as $\vec{B}'$ and the aligned coordinate vector as $\vec{B}$. Figure

5.8 (a) shows a schematic of the misaligned chip with respect to the coordinate system of the magnetic field. The rotation of the nanowire with respect to the magnet coordinate system is defined by three (extrinsic) Euler angles: α, β and γ. α and β determine the orientation of the whole chip, whereas γ defines the on-chip rotation of the nanowire. The Euler rotation matrices are given by

$$R_z(\alpha) = \begin{pmatrix} \cos(\alpha) & -\sin(\alpha) & 0 \\ \sin(\alpha) & \cos(\alpha) & 0 \\ 0 & 0 & 1 \end{pmatrix} \quad R_x(\beta) = \begin{pmatrix} 1 & 0 & 0 \\ 0 & \cos(\beta) & -\sin(\beta) \\ 0 & \sin(\beta) & \cos(\beta) \end{pmatrix} \tag{5.9}$$

$$R_y(\gamma) = \begin{pmatrix} \cos(\gamma) & 0 & \sin(\gamma) \\ 0 & 1 & 0 \\ -\sin(\gamma) & 0 & \cos(\gamma) \end{pmatrix}.$$

We transform from $\vec{B'}$ to $\vec{B}$ as follows

$$\vec{B} = R_y(\gamma)R_x(\beta)R_z(\alpha)\vec{B'}, \tag{5.10}$$

or in matrix form:

$$\begin{pmatrix} B_x \\ B_y \\ B_z \end{pmatrix} =$$

$$\begin{pmatrix} \cos(\alpha)\cos(\gamma) + \sin(\gamma)\sin(\beta)\sin(\alpha) & -\cos(\gamma)\sin(\alpha) + \sin(\gamma)\sin(\beta)\cos(\alpha) & \sin(\gamma)\cos(\beta) \\ \cos(\beta)\sin(\alpha) & \cos(\alpha)\cos(\beta) & -\sin(\beta) \\ -\sin(\gamma)\cos(\alpha) + \cos(\gamma)\sin(\beta)\sin(\alpha) & \sin(\gamma)\sin(\alpha) + \cos(\gamma)\sin(\beta)\cos(\alpha) & \cos(\gamma)\cos(\beta) \end{pmatrix}$$

$$\begin{pmatrix} B'_x \\ B'_y \\ B'_z \end{pmatrix}$$

$$\tag{5.11}$$

Due to increase of Cooper-pair breaking rate (Samkharadze et al., 2016; Annunziata et al., 2010), the kinetic inductance of a thin-film resonator increases with out-of-plane magnetic field more strongly than with in-plane magnetic field. Additionally, the induced circulating screening current in the outer loop of the gradiometer due to perpendicular magnetic flux increases the kinetic inductance by effectively current-biasing the loop (Annunziata et al., 2010; Tinkham, 2015). This causes the resonance frequency to decrease parabolically with an increasing out-of-plane magnetic field, and we can use the maximum of this parabola to determine where the out-of-plane field is zero. In order to avoid additional changes in the resonance frequency due to SQUID oscillations, we go to gate voltages where the wire is pinched-off and measure the resonance frequency as a function of the (out-of-plane) field B'_y. This measurement is repeated for increasing steps of B'_x (for α) or B'_z (for β), such that for each step a parabola is measured. At the maxima of the parabola's, $B_y = 0$. By applying the rotation matrix in Eq. (5.10), we can calculate α and β:

$$B_y = \cos(\beta)\sin(\alpha)B'_x + \cos(\alpha)\cos(\beta)B'_y - \sin(\beta)B'_z = 0 \tag{5.12}$$

For the α measurement, where $B'_z = 0$, this leads to

$$-\frac{B'_y}{B'_x} = \frac{\sin(\alpha)}{\cos(\alpha)} \approx \alpha \tag{5.13}$$

Likewise, for β

$$\frac{B'_y}{B'_z} = \frac{\sin(\beta)}{\cos(\alpha)\cos(\beta)} \approx \beta \tag{5.14}$$

To determine γ we align the field vector $\vec{B}'$ with the chip plane first:

$$\vec{B}'' = R_x(\beta)R_z(\alpha)\vec{B}'. \tag{5.15}$$

Then, the last rotation is simply given by $R_y(\gamma)$

$$\vec{B} = R_y(\gamma)\vec{B}''. \tag{5.16}$$

Since the last Euler angle γ determines the rotation of the nanowire in the plane of the superconducting circuit, we can no longer use the previous strategy to determine the orientation. Instead, we make use of the SQUID-loop, by measuring two-tone spectroscopy data and keeping track of the even ABS minima, as we increase B''_z. Due to the pre-alignment step in Eq. (5.15), $B_y = B''_y = 0$. Therefore, the flux shift of an ABS transition is caused by the B_x component of B''_z. Filling in Eq. (5.16) on the minima leads to

$$B_x = \cos(\beta)B''_x + \sin(\gamma)B''_z = c \tag{5.17}$$

where c is a constant. To first order, γ can be expressed as

$$\gamma = -\frac{B''_x}{B''_z} + c, \tag{5.18}$$

which is found by extracting the slope of a linear fit through the ABS minima.

With all the angles known, we can calculate the raw magnetic field vector $\vec{B}'$ necessary to create the desired field $\vec{B}$ in the rotated coordinate system via the inverse of the rotation matrix in Eq. (5.11).

5.8.4 Flux axis considerations

Throughout this work we use in-plane field to control the flux as discussed in the main text, this greatly reduced flux jumps compared to using B_y (see also Figure 5.9 and de Lange and Wesdorp (2023)). We define external flux Φ as the flux threading the loop by B_x. Due to the small misalignment, flux is swept with the x-axis current source (B'_x) around an aligned coordinate unless explicitly written as B_x to prevent having to set all three sources at each flux point. In Figures 5.3, 5.4, 5.11 and 5.12 we shift the flux axis by $\Phi_0/2$ to compensate for an uneven number of trapped fluxoids in the loops, i.e. $\Phi = \Phi' + ((n_r - n_l) \bmod 2)\Phi_0/2 + c$ where $\Phi' = (B'_x - \sin\gamma B_z)/3.65\,\text{mT}$ is the applied external flux compensated for the flux induced by the B'_x component of (large) B_z and c is a small additional offset discussed below.

Fluxoids get trapped when cooling down below the critical temperature in a small residual field and their number changes on timescales of months. Note that, dependent on the history of the magnetic-field sweep, a small additional residual flux was often present due to hysteresis in the magnet coils or on-chip currents. We found that hysteresis using the in-plane field (B'_x) was much less than the out-of plane field. To minimize effects of hysteresis, we performed the aligned field sweeps (e.g. Figure 5.3) by first finding the minimum of the even ABS and using that as a starting point for the aligned z-sweep. Similarly, define the position of the minimum of the even-parity transition to be $0.5\Phi_0$ at $B_z \sim 0$ in this work to compensate for small fixed flux offsets (i.e. $c \sim 0.05\Phi_0$, see data-repository) that arise after large fields have been swept or small residual B'_y, B'_z components are present.
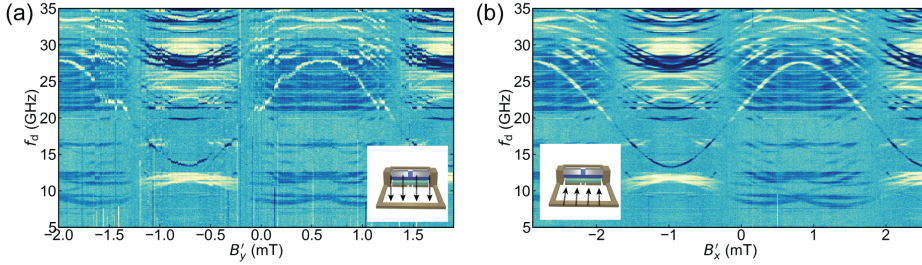
Figure 5.9: Flux tuning without jumps using a parallel magnetic field. Comparison of consecutive two-tone spectra taken using out-of-plane (B'_y) and in-plane magnetic field (B'_x) to tune flux at the same gate setting. The use of perpendicular field with respect to the superconducting chip plane exposes a large area to magnetic flux and thus creates vortices and circulating currents that cause flux jumps. We found that we could strongly reduce this using in-plane magnetic field through a vertical loop area defined by nanowire length times the vertical distance between the nanowire shell and the base NbTiN layer. For these measurements the gate voltage is set far away from the setpoint used in the rest of the manuscript (1.3 V).

5.9 Supporting datasets

5.9.1 Gate dependence of the spectrum

Figure 5.10 shows the transition spectrum as a function of the gate voltage at $\Phi \approx 0, \Phi_0/2$. The gate voltage tunes the transparency of the ABS. We show flux and field dependence at various points in gate space varying from low to high transparancy later in this Section. For $\Phi = 0$, the even transitions (bright lines) are at a maximum and the odd transitions (dark lines) at a minimum. For $\Phi = \Phi_0/2$ the opposite is true, which can be seen in the flux dependence in Figure 5.2. The colors for even and odd parity are reversed at $\Phi = 0$, since the sign of the shift is related to the curvature of the ABS energies, which switches sign (Park et al., 2020; Metzger et al., 2021). Similar to Tosi et al. (2019), we observe opposite dispersion of even and odd transitions as a function of gate voltage.
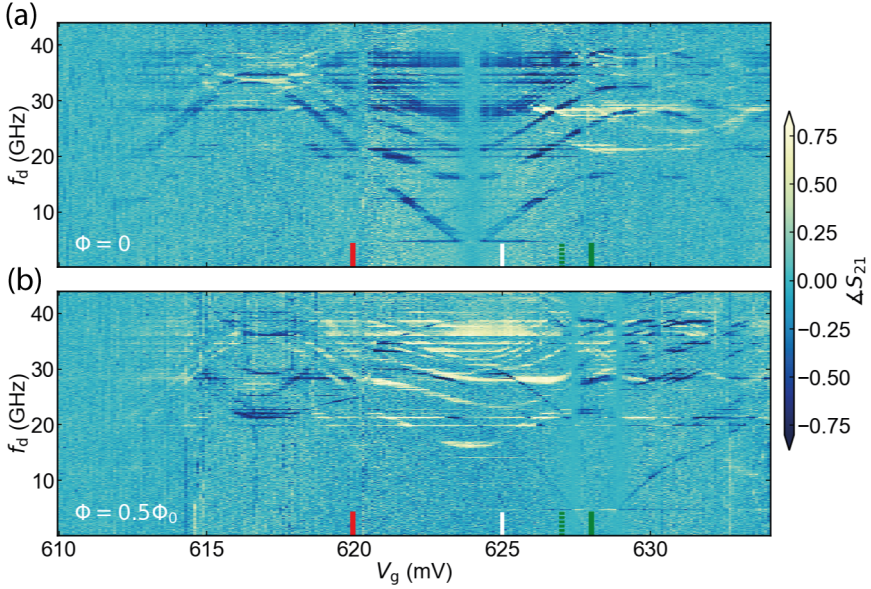
Figure 5.10: Gate dependence of the Andreev spectrum. Taken at external Flux: (a) $\Phi = 0$ and (b) $\Phi = \Phi_0/2$. Vertical bars indicate gate positions of Figure 5.11 (red), Figure 5.3, Fig. 5.11 & 5.12 (white) and Figure 5.4, 5.17 & 5.16 (green). Note that the green bar is indicative only and is not placed at 627 mV (full bar) where the high transparancy data was measured, but is put at 628 mV (dashed bar) as the data at high transparency was measured a month later after a gate jump occurred, and this gate sweep is from before the jump. The jump shifted the spectrum by $\approx$1 mV and caused additional small changes in the ABS energies at the shifted gate settings; gate jumps in general happened on timescales of weeks to months.

5.9.2 B_z **dependence at** V_g = 619.95 mV **(low transparency)**

We show the spectrum at 619.95 mV where the ABS have low transparency, both as a function of flux at zero field, and as a function of parallel field at $\Phi = 0.5\Phi_0$. Here, the slope of the linearly increasing odd intra-manifold spin-flip transition corresponds to an effective g-factor of 3.1, see extraction in the data-repository. The slight upward deviation of the odd-parity transition from the linear fit at higher fields could be explained by two possible causes. At higher magnetic field we can no longer keep the phase difference to stay at $\varphi = \pi$, i.e. due to the anomalous Josephson effect, thus the transition can move away from its minimum upward. Secondly, as shown in Figure 5.28, the D_a transition can obtain a relative phase shift with respect to the S_a transition, causing the transition to move upward. Finally, for even higher fields we expect the transition to come down again (as visible in Figure 5.4) because of the interaction with higher ABS manifolds and the continuum which come down with field.

This dataset was taken at the setpoint used to calculate the alignment angle γ in Section 5.8.3.
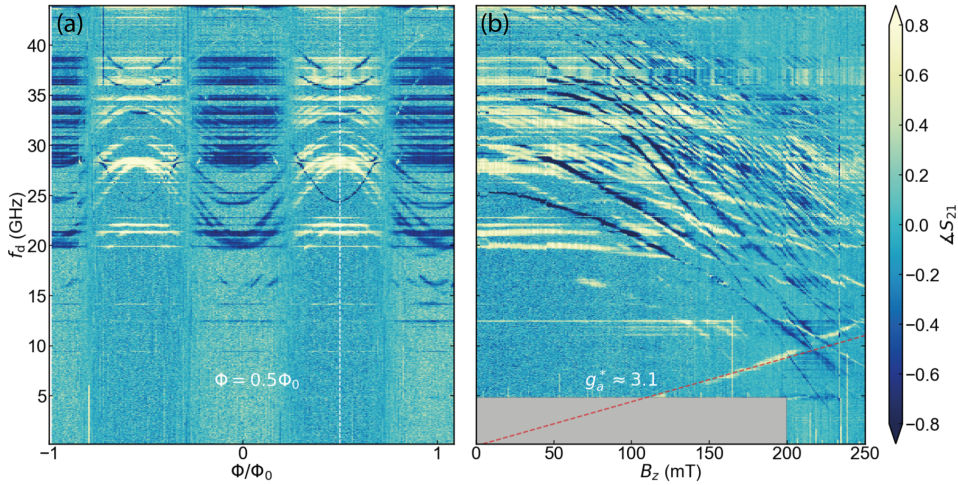

Figure 5.11: Parallel field dependence at V_g = 619.95 mV. (a) Zero field spectrum vs. flux (b) Spectrum as a function of parallel field, taken at constant flux $\Phi = 0.5\Phi_0$. No data was taken in the grey area.

5.9.3 Additional data at the gate voltage of Figure 5.3: $V_g = 625\,\text{mV}$ (medium transparency)
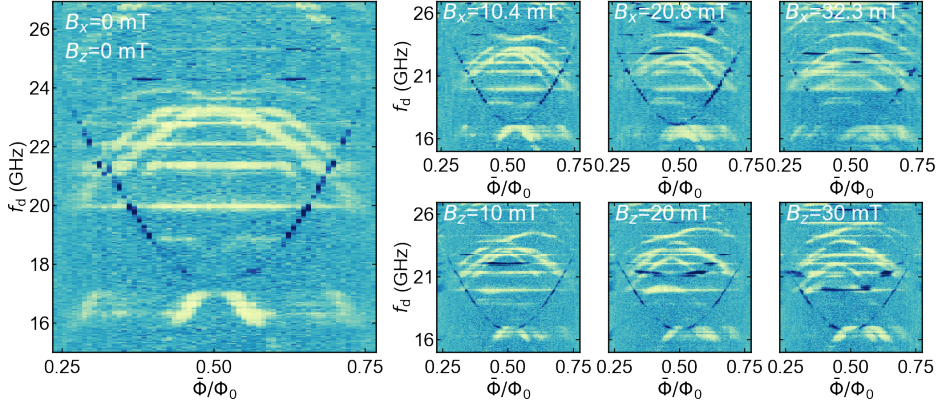
Field dependence of odd transitions

Figure 5.12: Field dependence of the odd transitions for parallel and perpendicular field, at the same gate voltage as Figure 5.3. We observe asymmetric splitting when applying parallel field B_z, which is opposite from the symmetric splitting observed in Tosi et al. (2019). This could indicate that the effective spin-orbit field is not fully along the y-axis as expected for a wire with the transport direction along the z-axis, but has a component along the z-axis as well. Note that flux Φ is denoted here by $\bar{\Phi}$, because it is swept here using B_x (as opposed to B_x') around the field setpoint written in the panels and an offset B_x is subtracted to center the minimum of the even transition at $0.5\Phi_0$.
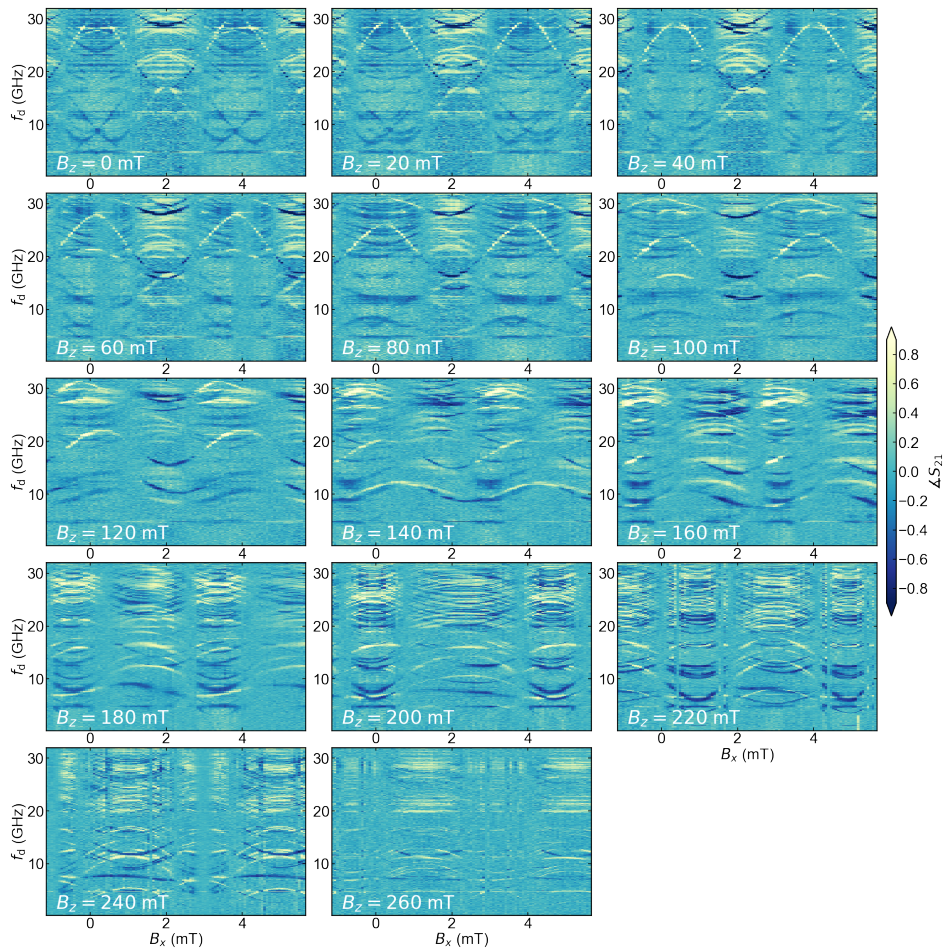
Flux dependence during parallel field sweep

Figure 5.13: Flux dependence at the same gate as in Figure 5.3. Note that the $\tilde{T}_0$ transition keeps its minimum at $B_x = 2\,\text{mT}$ up to $B_z = 160\,\text{mT}$, demonstrating the correct alignment, possibly compensating for some linear AJE, of the magnetic field used in Figure 5.3.

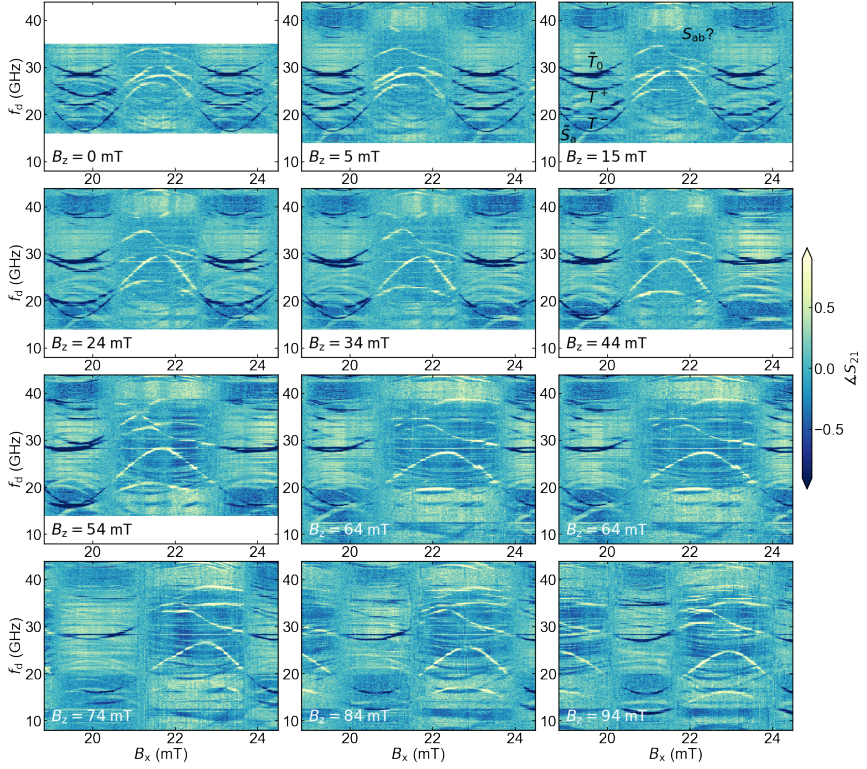## Additional flux dependence on spin-split even transitions

Figure 5.14: Flux dependence of hybridized singlet and triplet transitions at the same gate used in Figure 5.3: $V_g =$ 625 mV versus parallel magnetic field. This data was taken at 10 dBm higher drive power and finite $B_x = 22$ mT to increase visibility of the T_- and T_+ transitions. This data was measured to demonstrate the phase-dispersion of the triplet states and explore whether there are no other transitions than T_-, T_+ visible between the lowest even transition identified as S_a and the higher transition labeled as S_b without interactions. The non-interacting model would require two more transitions visible with similar dispersion, c.f. Fig.3 (c) in the main text and the discussion in Section 5.11.1. Additionally, hints of a camel-back shaped transition become visible above $\tilde{T}_0$ which could correspond to S_{ab} similar to what was observed in a recent work (Matute-Cañadas et al., 2022) (see labels at $B_z = 15$ mT). Note that at higher fields the transitions get distorted, possibly due to hybridization with other manifolds.

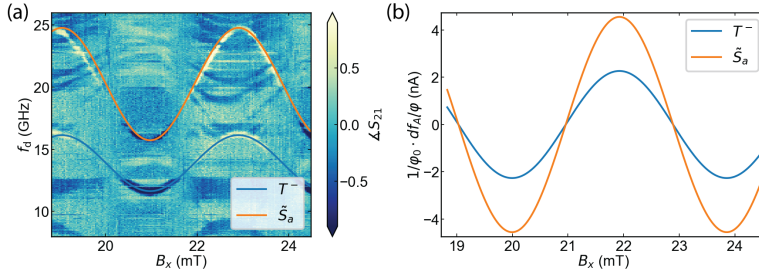## Estimate of supercurrent change due to the triplet state

Figure 5.15: Estimate of the supercurrent change when exciting the triplet and singlet at $B_z = 94\,\text{mT}$, where the two transitions are clearly visible and T_- is already split below $\tilde{S}_a$ (the last panel in Figure 5.14). To provide a rough estimate of the supercurrent carried by the triplet state T_-, we manually approximate the phase-dispersion of the even transitions (left panel) with $f_A = A * \sin(\varphi + b) + c$ resulting in $A = 2.3\,\text{GHz}$, $c = 14\,\text{GHz}$ for T_- and subsequently calculate the resulting supercurrent through the derivative $1/\varphi_0 * df_A/d\varphi$ with $\varphi_0 = \hbar/2e$ (right panel). Note that the $\tilde{S}_a$ transition seems very well approximated by using a twice as large amplitude $2A$ but $c = 20\,\text{GHz}$. This could be due to a much larger dispersion of the lower manifold compared to the higher manifold, see the discussion in Matute-Cañadas et al. (2022)

5

5.9.4 Figure 5.4 full dataset : Phase dependence at $V_g = 627\,\mathrm{mV}$ (high transparency)
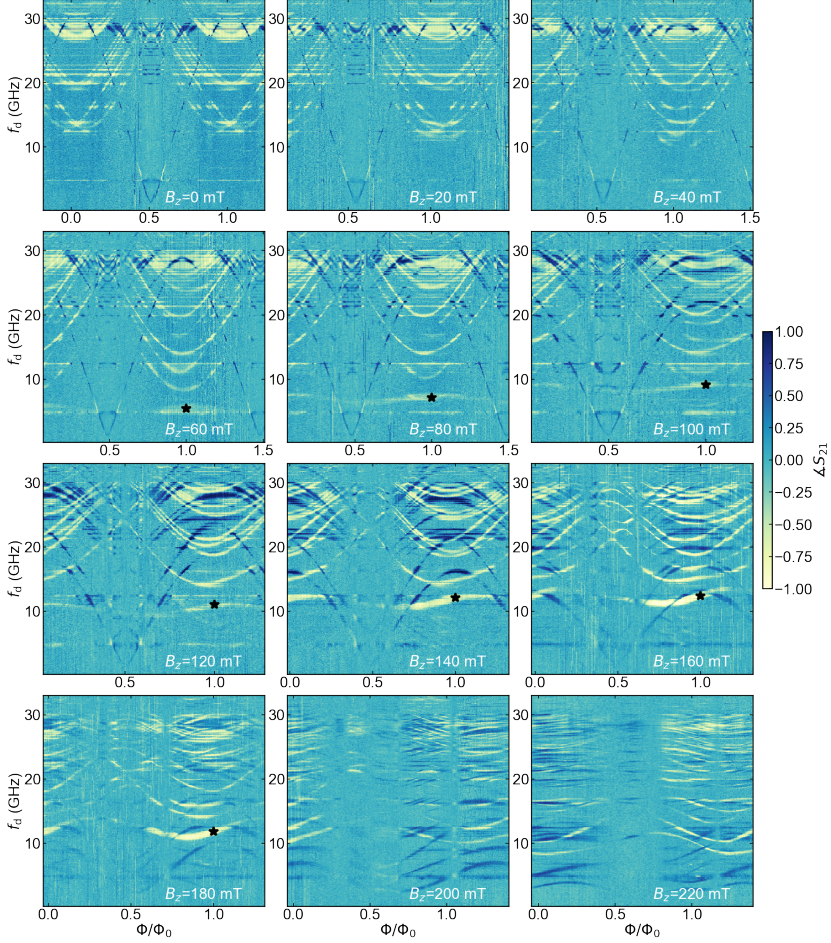

Figure 5.16: Full dataset corresponding to Figure 5.4. From 60 mT onwards, we see a bright, flat line coming up, which is the intra doublet transition D_a indicated with a black star at the extracted points used for Fig.4 (c) of the main text. Measurement taken at $V_g = 627\,\mathrm{mV}$ versus B_z. In the even parity manifold, S_a remains approximately constant near $\Phi = \Phi_0/2$ while reducing at $\Phi = 0$ due to interaction with other transitions. The spectra also show a strongly dispersing even triplet transition T_- come down in field faintly in the beginning but more apparent at higher fields.

Parity selective-spectroscopy at $B_z = 100\,\text{mT}$

In the main text, the junction parity was implied from the sign of the dispersive shift. The presence of crossings between the ABS and the resonator mode can result in sign-changes of the shift (Metzger et al., 2021). In order to make sure that we correctly labeled the parity of the transitions we have performed parity selective spectroscopy using the techniques of Chapter 4 at $B_z = 100\,\text{mT}$.
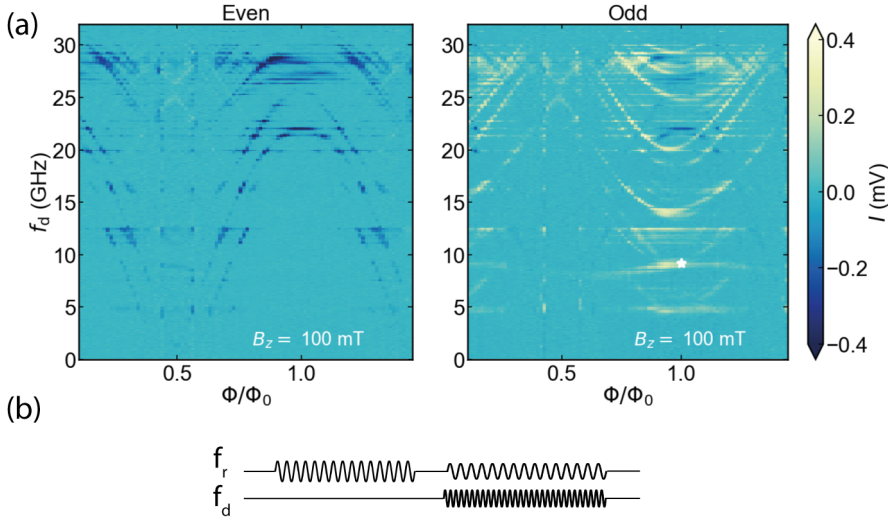

Figure 5.17: Parity selective spectroscopy at the gate voltage of Fig.4 at 100 mT confirming the odd parity nature of the intra-doublet transition indicated with a white star. (a) Spectra at 100 mT after post-selection on initial junction parity using the pulse sequence in (b). (b) The pulse sequence consists of a 20 µs readout pulse that measures the junction parity followed by a 20 µs spectroscopy pulse conditioned on the outcome of the first pulse. To increase contrast of the parity selection, we thresholded the parity selection keeping roughly 20% of the data. This was measured with the setup described in Chapter 4

5.9.5 Extended B_z dependence up to $1\,\text{T}$

An extended field sweep could show a revival of the spectrum if the gap was limited by the orbital effect (Kringhøj et al., 2021; Winkler et al., 2019; Antipov et al., 2018) or by a transition to a topological phase (Kitaev, 2001; Lutchyn et al., 2010; Oreg et al., 2010). At positive back-gate voltages, which is the case here, the hybrid states can form ring-like shapes due to surface accumulation (Winkler et al., 2019). Destructive interference then occurs at roughly half integer flux quanta threading through the nanowire cross-section with diameter d, i.e. $\frac{1}{4}\pi d B_z = \Phi_0/2$ (Kringhøj et al., 2021). In Figure 5.18.(a) we perform an aligned parallel field sweep for different initial fluxes to test the limiting field where we can observe the spectrum without being affected by a shift in phase due to the AJE or flux-jumps. We observe a crash of the spectrum at $\approx 300\,\text{mT}$ and extract $d = 65\,\text{nm}$ close to the 80 nm nanowire diameter. The sweep is continued up to 1 T as one would expect a revival around $\Phi_0 \sim 600\,\text{mT}$ if limited by orbital effects of a single state. We do not observe this, which can be the case if the many visible ABS have different effective wavefunction

cross-sections (Winkler et al., 2019). Another cause for the low visibility at high-fields could be a wrong choice of readout point due to ABS crossing the resonator.

Figure 5.18.(b) shows f_0, coupling quality factor Q_c and internal quality factor Q_i as a function of B_z during the sweeps. For each B_z, these quantities are extracted by fitting resonator traces to an asymmetric resonator model measured in transmission (Khalil et al., 2012). At least up to $B_z=1$ T, we do not observe a significant trend in the resonator's quality factors. Fluctuations may be caused by avoided crossings between ABS transitions and the resonator. Figure 5.18.(b) shows the loss of visibility in the spectrum around $B_z = \Phi_0/2$, is not related to limited field compatibility of the resonator. Furthermore, we observe an ESR dip in Q_i at $B_z = hf_0/(|g_e|\mu_B) = 172$ mT with g_e the electron g-factor where the resonator frequency matches the surface electron spin-flip frequency.
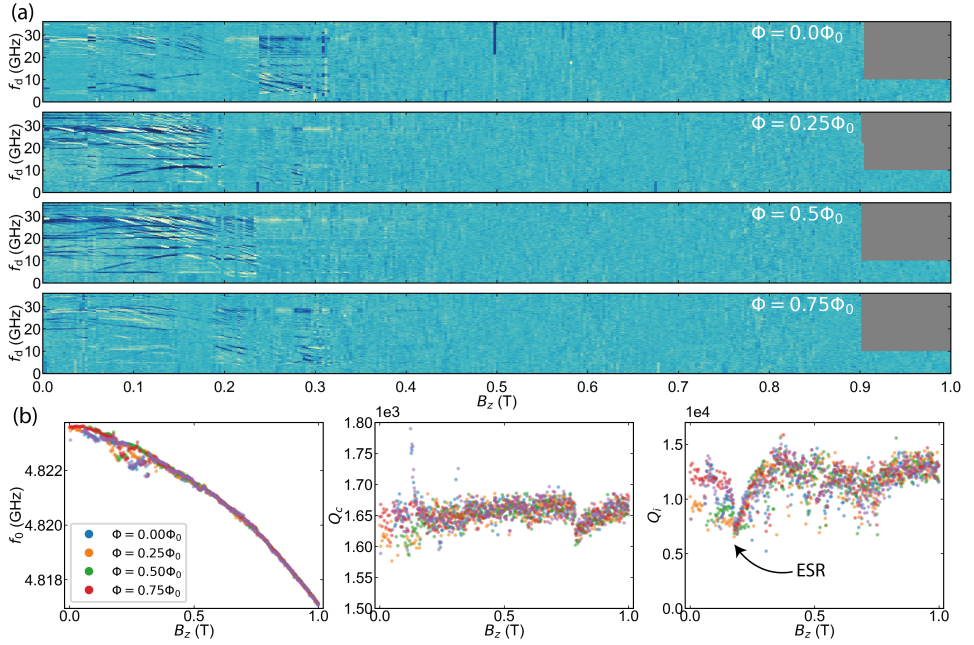

Figure 5.18: Extended B_z dependence up to 1 T **(a)** Parallel field sweeps at four different starting external flux points, to see the maximum field where a signal remains in spectroscopy. No revival is observed after the gap closing at 325 mT due to the orbital effect. Grey regions denote regions where no data is measured. **(b)** The resonance frequency f_0 extracted from a fit for the different flux points and field during the two-tone sweeps. Fits with a large χ^2 are discarded in order to filter out points where the ABS have avoided crossings with the resonator. f_0 Shows a parabolic decline with parallel field B_z due to an increase in kinetic inductance, which is caused by a magnetic-field induced increase in Cooper-pair breaking rate (Samkharadze et al., 2016; Kroll et al., 2019). Q_c stays fixed as a function of B_z and Q_i stays > 10k, except at points where crossings occur. There is however a clear dip in Q_i visible corresponding to the electron-spin-resonance frequency ($2\mu_B B_z = hf_0$).

5.10 Supporting data φ_0-effect

5.10.1 Data extraction procedure

To obtain the minima and maxima in Figure 5.5 of the main text and panel **d** of Figure 5.8, we performed the following data extraction protocol. This example is for finding a maximum.

1. Make an initial guess of the coordinates (Φ, f_d) of the minima and maxima. Then, construct a guess parabola p: a parabola of which the maximum is located at $(\Phi_{max}, f_{d,max})$.

2. Select a region of interest around the guess parabola: $\Phi \in [\Phi_{max} - 0.2\Phi_0; \Phi_{max} + 0.2\Phi_0] \cap f_d \in [p(\Phi) - 0.8\,\text{GHz}; p(\Phi) + 0.8\,\text{GHz}]$. In this region, we save the phase points exceeding a threshold as raw datapoints. We set the threshold to the 95th percentile of the selected region's phase data. For each flux point Φ, at most one datapoint is extracted by taking the median of the raw datapoints. The standard deviation σ is calculated for each flux value as well.

3. Fit a second order polynomial through the extracted datapoints, weighted by the inverse variance $1/\sigma^2$.

4. Subsequently, after visually inspecting the fits, we identify the coordinates of the maximum of the good fits as an estimate of the transition line maximum.
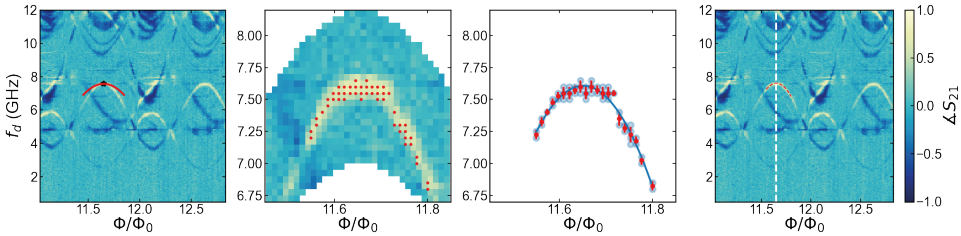

Figure 5.19: Data extraction steps. (a) Construct guess parabola. (b) Select region of interest, and extract datapoints with a threshold. (c) Fit a parabola through the extracted datapoints. (d) Identify the vertex of the parabola as the maximum.

5.10.2 Identification of parity of the transitions at high field for φ_0 sweeps

To extract the anomalous phase φ_0 from the two tone spectra in Figure 5.5, we followed the extrema of a single transition line as a function of gate voltage. Figure 5.20 (a) shows the anomalous phase shift of a transition line of both parities, where the white datapoints are used in the main text. We observe similar trends for both even and odd parity. To identify states of even and odd parity at the high magnetic field setting used here, we compare the gate dependence of the y-coordinate (f_d) of the extracted maxmima and minima for both parities with the gate spectrum at zero field, see Figure 5.20. Although the transition frequencies are significantly lowered due to the reduction of Δ, the even and odd traces still peak and dip at the same gate points as same parity transitions at $B_z = 0$. From this

we concluded that the transition traced in the main text have odd-parity. We therefore
tracked an even-parity state as well, which gave a similar φ_0 shift as the odd state.
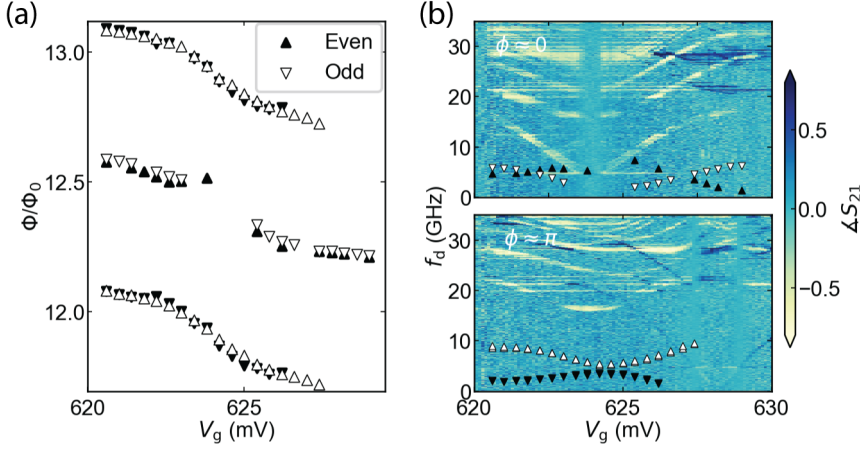

Figure 5.20: Even and odd labeling. (a) Scatterplot of extracted minima (⊠) and maxima (△) for an odd (white)
and even (black) transition in the two-tone dataset of Figure 5.5. For both parities, we observe a similar down-
ward trend, indicating a negative phase shift as a function of the gate voltage. (b) Comparison of the extracted
datapoints with the gate two-tone scans at zero field. The white datapoints qualitatively follow the behaviour of
the yellow lines, and the black points behave oppositely, like the blue lines, justifying the labeling of the white
triangles as odd and the black triangles as even.

5.10.3 Symmetry breaking in two-tone spectrum

Figure 5.21 shows one panel of Figure 5.5 (a). At V_g=622.2 mV, B_z=220 mT and B_x=45 mT,
highlighting that there is not only a global shift of the whole spectrum, but that the An-
dreev transitions are also strongly shifted with respect to each other and that there is no
symmetry axis to be found at $\varphi = 0, \pi$. Note that this observation alone rules out most
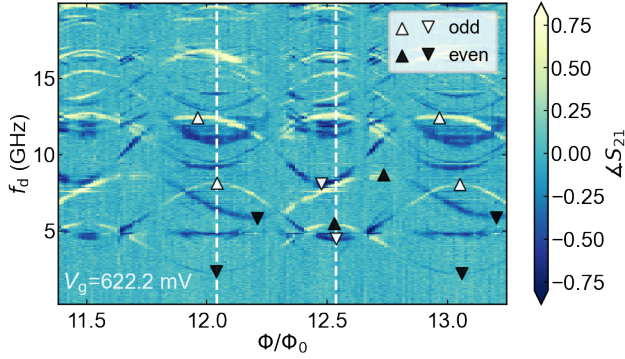trivial explanations for the AJE.

Figure 5.21: Symmetry breaking. Zoom-in of one of the panels of Figure 5.5(a) of the main text. Black and white triangles are guides to the eye placed on the extrema of even and odd transitions, respectively indicating strong asymmetry between different ABS transitions.

5.10.4 φ_0 under field-reversal

We have performed measurements of the φ_0-effect under reversal of the field vector ($B_x = 45\,\text{mT}$, $B_z = 225\,\text{mT}$), both for the spectroscopy and squid oscillations. This helps verify that indeed there is no phase shift due to a non-linear flux-phase relation (see Section 5.8.2), which could in turn be caused by a large shunt inductance relative to the junction inductance.
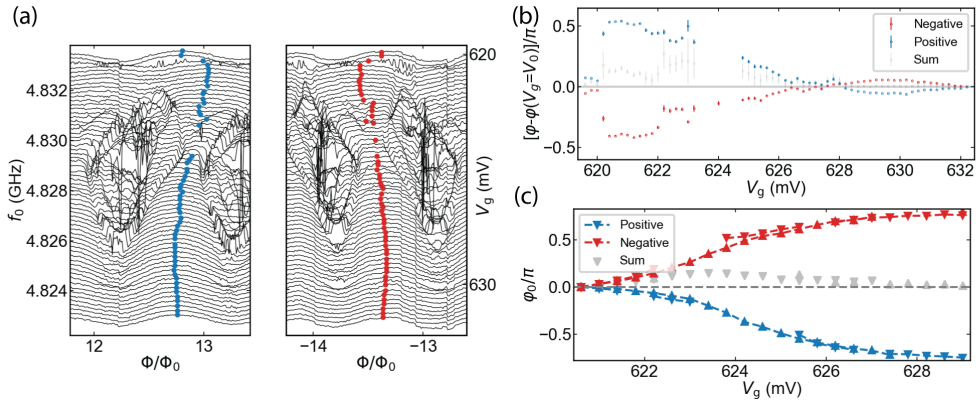

Figure 5.22: φ_0 effect under reversal of the field vector. (a) SQUID oscillations for both field directions. The vertical straight features are flux-jumps due to vortices in vicinity of the resonator, which appear as vertical lines because the gate is swept as the fast-axis. (b) Extracted phase shift from the SQUID oscillations for positive and negative fields. (c) Extracted φ_0-effect in two-tone spectroscopy under field reversal.

5.10.5 Field dependence of the φ_0-effect

We investigate the field-dependence of the anomalous Josephson effect by reducing the magnitude of the $\vec{B}$ starting from the vector shown in Figure 5.5($B_x = 45\,\mathrm{mT}$, $B_z = 225\,\mathrm{mT}$), while keeping the angle the same. We measure two-tone spectra, keeping track of the lowest visible transition. At 0 field, we do not find a significant phase-shift as expected, while for increasing field we observe a steep transition to a large phase shift. The data presented here resulted from tracing the transitions by hand, as the crowding of the spectra and lower resolution did not allow for the numerical methods presented above. To allow for verification, we have provided collections of images of the spectra with the traced maxima/minima in the data-repository. At some gate and field values data is missing because the transition was no longer visible in spectroscopy. We define φ_{ref} as the maximum phase extracted of the first 5 lowest gate values where we have data of the transition, as for some datasets the maxima/minima were not visible at $V_g = 620\,\mathrm{mV}$. By tracing the frequency of the traced transitions versus V_g we could additionally extract the parity of the transitions indicated for even parity by closed (open) symbols in Figure 5.23.
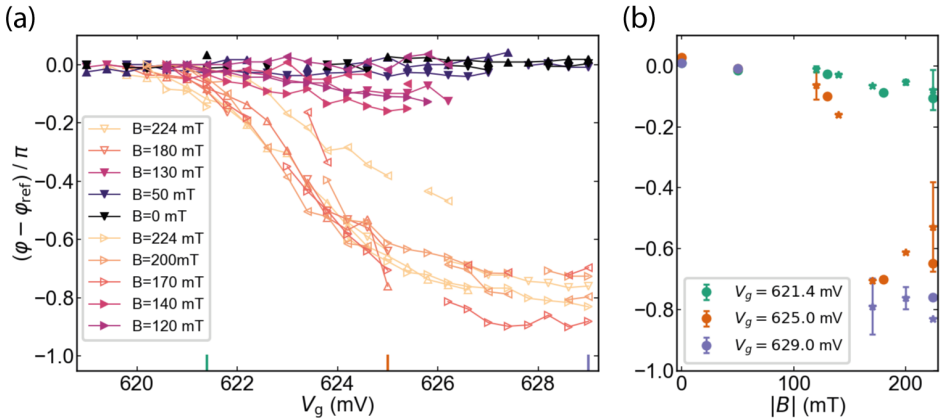
5

Figure 5.23: **(a)** Gate dependence of the anomalous phase for increasing magnetic field strength applied along the vector defined in Figure 5.5 of the main text. The markers represent two datasets tracing the maxima (minima) of visible low lying ABS versus gate and flux by upward (downward) triangles for dataset A and leftward (rightward) triangles for dataset B. **(b)** Same data as in (a) but shown as the total relative phase shifts (average of minima and maxima) for the gate values indicated by the same colored line-cuts in (a) versus field strength. Errorbars show the difference between the extracted relative phase shift of the minima and maxima of the same state, when data is available for both the minima and maxima.

5.10.6 Extracted g-factor of the lowest ABS manifold versus V_g

In an attempt to find a cause for the gate-dependence of the AJE, we have performed parallel field scans similar to Fig.3 (b) of the main text for the gate range where we measured the AJE. By extracting the slope of the spin-flip transition when visible we can extract the effective g-factor of the lowest ABS manifold. We found a strong gate-dependence of the effective g-factor of the lowest ABS manifold, correlated with the anomalous phase shift.

This is consistent with the scaling of the AJE magnitude with an effective Zeeman term.
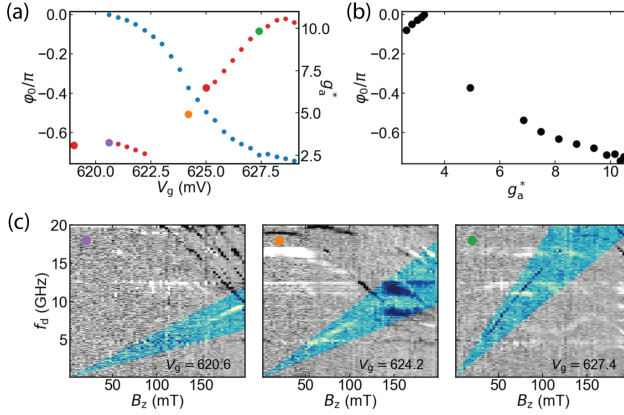

Figure 5.24: **Extracted g-factor of the lowest ABS manifold varying with V_g.** (a) φ_0 Of two-tone spectroscopy shown in main text (blue markers) versus g_a^* extracted by tracking D_a using parallel field sweeps at $\Phi \approx 0.5\Phi_0$ for various V_g (red markers). The thicker red markers indicate the extracted g-factors shown in Figure 5.3, S5, measured separately. (b) Correlation between φ_0 and g_a^*. (c) Example parallel field sweeps, see corresponding colored markers in (a), that were used to extract g_a^* of the lowest doublet transition D_a. Full dataset is provided in the data-repository. Note that in a similar sweep after a gate-jump had occured, we found a much less steep dependence of g_a^* on V_g (see data-repository) but there we did not have the φ_0 sweeps available to compare the correlation between the two.

5.11 Theoretical modeling

5.11.1 Non-interacting tight-binding simulations

Tight-binding simulations of the Josephson junction were performed using the Kwant package (Groth et al., 2014), and in particular adapting code from Laeven et al. (2020). We use the following two-dimensional Hamiltonian including Rashba spin-orbit coupling, Zeeman effect and a position dependent barrier potential

$$
\begin{aligned}
H = &\left(\frac{\hbar^2 k^2}{2m} - E_F \right) - e\phi(\mathbf{r}) \right) \sigma_0 \\
&+ \alpha(k_z \sigma_x - k_x \sigma_z) \\
&+ E_Z \cdot \sigma
\end{aligned}
\tag{5.19}
$$

From numerically solving the tight-binding Hamiltonian we obtain the BdG eigenenergies which give all required information as we assume no exchange interaction is present. We first take only the positive eigenvalues, due to the degeneracy induced by PH symmetry, $\{E_{i,\sigma}\}$, where i stands for the manifold index and σ the pseudo-spin direction. The low-energy Hamiltonian then is a sum over the Andreev levels (van Heck et al., 2017)

$$
H = \sum_{i,\sigma} E_{i,\sigma} (c_{i,\sigma}^\dagger c_{i,\sigma} - \frac{1}{2})
\tag{5.20}
$$

We simulate the junction using a 2D-grid with lattice constant of 5 nm. The grid consists of a 100 nm wide and 3000 nm long superconducting lead, where $\Delta \neq 0$ on each side of a 500 nm long junction, where $\Delta = 0$, and the rest of the parameters are kept equal in both sections. To approach the data qualitatively, we add two three side wide barriers at the left and right edge of the Josephson junction to emulate the effect of a reduction in the maxima of the ABS due to confinement (Beenakker and van Houten, 1992). In the device, the reduction of screening in the uncovered Josephson junction and possible Al-InAs interface barriers can cause these potential barriers. The resulting tight-binding grid is shown in Figure 5.25 together with a chemical potential sweep illustrating the first and second subband entry. Fabry-Perot oscillations are visible in the transparency due to the strong confinement. Settings used here are, $\alpha = 40$ meV nm, $g = 15$, $\Delta = 0.2$ meV, $m = 0.0023 m_e$ with m_e is the electron mass and the potential barrier height is set to 13 meV.
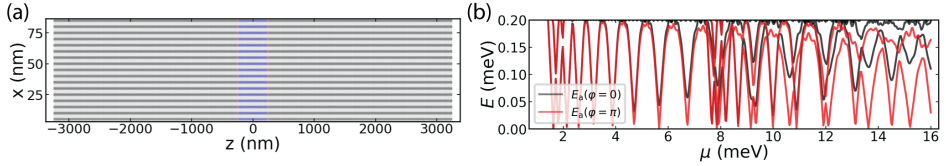

Figure 5.25: Kwant model. **(a)** Tight binding grid used for the simulations. **(b)** Chemical potential sweep using the grid in (a).

We first attempt to gain qualitative insight into the ABS spectrum by searching for a chemical potential that approximately matches the two lowest manifolds in the experimental data. We thus fine-tune to a "gate" point at $\mu = 9.20$ meV right after the second subband-entry where we have two ABS that disperse similarly in phase, see Figure 5.26(a). Here we perform a parallel-field dependence and observe the two ABS manifolds spin-split in field Figure 5.26(b), with different effective g-factors similar to the data. Next we will stay at this point and investigate the microwave absorption.

Matrix elements

We follow van Heck et al. (2017) to calculate the matrix elements of the current operator that give the transition spectrum. From diagonalizing H_{BdG} we get a set of eigenvalues $+E_m, -E_m$ and with corresponding eigenstates $\Psi_m, \mathscr{P}\Psi_m$, where $\mathscr{P}$ denotes the particle-hole operator. We can thus evaluate the current matrix elements $j_{n,m} = \langle \Psi_n | I_A | \Psi_m \rangle$. The diagonal elements give the contribution of the supercurrent of a single ABS level. The off-diagonal elements are useful when considering possible microwave transitions. We can use linear response theory to calculate the finite-temperature microwave susceptibility of the junction and thus get the absorption spectrum. This results in (van Heck et al., 2017)

$$\chi(\omega) = \sum_{n \geq m} |j_{n,\mathscr{P}m}|^2 \delta(\omega - (E_m + E_n))[1 - f(E_m) - f(E_n)] +$$
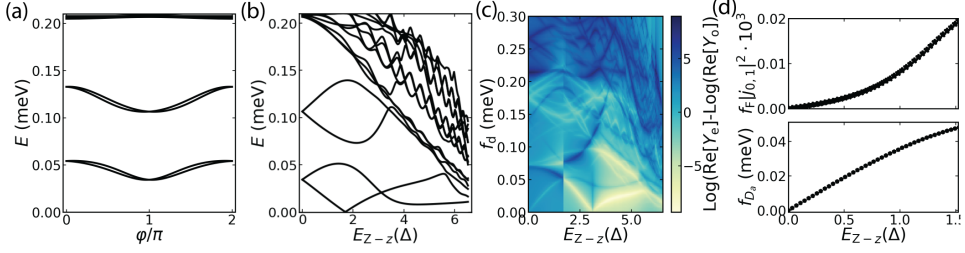$$\sum_{n \geq m} |j_{n,m}|^2 \delta(\omega - (E_n - E_m))[f(E_m) - f(E_n)] \tag{5.21}$$

Figure 5.26: Tight binding simulations at $\mu = 9.20\,\mathrm{meV}$ with the same settings as used in Fig.5.25. **(a)** Phase dependence of ABS energies at $B_z=0$. Two manifolds are visible inside the gap, spin-split due to spin-orbit interaction. **(b)** Field evolution at $\varphi = \pi$ of the ABS energies. **(c)** Linear response illustrating the resulting spectrum versus B_z at an effective temperature of $20\,\mu\mathrm{eV}$. The vertical line is due to a ground state fermion parity switch which swaps the assignment between even and odd for the lowest ABS. **(d)** Matrix element $j_{0,1}$ multiplied by the odd parity fermi-factor $f_F = [f(E_0) - f(E_1)]$ and transition frequency of D_a at the same effective temperature.
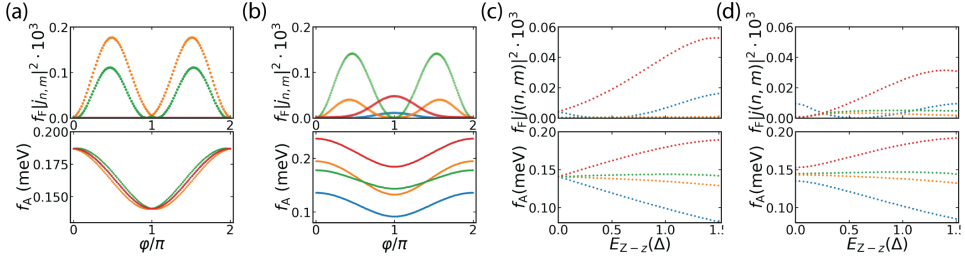

Figure 5.27: Matrix elements of even $\{M_{\mathrm{ab}}\}$ transitions at $\mu = 9.20\,\mathrm{meV}$ multiplied by the even-parity Fermi-factor $f_F = 1 - f(E_m) - f(E_n)$. The transitions (bottom panels) are colored with the same color as their corresponding matrix elements (top panels). **(a)** Phase dependence at $B_z = 0$. Here, only T_0 and S_{ab} have a finite matrix element. **(b)** Phase dependence at $E_{Z-z} = 1.2\Delta$. This illustrates that at $\varphi = \pi$, T_- and T_+ have a finite matrix element while T_0 and S_{ab} have zero matrix element there. **(c)** Field dependence at $\varphi = \pi$ without perpendicular field. At $\varphi = \pi$, S_{ab}, T_0 transitions have a zero matrix element. **(d)** Field dependence at $\varphi = \pi$ at finite $B_x(E_{Z-x} = 0.1\Delta)$. Here the S_{ab}, T_0 get a finite matrix element as well.

where $j_{n,\mathscr{P}m}$ is defined as $\langle \Psi_n | I_A | \mathscr{P}\Psi_m \rangle$ and the Fermi-Dirac function at finite temperature T is defined as

$$f(E) = \frac{1}{e^{(E-\mu)/k_B T} - 1} \tag{5.22}$$

where we take $\mu = 0$

In Figure 5.26(c) we show the microwave absorption versus field, similar to Figure 5.3. Note that we see qualitatively similar features: the odd (yellow) D_a transition coming up, the even S_a and the mixed transitions T_-, T_+, dispersing in field. Additionally, we do not observe the $|0\rangle \rightarrow |\uparrow_a\downarrow_b\rangle, |0\rangle \rightarrow |\downarrow_a\uparrow_b\rangle$ transitions.

To explore this further, we investigate the current operator matrix elements. The odd transition matrix element is shown in Figure 5.26(d) and increases with field as expected (Park and Yeyati, 2017; van Heck et al., 2017). The even-parity matrix elements are shown in Figure 5.27. Here we see that only at $\varphi = \pi$ the elements for the $|0\rangle \rightarrow |\uparrow_a\downarrow_b\rangle, |0\rangle \rightarrow |\downarrow_a\uparrow_b\rangle$ are zero and thus the transitions should appear when measuring the
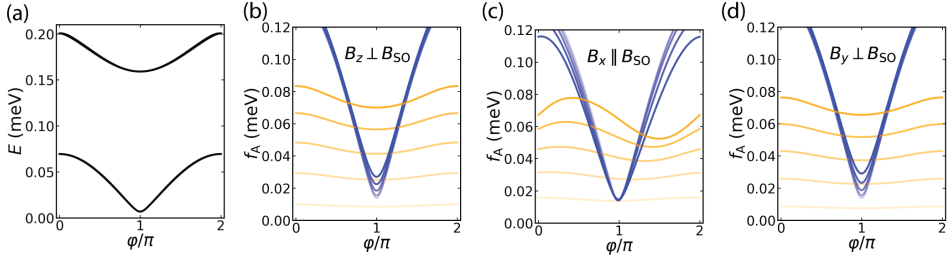
Figure 5.28: Relative shift in minimum of D_a transition compared to the S_a transition at high transparency ($\mu = 13.12\,\text{meV}$) versus different field directions. **(a)** BdG energies at $\mu = 13.12\,\text{meV}$. We observe two nearly degenerate manifolds. **(b) - (d)** Transition spectra of the lowest ABS manifold illustrating both the S_a (blue) and D_a (yellow) transition for increasing field strength and 3 different field directions. Darker colors indicate higher fields. The Zeeman energy used in (b), (d) ranges from $E_Z = 0.2 \rightarrow 2\Delta$ in equal steps. For (c), the parallel field direction, the Zeeman energy ranges from $E_Z = 0.1 \rightarrow 0.5\Delta$

phase-dependence as we did in Figure 5.14. Furthermore, we show the matrix elements versus field, and see that indeed only the T_-, T_+, matrix elements become finite at $\varphi = \pi$, while the others stay zero. This is lifted by applying a small B_x, where now also $|0\rangle \rightarrow |\uparrow_a\downarrow_b\rangle, |0\rangle \rightarrow |\downarrow_a\uparrow_b\rangle$ obtain a finite matrix element at $\varphi = \pi$. Thus we would have expected to see $|0\rangle \rightarrow |\uparrow_a\downarrow_b\rangle, |0\rangle \rightarrow |\downarrow_a\uparrow_b\rangle$ transitions in the data. This is by no means a complete data set as there are many parameters to vary, but we have investigated similar spectra at a few other chemical potential points – including for junctions without the double barrier close to the first sub-band entry, where the manifolds disperse oppositely and behave like the analytical expressions shown in (Park and Yeyati, 2017) – and found qualitatively similar conclusions. The visibility of the even-mixed transitions heavily depended on the exact chemical potential setting, and often they were not visible at all.

Field directions for a single ABS manifold
We now shift towards a chemical potential where the lowest ABS manifold is more transparant, to qualitatively match the situation in Figure 5.4. In Figure 5.28, we investigate the dispersion of the odd spin-flip transition D_a for three magnetic field directions relative to the effective spin-orbit field. We observe that the case displayed in Figure 5.28(c) is most similar to the data where $B \parallel B_{\text{SO}}$ as for the other directions there is no relative shift of the minimum of D_a with respect to the minimum of S_a. Thus, the data observed in Fig.4 of the main text and Figure 5.16 is consistent with a component of the spin-orbit along the wire axis, i.e. the z-axis. Note that we have not investigated whether a random disorder potential can change this picture.

5.11.2 Minimal model including exchange interaction
Here, we supply additional information about the minimal model including interaction presented in Eq.(1) in the main text to provide insight on the effect of each ingredient. The aim in this minimal model is to keep tunable the parameters that are relevant to reproduce the qualitative hierarchy of the lines (spin-orbit, magnetic field and Coulomb interaction) but to avoid an explicit description of other features such as the size of the junction, its transparency, the chemical potential or the superconducting pairing. To this

end, we consider the basis of two lowest spinless bare ABSs manifolds $i = a, b$, with energies E_i implicitly taking into account the latter features of the junction, and then introduce the spin-orbit, the magnetic field and the Coulomb interaction within this basis.

To describe the spin-orbit coupling, we project it on the bare ABSs, writing the spin-orbit Hamiltonian as:

$$\tilde{H}_{SO} = \sum_{i\sigma i'\sigma'} \langle i\sigma | H_{SO} | i'\sigma' \rangle \gamma_{i\sigma}^{\dagger} \gamma_{i'\sigma'} , \qquad (5.23)$$

where $\gamma_{i\sigma}^{\dagger}$ creates a quasiparticle with spin σ in manifold i, and $H_{SO} = \alpha/\hbar (p_z \sigma_x - p_x \sigma_z)$ is described with a 2D Rashba model, z being the direction parallel to the nanowire. Imposing time reversal symmetry on $\tilde{H}_{SO}$, we get the relations $\langle i\sigma | H_{SO} | i'\sigma \rangle = \langle i\bar{\sigma} | H_{SO} | i'\bar{\sigma} \rangle^*$ and $\langle i\sigma | H_{SO} | i'\bar{\sigma} \rangle = -\langle i\bar{\sigma} | H_{SO} | i'\sigma \rangle^*$, where it has been used $\mathcal{T} c \gamma_{i,\sigma} \mathcal{T}^{-1} = c^* \sigma \gamma_{i,\bar{\sigma}}$. Thus, we can write:

$$\bar{H}_{SO} = i\alpha_{\parallel} \left(\gamma_{a\uparrow}^{\dagger} \gamma_{b\downarrow} + \gamma_{a\downarrow}^{\dagger} \gamma_{b\uparrow} \right) - i\alpha_{\perp} \left(\gamma_{a\uparrow}^{\dagger} \gamma_{b\uparrow} - \gamma_{a\downarrow}^{\dagger} \gamma_{b\downarrow} \right) + \text{H.c.}, \qquad (5.24)$$

where $\alpha_{\perp(\parallel)} \in \mathbb{R}$ are treated as fitting parameters but can be related with the spatial profile of the basis wavefunctions $i\alpha_{\perp(\parallel)} = (\alpha/\hbar)\langle a | p_{x(z)} | b \rangle$. A more general spin-orbit Hamiltonian can be devised just imposing time reversal symmetry, resulting in the non-diagonal terms $\alpha_s \gamma_{a\uparrow}^{\dagger} \gamma_{b\uparrow} + \alpha_s^* \gamma_{a\downarrow}^{\dagger} \gamma_{b\downarrow} + \alpha_d \gamma_{a\uparrow}^{\dagger} \gamma_{b\downarrow} - \alpha_d^* \gamma_{a\downarrow}^{\dagger} \gamma_{b\uparrow} + H.c.$, with $\alpha_{s,d} \in \mathbb{C}$. We checked that this coupling provides qualitatively similar results.

Assuming that these basis wavefunctions are separable in $|i\rangle = |\phi_{iz}\rangle |\phi_{ix}\rangle$, we expect the transverse part $i\alpha_{\perp} = -(\alpha/\hbar)\langle\phi_{az}|\phi_{bz}\rangle\langle\phi_{ax}|p_x|\phi_{bx}\rangle$ to be negligible in situations with almost spatially symmetric transverse confining potentials ($V(x) \approx V(-x)$) where both manifolds share the same channel. This would happen because both $|\phi_{ax}\rangle$ and $|\phi_{bx}\rangle$ would have approximately the same spatial parity around $x = 0$, and thus $\langle\phi_{ax}|p_x|\phi_{bx}\rangle \approx 0$. However, our case likely corresponds to a multichannel situation, given the moderate length of the junction and the existence of multiple intermanifold single QP transitions visible in the spectroscopy over φ. Thus, each ABSs manifold would arise from a different transverse channel, enabling a finite $\alpha_{\perp}$. Still, this separation is not complete because of the anticrossings, which are a consequence of a non-zero $\alpha_{\parallel} \propto \langle\phi_{ax}|\phi_{bx}\rangle$. Nevertheless, for simplicity, in order to estimate a lower bound for the spin-orbit strength we use the case where the manifolds 1, 2 strictly correspond to different channels. This yields $|\langle\phi_{ax}|p_x|\phi_{bx}\rangle| \leq \hbar C/W$, with W the width of the nanowire and C a factor of order ~ 1 that depends on the confinement potential. Then, using the fitted parameter $\alpha_{\perp} \approx 5 \text{GHz}$ and $|\langle\phi_{az}|\phi_{bz}\rangle| \leq 1$, we get $\alpha = \alpha_{\perp}\hbar/(\langle\phi_{az}|\phi_{bz}\rangle\langle\phi_{ax}|p_x|\phi_{bx}\rangle) \geq 0.02W$ meVnm (W in nm). This provides a lower bound of ~ 2 meVnm for $W \sim 100$nm.

It must be highlighted that even if the actual specific microscopic origin of the spin orbit effective parameters is arguable, their presence is necessary in order to reproduce the structure of the even transitions and their anticrossings. Note that the spin-orbit interaction must be taken into account even though we are considering the case $\varphi = \pi$, where it does not affect the single-particle Andreev levels degeneracy due to Kramers' theorem (Béri et al., 2008), since we are interested in the two-particle states as well. Nevertheless, the predicted unbroken degeneracy of $T_{\pm}$ at zero field (Fig. 5.29(a)iii) suggests that it should be improved to account for the full splitting in $\varphi = \pi$ that is sometimes observed in other spectra, for example introducing a third manifold, which allows to avoid that degeneracy.

The behaviour of ABSs energies with small Zeeman fields depends on the interplay between the spin orbit, the transmission of the junction and the chemical potential (van Heck et al., 2017). In our simple model, we introduce effective g-factors for the bare ABSs as fitting parameters.

Finally, to describe the Coulomb interaction we use a ferromagnetic effective exchange. The Coulomb interaction in the nanowire is strongly screened by the environment and its free charges, rendering the interaction approximately local. However, the form of the interaction in the subspace of the ABSs is more convoluted because of their spatial overlap. In the states with 2 QPs, due to this overlap, the interaction leads to an effective ferromagnetic coupling between the quasiparticle spins, as in the case of Hund's rule in atomic physics.

The full Hamiltonian is projected over the states with 1 and 2 quasiparticles, resulting in the matrices

$$(H)_{1QP} = \begin{pmatrix} E_a + g_a^* B_z & 0 & -i\alpha_\perp & i\alpha_\parallel \\ 0 & E_a - g_a^* B_z & i\alpha_\parallel & i\alpha_\perp \\ i\alpha_\perp & -i\alpha_\parallel & E_b + g_b^* B_z & 0 \\ -i\alpha_\parallel & -i\alpha_\perp & 0 & E_b - g_b^* B_z \end{pmatrix}, \tag{5.25}$$

in the basis $\mathcal{B}_{1QP} = \{|1\uparrow\rangle, |1\downarrow\rangle, |2\uparrow\rangle, |2\downarrow\rangle\}$, where the constant term $-\frac{3J}{8}$ has been neglected, and

$$(H)_{2QP} = \begin{pmatrix} 2E_a & 0 & i\alpha_\parallel & i\sqrt{2}\alpha_\perp & -i\alpha_\parallel & 0 \\ 0 & E_a+E_b & 0 & (g_a^*-g_b^*)B_z & 0 & 0 \\ -i\alpha_\parallel & 0 & \begin{matrix}E_a+E_b-J\\+(g_a^*+g_b^*)B_z\end{matrix} & 0 & 0 & -i\alpha_\parallel \\ -i\sqrt{2}\alpha_\perp & (g_a^*-g_b^*)B_z & 0 & E_a+E_b-J & 0 & -i\sqrt{2}\alpha_\perp \\ i\alpha_\parallel & 0 & 0 & 0 & \begin{matrix}E_a+E_b-J-\\(g_a^*+g_b^*)B_x\end{matrix} & i\alpha_\parallel \\ 0 & 0 & i\alpha_\parallel & i\sqrt{2}\alpha_\perp & -i\alpha_\parallel & 2E_b \end{pmatrix}, \tag{5.26}$$

in the basis $\mathcal{B}_{2QP} = \{|S_a\rangle, |S_{ab}\rangle, |T_+\rangle, |T_0\rangle, |T_-\rangle, |S_b\rangle\}$.

In order to visualize the effect of each ingredient, we plot in Fig. 5.29 the evolution with magnetic field in 3 situations. In Fig. 5.29(a.i), without J and α, in Fig. 5.29(a.ii) with J without α, and in Fig. 5.29(a.iii) with J and α. The combination of SO and interaction acts as an effective anisotropic exchange (Katsaros et al., 2020). Note that the ordering of the lines depends on the relative strenghts of J and the energies E_a and E_b, therefore with stronger J it is possible to have S_a above T_0 and thus flip $\tilde{S}_a$ and $\tilde{T}_0$. This is actually the case in the fit of the data in the main text in Fig.3, but since they are strongly hybridized, we kept the notation where $\tilde{S}_a$ is the lowest state for clarity.

An overlay of the simple fit using the LMFIT package (Newville et al., 2021) shown in Fig.3(c) of the main text is shown in Fig. 5.29(b). For the fit, we extracted the positions of the four lowest even transitions and the lowest odd interband transitions at zero field by fitting lorentzians to the peak positions (see data-repository). We then let LMFIT determine the energies E_a, E_b, J and $\alpha_\perp$ by fitting both the odd and even parity diagonalization

simultaneously [white markers in Figure 5.29(b)]. The dispersion in field in the low-field limit is determined solely by the g-factors of manifold a, b. For the g-factors we first extract the coordinates of the D_a [yellow markers in Figure 5.29(b)], T_+ and T_- transitions [blue markers in Figure 5.29(b)] for low fields where they are visible (see data-repository for extraction details). The g-factor of the lowest manifold g_a^* is then fit by fitting the slope of the data corresponding to D_a in the range between 80 and 120 mT and g_b^* is extracted via $g^* = \pm 1/2(g_a^* + g_b^*)$ from the average slope g^* of T_+ and T_-, which is extracted for data up to ~ 30 mT to make sure the avoided crossing does not interfere with the fit. For the T_+ and T_- the transitions were not visible at zero field, so we used the average of the crossing point of the linear fits with the y-axis as an estimate for their zero-field position. We set $\alpha_\parallel$ separately to the size of the avoided crossing extracted from the data.

In the modeling of the data we have so far focused on fitting the transitions corresponding to the two lowest energy manifolds. As discussed in the main text, and visible in the spectrum in Fig.3a, 3b (or Figure 5.29), more bundles of odd-parity transitions are present in the data at higher frequency, which we presume correspond to transitions from the lowest manifold a to manifold $c, d, \dots$ Notice that it could be possible to include more manifolds in the modeling to account for the higher frequency odd-parity transition bundles I_{ac}, I_{ad} at ~ 23 GHz, ~ 29 GHz (yellow colored in Figure 5.29), without affecting qualitatively the low-frequency even-parity spectrum. Unfortunately, this introduces many additional parameters for the spin-orbit matrix elements and exchange couplings between manifolds and, as a result, a meaningful fit and analysis of these parameters would require the knowledge of the even-parity transitions at frequencies beyond the measured range. Yet, for the sake of completeness we show in Fig. 5.30 the result of introducing a third manifold, which allows to model the bundle I_{ac}. In this case, and in general for a similar model with several manifolds, the spin-orbit Hamiltonian $\bar{H}_{SO}$ includes combinations for all pairs of manifolds α and β, with matrix elements $\alpha_s^{\alpha\beta}$, $\alpha_d^{\alpha\beta}$. To model the interaction, we use effective intermanifold exchange couplings $-J^{\alpha\beta}\vec{S}_\alpha\vec{S}_\beta$.
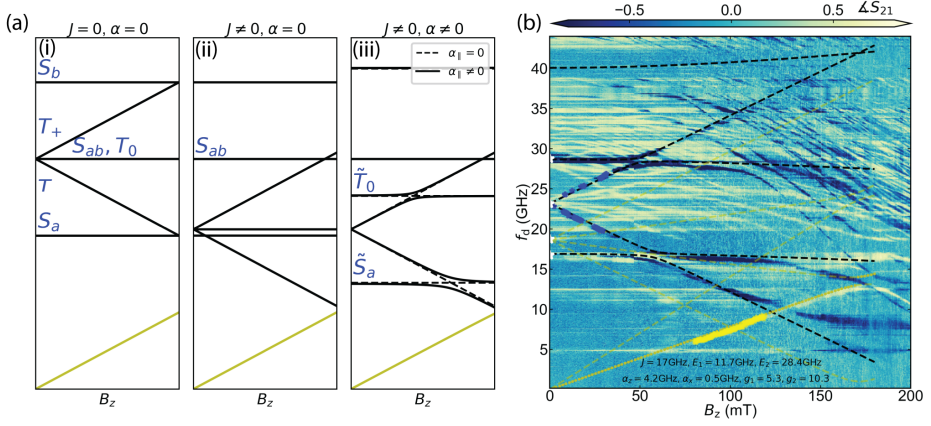
Figure 5.29: **(a)** Minimal model with example parameters to illustrate the effect of each ingredient separately. (i) the spectrum without exchange interaction and equal g-factors, (ii) the spectrum with exchange interaction, but zero spin-orbit interaction, (iii) the spectrum both with spin-orbit interaction and exchange interaction. This motivates the sketch made in Fig 2.d in the main text. Unitless parameter chosen are: $E_a = 1.2$, $E_b = 2.4$, $\alpha_\perp = 0.5$, $\alpha_\parallel = 0.1$, $g_a^* = g_b^* = 0.8$, $J = 0.85$. **(b)** Fit of the data using real units as shown in Fig.3(c) of the main text overlayed on the data. White markers indicate extracted data points used for the fit of $E_a, E_b, \alpha_\perp, J$ and yellow and blue markers for the fitting of g_a^* and g^* respectively.
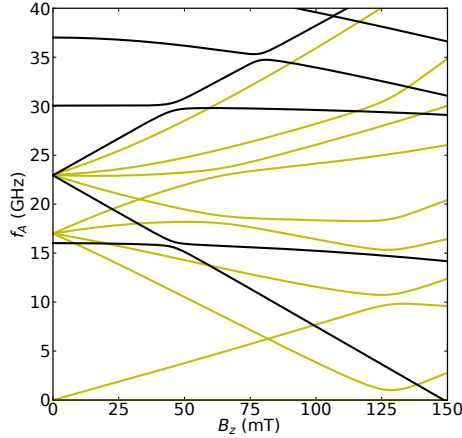

Figure 5.30: Model with 3 manifolds reproducing the second set of odd-parity bundles I_{ac} at $\sim 23\,\mathrm{GHz}$. Several even transitions lie beyond the $40\,\mathrm{GHz}$ limit. Spin-orbit coupling produces anticrossings between T_+ and one of the higher even transitions, and between some lines of the I_{ab} and I_{ac} bundles. Parameters (in GHz): $E_{a,b,c} = 15.3, 29.38, 30.37$, $g_{a,b,c} = 4.77, 17.46, 2.043$, $J_{ab,ac,bc} = 81.97, -0.23, -29.83$, $\alpha_s^{ab,ac,bc} = 4.91i, -6.34i, 2.46i$, $\alpha_d^{ab,ac,bc} = 0.5i$.

5.12 Acknowledgments

6

Andreev bound states in InSb-Al nanowire Josephson junctions defined using shadow-wall lithography in a circuit-QED architecture

To expand the toolbox of semiconductor-superconductor hybrid circuit electrodynamics, we demonstrate shadow-wall lithography techniques on a superconducting NbTiN circuit to study Andreev bound states (ABS) in gate-tunable InSb-Al hybrid Josephson junctions. We embed the junctions into a radio-frequency SQUID that modulates the inductance of a magnetic-field-compatible resonator. In the gate-dependence of Andreev pair transitions when half a flux quantum is penetrating the SQUID loop, we observe high transparency ABS over a large range in gate voltage. Furthermore, by investigating the flux and magnetic field dependence up to 200 mT we observe the direct spin-flip transition in the lowest manifold, yielding an effective g-factor of ~ 16.5. Finally we compare the device parameters which we extract from microwave spectroscopy to those obtained from an additional Josephson junction characterized by transport measurements and fabricated following the same fabrication flow. The results and methods of this work may guide the design of future hybrid circuits with more complex geometries and material combinations.

6.1 Introduction

Circuit quantum electrodynamics (circuit-QED) techniques have been shown to provide high energy and time resolution in the study of semiconductor-superconductor hybrid devices. So far, most applications involving semiconductor-superconductor hybrid nanowires in superconducting circuits have focused on InAs-Al nanowires with etched junctions due to their established fabrication process (de Lange et al., 2015; Larsen et al., 2015; Pita-Vidal et al., 2020; Hays et al., 2018, 2020, 2021; Wesdorp et al., 2023, 2024; Splitthoff et al., 2022; Bargerbos et al., 2020, 2022; Pita-Vidal et al., 2023a). Recently, shadow lithography (Khan et al., 2020; Heedt et al., 2021; Borsoi et al., 2021; Goswami et al., 2023), where the junction remains untouched by an etchant, has been shown to produce highly transparent and pristine Josephson junctions. Furthermore, using on-chip shadow-walls has enabled versatile junction geometries and allowed noninvasive contacting of small sections of the nanowire, a key element in a series of recent experiments demonstrating high efficiency Cooper pair splitting (Wang et al., 2022) and artificial Kitaev chains (Dvir et al., 2023; Bordin et al., 2023). However, the incorporation of shadow-wall lithography with circuit-QED devices has remained elusive due to the increased fabrication complexity in combination with potentially increased dielectric losses in the microwave circuits.

In this work, we combine on-chip shadow-wall lithography of nanowire Josephson junctions with a magnetic field compatible superconducting circuit. The technique can be used for various material combinations. Here we use InSb nanowires coated with epitaxial Al (Heedt et al., 2021; Borsoi et al., 2021). InSb has several properties that differ from InAs typically used in previous works involving superconducting circuitry. InSb has a lower disorder (Van Weperen et al., 2013; Plissard et al., 2012; Gül et al., 2015; Gill et al., 2016; Kammhuber et al., 2016; Badawy et al., 2019), lower effective mass, stronger spin-orbit coupling (van Weperen et al., 2015; Kammhuber et al., 2017) and higher g-factor (Van Weperen et al., 2013; Kammhuber et al., 2016). These properties are beneficial for the creation of local triplet pairing, relevant for the search of topological phases of matter (Kitaev, 2001; Lutchyn et al., 2010; Oreg et al., 2010), as well as for creating and manipulating the spin of Andreev bound states to make Andreev spin qubits (Hays et al., 2021; Pita-Vidal et al., 2023a,b).

We investigate the microwave spectrum of Andreev bound states in shadow-defined InSb-Al Josephson junctions. Andreev bound states (ABSs) are microscopic fermionic states that carry supercurrent in Josephson junctions and come in spin-degenerate Kramers pairs (Kulik, 1970; Beenakker, 1991), which we will refer to as manifolds in the following. They are sensitive to the microscopic details of the junction and serve as excellent probes of the junction properties. Since the superconducting gap Δ_{Al} of aluminum is around $h \cdot 45\,\text{GHz}$, where h is Planck's constant, we use conventional circuit-QED techniques to probe transitions between Andreev levels that have energies $< \Delta_{Al}$. The use of superconducting circuits to probe ABSs directly has recently brought about a series of exciting results, including manipulating individual bound states in atomic break junctions (Janvier et al., 2015) and InAs nanowires (Hays et al., 2018), observing sub-µeV spin-splitting of bound states due to spin-orbit coupling (Tosi et al., 2019; Hays et al., 2020), coherent control over a single superconducting spin (Hays et al., 2021; Pita-Vidal et al., 2023a) and probing of multiple interacting superconducting spins in a single junction (Wesdorp et al., 2024; Matute-Cañadas et al., 2022) and in two junctions separated by a long distance (Pita-Vidal
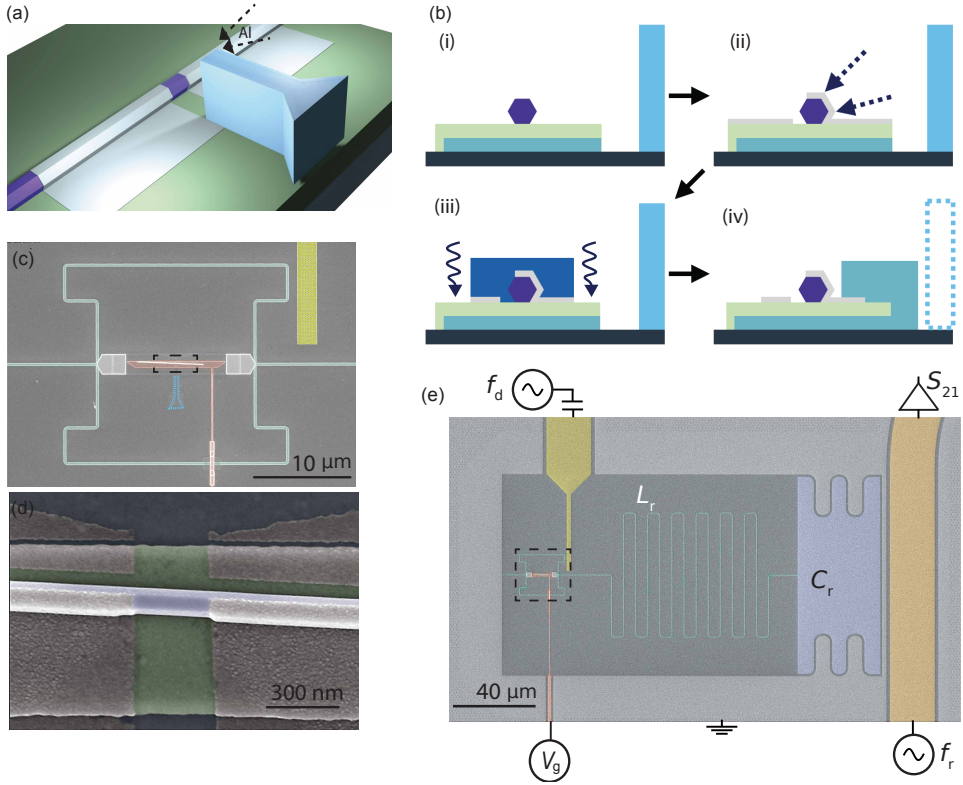
Figure 6.1: Illustration of the shadow wall-lithography technique and our device. **(a)** Schematic of Josephson junction creation using shadow-wall lithography. Al (grey) is deposited under an angle (direction indicated with the arrows) on an InSb nanowire (purple), while an HSQ wall (light blue) creates a shadow that defines the Josephson junction. Other circuit elements are not shown here. **(b)** Fabrication flow. (i) An InSb nanowire (purple) is deposited on a dielectric (green) separating a pre-patterned NbTiN readout circuit (teal) with shadow walls (light-blue) already deposited and lithographically defined. (ii). Aluminum (grey) is deposited globally on the chip under a 15 and 45 degree angle (shadow of the wall is not shown here). (iii) The aluminium is removed on the rest of the chip except for a small region around the nanowire defined by a removable soft mask (dark-blue). (iv) The remaining aluminum is contacted to the NbTiN circuit and the smart walls are removed during liftoff. **(c-e)** False colored scanning electron micrographs of the complete circuit of a representative device (device C; identically designed to device B). **(c)** Zoom in of the SQUID loop [dashed box in (e)] with the removed shadow wall indicated by the dashed line (light blue). Colored are the gate line (red), and the drive-line (yellow). **(d)** Zoom in of the nanowire Josephson junction (dashed box in (c)). The materials are colored corresponding to (a), (b). **(e)** Complete circuit for the device. The resonator consists of a capacitor (purple) that is connected through an inductor (green) via the SQUID loop to the ground plane. The resonator is capacitively coupled to a feedline (amber). The nanowire is placed in the central arm of the SQUID and is tunable with an electrostatic gate (red), a microwave drive is capacitively coupled to a drive-line (yellow).

et al., 2023b). These new developments motivate the extension of superconducting circuits to study Andreev states in more complex geometries and material platforms, which we present here.

In this research article, we first study microwave transitions that excite Cooper pairs to

an Andreev manifold using a microwave drive. We focus on the dependence of such transitions versus applied electrostatic gate voltage as well as magnetic flux. These transitions are especially sensitive to disorder in the junction region when the applied flux equals half a flux quantum (Beenakker, 1991). At this flux setting, we find high-transparency bound states over large ranges of gate voltage consistent with an elastic scattering length $l_e \geq L \sim 150 - 300\,\text{nm}$, where L is the junction length. We proceed with applying an in-plane magnetic field, observing a switch in the ground state parity of the lowest Andreev manifold. This parity switch, together with spin-orbit coupling, allows for a directly driven spin-flip excitation of a quasiparticle occupying the lowest-energy Andreev manifold, reproducing recent results in InAs nanowires (Wesdorp et al., 2024), relevant for direct manipulation of Andreev spin qubits (Pita-Vidal et al., 2023a,b). Finally we measure a junction using conventional DC transport techniques for a device that has seen an identical fabrication flow, to complement the results obtained using microwave spectroscopy.

6.2 Fabrication details

The superconducting circuit and gate dielectric are patterned using the methods described in Wesdorp et al. (2023). The circuit consists of a layer of $\sim 20\,\text{nm}$ NbTiN sputtered on a high resistivity Si wafer. The wafer is initially covered with $100\,\text{nm}$ Si_3N_4 deposited using low pressure chemical vapor deposition and cleaned with HNO_3 prior to the NbTiN deposition. The circuit is subsequently patterned using standard electron-beam lithography and etched using fluor-based reactive ion etching (SF_6/O_2). The $\sim 28\,\text{nm}$ Si_3N_4 gate dielectric and the dielectric for overpasses to connect the ground plane across the DC lines are then deposited using plasma-enhanced chemical vapor deposition at 300°, patterned using lithography and etched using buffered oxide etchant. Finally, another layer of approximate $60\,\text{nm}$ NbTiN is sputtered and patterned using liftoff to create on-chip overpasses.

We then proceed with adding shadow walls on the chip and placing the nanowires. This step is followed by the shadowed evaporation of aluminum as described in (Borsoi et al., 2021; Heedt et al., 2021). In particular, the walls are patterned using hydrogen silsesquioxane (HSQ) (Mazur et al., 2022), which results in high-aspect ratio SiO_x walls of height $800\,\text{nm}$ and width varying between 150 and $300\,\text{nm}$ to define the junction size. After the wall placement, hexagonal InSb nanowires (Badawy et al., 2019), of nominal diameter $\sim 110\,\text{nm}$ are placed on the gates close to the walls using a nanomanipulator. The interface of the semiconductor is crucial to obtaining a good proximity effect (Chang et al., 2015), thus prior to the Al deposition the native oxide is removed from the nanowire by exposing the device to a flow of atomic hydrogen radicals thermally dissociated by a filament at $1700\,\text{K}$ at $550\,\text{K}$ substrate temperature after which the Al is deposited at $138\,\text{K}$ without breaking the vacuum and oxidized at $200\,\text{mTorr}$ for 5 minutes while cold (Heedt et al., 2021; Borsoi et al., 2021). The InSb is proximizited by Al after a double-angle Al deposition under 15 and 45 degrees with respect to the substrate (4 times $4.5\,\text{nm}$ is deposited alternating the angle at $0.05\,\text{Å/s}$) to cover 3 facets of the nanowire resulting in $\sim 17\,\text{nm}$ Al at the central facet, and $\sim 8\,\text{nm}$ Al at the substrate and top and bottom facets. The shadow wall prevents Al deposition in a short section of the wire defining the Josephson junction. An illustration of the core principle of the shadow-wall lithography is shown in Figure 6.1a. The use of Al as a superconductor in combination with InSb is known to show intermixing at the Al/InSb interface, an effect that scales with temperature (Boscherini et al., 1987;

Thomas et al., 2019). This unstable Al/InSb interface increases the difficulty of fabrication as all processes subsequent to the Al deposition have to be performed at room-temperature which prohibits hot baking of resist (Heedt et al., 2021; Borsoi et al., 2021) and requires freezing of the sample in storage.

Since the Al is deposited globally on the chip, we perform a coarse etch using transene-D after lithographically defining a vacuum baked soft poly-methyl-methacrylate (PMMA) etch mask around the junction region (Moehle et al., 2022), which covers the whole nanowire to prevent damage during the etch, depicted in Figure 6.1b, step (iii). The remaining aluminum is subsequently contacted in a final NbTiN liftoff step preceded by argon-milling to remove the native oxide on the aluminum. The additional contacting step is necessary, because the evaporated Al does not provide good contact to the NbTiN base layer. Note that the contacting step is not on the nanowire, potentially avoiding spurious heating of the wire in the Ar milling step. Additionally, because of the (removable) PMMA mask we can define arbitrarily large contact areas, which increased the yield of our devices. The shadow walls are removed from the chip during the lift-off of the NbTiN contacts.

6.3 Circuit Design

Having established the junction fabrication process, we now explain the superconducting circuit elements in more detail. The resonator, visible in Figure 6.1e consists of a superconducting island with a large capacitance to ground and connected to ground via an inductor in series with a radio-frequency superconducting interference device (rf-SQUID), see Section 6.8.1 for detailed circuit parameters. The resonator is capacitvely coupled to an on-chip transmission line for readout. An electrostatic gate below the nanowire tunes its electron-density. A drive line is used to excite transitions between Andreev levels in the Josephson junction by creating an RF voltage difference over the SQUID to ground. The junction can be phase-biased using an externally applied magnetic flux Φ through the SQUID loop, either by using an on-chip flux-bias line, or by applying a magnetic field perpendicular to the nanowire axis, but in the chip plane (Wesdorp et al., 2024). The loop design is gradiometric, to minimize the effective area sensitive to perpendicular field and the magnetic field is aligned using the methods described in Ref. (Wesdorp et al., 2024), which has a similar loop design. Field alignment is essential to minimize the creation of vortices which may cause flux jumps when changing the field.

6 Andreev bound states in InSb-Al nanowire Josephson junctions defined using shadow-wall lithography
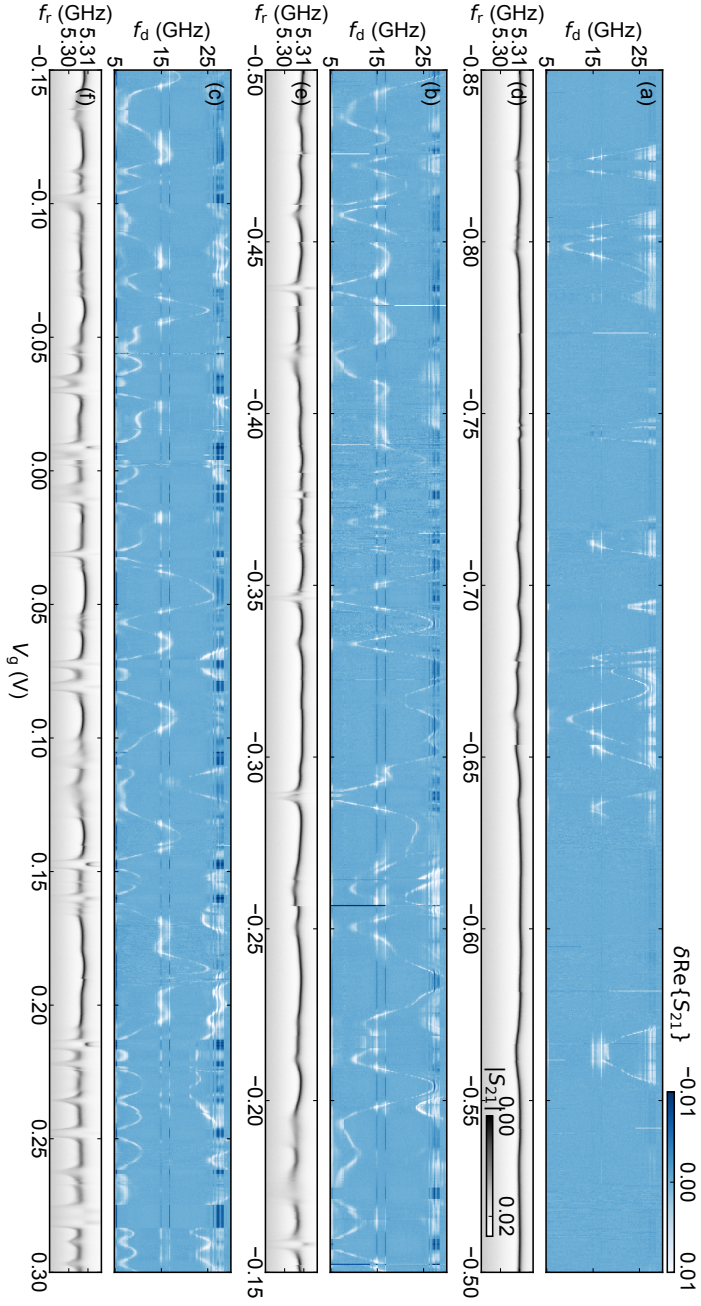152
in a circuit-QED architecture

Figure 6.2: Spectroscopy as a function of gate at $\Phi \approx \Phi_0/2$, where $\Phi_0 = h/2e$ is the magnetic flux quantum, in a 150 nm wide Josephson junction (device A). **(a - c)** Microwave spectroscopy over a large range of gate voltage from -0.85 V in (a) to 0.30 V in (c). The inset in (a) illustrates the observed pair transition for the lowest manifold and the relation between the energy of the ABS at $\Phi = 0.5\Phi_0$ and its transparency. The colormap indicates the real part of the change in measured transmission coefficient $\delta Re\{S_{21}\}$ (see Section 6.8.1) **(d-f)** Measurements of the resonator spectroscopy $|S_{21}|$ taken interleaved with the spectroscopy traces to determine the readout point. The colorbar is shared between panels (a) and (b,c) as well as between (d) and (e,f).

6.4 Microwave Spectroscopy

We carried out measurement on two chips each with four devices as well as additional test devices for DC transport measurements (see Sec. 6.8.6). For each of the eight resonator devices we show the gate and flux characterization monitoring only the resonator response in Section 6.8. We found that all resonators responded to gate voltages and allowed for full pinch-off of the junctions. Additionally, all devices showed SQUID oscillations, an indication that the Josephson junctions are functional.

First, we test the resonator quality factors. For the four resonators that do not include an on-chip flux line we find internal quality factors Q_i ranging from $20 \cdot 10^3 - 35 \cdot 10^3$, much larger than the quality factor due to the coupling to the readout line $Q_c \sim 2 \cdot 10^3 - 3 \cdot 10^3$ and comparable to similar devices fabricated using InAs etched junctions (Wesdorp et al., 2024, 2023). These results indicate that we successfully managed to integrate the InSb nanowire with shadow defined junctions into a circuit-QED platform without introducing additional large dielectric losses. The devices with an on-chip flux bias line had much lower internal quality factors $Q_i \sim Q_c$ due to overcoupling of the resonator to the flux line.

In the following section, we focus on two devices, A and B, both of which do not have on-chip flux lines, and we measure the Andreev spectra of the shadowed Josephson junctions.

6.4.1 Electrostatic control of highly transparent Josephson junctions

Using device A, we set the flux at $\Phi = 0.5\Phi_0$, where $\Phi_0 = h/2e$ is the magnetic flux quantum, for having the ABS pair transitions at their energy minima and we vary the electrostatic potential of the gate underneath the nanowire, shown in Figure 6.2. For each gate voltage, we measure the transmission through the transmission line S_{21} with a tone at f_r in a range around the resonance frequency of the resonator, $f_0 \sim 5.31\,\text{GHz}$ (Figure 6.2d-f), and the excitation spectrum (Figure 6.2a-c) interleaved. From the measurement of the absolute value of the response $|S_{21}|$ we determine f_0 of the resonator and measure spectroscopy at a readout point near f_0. When the drive frequency f_d is resonant with an ABS transition, this results in a change of the transmission δS_{21} (see Section 6.8.1 for more details), due to the coupling between ABS transitions and the resonator mode (Zazunov et al., 2003; Metzger et al., 2021).

In Figure 6.2a,d, when the voltage is strongly negative at -0.85 V and below, the nanowire does not conduct and therefore no modulations of the resonator frequency are visible. When we increase the voltage, isolated resonances start appearing in the spectrum, resembling a situation where the chemical potential of the junction is comparable to the disorder potential and, thus, for certain values of the gate voltage we observe resonant increases in the junction transmission. At the junction resonances, the resonator frequency, f_0, is pushed downward, resulting from the dispersive and inductive shift induced by the Andreev pair transitions (Janvier et al., 2015; Hays et al., 2018; Metzger et al., 2021). As the gate voltage increases (Figure 6.2b,e) and the chemical potential of the junction increases, we observe an Andreev pair transition that resides at low frequencies for extended gate ranges. Additionally, we observe avoided crossings between the resonator and the ABS transitions when their frequencies are below f_0. This continuous high transparency over a large gate range, as opposed to isolated resonances, is consistent with what one would expect from low-disorder junctions, where the junction length L is on the order of the
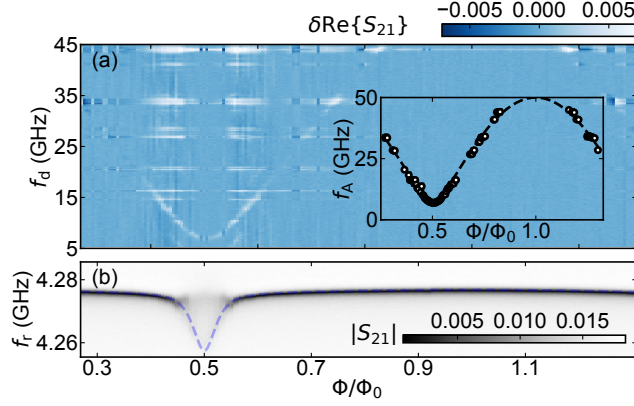
Figure 6.3: Flux dependence of device B at $V_g = -560\,\text{mV}$. **(a)** Two tone spectrum versus flux. Inset shows a fit of the extracted even pair transition frequency to Equation (6.1) yielding $\Delta^*/h = 25\,\text{GHz}$, $\tau = 0.983$. **(b)** Resonator spectroscopy in the same flux range as in panel (a). The data in (b) is measured interleaved with the data in (a). Overlayed with a dashed line is the total flux dependent resonator shift calculated from the extracted pair transition shown in (a) without additional fit parameters (See Section 6.8.3 for details). For Φ away from 0.5 the dashed line falls on top of the resonator trace.

elastic scattering length l_e. At the largest gate voltages (Figure 6.2c,f), we observe additional higher frequency transitions in the measurement range, indicating that multiple Andreev levels are present below the superconducting gap. This is expected when several transverse subbands in the proximitized semiconductor are occupied, i.e an increase in the electron density, within the wire for more positive gate voltages (see Appendix 6.8.7 for additional gate-dependence of this device and of device B).

6.4.2 Flux dependence
We will now further investigate the regime where the density of Andreev levels in the nanowire is low by studying the flux dependence of the Andreev transition frequency using device B (see Table 6.1 for an overview of the devices, additional flux dependence of device A at $V_g = 661.5\,\text{mV}$ is shown in Appendix 6.8.3). In Figure 6.3a we observe the typical dispersion of an Andreev pair transitions as well as in Figure 6.3b the accompanying resonator response. The pair transition frequency moves towards its minimum frequency around $\Phi/\Phi_0 = 0.5$, which corresponds to the flux setpoint of Figure 6.2. As displayed in the inset of Figure 6.3a, we fit the transition frequency to the flux-dependence of a single-channel junction model (Beenakker, 1991)

$$hf_A = 2\Delta^* \sqrt{1 - \tau \sin^2(\pi\Phi/\Phi_0)}, \tag{6.1}$$

where Δ^* represents an effective superconducting gap, discussed further below, and τ is the transparency of the manifold. From the fit, we extract an effective gap $\Delta^*/h = 25\,\text{GHz}$ and a transparency $\tau = 0.983$ indicating high tranparancy. We subsequently calculate the expected shift in resonator frequency δf due to this single pair transition using the estimated circuit parameters (see Section 6.8.3). This estimate is shown as the dashed line
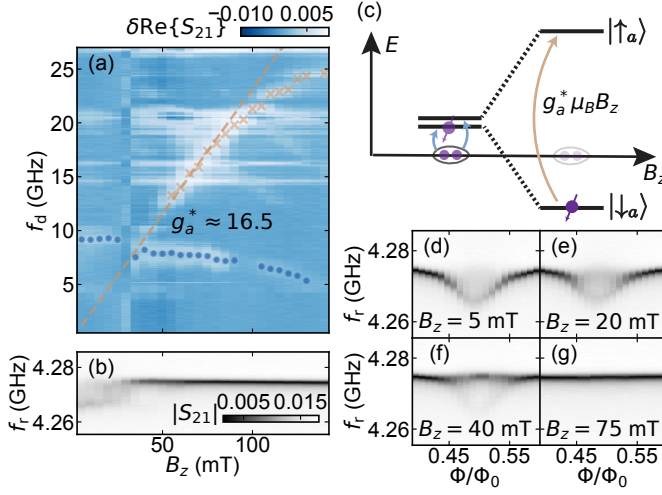
Figure 6.4:   Parallel magnetic field dependence at $\Phi \approx 0.5\Phi_0$ at $V_g = -560\,\text{mV}$ in device B. **(a)** Microwave spectroscopy of the Andreev levels as a function of the magnetic field B_z at approximately fixed flux (see Appendix 6.8.1 for the flux calibration and Figure 6.10 for additional data illustrating the spin-flip transition). The lowest pair-transition (also shown in Figure 6.3) is highlighted with round dots at the extracted peak positions. At higher field, the intra-manifold spin-flip transition is highlighted with crosses. From the initial slope of the spin-flip transition we extract a g-factor $g_a^* = 16.5 \pm 0.2$ of the lowest ABS manifold. **(b)** Accompanying resonator spectroscopy measured interleaved with (a). **(c)** Level diagram of the lowest ABS manifold visible. At zero field we drive the pair transition, indicated with two blue arrows. The Zeeman energy splitting causes the spin down level to cross the Fermi level making the singly occupied ABS the ground state and allows driving of the direct spin-flip transition at frequency $g_a^* \mu_B B_z / h$ indicated with a single amber arrow. **(d-g)** Resonator spectroscopy versus flux at selected B_z.

in Figure 6.3b. The good match indicates that, although other ABS manifolds may be present above the measured range, the resonator response is dominated by a single ABS.

6.4.3 Magnetic field dependence

We now focus on the spin-character of the bound state by additionally exploring the dependence on a parallel magnetic field, see Figure 6.4, at the same gate voltage as used in Figure 6.3. We align the magnetic field with respect to the chip plane to mitigate flux jumps (see Ref. (Wesdorp et al., 2024) for the alignment procedure). In Figure 6.4(a) the dependence of the Andreev spectrum on the field B_z along the wire axis is shown at approximately $\Phi \sim 0.5\Phi_0$. To measure the data, for each step in B_z, a flux sweep around $0.5\Phi_0$ is performed in which we can readily identify the even pair transition as well as the flux point $\Phi = 0.5\Phi_0$ at the minimum of the dispersion (see Section 6.8). The resulting data at $\Phi \sim 0.5\Phi_0$ is shown in Figure 6.4a and the interleaved resonator measurements are shown in Fig. 6.4(b). In particular, we highlight two main features of a single ABS manifold in magnetic field, the pair transition (Janvier et al., 2015; Hays et al., 2018) (see the circles in Figure 6.4a) and the direct spin-flip transition within the manifold (Wesdorp et al., 2024; Metzger et al., 2021) (see the crosses in Figure 6.4a) which appears only at larger magnetic field. Around zero field, the pair transition does not disperse since it involves exciting op-

posite spin Andreev levels. However, at larger magnetic field, the pair transition is pushed by interaction with higher energy Andreev manifolds (van Heck et al., 2017). In contrast to the pair-transition, the odd-parity direct spin-flip transition scales linearly with field at fields below around 50 mT and allows for the direct extraction of the effective Landé g-factor of the lowest Andreev manifold $g_a^* \sim 16.5$. This hybrid g-factor is consistent with InSb/Al as $|g_{InSb}| \sim 30 - 50$ and $|g_{Al}| \sim 2$.

For fields below 50 mT, we observe a splitting of the resonator response (Figure 6.4b) corresponding to even or odd parity occupation of the lowest ABS manifold, as typically observed in experiments on InAs nanowires (Hays et al., 2018, 2020, 2021; Tosi et al., 2019; Wesdorp et al., 2023, 2024). The occupations are indicated schematically by the Cooper-pair and single quasiparticle in the lowest Andreev level in Figure 6.4c, respectively. This splitting is also seen in the flux dependence of the resonator response, shown in Figure 6.4d for selected field values. When the lowest-energy spin state crosses the even parity zero field ground state energy (fixed at 0 energy in Figure 6.4c), a quantum phase transition occurs where the ground state parity switches from even to odd (van Woerkom et al., 2017; Bargerbos et al., 2022). In the odd-parity phase, the resonator response, see Figure 6.4g, is no longer strongly dispersing with flux, as expected, because the dispersion of the excited Andreev level cancels the dispersion of the unoccupied state in the manifold. Although, note that spin-orbit and charging effects could cause a small dispersion (Park and Yeyati, 2017; Chtchelkatchev and Nazarov, 2003; Kurilovich et al., 2021). The zero energy crossing and associated ground state parity switch can also be seen in the ABS spectrum as a crossing of the pair transition and the direct spin-flip transition (van Woerkom et al., 2017; van Heck et al., 2017). Note that the appearance of the odd-parity transition is rather gradual since the phase transition from even-favored occupation to odd-favored occupation is not discrete, but continuous. Possibly due to a high effective bath temperature of quasiparticles, often seen in superconducting circuits (Glazman and Catelani, 2021). Nevertheless, the magnetic-field-induced parity switch stabilizes the odd parity ground state and thus can be exploited for the creation of Andreev spin qubits similar to the use of charging energy in superconducting quantum dots (Bargerbos et al., 2022; Pita-Vidal et al., 2023a). The remaining visibility of the pair transition after the parity switch could be related to a small residual even parity population and microwave induced parity polarization effects (Wesdorp et al., 2023).

6.5 DC transport measurements

We now proceed with measurements of a Josephson junction on the same chip as device A with leads that allow DC access, shown in Figure 6.5a. Using this device, we complement the microwave spectroscopy characterization with standard DC characterization measurements of a device fabricated with the same steps. These transport measurements are done using standard lock-in amplifier techniques. When the device is current-biased, see Figure 6.5b, we can measure the differential voltage drop across the Josephson junction and observe a switching current of ~ 10 nA at $V_g = 0$, and maximally ~ 18 nA in the more open regime (see Section 6.8.6). When applying a parallel magnetic field, the switching current gradually goes to zero at around 200 mT. At magnetic fields around 200 mT, the microwave response of the two tone spectroscopy disappeared, which we now understand as being due to vanishing critical current of the junctions.
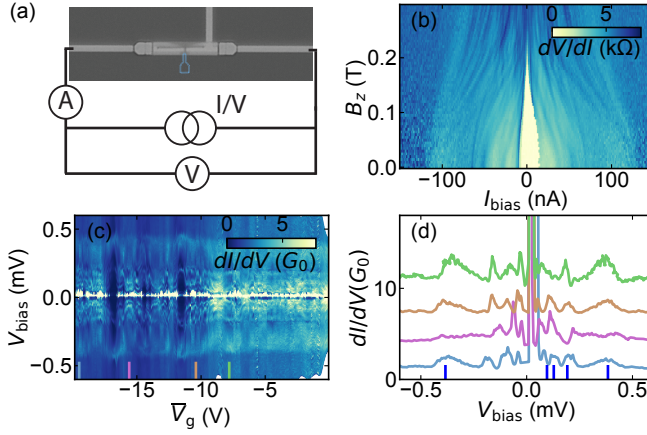
Figure 6.5: DC supercurrent characterization of device D - a device following the same fabrication flow as the resonator devices and located on the same chip as device A. The shadowed junction is 150 nm long. **(a)** Optical microscope image of the device and measurement schematic, with the position of the shadow wall sketched in blue. **(b)** Current-bias versus in-plane magnetic field B_z while measuring the differential junction resistance dV/dI using standard lock-in techniques. **(c)** Voltage bias measurements (corrected for series line resistance) versus applied gate voltage on the bottom gate electrode. **(d)** Linecuts at the gate settings indicated in (c), the upper three linecuts are each shifted by 3 times $G_0 = 2e^2/h$ per linecut for visibility. From the peaks at 2Δ we extract a gap of $\Delta = 202\,\mu eV = h \cdot 48\,GHz$ (grey markers). Additionally, we observe gate-dependent peaks at values $\sim 2\Delta/ne$, where n is a positive integer and e is the absolute value of the electron charge, corresponding to multiple Andreev reflection processes indicated by blue markers.

We also explore the device in voltage bias, where we measure the differential conductance versus applied voltage on the electrostatic gate underneath the nanowire. Note that the lever arm of the gate is not comparable to that of the devices measured with microwave spectroscopy, due to a small gap in the gate-line, connecting to the bottom gate shown in Figure 6.5a. In the gate-dependence, Fig. 6.5c, we observe typical peaks corresponding to the superconducting gap Δ at $eV = \pm 2\Delta$, where V is the applied bias voltage and e the absolute value of the electron charge, (see Fig. 6.5d and additional information in Section 6.8.6) yielding $\Delta \sim h \cdot 48\,GHz \sim 202\,\mu eV$. Additionally, we observe peaks in conductance at voltages of $\Delta/2ne$, where n is a positive integer, corresponding to multiple Andreev reflections of order n, up to third order (blue indicators in Figure 6.5d). These are an indication of high junction transparency, consistent with the measurements of the microwave spectrum.

6.6 Discussion

In this work, we have performed microwave spectroscopy of Andreev bound states in an InSb-Al Josephson junction. In addition to the measurements discussed so far, we have studied the transition linewidths of the pair transitions, see Appendix 6.8.4, for various setpoints in device A, resulting in typical transition linewidths of $150 - 400\,MHz$ ($\sim 0.5 - 1.5\,\mu eV$) varying with V_g and the transition frequency. Moreover, we measured the dependence of the linewidth γ on gate and power for an additional device C and found

$\gamma \geq 2\pi \cdot 250\,\mathrm{MHz}$ minimal at extrema versus gate voltage (Appendix 6.8.4) consistent with the linewidth being charge-noise limited, as also suggested in a previous work (Hays et al., 2020). When saturating the transition with a strong drive pulse, we find relaxation times of around 4 µs, see Appendix 6.8.5. On the other hand, possibly due to the strong dephasing, we did not observe coherent Rabi oscillations and, consequently, we cannot extract a dephasing time for the pair transition.

A key technical challenge in this work was the integration of shadow evaporation with circuit-QED devices. In an earlier iteration of the devices, a Si_3N_4 hard mask deposited at room-temperature and patterned using liftoff was used for the Al etching step. However, in this way, the dielectric mask remains on the junction, which we suspect to contain trapped charges and thus noise close to the vital junction region. This in turn could cause ABS linewidths of up to several GHz, negating most advantages of embedding the junctions in a circuit-QED setup.

From additional DC transport measurement, we found a superconducting gap of around $\Delta/h \sim 48\,\mathrm{GHz}$ (see Section 6.8.6) while in the fit in Figure 6.3 to the microwave spectroscopy data yields an effective gap Δ^* smaller than Δ as often seen in microwave spectroscopy (van Woerkom et al., 2017; Hays et al., 2018, 2020; Tosi et al., 2019; Hays et al., 2021; Wesdorp et al., 2023, 2024). This has previously been thought to be caused by a reduced induced gap in the semiconductor (van Woerkom et al., 2017; de Moor et al., 2018; van Loo et al., 2023), a finite dwell time due to confinement (Beenakker and van Houten, 1992; Fatemi et al., 2022; Kurilovich et al., 2021) or finite junction length (Park and Yeyati, 2017; Tosi et al., 2019; Hays et al., 2020). We believe a combination of the latter two is the most likely explanation for the observed Δ^*, since we measured the data in Figure 6.3 close to pinch-off.

A finite junction length, however, also results in higher Andreev manifolds below Δ and accompanying intermanifold transitions. During the measurements performed in this work, we have not seen odd-parity intermanifold transitions at zero field. These transitions involving exciting a single quasiparticle are ubiquitously present in typical gate sweeps performed in InAs devices (Tosi et al., 2019; Wesdorp et al., 2024; Hays et al., 2020) with junctions of comparable length (150-500 nm). Although the cause of this discrepancy is presently unclear, there are multiple potential reasons. Since the elastic scattering length in InSb ($\sim 300\,\mathrm{nm}$ (Van Weperen et al., 2013)) is expected to be larger than for InAs ($\sim 100\,\mathrm{nm}$ (Doh, 2005)), the coherence length of the hybrid is also expected to be larger, assuming a dirty superconductor limit (Tinkham, 2015). Thus, the effective junction length relative to the coherence length is expected to be smaller for InSb. A shorter effective length may result in the InSb junctions acting akin to the short junction limit. Another possibility is that the quasiparticle lifetimes are not sufficiently long or the trapping and detrapping rates are too unbalanced to observe the odd-parity states and a detailed study of the quasiparticle dynamics in InSb junctions could further elucidate this aspect (Wesdorp et al., 2023; Fatemi et al., 2022). In the scanning electron micrographs of the devices (Figure 6.1d), it is visible that the junction has a thinner section Al of thickness around 8 nm near the junction due to a slight tilt of the walls causing the two deposition angles to have a different effective shadow mask. This junction geometry could lead to a larger gap near the junction, which could act as a barrier to quasiparticle poisoning events in the junction. Finally, it could be that the inter-manifold excitations are too short lived, with

corresponding too large linewidths, to be observed in this work.

6.7 Conclusion

We have demonstrated a proof of principle combination of superconducting circuits with in-situ shadow-wall evaporated InSb/Al Josephson junctions. We have found the addition of the shadow walls to not limit the resonator internal quality factor, thus opening up the path towards coherent superconducting qubits using these junctions similar to what has been shown using InAs/Al etched junctions (de Lange et al., 2015; Larsen et al., 2015). Furthermore, by investigating the pair transition spectrum of several devices, we found high transparency Andreev states over extended gate ranges, consistent with high-quality junctions. The high transparency is also confirmed by the observation of multiple Andreev reflections in a device characterized using DC transport techniques following the same fabrication flow. Additionally, by applying a magnetic field, we observe a direct spin-flip transition of the lowest Andreev manifold recently observed (Wesdorp et al., 2024; Metzger et al., 2021; Bargerbos et al., 2023a) and manipulated (Pita-Vidal et al., 2023a) in InAs devices. From DC characterization measurements, we find that the supercurrent remains finite until ~ 200 mT. Combined with the large effective g-factors, this opens up the path towards Andreev spin qubit experiments in InSb (Wesdorp et al., 2024; Hays et al., 2021; Pita-Vidal et al., 2023a), although further work is needed to test the achievable lifetimes in InSb. Our work also demonstrates important ingredients needed to embed current efforts towards artificial Kitaev chains (Leijnse and Flensberg, 2012; Dvir et al., 2023; Bordin et al., 2023), or Andreev molecules (Pillet et al., 2019; Kornich et al., 2019; Matsuo et al., 2023; Su et al., 2017), into superconducting circuits. Our work thus opens up for such experiments to benefit from the energy resolution as well as a large body of well-developed control and measurement techniques offered by superconducting circuits.

6

6.8 Supplementary information

6.8.1 Methods

Device information

For this work we measured 8 microwave devices and 2 DC devices on 2 identically designed chips (see Figure 6.6) in separate cooldowns for the data presented in the main text, using a soft etching mask for the Al etching step as described in the main text. Furthermore, we initially measured 8 other devices on two chips in two cooldowns with a hard etch mask as described in the discussion. The device overview is summarized in the Table 6.1.

Circuit parameters

We now explain the procedure used to extract the device parameters (see Figure 6.7 for the circuit diagram). From COMSOL simulations we estimate the capacitance $C_r \sim 47\,\text{fF}$. The inductance is set by the length and width of the inductors and the kinetic sheet-inductance L_k of the chip (Annunziata et al., 2010). We used nominally 300 nm wide and 22 nm thick NbTiN inductors. The resonator frequency was designed by varying the number of meanders and thus the total inductor length, the capacitance was kept the same for all devices to facilitate relative frequency targeting. By matching the measured resonance frequency in pinch-off (see Figure 6.13) to the calculated value from the designed inductor dimensions and simulated capacitance C_r we estimate L_k, which varied between the chips and was found to be $\sim 9.3\,\text{pH}/\square$ for chip 1 and $\sim 8.4\,\text{pH}/\square$ for chip 2. We then used these values of L_k to estimate the shunt-inductance per arm of the rf-SQUID and resonator series inductance, which was $L_s = 1.5\,\text{nH}, L_r = 28.68\,\text{nH}$ for device B and $L_s = 0.72\,\text{nH}, L_r = 18.75\,\text{nH}$ for device A. These are the values used to determine the resonator shift in Equation (2.36).

Name	Chip legend	l_{JJ}	FB
device A	Chip 2 rf-C	150 nm	no
device B	Chip 1 rf-B	300 nm	no
device C	Chip 1 rf-D	150 nm	yes
device D	Chip 2 DC-A	150 nm	-
device E	Chip 1 DC-A	150 nm	-

Table 6.1: Main measured devices and their properties. We measured additionally 5 microwave devices not listed here, for which we show SQUID oscillations and pinch-off data in Figures 6.11 and 6.12
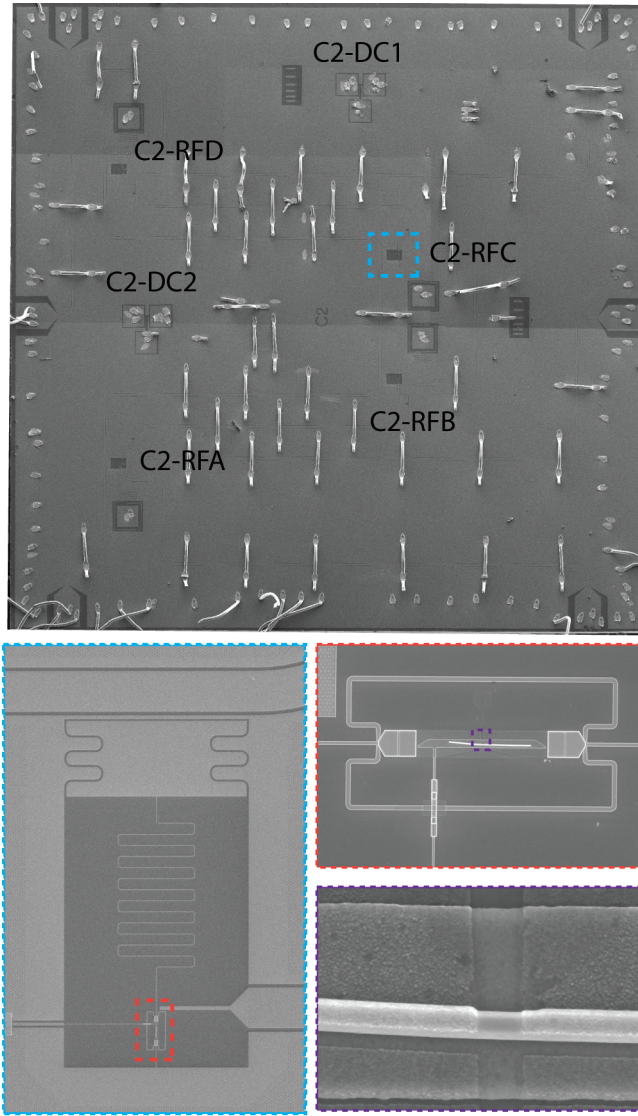
Figure 6.6: Additional device images without false coloring. From top to bottom: stitched scanning electron-micrographs of chip 2 measured after unbonding. The devices are labeled corresponding to the legend shown in Table 6.1. The chip contains 6 RF input ports. Two for the readout input and output line and two for the drive-line that is coupled to all devices capacitively. Additionally there are two input ports for the on-chip flux bias lines. Bottom panels electron micrographs of device A (C2-RFC) located on this chip indicated with the blue dashed square.

Measurement setups

Chip 1, containing device B and C was measured in a *Leiden cryogenics* dilution refrigerator with the setup shown in Figure 6.8 and Chip 2, containing device A and D, in an *Oxford*
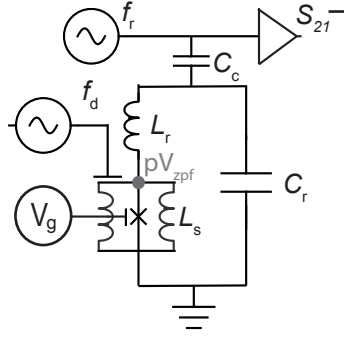
Figure 6.7: Circuit diagram of an microwave device with relevant parameters indicated. The resonator consists of a capacitance C_r and inductance L_r put in series with an RF squid loop containing the JJ. Also indicated are the readout line, gate line and drive line.

Triton dilution refrigerator with the setup shown in Figure 6.9 at approximately 20 mK base temperature. Both setups had a 6-1-1 T vector magnet installed, which was anchored to the 4K stage (not shown). The x and y axes of the vector magnet were controlled with a *Yokogawa GS610* current source for fine control. The chip was connected to 6 RF lines, two for the feedline input and output and two for the drive line input and output that was used to drive all four devices. Two additional RF lines were connected to on-chip flux bias lines which were controlled using a *Yokogawa GS200* current source. Spectroscopy measurements were performed using a *R&S ZNB20* vector network analyser connected to the input and output lines. One port of the the driveline was connected to a high frequency microwave source *Agilent E8267D* or *R&S SMA100B*.

The device enclosure contained the chip, glued using silver-epoxy on to a gold-plated copper block and bonded to a custom made printed circuit board, which were embedded in the copper device enclosure filled with ecosorb foam. The DC lines were additionally filtered on the PCB with low-pass π-filters.
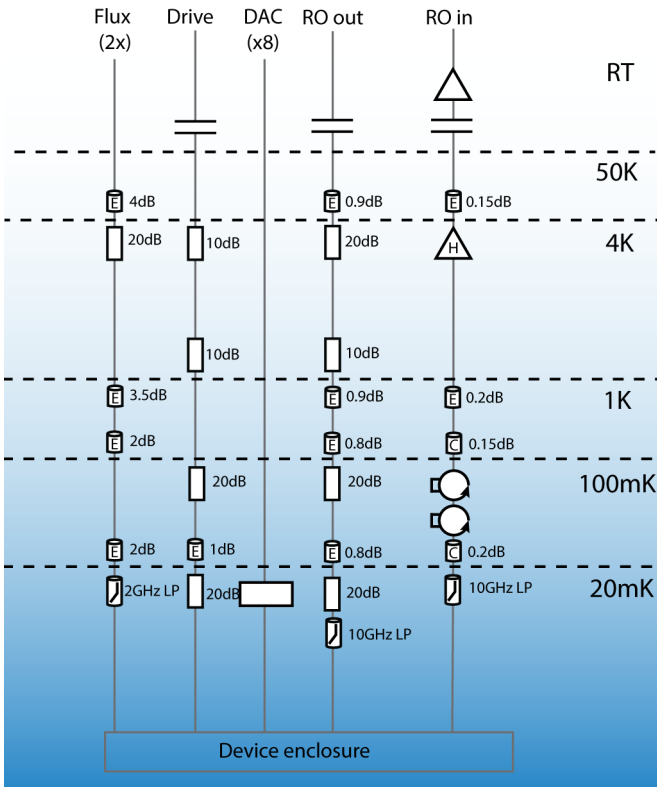
Figure 6.8: Cryogenic wiring diagram of setup 1 used to measure chip 1. At every temperature stage custom made ecosorb filters (E) and copper powder filters (C) were embedded in the feedthroughs of which the attenuation is specified at 10 GHz. The second flux line (not shown) had less strong ecosorb filters with average attenuation of 0.5dB at 10 GHz

Figure 6.9: Cryogenic wiring diagram of setup 2 used to measure chip 2. Ecosorb filters are indicated with dB/GHz. Low pass filters (LP) are indicated with their cutoff frequency. The output signal is amplified by a *Lincoln Labs* traveling wave parametric amplifier (T), a *LNF* 4-8GHz HEMT anchored to the 4K plate and a *Mitec* 30dB, 0.1 − 8 GHz room temperature amplifier.
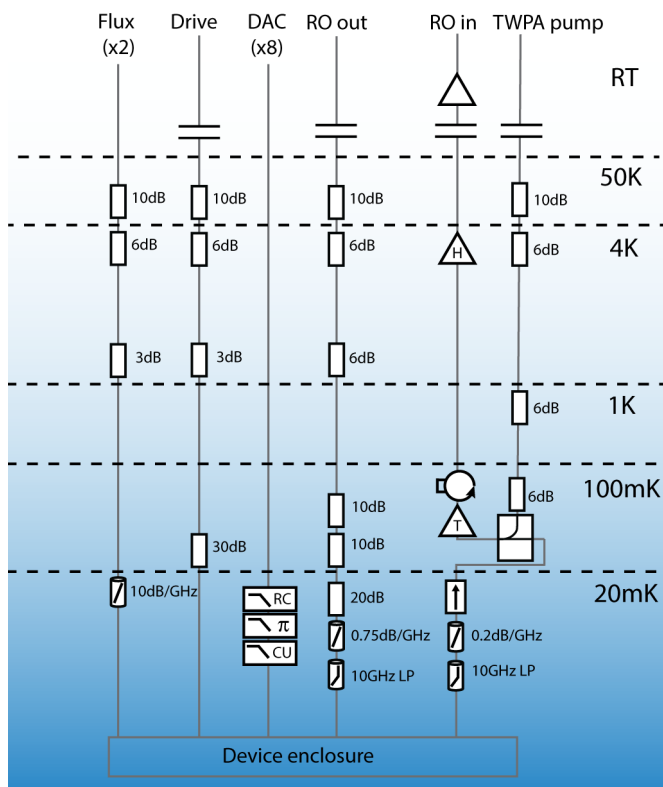
Signal processing

Spectroscopy data. For the two-tone spectroscopy data of this work we measure the complex signal S_{21} with a vector network analyser at a readout frequency f_{r} that is set close to the resonator frequency f_0. To obtain $\delta\mathrm{Re}S_{21}$ we rotate the complex S_{21} in the I-Q plane by maximizing the variance of each frequency sweep (vertical linecut) in the real part. We then subtract a background which is equal to the median value of each vertical linecut to compensate for the variation of readout frequency and only display the change in readout signal due to driving of transitions. For the higher frequency spectroscopy sweeps shown in the supplement we additionally subtract a horizontal background, i.e. the median of the data in the V_{g} direction when indicated with $\delta\mathrm{Re}\{\bar{S}_{21}\}$ to effectively filter out circuit resonances which appear as horizontal lines in the spectra and increase the relative visibility of the dispersing ABSs.
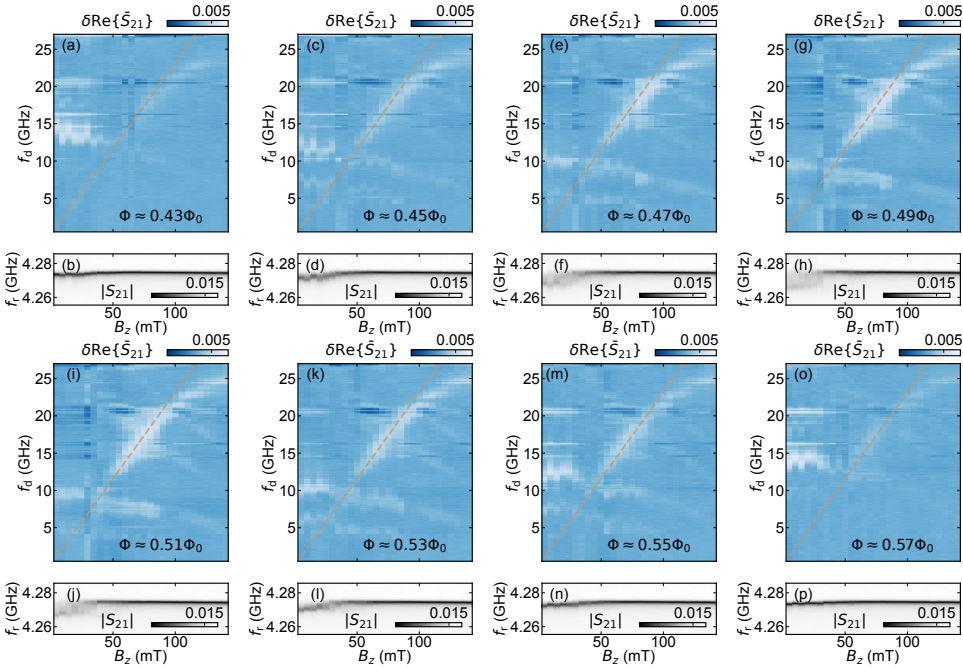

Figure 6.10: Extended data for the spin-flip transition. Here we show additional data for other flux values, other than that which was shown in Figure 6.4. (a-o) Two-tone spectroscopy with horizontal background subtraction for the flux values indicated. (b-p) Accompanying single-tone data. The dashed lines indicate the fitted linear slope of the spin-flip transition extracted from the data of Figure 6.4 at $\Phi \approx 0.5\Phi_0$.

Processing for Figure 6.3. We measured for each value of B_z a spectroscopy versus Φ around $\Phi = 0.5\Phi_0$, because sometimes flux jumps occurred during the steps in B_z. We then defined $\Phi = 0.5\Phi_0$ by setting it equal to the flux value at the minimum of the pair transition, which was extracted by hand after visual inspection of the spectra. These linecuts at $\Phi = 0.5\Phi_0$ for each B_z are shown in Figure 6.3. In Figure 6.10 we show the resulting spectra

for values other than $\Phi = 0.5\Phi_0$.
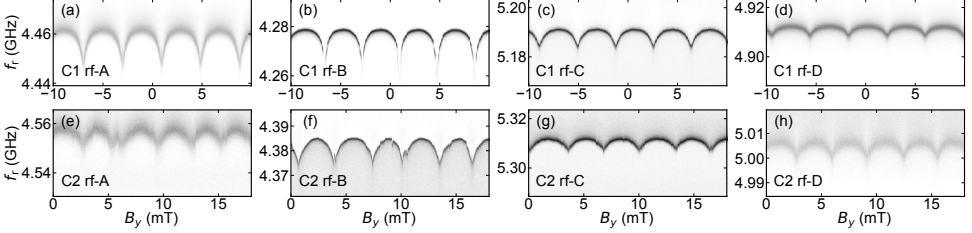
6.8.2 Basic characterization

Figure 6.11: SQUID oscillations in all microwave devices of chip 1 (a-d) and chip 2 (e-f).

Flux characterization In order to test whether an microwave device is functional we monitor the resonator frequency as a function of applied flux Φ at fixed V_g in the open regime. Flux is applied using in-plane field B_y which is perpendicular to wire axis (Wesdorp et al., 2024), to mitigate flux jumps seen when applying perpendicular field B_x as is the more usual approach. The loop is thus defined vertically upwards from the chip plane and the size is approximately defined by the height of the dielectric ($\sim 28\,\text{nm}$) times twice the length of the gate ($\sim 10\,\mu\text{m}$), resulting in an effective area of $0.56\,\mu\text{m}$ and expected flux periodicity of $\sim 3.7\,\text{mT}$. Each microwave devices measured showed SQUID oscillations as depicted in Figure 6.11 with similar flux periods. All devices in chip 1 (a-d) and chip 2 (e-f) show clear SQUID oscillations demonstrating high junction yield. Measurements were performed with the junctions open ($V_g = 0$ for chip 1 and $V_g = 500\,\text{mV}$ for chip 2). A parallel field of 12 mT was on to reduce flux jumps resulting from superconducting bond wires for the measurements of chip 1. For chip 2 the measurements were performed at $B_z = 0$ illustrating occasional jumps.

Gate characterization The presence of Andreev states is then detected by inspecting the gate dependence at $\Phi = 0.5\Phi_0$. The gate response is shown in Figure 6.12. Devices are generally open at $V_g = 0$, but show considerable variation in pinch-off Voltages. From the resonator response with the nanowire in pinch-off we extract the internal and external quality factor in Figure 6.13 by fitting S_{21} to a general assymetric resonance lineshape defined in Khalil et al. (2012).
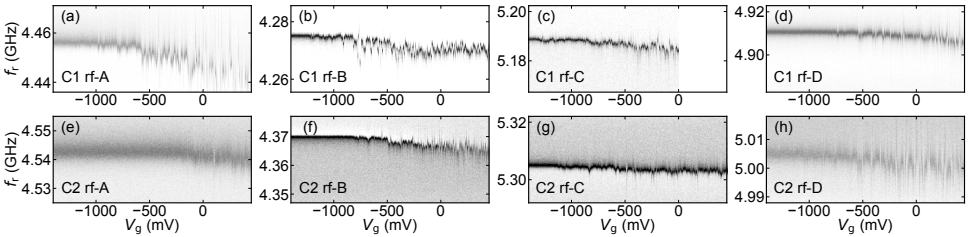

Figure 6.12: Pinch-off curves taken at $\Phi \sim 0.5\Phi_0$ for all rf-devices of chip 1 (a-d) and chip 2 (e-f). Data for C1C was not measured beyond $V_g = 0$.
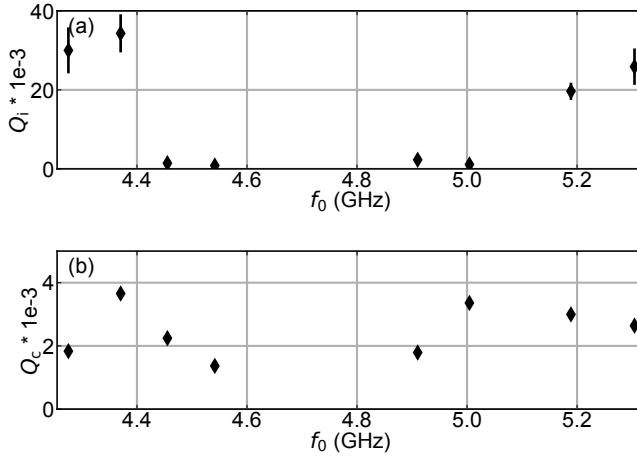
Figure 6.13: Summary of resonator properties. (a) extracted internal quality factor Q_i and resonance frequency f_0 from the data shown in Figure 6.12 near pinch-off. (b) Extracted coupling quality factor for the same resonators. For both panels, the markers and errorbars indicate the average extracted value and standard deviation of Q_i or Q_c for the first 10 gate voltages in the pinch-off curves, respectively.

6.8.3 Theory of flux-dependence and additional data

Description of coupling between the resonator and a single ABS in the short junction limit

The fit performed in Figure 6.3 to a single channel short junction model (Beenakker, 1991), although simplistic, was found to match the data well. In Section 2.3.2 we describe the theory used to estimate the shift of the resonator mode using the current and inductance operators derived for a single channel short junction in Refs. (Zazunov et al., 2003; Bretheau, 2013).

This shift, calculated using the extracted circuit parameters from Section 6.8.1 is what is overlayed over the resonator measurements in for Figure 6.3(b) and Figure 6.15(b).
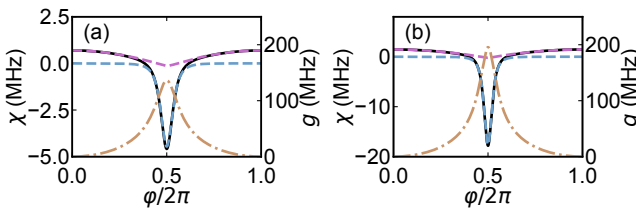

Figure 6.14: Theoretical dispersive shifts and coupling strength based on the parameters of device A, B and the fitted Andreev states in the flux dependence. The inductive shift (purple dashed line) and dispersive shift (blue dashed line) yield the total resonator response χ as described in Equation (2.36) (black line). Additionally we show the expected coupling strenght g (brown alternating dashed dotted line). (a) results for device A. (b) results for device B.
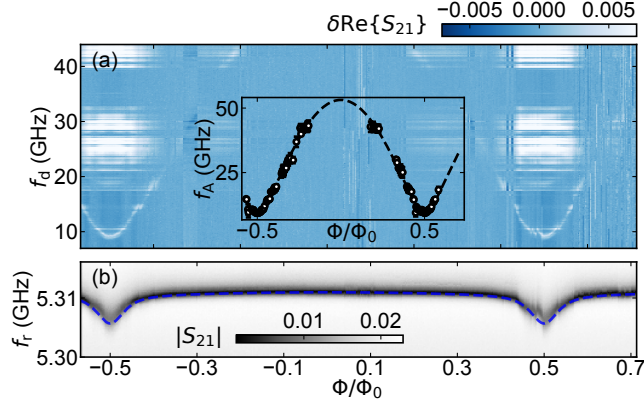
Figure 6.15: Flux dependence of device A, at $V_g = -661.5$ mV. (a) Two-tone spectrum and fit to Equation (6.1). Extracted parameters are $\tau = 0.968, \Delta/h = 26.6$ GHz. (b) Resonator spectroscopy measured interleaved with the spectrum. Blue dashed line indicates the expected resonator shift due to the ABS transition fit in (a), see Equation (2.36) and the fitted parameters from (a). The discontinuities most prominently visible at $\Phi = 0.5\Phi_0$ correspond to small flux jumps that occured during sweeping of the field for this dataset.

Flux dependence of device A at low gate voltage

For device A, we have shown a gate dependence of the spectrum in Figure 6.2 and Figure 6.23. In Figure 6.15 we measure the flux-dependence of the spectrum at $V_g = -661.5$ mV near a local maximum in the ABS transparency at an isolated resonance in gate voltage (see Figure 6.2). We again fit to Equation (6.1) the extracted transition frequency, similar to Figure 6.3. Interestingly, we again find that the total resonator shift from Equation (2.36) for the fit ABS transition matches the observed shift well. Note that the bare-resonator frequency here was calculated by subtracting the inductive shift from the value extracted at $\Phi = 0$ instead of being taken from the pinch-off curves.

6.8.4 Estimates of the linewidth from spectroscopy of the pair transition

In Figure 6.16 we show linewidths extracted at the lowest possible power for device A. To extract the linewidth, we fit a Lorentzian function of the form

$$y(f_d) = \frac{a}{\pi} \frac{(\sigma/2)}{(f_d - f_0)^2 + (\frac{\sigma}{2})^2} + b \tag{6.2}$$

to Re$\{S_{21}\}$ of a frequency sweep to extract the linewidth $\gamma = 2\pi\sigma$, where f_0 is the center frequency of the transition, a, b are a scaling and offset respectively to normalize the data. Note that for some points, we had to manually pick the lowest possible power after visual inspection of the fit quality. For too low power, the fitting failed due to low signal to noise ratio of the data. Thus, this extraction results in an upper bound on γ.

For device C we measure a power dependence versus applied gate voltage and extract the linewidth of the lowest frequency pair transition in a small gate range around an
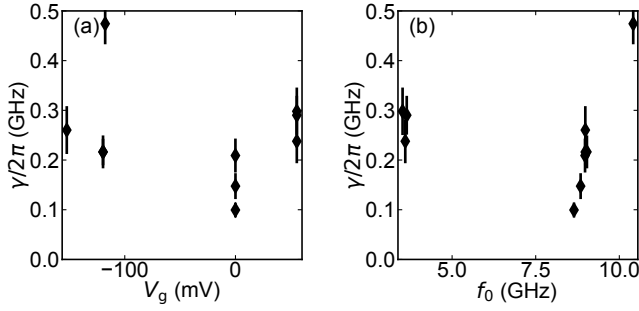
Figure 6.16: Extraction of transition linewidth of the lowest Andreev pair transition in device A at low power extracted from various measured power dependencies in spectroscopy. See text for the extraction procedure. Panel (a) shows the extracted linewidth γ versus gate setting, while panel (b) shows the same data versus the pair transition frequency.
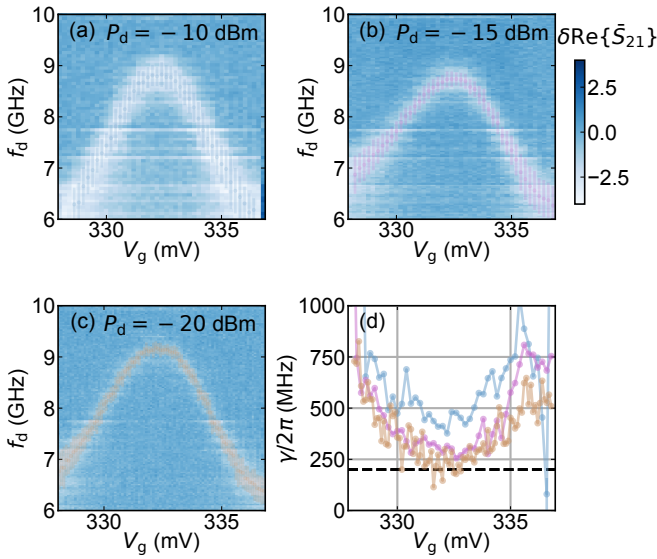
Figure 6.17: Linewidth extracted versus gate at various drive-power settings for device C. Panels (a-c) show spectroscopy versus V_g with Lorentzian fits to Equation (6.2) results on top of the data. (d) Extracted linewidths for data in panels (a-c) with corresponding colors. Dashed black line is a guide to the eye for $\gamma/2\pi = 200\,\mathrm{MHz}$

.

extremum in gate Figure 6.17. Since the linewidth increases with increasing df/dV_g, the linewidth in this device is to a large extend limited by charge noise.

6.8.5 Partial time-domain characterization

In an attempt to characterize the lifetime of the pair transition of device C, we use a Quantum Machines OPX to IQ-modulate the readout and drive tones with baseband pulses in Figure 6.18 with a room-temperature setup nearly identical to Pita-Vidal et al. (2023b). We investigate the pair transition in gate regime shown in Figure 6.18a,b at $\Phi = 0.5\Phi_0$. We then fix the pair transition at around 9 GHz (see Figure 6.18c). The decay time is measured by applying an upconverted saturation pulse resonant with the pair transition followed by a ∼ 1 µs readout pulse on the resonator. From the exponential decay of the signal, we extract a decay time of $T_{\text{decay}} \sim 4.1\,\mu s$. This decay time is on the similar to lifetimes of the Andreev pair qubit observed in earlier works on InAs (Hays et al., 2018; Janvier, 2016). On the other hand, we observe no clear Rabi oscillations when varying the pulse time and amplitude at a fixed frequency. Instead, we see a signal that saturates with increasing pulse lengths and higher amplitudes. A typical example versus pulse length and drive frequency at fixed amplitude is shown in Figure 6.18e, where the response is strongest on resonance with the pair transition at 9.05 GHz. Without the unambiguous observation of Rabi oscillations, we cannot rule out that the observed decay time could also correspond to the parity lifetime if the strong drive causes a change in parity as observed recently in Wesdorp et al. (2023). The absence of quasiparticle poisoning observed without a drive tone at most gate setpoints in device A, although beneficial for device operation, prohibited the individual extraction of these lifetimes.

The measured transition linewidth in spectroscopy of around ∼ 150 MHz gives an lower bound on the intrinsic dephasing time of the pair transition and corresponds to $T_2^* \geq 1\,\text{ns}$, which could explain the lack of visible Rabi oscillations with ns-long pulses. For shorter pulses, the required power to see saturation could cause population of the readout resonator from leakage in the I-Q modulation unit. As such, we were not able to obtain a signal for the high power settings.

6.8.6 Supplementary DC transport

To complement the microwave characterization, we report on measurements of 150 nm wide junctions (device D, E) that saw the same fabrication flow in DC transport (see Figure 6.5 for a device image). As stated in the main text, the bondpad to the gate underneath the nanowire had a small gap, resulting in a much lower lever arm of the gate for the DC devices compared to the microwave devices.

Superconducting gap extraction

We extract the superconducting gap Δ by extracting the 2Δ peak in a voltage biased measurement (see Figure 6.19). The peak is extracted by the following procedure: We first smooth the data using a Gaussian filter, followed by subtracting a mean background. Then we normalize the data to the maximum signal of the conductance found within a range of about 0.3 meV and specify the gap as the first value coming from positive (negative) bias that reaches a threshold percentage of the maximum conductance. The threshold was set such to find the peak at the onset of the peak. The extracted Δ in Figure 6.19 decreases with gate, consistent with what is observed in previous work (van Loo et al., 2023). To heuristically account for the variation with gate voltage, the value of Δ quoted in the main text is taken as the average of the V_{g} dependence shown as a dashed line in Figure 6.19b.
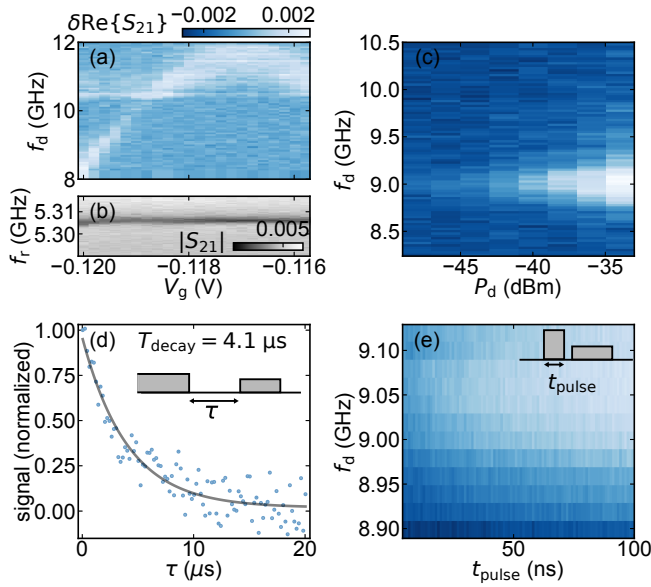
Figure 6.18: Partial time domain characterization in device A at $\Phi = 0.5\Phi_0$. (a,b) Gate dependence in spectroscopy of the pair transition near the setpoint. (c) Power dependence of the transition at $\sim 9\,\text{GHz}$. (d) Decay time measurement in which a long saturation pulse is followed by a measurement after waiting a time τ (see inset). (e) Typical Rabi experiment versus carrier frequency, where the length t_{pulse} of a drive pulse resonant with the pair transition at fixed amplitude is followed directly by a readout pulse (see inset).

6

Additional supercurrent data

The maximum switching current observed in DC transport in device D was $I_{\text{sw}} \sim 18\,\text{nA}$, as visible in the gate dependence of Figure 6.20a and the linecut in Figure 6.20b. In a second DC device (device E) we only measured up to $V_g = 0$ and obtained $I_{\text{sw}} \sim 9\,\text{nA}$, shown in Figure 6.20c.

6.8.7 Supplementary gate dependence of the ABS spectrum

In this section we show additional spectroscopy datasets varying the gate voltage underneath the nanowire while at $\Phi \sim 0.5\Phi_0$. These devices were selected for further investigation as they showed the highest quality (lowest linewidth) ABS pair transitions. The data shown in Figure 6.3 and Figure 6.4 was measured on device B. The corresponding gate dependence (see Figure 6.21) measured at vanishing magnetic field and at $\Phi \sim 0.5\Phi_0$ shows a similar trend as in device A. Near pinch-off, isolated resonances and a single low-lying pair transition (i.e. a single ABS doublet) is visible and at more positive gate voltage multiple ABSs come into the measurement range consistent with more conduction channels opening up in the nanowire. Note that in additions to pair transitions that excite a single ABS manifold, some pair transition could be corresponding to excitations of distinct ABS manifolds as identified recently in Refs. (Matute-Cañadas et al., 2022; Wesdorp et al., 2024). Additionally, we show a second dataset measured up to higher frequencies of device A to complement the data shown in Figure 6.2.
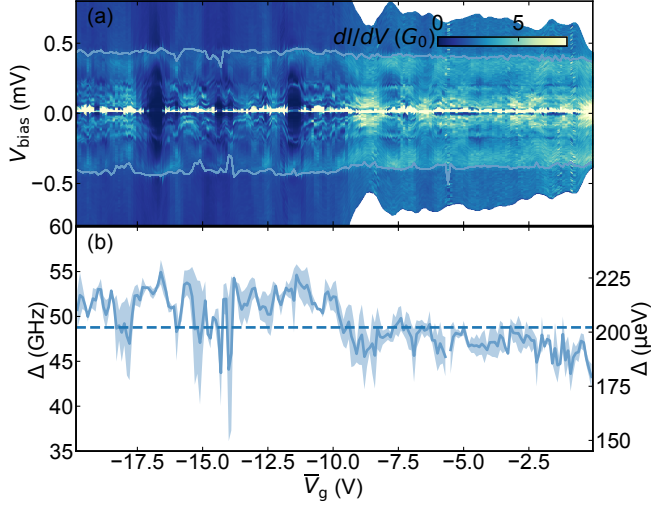
Figure 6.19: Extracted from the DC transport measurement. (a) Same data as presented in Figure 6.5 with the extracted gap overlayed. (b) results of extracted gap. Shadow indicates the difference between the extracted gap for positive and negative bias voltage. The dashed line indicates the mean of the data corresponding to a value of $\Delta \sim 48\,\text{GHz} = 202\,\mu\text{eV}$

6
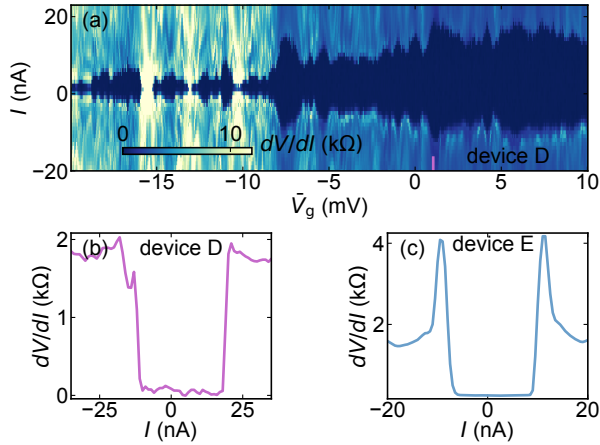
Figure 6.20: Switching current in device D, E. (a) gate dependence of device D in same range as Figure 6.19. (b) linecut at maximal supercurrent illustrated with the same colored marker in (a). (c) current bias measurement at $V_g = 0$ in an additional DC device (device E on chip 1)
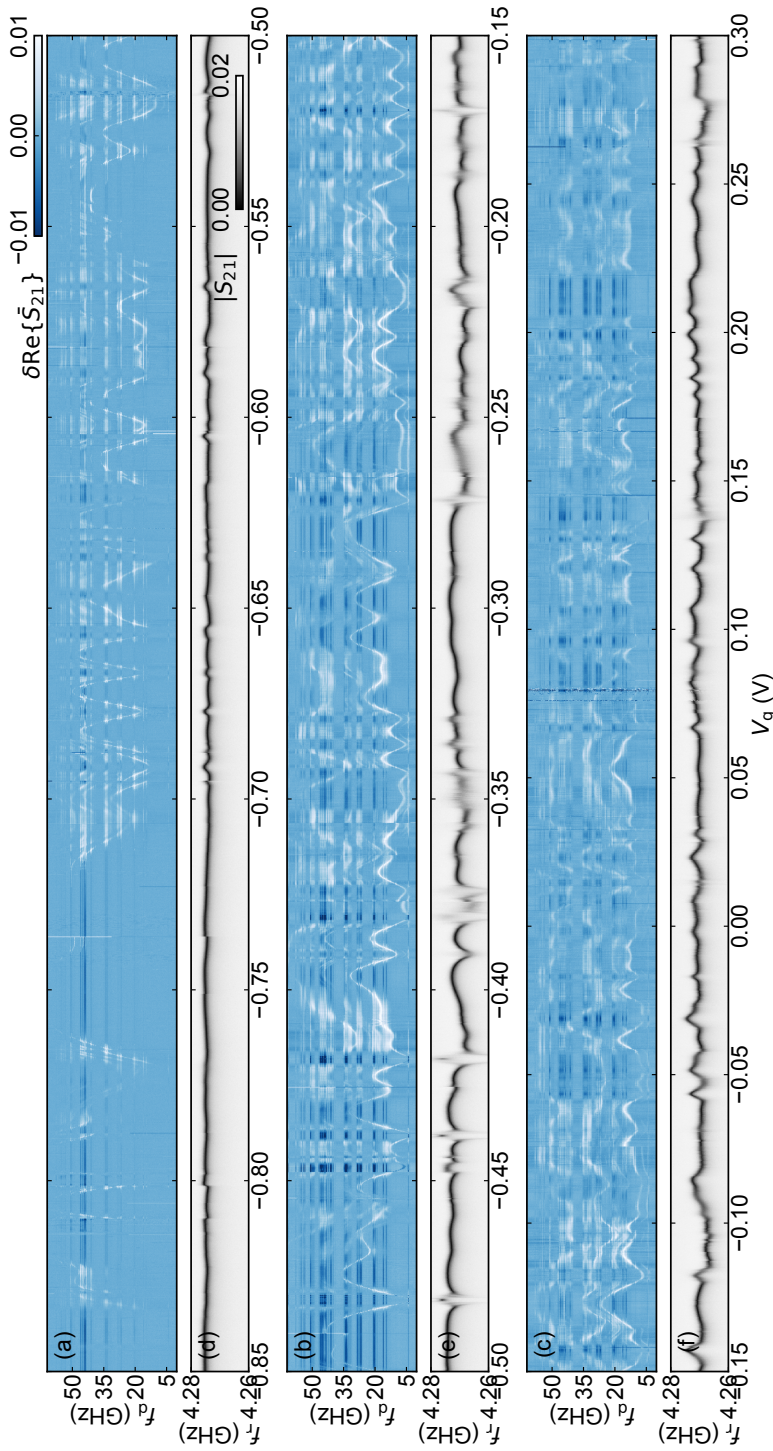
Figure 6.21: Gate dependence device B at $\Phi \sim \Phi_0/2$. Note the data of (b,c) was measured first from negative to positive before sweeping the gate back and measuring (a).
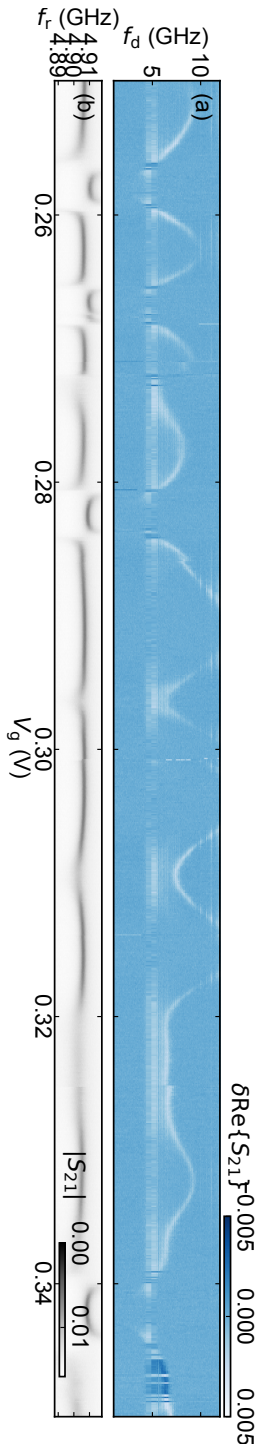
Figure 6.22: Gate dependence of device C at $\Phi \sim \Phi_0/2$.
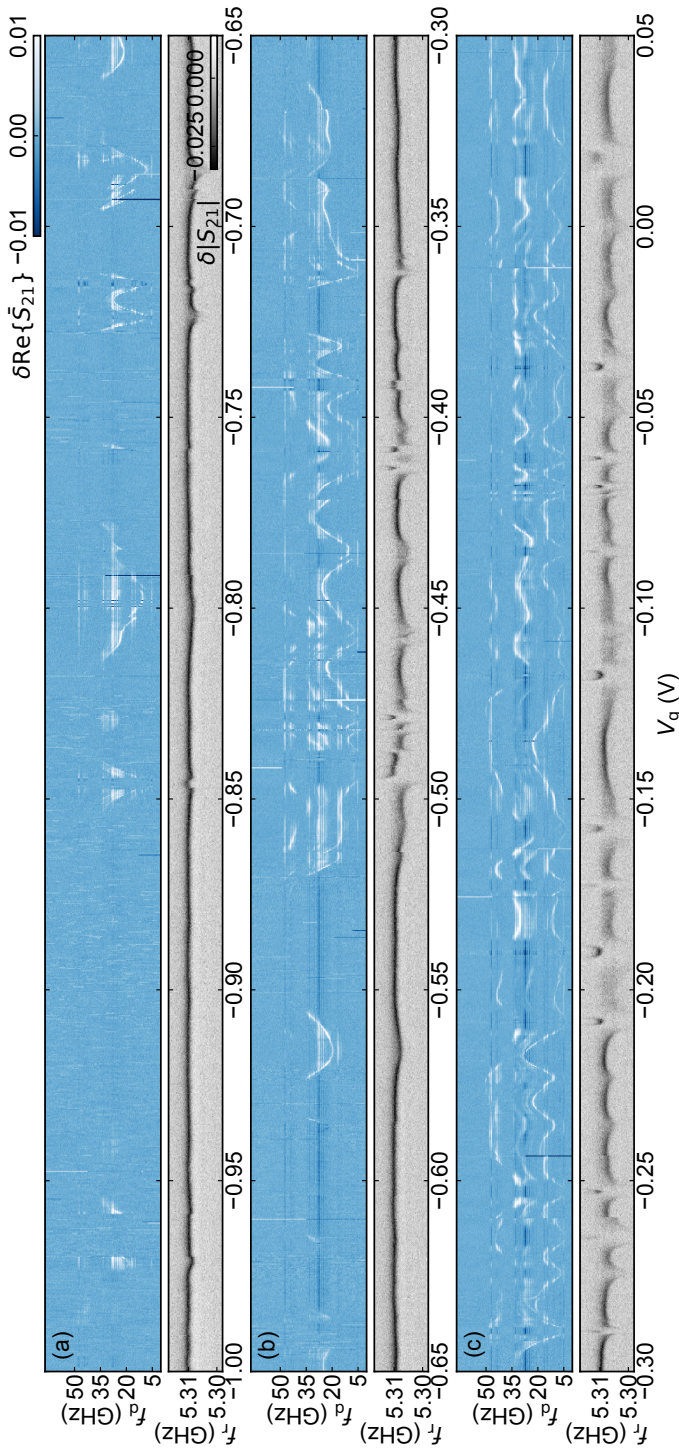
Figure 6.23: Higher range gate sweep of device A. For the single-tone traces we show $\delta|S_{21}|$ indicating that we subtracted a background that does not vary with gate voltage and comes from the travelling wave parametric amplifier.

6.9 Acknowledgements

6.10 Data availability

Data, processing and scripts for the presented figures will be made available online

6.11 Author contributions

JJW, CKA, LPK conceived the experiment. CKA, LPK supervised the project. PR, JJW, AV designed the devices with input from all coauthors. PR, JJW, AV measured the data on the presented round of devices and earlier iteration of devices with a hard mask with input from LJS, MPV, AB and CKA. JJW, PR performed the data analysis with input from LJS, MPV, AV, AB, NVL, GM and CKA. JJW, PR, MPV fabricated the devices. NVL deposited the nanowires. JCW, GM, NVL deposited the Al films. JJW, CKA wrote the manuscript with input from all coauthors.

6

7

Strong tunable coupling between two distant superconducting spin qubits

Superconducting (or Andreev) spin qubits have recently emerged as an alternative qubit platform with realizations in semiconductor-superconductor hybrid nanowires (Hays et al., 2021; Pita-Vidal et al., 2023a). In these qubits, the spin degree of freedom is intrinsically coupled to the supercurrent across a Josephson junction via the spin-orbit interaction, which facilitates fast, high-fidelity spin readout using circuit quantum electrodynamics techniques (Hays et al., 2020). Moreover, this spin-supercurrent coupling has been predicted to facilitate inductive multi-qubit coupling (Chtchelkatchev and Nazarov, 2003; Padurariu and Nazarov, 2010). In this work, we demonstrate a strong supercurrent-mediated coupling between two distant Andreev spin qubits. This qubit-qubit interaction is of the longitudinal type and we show that it is both gate- and flux-tunable up to a coupling strength of $178\,\mathrm{MHz}$. Finally, we find that the coupling can be switched off in-situ using a magnetic flux. Our results demonstrate that integrating microscopic spin states into a superconducting qubit architecture can combine the advantages of both semiconductors and superconducting circuits and pave the way to fast two-qubit gates between remote spins.

7

7.1 Introduction

Semiconducting spin qubits (Hanson et al., 2007; Loss and DiVincenzo, 1998) have proven to be a promising platform for quantum information processing. In such qubits, quantum information is encoded in the spin degree of freedom of electrons or holes localized in quantum dots, which leads to long lifetimes and a naturally large energy separation between computational and non-computational states. Moreover, their small size makes them attractive candidates for large-scale quantum devices (Vandersypen et al., 2017; Burkard et al., 2023). However, it remains challenging to engineer a direct spin-spin coupling between remote spin-qubits as their interaction strength decays rapidly with distance. Ongoing efforts to overcome this challenge focus on engineering a coupling between distant spin-qubits mediated by microwave photons in superconducting resonators (Mi et al., 2018; Landig et al., 2018; Samkharadze et al., 2018; Borjans et al., 2020; Harvey-Collard et al., 2022; Yu et al., 2023). For such photon-mediated spin-spin coupling, the interaction strength is currently limited to the order of 10 MHz, which makes the implementation of fast, long-range two-qubit gates an outstanding challenge (Harvey-Collard et al., 2022; Burkard et al., 2023). Moreover, the transverse character of the coupling puts a constraint on the available qubit frequencies.

An alternative approach to engineer remote spin-spin coupling is to embed the spin-qubit into a Josephson junction creating a so-called Andreev spin qubit (ASQ) (Hays et al., 2021; Pita-Vidal et al., 2023a), where the qubit states carry a spin-dependent supercurrent [Tosi et al. (2019); Hays et al. (2020), Chapters 4, 5, Hays et al. (2021); Bargerbos et al. (2023a); Pita-Vidal et al. (2023a)]. Recent experiments have demonstrated that a single ASQ can be operated coherently with strong coupling of the spin states to superconducting circuits (Hays et al., 2021; Pita-Vidal et al., 2023a). Similarly, it has been predicted that large spin-dependent supercurrents can lead to strong, longitudinal, long-range and tunable spin-spin coupling (Chtchelkatchev and Nazarov, 2003; Padurariu and Nazarov, 2010), thus, overcoming the challenges imposed by the coupling being only a second-order interaction in previous photon-mediated implementations of spin-spin coupling as well as circumventing any strong constraints on the qubit frequencies.

Here, we investigate the supercurrent-mediated coupling between two ASQs by analyzing the influence of a shared Josephson inductance on the coupling strength using the setup in Fig. 7.1. Specifically, we design a device formed by two Andreev spin qubits, ASQ1 and ASQ2, connected in parallel to a third Josephson junction with gate-tunable Josephson inductance, thus defining two superconducting loops (Fig. 7.1a). Microscopically, the longitudinal coupling between the qubits directly results from the main characteristic of Andreev spin qubits: their spin to supercurrent coupling. The state-dependent supercurrent of one qubit results in a spin-state-dependent circulating supercurrent through the loop arm containing the other qubit. We show that the qubit-qubit coupling in this configuration can be in-situ controlled by the flux through the superconducting loops as well as by changing the Josephson inductance of the shared junction using an electrostatic gate. In particular, we reach the strong longitudinal coupling regime where the coupling strength is larger than the qubit linewidths. Moreover, we show that the coupling can be switched fully off for particular values of the flux, which makes this platform appealing as an alternative for implementing fast flux-controlled two-qubit gates between spin qubits.
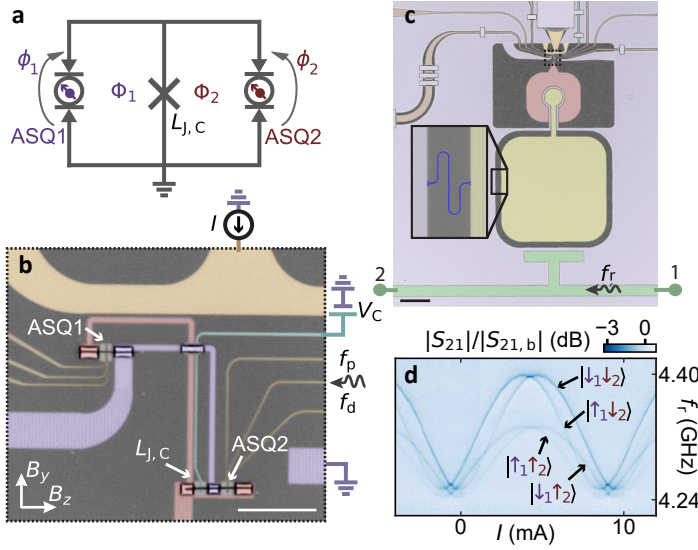
Figure 7.1: **Device and readout. a** Circuit diagram of two coupled Andreev spin qubits (ASQ1 and ASQ2) connected to a coupling junction with a tunable Josephson inductance $L_{J,C}$. Φ_1 and Φ_2 are the magnetic fluxes through the two loops. **b** False-colored optical microscope image of the device. The ASQs are placed between a transmon island (red) and ground (purple). The three Josephson junctions are implemented in two separate Al/InAs nanowires, with one containing ASQ1 and the other containing ASQ2 and the coupling junction. The in-plane magnetic field directions are denoted as B_z and B_y, approximately parallel and perpendicular to the nanowires axis, respectively. Additional flux control is achieved through the applied current I in the flux line (amber). Each ASQ is electrostatically controlled by three gates below the nanowire (brown), while the coupling junction is controlled by one gate line (cyan) at voltage V_C. The drive tones f_d and f_p are applied through the central gate of ASQ2. See the Supplementary Information(Section 7.7) for further details about the geometry of the loops area. **c** Zoomed out false-colored optical microscope image showing the transmon island (red) capacitively coupled to a lumped-element readout resonator, consisting of a capacitor (yellow) and an inductor (blue, inset). The resonator is further capacitively coupled to a coplanar waveguide (green center conductor) with input and output ports labeled as 1 and 2, respectively. A readout tone f_r is applied through the waveguide. Scale bars in **b** and **c** correspond to $10\,\mu$m and $100\,\mu$m, respectively. **d** Amplitude of the transmission through the readout circuit, $|S_{21}|$, divided by the background, $|S_{21,b}|$, as a function of the current through the flux line, I. The measurement is performed at a magnetic field of $B_z = 0$ with a fixed $\Phi_2 \sim -\Phi_0/4$, set by $B_y = -1.04\,$mT.

7.2 Device

In our device, each ASQ is hosted in a quantum dot Josephson junction which is implemented in a separate Al/InAs nanowire and controlled by three electrostatic gates placed beneath the nanowires (Fig. 7.1b). Throughout this work, the gate voltages are fixed as specified in the Supplementary Information (Section 7.7). Moreover, we define an additional regular Josephson junction with gate-tunable Josephson inductance $L_{J,C}$ in one of the nanowires. The nanowires are galvanically connected to a NbTiN circuit which defines the superconducting loops forming a double-loop superconducting quantum interference device (SQUID). We denote by Φ_1 and Φ_2 the external magnetic fluxes through each of the loops. The qubit frequency for ASQi, f_i, where $i = 1, 2$, is set by the energy difference between the spin-states, $|\uparrow_i\rangle$ and $|\downarrow_i\rangle$, which is controlled by the magnetic field due to the Zeeman effect. We denote the in-plane magnetic field directions as B_z, approximately

along the nanowires, and B_y, approximately perpendicular to the nanowires. See also Supplementary Information (Section 7.7) for additional details on the field alignment. The B_y component of the magnetic field is moreover used to tune Φ_1 and Φ_2. Note that, while B_y is applied in the chip plane, it still threads flux through the loops due to the elevation of the nanowires with respect to the NbTiN circuitry. This reduces flux jumps compared to using out-of-plane field B_x for flux tuning, as discussed in Chapter 3. Φ_1 and Φ_2 set the phase drops over the junctions, $\phi_1 \sim \frac{2\pi}{\Phi_0}\Phi_1$ and $\phi_2 \sim \frac{2\pi}{\Phi_0}\Phi_2$ in the limit of small $L_{J,C}$, where Φ_0 denotes the magnetic flux quantum. The current through the flux line, I, tunes Φ_1 and leaves Φ_2 nearly unaffected, as the loop corresponding to Φ_2 is placed near the symmetry axis of the flux line (see Supplementary information (Section 7.7)). The drive pulses, with frequencies f_d and f_p, are sent through the central gate of ASQ2 and are used to drive both qubits. We find that it is possible to drive ASQ1 using the gate line of ASQ2 possibly due to cross-coupling between the gate lines corresponding to both qubits or to cross-coupling between the gate line and the transmon island. The coupling junction is controlled by a single electrostatic gate whose voltage, V_C, is varied to tune $L_{J,C}$ (Doh, 2005).

To enable readout of the ASQ states, the double-loop SQUID in which the ASQs are hosted is placed between a superconducting island (red) and ground (purple), forming a transmon circuit (Koch et al., 2007; Larsen et al., 2015; de Lange et al., 2015) (Fig. 7.1b, c). These circuit elements are implemented in 20 nm-thick NbTiN for magnetic field compatibility (Samkharadze et al. (2016); Kroll et al. (2018, 2019); Pita-Vidal et al. (2020); Kringhøj et al. (2021); Uilhoorn et al. (2021), Chapter 5). The transmon frequency depends on the energy-phase relation of the double-loop SQUID, which in turn depends on the states of both ASQs (Bargerbos et al., 2023a). The transmon is subsequently dispersively coupled to a lumped element readout resonator, which is coupled to a feedline implemented with a coplanar waveguide and monitored in transmission using a probe tone at frequency f_r. The readout mechanism is illustrated in Fig. 7.1d, which shows the four possible frequencies of the readout resonator, caused by the different dispersive shifts of the four spin states of the combined ASQ1-ASQ2 system (Blais et al., 2004): $\{|\uparrow_1\uparrow_2\rangle, |\uparrow_1\downarrow_2\rangle, |\downarrow_1,\uparrow_2\rangle, |\downarrow_1\downarrow_2\rangle\}$. Note that spin is not a well defined quantum number for these states, see [1]. The measurement is taken at zero magnetic field where all spin states are thermally occupied on average, since the energy splitting between them is between 0.5 and 1 GHz (see Supplementary Information (Section 7.7)), which is smaller than typical effective temperatures on the order of 100 mK observed in these devices (Pita-Vidal et al., 2023a). Therefore, the lines corresponding to all four states are visible. This result already illustrates the presence of two separate ASQs in the system. We will now move on to the characterization of these qubits before we turn our attention to the two-qubit coupling.

7.3 Individual Andreev spin qubit characterization

We first characterize each ASQ separately, while the junction containing the other qubit is pinched-off electrostatically using the voltages on its gates (Figure 7.2), following the methods of Pita-Vidal et al. (2023a). To set the qubit frequencies, we apply a magnetic field

---

[1]In an ASQ, the spin is hybridized with spatial degrees of freedom, and thus the eigenstates are rather pseudo-spin states. Similar to previous works (Hays et al., 2021; Pita-Vidal et al., 2023a), we will refer to the eigenstates as spins for simplicity.

$B_r = 35\,\mathrm{mT}$ in the y-z plane, 0.1 radians away from the B_z direction (see Supplementary Information (Section 7.7)). This field sets $f_1 \in [6, 9]$ GHz and $f_2 \in [2, 4.5]$ GHz for ASQ1 and ASQ2, respectively. We note that the qubit frequencies are significantly different due to mesoscopic fluctuations in the gate-dependence of the spin-orbit direction and g-factor of each ASQ, see also Fig. 7.2 and Supplementary Information (Section 7.7). Qubit spectroscopy is then performed by monitoring the transmission through the feedline near the readout-resonator frequency, while applying a drive tone with frequency f_d to the central gate line of ASQ2, see Fig. 7.2a, b. On resonance with the qubit transition, we observe a strong change in transmission because spin-orbit coupling and a magnetic field enable electrical driving of the spin [Chapter 5, Metzger (2022); Bargerbos et al. (2023a)]. The qubit frequencies, f_1 and f_2, can be tuned by flux, as shown in Fig. 7.2a and b. Note that the phase dispersion is expected to be sinusoidal, see Padurariu and Nazarov (2010); Pavešić et al. (2023), as is the case for ASQ2. However, for ASQ1 we rather observe a skewed sine. From the ratio of the inductance of ASQ1 and $L_{J,C}$ we rule out a non-linear flux-phase relation. so the skewness is currently of unknown origin and could be related to higher orbitals in the quantum dot. While flux tuning provides fine-tuning of the qubit frequency within a frequency band of a few GHz set by the spin-orbit coupling strength, we can also tune the qubit frequencies over a larger range by varying the magnetic field, due to the Zeeman effect. From the magnetic field dependence of the frequencies we extract the g-factor of each ASQ, see Fig. 7.2c. We find that the different g-factors are consistent with earlier work (Vaitiekėnas et al., 2018; Bargerbos et al., 2023a) and Figure 5.24, see also Supplementary Information (Section 7.7).

Next, we characterize the coherence properties of each ASQ at the frequencies indicated with markers in Fig. 7.2a and b. At these setpoints, we extract energy decay times of $T_1^{\mathrm{ASQ1}} = 3.3 \pm 0.1\,\mu\mathrm{s}$ and $T_1^{\mathrm{ASQ2}} = 11.8 \pm 0.4\,\mu\mathrm{s}$ for ASQ1 and ASQ2, respectively, where the reported uncertainties are the 1σ confidence intervals from the fit. These decay times are to a large extent limited by Purcell decay to the transmon qubit (see Supplementary Information (Section 7.7)). Furthermore, from a Ramsey experiment, we extract dephasing times of $T_2^{*\mathrm{ASQ1}} = 7.6 \pm 0.2\,\mathrm{ns}$ and $T_2^{*\mathrm{ASQ2}} = 5.6 \pm 0.2\,\mathrm{ns}$ for ASQ1 and ASQ2, respectively, which are comparable to times found in earlier works (Hays et al., 2021; Pita-Vidal et al., 2023a). For these measurements, we use Gaussian pulses with a full width at half-maximum (FWHM) of 4 ns, which is comparable to T_2^*. Therefore, the $\pi/2$ pulses cannot be considered instantaneous, which is the conventional assumption in a Ramsey experiment. Rather, a non-zero overlap of the pulses of order T_2^* can result in an overestimation of the extracted T_2^*, as further discussed in the Supplementary Information (Section 7.7). Therefore, these numbers should be interpreted as an upper bound to the pure dephasing times. Furthermore, we extract echo times of $T_{2\mathrm{E}}^{\mathrm{ASQ1}} = 17.3 \pm 0.4\,\mathrm{ns}$ and $T_{2\mathrm{E}}^{\mathrm{ASQ2}} = 17.4 \pm 0.4\,\mathrm{ns}$, see Supplementary Information (Section 7.7), three times larger than T_2^*, which points at low-frequency noise being a strong contributor to dephasing, consistent with previous observations in InAs-based spin qubits (Nadj-Perge et al., 2010; Hays et al., 2021; Pita-Vidal et al., 2023a).
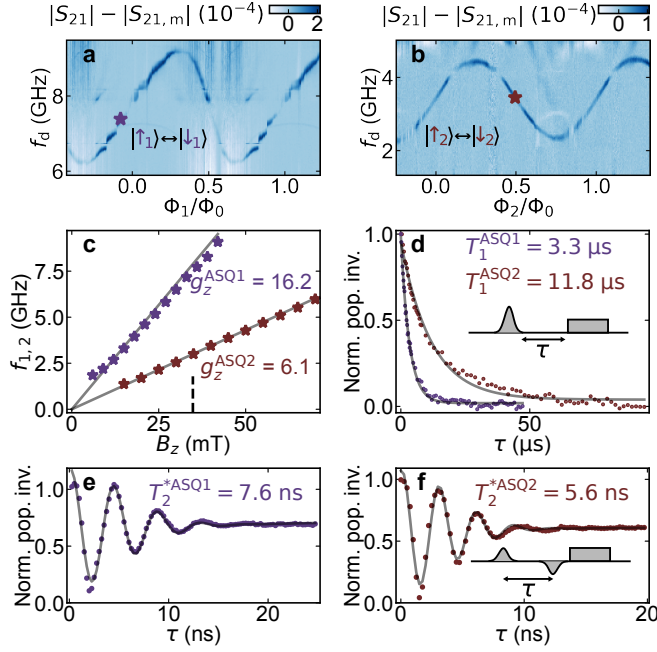
Figure 7.2: **Individual Andreev spin qubit properties**. **a, b** Readout signal amplitude with the median background subtracted, $|S_{21}| - |S_{21,m}|$, showing qubit spectroscopy of ASQ1 (versus Φ_1) and ASQ2 (versus Φ_2), respectively. During spectroscopy of one qubit, the other qubit is turned off by setting its gates to -1 V. We set $B_r = 35$ mT for both panels (indicated in **c** with a dashed line). **c** Qubit frequency versus B_z for both ASQs. f_i is calculated as the average between its maximum and minimum values versus flux. The grey lines indicate a linear fit to the data from which we extract the g-factors indicated in the labels. **d** Energy decay time (T_1) measurements of both ASQs at the frequency setpoints indicated in **a, b** ($f_1 = 7.4$ GHz and $f_2 = 3.4$ GHz, respectively). The experiment was performed by sending a π-pulse followed, after a delay τ, by a readout pulse (see inset). **e, f** Measurements of the coherence times (T_2^*) of ASQ1 and ASQ2 at the same setpoints, measured using a Ramsey experiment. Oscillations with a period of 4 ns (for **e**) and 3 ns (for **f**) are realized by adding a phase to the final $\pi/2$ pulse proportional to the delay time τ. The pulse sequence is shown in the inset for a phase of π. T_2^* is extracted by fitting a sine with a Gaussian decay envelope. The experiments were performed using Gaussian pulses with a FWHM of 4 ns. All datasets are averaged over $3 \cdot 10^5$ shots, readout time ranges from 1 to 2 µs and the total measurment time for $T_2^{*,ASQi}$ ranges from around 10 min for ASQ1 to around 30 min for ASQ2. The normalized population inversion on the y-axis of panels **d**-**f** is defined as the measured signal normalized by the signal difference between having sent no pulse and a π-pulse before the readout pulse.

7.4 Longitudinal coupling

Having two Andreev spin qubits, we describe the joint system by the following Hamiltonian with the two qubits coupled longitudinally with coupling strength J (Padurariu and Nazarov, 2010):

$$H = -\frac{\hbar\omega_1}{2}\sigma_1^z - \frac{\hbar\omega_2}{2}\sigma_2^z - \frac{hJ}{2}\sigma_1^z\sigma_2^z, \tag{7.1}$$

where $\omega_i = 2\pi f_i$ and $\sigma_i^z = |\downarrow_i\rangle\langle\downarrow_i| - |\uparrow_i\rangle\langle\uparrow_i|$ denote the phase-dependent spin-flip frequency and the z Pauli matrix of ASQi, respectively, h is the Planck constant and $\hbar = h/(2\pi)$. In this description, the longitudinal term $\frac{-hJ}{2}\sigma_1^z\sigma_2^z$ originates from the fact that the spin-dependent supercurrent of ASQ1 induces a spin-dependent phase difference over ASQ2, thus changing its transition frequency by $\pm J$, and vice versa. Importantly, the longitudinal coupling does not arise from direct wavefunction overlap (Spethmann et al., 2022) or magnetic interactions as the spins are separated by a distance of approximately 25 µm. From this physical understanding of the interaction, we can express the coupling strength J as a function of the circuit parameters by (Padurariu and Nazarov, 2010)

$$J(L_{J,C}, \Phi_1, \Phi_2) = \frac{1}{2h}\frac{L_{J,C}L_{ASQ}(\Phi_1,\Phi_2)}{L_{J,C} + L_{ASQ}(\Phi_1,\Phi_2)}I_1(\Phi_1)I_2(\Phi_2). \tag{7.2}$$

Here, we define $L_{ASQ}(\Phi_1,\Phi_2)$ as the total spin-independent inductance of the two ASQs in parallel and the magnitude of the spin-dependent current is captured by $I_i(\Phi_i)$ which denotes the difference in supercurrent across ASQi for its two possible spin states. In this expression, one of the main features of the device becomes apparent: the coupling is tunable with flux and can be switched to zero when either I_1 or I_2 are set to zero.

We now proceed to investigate the spin-spin coupling at the same gate voltages and magnetic field used for Figure 7.2. To this end, we open both loops simultaneously and set Φ_1 and Φ_2 at points where the slopes of the qubit frequencies $\partial f_i/\partial\Phi_i \propto I_i$ are large, close to $\Phi_1 \sim 0$ and $\Phi_2 \sim \Phi_0/2$. When the two qubits are longitudinally coupled, the transition frequency of each of them depends on the state of the other, as schematically depicted in Figure 7.3a and d. In each panel, the blue arrows indicate the two possible frequencies of one qubit, separated by twice the coupling strength, J, for the two possible states of the other qubit. To determine the magnitude of the coupling strength, we perform the following measurements: First, we determine $f_2 - J$ by performing qubit spectroscopy of ASQ2 starting from the ground state, $|\downarrow_1\downarrow_2\rangle$, where ASQ1 is in the spin-down state (black trace in Fig. 7.3b). Then, we repeat the spectroscopy while applying another continuous pump tone at a frequency f_p resonant with the spin-flip transition of ASQ1, driving $|\downarrow_1\downarrow_2\rangle \leftrightarrow |\uparrow_1\downarrow_2\rangle$. The presence of this additional tone results in ASQ1 being in a mixture of $|\downarrow_1\rangle$ and $|\uparrow_1\rangle$. When performing spectroscopy of ASQ2 under these conditions (red trace in Fig. 7.3b), we observe the emergence of a second peak corresponding to the shifted frequency of ASQ2 due to ASQ1 having population in its excited state, $|\uparrow_1\rangle$. This frequency splitting arises from the longitudinal coupling term and, thus, we determine the value of $J = -178 \pm 3$ MHz from a double Gaussian fit as half of the difference between the two frequencies (see the Supplementary Information for details on the fit procedure (Section 7.7)). Since the coupling term is symmetric with respect to the two qubits, we should observe the same frequency splitting when we exchange the roles of ASQ1 and ASQ2, see Fig. 7.3e
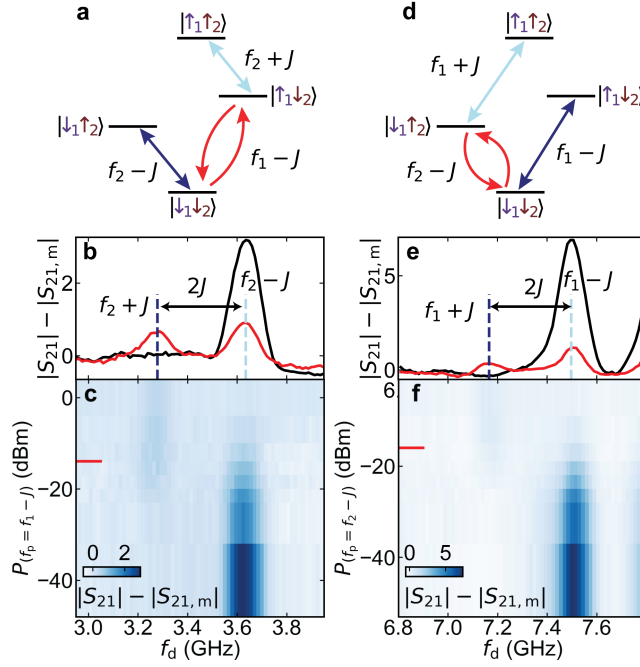
Figure 7.3: **Strong longitudinal coupling between the two Andreev spin qubits. a** Energy level diagram of the combined ASQ1-ASQ2 system with the levels (horizontal black lines) labeled by the states of both qubits (ASQ1 in purple, ASQ2 in maroon). The diagonal arrows denote the two different transition frequencies ($f_2 \pm J$) of ASQ2 depending on the state of ASQ1. Note that J is negative in this illustration and for the data presented in this figure. **b** Spectroscopy of ASQ2 as a function of the drive frequency f_d. The black and red lines indicate the readout signal amplitude with the background subtracted, $|S_{21}| - |S_{21,m}|$, with and without a pump tone resonant with ASQ1 at frequency $f_p = f_1 - J$, respectively. The pump tone is indicated with red arrows in **a**. **c** Power dependence of the pump tone. The red line indicates the power used for the red line in **c**. We indicate the power at the source output. **d-f** Similar to panels **a-c**, but with the roles of ASQ1 and ASQ2 exchanged. In this case, the pump tone drives ASQ2 at a frequency $f_p = f_2 - J$, while performing spectroscopy of ASQ1.

(note that the increase in amplitude around 7.8 GHz is unrelated to the ASQs but due to a resonance of the traveling wave parametric amplifier). From this measurement, we extract a value of $J = -165 \pm 4$ MHz similar to the value we extracted before. We speculate that the modest difference between the values of J extracted from the measurements of both qubits may be due to temporal instabilities, which we found to be present in the system. We additionally measure the qubit spectroscopy as a function of the pump tone power, shown in Fig. 7.3c and f, and we observe a power dependence on the peak amplitude. At low powers, not enough excited population is generated in the ASQ while the second peak gradually appears at higher powers. At too high powers, the readout resonator shifts too much due to the non-linearity of the resonator mode and it becomes more lossy, which results in a reduced signal (at even higher power both peaks fully disappear). Additional data and a numerical analysis of the expected pump power dependence and relative peak heights, in agreement with the experimental observations, can be found in the Supplementary Information (Section 7.7).

Next, we compare the extracted value of J to the linewidth of the ASQ transitions and find $J = 165\,\text{MHz} > 28\,\text{MHz} = 1/(2\pi T_2^{*\text{ASQ2}})$, indicating that the system is in the strong longitudinal coupling regime. This value of J puts a speed limit for a controlled-Z two-qubit gate at a time of $t = 1/(4J) = 1.4\,\text{ns}$ and a coherence limit on the average gate fidelity of around 85%, which will be explored in future experiments. Such a two-qubit gate, combined with single qubit rotations, enables a universal set of gates. On the other hand, such a fast gate would require distortion-free flux pulses (Rol et al., 2020), with a rise time much smaller than the gate time of 1.5 ns. This two-qubit gate time is much faster than typical fast two-qubit gates with superconducting qubits ($10 - 45\,\text{ns}$ (AI, 2019; Rol et al., 2019)) and comparable to the fastest short distance exchange gates in spin qubits coupled via directly overlapping wavefunctions (Loss and DiVincenzo, 1998; Hendrickx et al., 2020, 2021).

7.5 Tunability of the coupling strength

We have so far investigated the coupling strength at fixed gate voltages and flux. We now investigate the dependence of J on different control parameters and demonstrate that it is tunable as predicted by Eq. (7.2) (Padurariu and Nazarov, 2010). We vary Φ_1 using the flux line, see Fig. 7.4a, and find that the coupling strength is directly proportional to I_1, as expected. The current difference across ASQ1, I_1, is extracted from a measurement of the qubit frequency as a function of flux, as shown in Fig. 7.4d. Note that, by varying the flux, we not only vary the magnitude of J, but also switch its sign, crossing zero coupling. Thus, the two ASQs can be fully uncoupled by setting $J = 0$ at the flux points which maximize or minimize $f_i(\Phi_i)$, and where thus $I_i = 0$, for either one of the qubits. The coinciding of zero coupling with these frequency-extrema is useful as these are the first-order flux-insensitive points of the qubit transition frequency. Two representative situations in which the ASQs are coupled and uncoupled at nearby flux points are shown in Fig. 7.4b and c, respectively. The data was measured and analyzed using the same procedure as described for Figure 7.3.

We overlay the Φ_1-dependence of the coupling strength with the expected dependence from Equation (7.2). The values of $L_{\text{J,C}} = 8.4\,\text{nH}$ and $I_2 \sim h\partial f_2/\partial\Phi_2|_{\Phi_2=0.51\Phi_0} = -2.52\,\text{nA}$ are fixed and independently extracted from measurements of the transmon frequency and of $f_2(\Phi_2)$, respectively. $L_{\text{ASQ}}(\Phi_1)$ is calculated as the parallel combination of the spin-independent Josephson inductances of both qubits, which are determined from separate transmon spectroscopy measurements (see Supplementary Information (Section 7.7)) and $I_1(\Phi_1) \sim h\partial f_1/\partial\Phi_1$ is estimated from Fig. 7.4d. As shown in Fig. 7.4a, the measured $J(\Phi_1)$ is in good agreement with Eq. (7.2).

Finally, we investigate the $L_{\text{J,C}}$ tunability of J by fixing $\Phi_1 = -0.07\Phi_0$, which sets $I_1 = 2.16\,\text{nA}$, and varying the value of V_{C} (see Supplementary Information for the corresponding qubit parameters (Section 7.7)). We observe an increase of the magnitude of J as the value of $L_{\text{J,C}}$ is increased, as shown in Fig. 7.4e. The measured data follows to a large extent the dependence expected from Eq. (7.2), indicated with a continuous line in Fig. 7.4e. The $|J|$ increase is limited to a maximum when the coupling junction $L_{\text{J,C}}$ becomes comparable to the finite spin-independent inductance L_{ASQ} of the ASQs. For the solid line in Figure 7.4e we use the independently measured value $L_{\text{ASQ}}(\Phi_1 = -0.07\Phi_0, \Phi_2 = 0.51\Phi_0) = 102.0\,\text{nH}$. For comparison, the dashed line depicts the limit of $L_{\text{ASQ}} \gg L_{\text{J,C}}$.
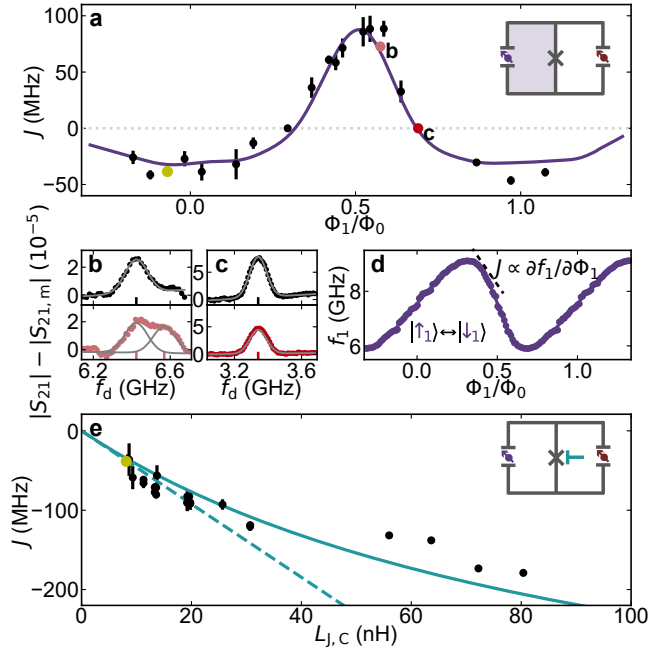
Figure 7.4: **Tunability of the coupling strength.** **a** Qubit-qubit coupling strength, J, as a function of flux in the loop containing ASQ1, Φ_1, see also inset, at fixed $\Phi_2 \sim 0.51\Phi_0$. The purple line shows the expected dependence from Eq. (7.2). **b, c** Representative fits at two Φ_1 points highlighted with colored (and letter marked) markers in **a**. The signal measured in the absence of a pump tone (black markers) is fit with a single Gaussian (black line), to determine $f_i - J$ (vertical black line in the x axis). The signal measured in the presence of a pump tone at the other ASQ (colored markers) is additionally fitted (colored line) to determine $f_i + J$. The grey lines in **b** show the two individual Gaussians. **d** Frequency of ASQ1, f_1, versus Φ_1 (markers) and interpolation (line) used to estimate $I_1(\Phi_1) \sim h\partial f_1/\partial\Phi_1$. **e** Qubit-qubit coupling strength J at fixed $\Phi_1 = -0.07\Phi_0$ and as a function of $L_{J,C}$, which is varied using the gate-voltage at the coupling junction (see inset). The continuous line shows the dependence from Eq. (7.2), while the dashed line shows a linear dependence $Jh = L_{J,C}I_1I_2/2$. The yellow marker in **a** and in **e** is a shared point between the two panels. In **a** and **e**, the markers and error bars represent the best-fit values of J (see panels **b, c**) and their estimated standard errors (one-sigma confidence intervals), respectively.

7.6 Conclusions

In conclusion, we have extended earlier results demonstrating single Andreev spin qubits (Hays et al., 2021; Pita-Vidal et al., 2023a) and integrated two InAs/Al-based ASQs within a single transmon circuit. The two ASQs are separated by around 25 μm, two orders of magnitude larger than the size of the individual qubit wavefunctions. Both ASQs showed comparable coherence properties to those reported in prior work (Hays et al., 2021; Pita-Vidal et al., 2023a). We have shown strong supercurrent-mediated coupling between the two Andreev spin qubits and found that the coupling strength, J, can be tuned with either a magnetic flux or an electrical voltage. In particular, we have shown that J can be fully suppressed using a magnetic flux. This switchability of the coupling is essential for the use of longitudinally coupled Andreev spin qubits to perform quantum computation. Furthermore, the high sign and magnitude tunability of J could have applications for the use of An-

dreev spin qubits to perform analog quantum simulations. More generally, Andreev spin qubits could in the future provide an independent platform for quantum computing and simulation or, alternatively, they may be incorporated into existing spin qubit platforms and serve as readout modules or long-distance couplers. Independently of the precise use-case for Andreev spin qubits, we emphasize that strong spin-spin coupling as demonstrated here will be an essential requirement, although smaller dephasing rates would be desired.

Previous works suggest that one possible mechanism limiting dephasing is coupling to the large nuclear spins of InAs (Nadj-Perge et al., 2010; Hays et al., 2021; Pita-Vidal et al., 2023a). While the origin of dephasing must be further investigated, this suggests that a possible route to increase the dephasing times is implementing Andreev spin qubits in an alternative nuclear-spin-free material such as germanium (Hendrickx et al., 2018; Vigneau et al., 2019; Scappucci et al., 2020; Tosato et al., 2023; Valentini et al., 2023). We expect that future efforts using alternative materials could both provide a path towards integration in more established semiconductor-based quantum architectures as well as strongly increased coherence times. If longer coherence times can be achieved, in combination with the strong qubit-qubit coupling demonstrated here, Andreev spin qubits will emerge as an encouraging platform for the realization of high-fidelity two-qubit gates between remote spins.

7.7 Supplementary information

7.7.1 Theoretical description of longitudinal ASQ-ASQ coupling

General description of the estimation of J used in the main text

We derive a general expression for the coupling strength J in terms of Andreev current operators. The derived expression facilitates the data analysis presented in the main text, where we use the experimentally obtained current-phase relationship, which differs from that expected from the ideal quantum dot junction theory (Padurariu and Nazarov, 2010; Bargerbos et al., 2023a). The current operator for each individual ASQ can be expressed as $\hat{I}_i = -\frac{2\pi}{\Phi_0}\frac{\partial H_i}{\partial \phi_i}$, where $i = 1, 2$. Here, $\Phi_0 = h/2e$ denotes the magnetic flux quantum, $H_i = -\frac{\hbar\omega_i(\phi_i)}{2}\sigma_i^z$ in the subspace of the two spinful doublet states, ϕ_i is the phase drop across ASQi, σ_i^z is the z Pauli matrix for ASQi and the z axis is chosen along the spin-polarization direction for each qubit. As a result, the current operator can be related to the qubit frequency by

$$\hat{I}_i = \frac{\pi h}{\Phi_0}\frac{\partial f_i(\phi_i)}{\partial \phi_i}\sigma_i^z = \frac{I_i}{2}\sigma_i^z, \qquad (7.3)$$

where we have defined the amplitude of the spin-dependent current $I_i = \frac{2\pi h}{\Phi_0}\frac{\partial f_i(\phi_i)}{\partial \phi_i} \approx h\frac{\partial f_i(\Phi_i)}{\partial \Phi_i}$ as in the main text, where the last approximation holds in the limit of $L_{J,C} \ll L_{J,i}^I, L_{J,i}^\sigma \forall i$, such that the phase drop can be directly related to the external flux applied through the loop: $\phi_i = \frac{2\pi}{\Phi_0}\Phi_i$. In the subspace of the doublet states for each ASQ we can expand the two-qubit Hamiltonian to first order around the phase bias ϕ_1, given by the perturbation of the current through ASQ2, $\delta\phi_1 = \frac{2\pi}{\Phi_0}M\hat{I}_2$. Here, M denotes an effective mutual inductance that

determines how much phase drops over ASQ1 due to a current in ASQ2. We obtain

$$
\begin{aligned}
H &= H_1(\phi_1 + \delta\phi_1) + H_2(\phi_2) \\
&= H_1\left(\phi_1 + \frac{2\pi}{\Phi_0} M\hat{I}_2\right) + H_2(\phi_2) \\
&\approx H_1(\phi_1) + \frac{2\pi}{\Phi_0}\frac{\partial H_1(\phi_1)}{\partial\phi_1} M\hat{I}_2 + H_2(\phi_2) \\
&= H_1(\phi_1) + H_2(\phi_2) - M\hat{I}_1\hat{I}_2 \\
&= -\frac{\hbar\omega_1}{2}\sigma_1^z - \frac{\hbar\omega_2}{2}\sigma_2^z - \frac{1}{4}MI_1 I_2 \sigma_1^z\sigma_2^z.
\end{aligned}
\tag{7.4}
$$

In the limit of $L_{\mathrm{J,C}} \ll L_{\mathrm{J},i}^\sigma \forall i$, where $L_{\mathrm{J},i}^\sigma$ is the spin-dependent Josephson inductance of ASQi, M is given by the parallel combination of the spin-independent inductances of the three SQUID branches, $M = \frac{L_{\mathrm{J,C}}L_{\mathrm{ASQ}}}{L_{\mathrm{J,C}}+L_{\mathrm{ASQ}}}$. Here, $L_{\mathrm{ASQ}}(\phi_1,\phi_2)$ is the parallel combination of the spin-independent Josephson inductances of the ASQs:

$$
\frac{1}{L_{\mathrm{ASQ}}(\phi_1,\phi_2)} = \frac{\cos(\phi_1)}{L_{\mathrm{J},1}^I} + \frac{\cos(\phi_2)}{L_{\mathrm{J},2}^I}.
$$

By comparison to Eq. (1) in the main text, we thus find

$$
J = \frac{M}{2h}I_1 I_2 = \frac{1}{2h}\frac{L_{\mathrm{J,C}}L_{\mathrm{ASQ}}}{L_{\mathrm{J,C}}+L_{\mathrm{ASQ}}}I_1 I_2.
\tag{7.5}
$$

Analytical and numerical calculation of J assuming a sinusoidal current-phase relation

A simple model of the Hamiltonian for each ASQ is given by (Padurariu and Nazarov, 2010; Bargerbos et al., 2023a)

$$
H_i(\phi_i) = -E_{\mathrm{J},i}^I\cos\phi_i + E_{\mathrm{J},i}^\sigma\sigma_i^z\sin\phi_i,
\tag{7.6}
$$

where $E_{\mathrm{J},i}^I = \Phi_0^2/(4\pi^2 L_{\mathrm{J},i}^I)$ and $E_{\mathrm{J},i}^\sigma = \Phi_0^2/(4\pi^2 L_{\mathrm{J},i}^\sigma)$ denote the spin-independent and spin-dependent Josephson energies, respectively. The total Hamiltonian of the coupled system of Fig. 1(a) in the main text is thus

$$
\begin{aligned}
H(\phi) &= H_1(\varphi_1 - \phi) + H_2(\varphi_2 - \phi) + E_{\mathrm{J,C}}\cos(\phi) \tag{7.7} \\
&= -E_{\mathrm{J},1}^I\cos(\varphi_1 - \phi) + E_{\mathrm{J},1}^\sigma\sigma_1^z\sin(\phi - \varphi_1) - E_{\mathrm{J},2}^I\cos(\varphi_2 - \phi) + E_{\mathrm{J},2}^\sigma\sigma_2^z\sin(\varphi_2 - \phi) + -E_{\mathrm{J,C}}\cos\phi,
\end{aligned}
\tag{7.8}
$$

where $E_{\mathrm{J,C}} = \Phi_0^2/(4\pi^2 L_{\mathrm{J,C}})$ and the reduced flux, $\varphi_i = 2\pi\Phi_i/\Phi_0$, is the magnetic flux through the loop containing ASQi expressed in units of phase.

   Analytical solution. Following Padurariu and Nazarov (2010), assuming the energy-phase relation in Eq. (7.6), the lowest order in $E_{\mathrm{J},1}^\sigma/E_{\mathrm{J,C}}$ and $E_{\mathrm{J},2}^\sigma/E_{\mathrm{J,C}}$ yields the coupling energy in the form

$$
J = -2\frac{E_{\mathrm{J},1}^\sigma E_{\mathrm{J},2}^\sigma}{|\tilde{E}|}\cos(\varphi_{\tilde{E}} - \varphi_1)\cos(\varphi_{\tilde{E}} - \varphi_2),
\tag{7.9}
$$

where

$$\tilde{E} = E_{J,1}^I e^{i\varphi_1} + E_{J,2}^I e^{i\varphi_2} + E_{J,C}. \tag{7.10}$$

Numerical diagonalization. To go beyond the limit of Equation (7.9), i.e. for strong coupling, where the phase-drop on each ASQ is no longer linearly related to the applied flux, we solve the eigenenergies of the system numerically. For a given set of parameters, the energies of the four possible states of the qubit-qubit system ($E_{\uparrow\uparrow}$, $E_{\downarrow\uparrow}$, $E_{\uparrow\downarrow}$ and $E_{\downarrow\downarrow}$) are obtained as the minima in ϕ of the four eigenvalues of $H(\phi)$. From these four energies, we calculate the coupling strength J given the longitudinal (or Ising) type coupling Hamiltonian presented in Eq. (1) in the main text. In this situation, the four eigenenergies of the coupled system are

$$E_{\uparrow\uparrow} = \frac{\hbar\omega_1}{2} + \frac{\hbar\omega_2}{2} + \frac{hJ}{2}, \tag{7.11}$$

$$E_{\downarrow\uparrow} = -\frac{\hbar\omega_1}{2} + \frac{\hbar\omega_2}{2} - \frac{hJ}{2}, \tag{7.12}$$

$$E_{\uparrow\downarrow} = \frac{\hbar\omega_1}{2} - \frac{\hbar\omega_2}{2} - \frac{hJ}{2}, \tag{7.13}$$

$$E_{\downarrow\downarrow} = -\frac{\hbar\omega_1}{2} - \frac{\hbar\omega_2}{2} + \frac{hJ}{2}. \tag{7.14}$$

Thus, from the numerically solved eigenenergies, we can find J as

$$J = \frac{1}{2h}(E_{\uparrow\uparrow} - E_{\uparrow\downarrow} - E_{\downarrow\uparrow} + E_{\downarrow\downarrow}). \tag{7.15}$$

Numerics including the transmon degree of freedom. To fit the transmon spectroscopy data presented in Sec. 7.7.3 and 7.7.6, we add a charging energy term to Equation (7.8) corresponding to the transmon island and numerically diagonalize the resulting Hamiltonian in the phase basis (Bargerbos et al., 2020; Kringhøj et al., 2020)

$$H_{\text{Transmon}} = -4E_c\partial_\phi^2 + H(\phi) \tag{7.16}$$

where E_c denotes the charging energy of the transmon island and $H(\phi)$ is defined in Equation (7.8).

Method comparison

Given the different approaches to calculate J, we now compare the different methods assuming the sinusoidal energy-phase of Equation (7.6), see Figs. 7.5 and 7.6. The analytical expression of Equation (7.9) is indicated with dashed lines. The continuous lines are obtained numerically from exact diagonalization of the total Hamiltonian in Equation (7.8) using Equation (7.15). The numerical diagonalization and the analytical expression of Equation (7.9) show near perfect agreement. Only when $E_{J,i}^\sigma \sim E_{J,C}$ (Figure 7.5c) a slight deviation is visible since Equation (7.9) is only valid in the limit $E_{J,i}^\sigma \ll E_{J,C}$. We then test the estimate of J on the sinusoidal energy-phase relation of Equation (7.6) using Equation (7.5), which is also used in the main text for the experimentally obtained energy-phase relation. This is shown with dotted lines, for different sets of parameters. In Fig. 7.5 we

use parameters corresponding to the limit $L_{J,C} \ll L_{J,i}^\sigma, L_{J,i}^I \forall i$ and, given the agreement between the different methods, we note that the approximations made in Sec. 7.7.1 are valid. Thus, the general estimate from Eq. (7.5) (dotted line) agrees well with the exact value of J found by numerical diagonalization of the full Hamiltonian, as expected. To illustrate the estimates obtained from the different methods outside of this limit, we use values of $E_{J,i}^I$ in Fig. 7.6 that instead deviate from the limit $L_{J,C} \ll L_{J,i}^I \forall i$. In this case, we see that the estimate from Eq. (7.5) deviates strongly from the exact numerical calculation due to the non-linear flux-phase relation.
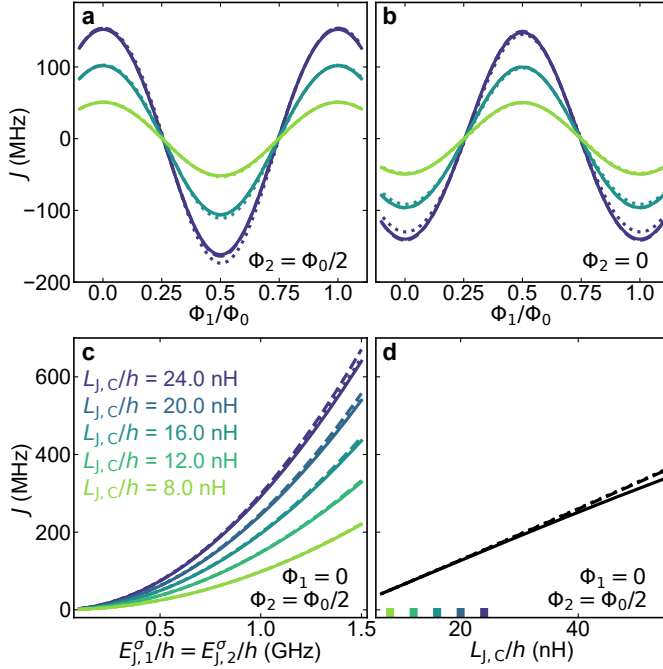

Figure 7.5: **Qubit-qubit coupling strength** J **as a function of model parameters. a, b** Φ_1 dependence of the coupling strength J at fixed $\Phi_2 = \Phi_0/2$ and $\Phi_2 = 0$, respectively. **c** $E_{J,i}^\sigma$ dependence of J at fixed $\Phi_1 = 0$ and $\Phi_1 = \Phi_0/2$, for various $L_{J,C}$ values. **d** $L_{J,C}$ dependence of J at fixed $\Phi_1 = 0$ and $\Phi_1 = \Phi_0/2$. For all panels $E_{J,1}^\sigma/h = 0.82\,\text{GHz}$, $E_{J,2}^\sigma/h = 0.63\,\text{GHz}$, $E_{J,1}^I/h = 0.2\,\text{GHz}$ and $E_{J,2}^I/h = 0.3\,\text{GHz}$, excepting for panel c where the values of $E_{J,1}^\sigma$ and $E_{J,2}^\sigma$ are varied. The continuous lines indicate the results obtained from direct diagonalization of Hamiltonian (7.8) using Eq. (7.15), the dashed lines, which mostly fall on top of the solid lines, indicate the analytic limit of Eq. (7.9) (Padurariu and Nazarov, 2010) and the dotted lines indicate the limit of Eq. (7.5) used in the main text. Note that, for panel **d**, the values of $I_i \sim h\frac{\partial f_i(\Phi_i)}{\partial \Phi_i}$ are calculated for each value of $L_{J,C}$. This differs from what is done in Fig. 4e in the main text, where the values of I_i are estimated at a fixed $L_{J,C}$ point and used for the complete $L_{J,C}$ range.
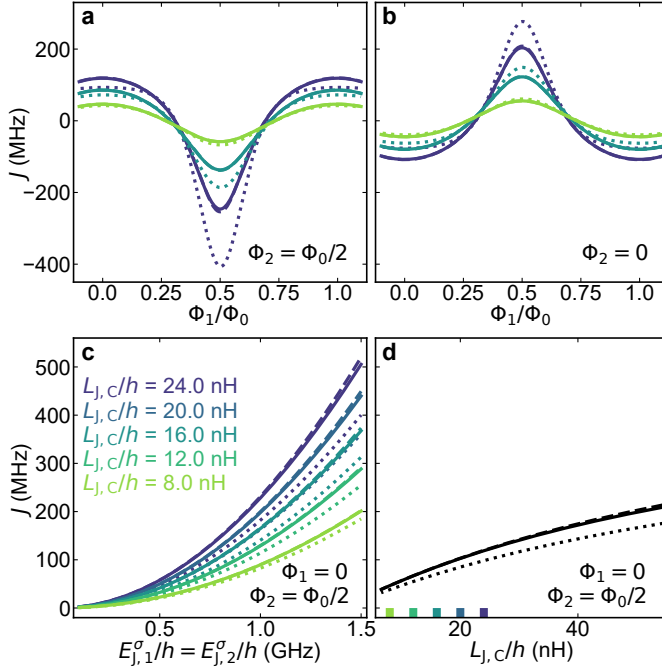
Figure 7.6: Same as Fig. 7.5 but for $E_{J,1}^I/h = 2.30\,\text{GHz}$ and $E_{J,2}^I/h = 0.45\,\text{GHz}$.

Master equation approach to longitudinal coupling experiment

We now present a simple master equation simulation to investigate the effect of the drives on the coupled two-qubit system in presence of decay. We solve the Lindblad master equation for the time evolution of the system density matrix, ρ, of the following form

$$\dot{\rho} = [\rho, H'] - \sum_n \frac{1}{2}\left[2C_n\rho C_n^\dagger - \rho C_n^\dagger C_n - C_n^\dagger C_n\rho\right], \tag{7.17}$$

where H' describes the two-qubit system in the rotating frame of the two drives, which have certain detuning Δ_i from qubit i. This results in the following Hamiltonian

$$H'/\hbar = \frac{\Delta_1}{2}\sigma_2^z + \frac{\Delta_2}{2}\sigma_2^z + \frac{\Omega_{p1}}{2}\sigma_1^x + \frac{\Omega_{p2}}{2}\sigma_2^x + 2\pi\frac{J}{2}\sigma_1^z\sigma_2^z, \tag{7.18}$$

where Ω_{pi} denotes the drive amplitude of the tone near qubit i and $\Delta_i = \omega_i - \omega_{pi}$ is the detuning of that drive frequency with the qubit frequency. Additionally, we apply the collapse operators C_n on the individual qubits to simulate the effect of finite T_1 and T_2: $C_n \in \{\sqrt{\gamma_{1,1}}\sigma_1^-, \sqrt{\gamma_{\phi_1}/2}\sigma_1^z \sqrt{\gamma_{1,2}}\sigma_2^-, \sqrt{\gamma_{\phi_2}/2}\sigma_2^z\}$, where $\gamma_{1,i} = 1/T_1^{\text{ASQ}i}$, $\gamma_{\phi_i} = 1/T_2^{\text{ASQ}i}$, $\sigma_i^+ = |\uparrow_i\rangle\langle\downarrow_i|$ and $\sigma_i^- = |\downarrow_i\rangle\langle\uparrow_i|$. We then solve Equation (7.17) for the steady state solution using Qutip (Johansson et al., 2013). From the above evolution of the master equation under a certain drive amplitude, we obtain the populations of the states $\{|\uparrow_1\uparrow_2\rangle, |\uparrow_1\downarrow_2\rangle, |\downarrow_1\uparrow_2\rangle, |\downarrow_1\downarrow_2\rangle\}$. Then, assuming a dispersive shift for each state and a linewidth of the resonator mode, we

calculate the signal as the sum of populations times the displaced Lorentzians corresponding to each state and subtract the median for each linecut as is done with the experimental data. We compare the data measured in Fig. 3 of the main text to the master equation simulation with realistic parameters, as shown in Figure 7.7. The simulations reproduce the main features seen in the data.
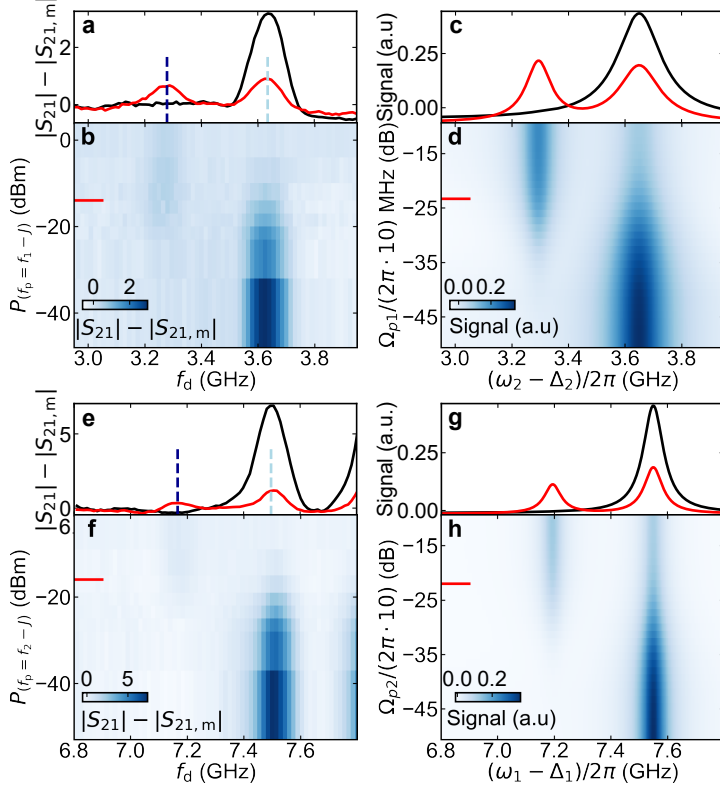

Figure 7.7: **Comparison between experiment and master-equation simulation. a-b, e-f** Experimental data of longitudinal coupling measurement repeated from Fig. 3 of the main text. **c-d, g-h** Results of master equation simulations of the corresponding experimental data. **c-d** ASQ1 is driven with a pump tone at $f_p = f_1 - J$, while doing spectroscopy on ASQ2. **g-h** ASQ2 is driven with a pump tone at $f_p = f_2 - J$, while doing spectroscopy on ASQ1. We use the following parameters: the spectroscopy drive amplitude for ASQi is set to $\Omega_{pi}/2\pi = 2\,\text{MHz}$ which power broadens the observed linewidths similar to the experiment. The drive frequency of the third tone is set such that $\Delta_i = -J$, and the power is shown on the y-axis of the 2D maps in dB, similar to the experiment. T_1 and T_2^* are set to their values shown in Fig. 2 of the main text using the collapse operators and $\omega_i/(2\pi)$ of ASQi are set to $f_i - J$. The dispersive shifts are assumed larger than the linewidth of the resonator here such that the signal is only sensitive to the change in $|\downarrow_1\downarrow_2\rangle$ population. In all simulations, we fix $J = 178\,\text{MHz}$.

The peak height difference between the drive being on and off (black and red linecuts in Figure 7.7) depends on the difference between the initial and final populations $P_{\downarrow\downarrow}$ of $|\downarrow_1\downarrow_2\rangle$ in the limit of large dispersive shift, which we consider here for simplicity. Consider the case where we apply a spectroscopy tone at $f_2 - J$ on ASQ2, in the absence of a pump tone. In steady state, we get $P_{\downarrow\downarrow} = P_{\downarrow\uparrow} = 0.5$ and $P_{\uparrow\uparrow} = P_{\uparrow\downarrow} = 0$ due to the spectroscopy

saturating ASQ2. Now, if we set a separate pump tone driving ASQ1 at $f_p = f_1 - J$ to a sufficiently high amplitude Ω_{p1}, we obtain $P_{\downarrow\downarrow} = P_{\downarrow\uparrow} = P_{\uparrow\downarrow} = 0.33$. Thus the height of the driven peak at $f_2 + J$ (red right peak) should be the height of the undriven (black) peak divided by a factor of $0.5/(0.5 - 0.33) \sim 2.94$ (as opposed to a factor of 2 which one might naively expect). The residual lowering of the peak observed in the experiment, we attribute to additional losses in the resonator mode under a strong drive. The height of the peak at $f_2 - J$, on the other hand, is expected to have a similar height if no T_1 decay is present. In presence of finite and similar T_1 for ASQ1 and ASQ2, however, the final populations end up becoming $P_{\downarrow\downarrow} = P_{\downarrow\uparrow} = P_{\uparrow\downarrow} = P_{\uparrow\uparrow} = 0.25$, thus increasing the signal at $f_2 - J$ and leading to a higher peak reaching half the height of the undriven peak at $f_2 + J$ (as also seen in in Figure 7.7(d)). However, beyond these limiting cases, depending on the exact ratio of the T_1 lifetimes of ASQ1 and ASQ2 the steady-state populations will vary.

7.7.2 Methods

Device overview

The physical implementation of the device investigated is shown in Fig. 7.8. The chip, 6 mm long and 6 mm wide, consists of two devices coupled to a single transmission line with an input capacitor to increase the directionality of the outgoing signal (Fig. 7.8h). For the experiments performed here, only the device discussed in the main text, highlighted in Fig. 7.8g, was measured. The resonator of the second device (uncolored device in Fig. 7.8g) was not functional and thus was not investigated.

For each device, a lumped element readout resonator is capacitively coupled to the feedline (Fig. 7.8e). The resonator is additionally capacitively coupled to the transmon island, which is connected to ground via three Josephson junctions in parallel (the coupling junction, ASQ1 and ASQ2) defining two loops (Fig. 7.8b). The loops implementation is sketched in Fig. 7.9. The three junctions are implemented on two separate Al/InAs nanowires. The junctions are defined by etching the aluminum shell of the nanowire in a 95 nm-long section for the coupling junction and 215 nm-long sections for each of the ASQ junctions. The coupling junction is controlled by a single 200 nm-wide electrostatic gate centered at the middle of the junction, controlled with a DC voltage V_C. Each of the quantum dot junctions is defined by three gates consisting of two 50 nm wide tunnel gates (L, R) surrounding a 60 nm wide plunger gate (P), separated from each other by 45 nm (Fig. 7.8c, d). We define the DC voltages used for the left and right tunnel gates as V_{LP1} and V_{R1} for ASQ1 or V_{L2} and V_{R2} for ASQ2. The plunger gate of ASQ1 is also set to V_{LP1} because it was shorted to the left tunnel gate due to a fabrication imperfection. All gate lines except for the plunger lines incorporate a fourth-order Chebyshev LC-LC filter with a cut-off frequency at 2 GHz (see Fig. 3.4). The first and second inductive elements, of 5.2 nH and 6.1 nH respectively, are implemented using thin strips of NbTiN with widths of 3.5 μm and 300 nm, respectively. The first and second capacitive elements, of 2.45 pF and 2.08 pF respectively, are implemented with parallel plate capacitors. The plunger gate of ASQ2 is connected to a bias-tee on the printed circuit board formed by a 100 kΩ resistor and a 100 pF capacitor. This permits the simultaneous application of a DC signal, V_{P2}, to control the level of the quantum dot junction, and microwave tones, f_d and f_p, to drive either of the spin-flip transitions or the transmon. We also drive ASQ1 using the same gate line, because the bias-tee at the plunger gate of ASQ1 was not functional. The flux
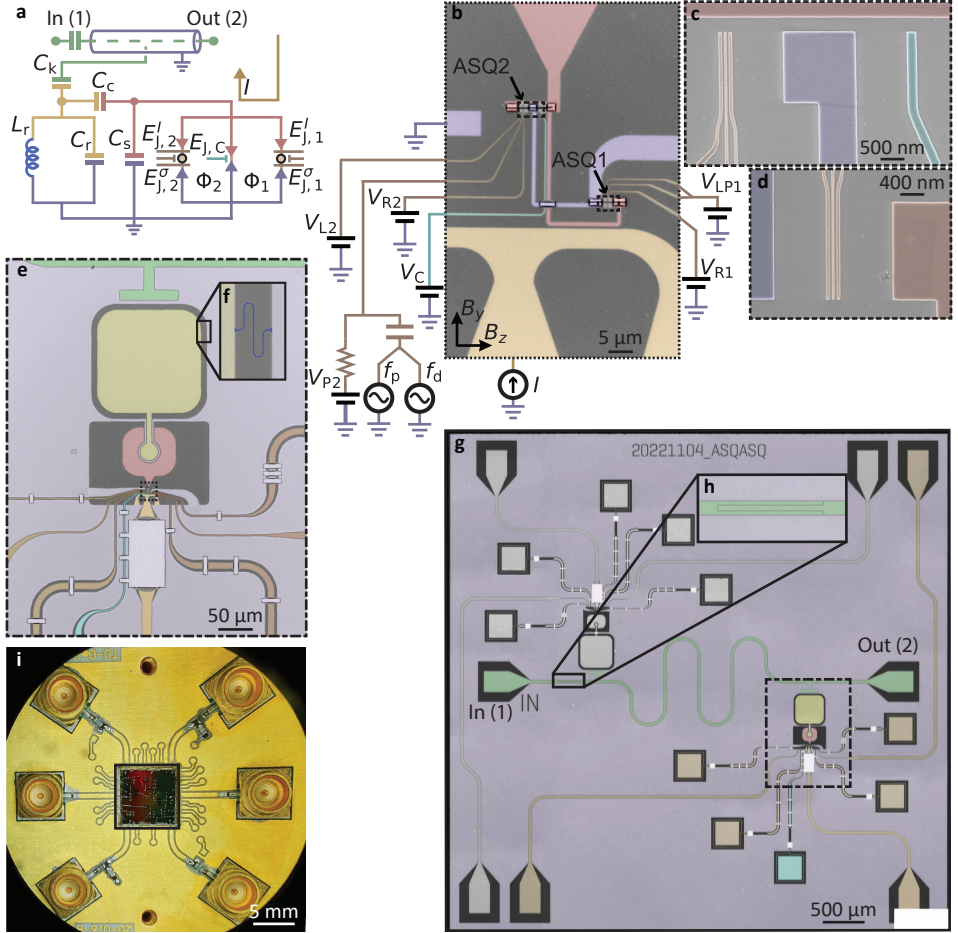
Figure 7.8: **Device overview. a** Diagram of the full microwave circuit. A coplanar waveguide (green center conductor) transmission line with an input capacitor is capacitively coupled to a grounded LC resonator. The resonator consists of an island (yellow) capacitively and inductively (blue) shunted to ground (purple). The resonator is in turn capacitively coupled to a transmon island (red), which is shunted to ground capacitively as well as via three parallel Josephson junctions. The coupling junction is controlled by a single electrostatic gate (cyan) and each of the two Andreev spin qubits is controlled by three electrostatic gates (brown). The RF drive tones f_d and f_p are sent through the plunger gate of ASQ2. The current through the flux line (amber), I, controls the flux thread through the loop containing ASQ1, Φ_1, and leaves Φ_2 nearly unaffected. **b** False-colored optical microscope image of the loops area. The three Josepshon junctions are implemented in two separate Al/InAs nanowires, one of them containing the coupling junction and ASQ2 and the other containing ASQ1. The B_y component of the magnetic field is used to tune Φ_1 and Φ_2, see Figure 7.9 for detailed sketch of the loops geometry. B_z is the magnetic field component approximately parallel to the nanowires axis. **c, d** False colored scanning electron microscope (SEM) images of the gates areas taken before the deposition of the gate dielectric and nanowire. **e** False-colored optical microscope image of the device showing the qubit island (red), the resonator island (yellow), the 200 nm-wide resonator inductor (blue, enlarged in **f**), the transmission line (green), the electrostatic gates (brown and cyan) the flux line (amber) and ground (purple). **g** False-colored optical microscope image of the whole 6×6 mm chip containing two nearly identical devices coupled to the same transmission line, which has an input capacitor, enlarged in **h**. The measured device is false-colored, while the second device was not investigated. **i** Chip mounted on a printed circuit board (PCB).

through the loop containing ASQ1 is controlled using a flux line (shown in amber). Its design in the area of the loops was inspired by Chapter 6. We furthermore incorporate a 25 pF parallel plate capacitor near the end of the flux line which, together with the 1 nH inductance of the rest of the flux line, implements an LC low-pass filter with a cut-off at 1 GHz.
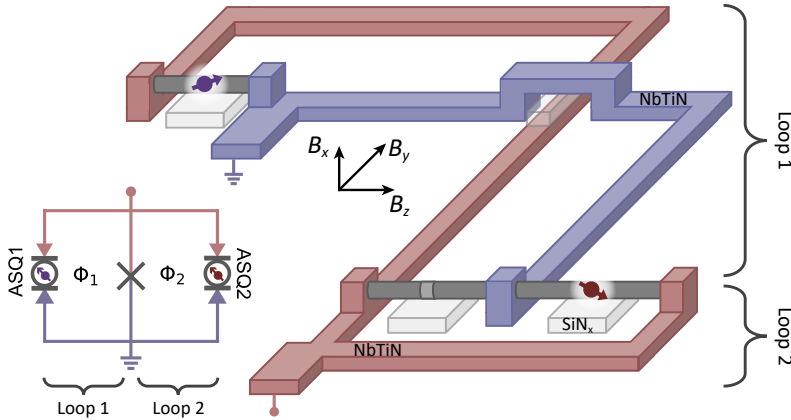

Figure 7.9: **Loops geometry.** Diagram of the loops area shown in Fig. 7.8b. Red and purple NbTiN segments denote segments connected to the transmon island and ground, respectively. The loop containing the coupling junction and ASQ2 (loop 2) is a planar loop with the same geometry as those in Bargerbos et al. (2022, 2023a); Pita-Vidal et al. (2023a). The loop containing the coupling junction and ASQ1 (loop 1) is a twisted gradiometric loop formed by two subloops. Equal of out-of-plane magnetic fields B_x through each of the two subloops result in nearly opposite contributions to the flux Φ_1, rendering loop 1 nearly insensitive to out-of-plane magnetic field noise. The nanowires are elevated with respect to the NbTiN plane due to the gate dielectric (light grey). This defines, for each loop, a loop area perpendicular to B_y. B_y can thus be used to control the flux through the loops while keeping the out-of-plane field component (B_x) fixed, reducing the occurrence of external flux jumps (de Lange and Wesdorp, 2023).

Summary of device parameters

Bare resonator frequency, $f_{r,0}$	4.229 GHz	Resonator Q_c	1.3k
Resonator Q_i	~ 35k	Transmon decay time, T_1^t	53.6 ns
Resonator-tmon coupling, g/h	~ 287 MHz	Transmon Ramsey time, T_{2R}^t	80.0 ns
Transmon charging energy, E_c/h	200 MHz		

Table 7.1: **Values of relevant device parameters.** The resonator bare frequency and quality factors are measured when all electrostatic gates are at -1000 mV and thus all three junctions are pinched off (see Fig. 7.11). The transmon charging energy is extracted from the transmon anharmonicity in two-tone spectroscopy. The resonator-transmon coupling is extracted from a single-tone spectroscopy measurement at their anti-crossing (see Fig. 7.13). The transmon coherence values were measured with both ASQs in pinch off and at $V_C = 1500$ mV, which sets the transmon frequency to $f_t = 5.45$ GHz.

Nanofabrication details

The device fabrication occurs in several steps identical to that described in (Bargerbos et al., 2022), and repeated here for the sake of completeness. The substrate consists of 525 μm-thick high-resistivity silicon, covered in 100 nm of low-pressure chemical vapor deposited Si_3N_4. In the first step, a 4-inch wafer of such substrate is cleaned by submerging it for 5 min in HNO_3 while ultasonicating, followed by two short H_2O immersions to rinse the HNO_3 residues. Afterwards, a 20 nm-thick NbTiN film is sputtered on top of the substrate using an *AJA International ATC 1800* sputtering system. Subsequently, Ti/Pd e-beam alignment markers are patterned on the wafer, which is thereafter diced into smaller individual dies of approximately 12 mm×12 mm. In the next step, the gate electrodes and the rest of the NbTiN circuit elements are patterned on one die covered by 110 nm-thick *AR-P 6200* (positive) e-beam resist using electron-beam lithography. The structures are then etched using SF_6/O_2 reactive ion etching for 47 s. Subsequently, 28 nm of Si_3N_4 dielectric are deposited on top of the gate electrodes using plasma-enhanced chemical vapor deposition and etched in patterns with a buffered oxide etchant (for 3 min). This dielectric is used as a gate dielectric, as well as as the dielectric for the crossovers at the DC gate lines and flux line and for the crossover that generates the twist in the loop containing ASQ1.

The nanowires are deterministically placed on top of the dielectric using a nanomanipulator and an optical microscope. These nanowires are ~10 μm-long epitaxial superconductor - semiconductor nanowires with a 110 nm-wide hexagonal InAs core and a 6 nm-thick Al shell covering two of their facets, in turn covered by a thin layer of aluminium oxide. The growth conditions were almost identical to those detailed in Krogstrup et al. (2015), with the only two differences being that this time the As/In ratio was 12, smaller than in Krogstrup et al. (2015), and that the oxidation of the Al shell was now performed in-situ, for better control, reproducibility and homogeneity of the oxide layer covering the shell. Inspection of the nanowire batch, performed under a scanning electron microscope directly after growth, indicated an average wire length of 9.93 ± 0.92 μm and an average wire diameter of 111 ± 5 nm.

After nanowire placement, three sections of the aluminium shells are selectively removed by wet etching for 55 s with *MF-321* developer. These sections form the two quantum dot junctions and the coupling junction, with lengths 215 nm and 95 nm, respectively.

After the junctions etch, the nanowires are contacted to the transmon island and to ground by a 110 s argon milling step followed by the deposition of 150 nm-thick sputtered NbTiN. Finally, the chip is diced into 6 by 6 millimeters, glued onto a solid gold-plated copper block with silver epoxy, and connected to a custom-made printed circuit board using aluminium wire-bonds (Fig. 7.8g).

Cryogenic and room temperature measurement setup

The device was measured in an *Oxford instruments Triton* dilution refrigerator with a base temperature of approximately 20 mK. Details of the wiring at room and cryogenic temperatures are shown in Fig. 7.10. The setup contains an input radio-frequency (RF) line, an output RF line, an extra RF line for the drive tones, a flux-bias line and multiple direct current (DC) lines used to tune the electrostatic gate voltages. The DC gate lines are filtered at base temperature with multiple low-pass filters connected in series. The input, flux and drive RF lines contain attenuators and low-pass filters at different temperature stages, as indicated. In turn, the output RF line contains amplifiers at different temperature stages: a traveling wave parametric amplifier (TWPA) at the mixing chamber plate ($\approx$ 20 mK), a high-electron-mobility transistor (HEMT) amplifier at the 4 K stage, and an additional amplifier at room temperature. A three-axis vector magnet, for which the y and z coils are illustrated by yellow rectangles in Fig. 7.10 (x-axis not shown), is thermally anchored to the 4 K temperature stage, with the device under study mounted at its center. The three magnet coils are controlled with *Yokogawa GS610* current sources. The current through the flux line, I, is controlled with a *Yokogawa GS200* current source. At room temperature, a vector network analyzer (VNA) is connected to the input and output RF lines for spectroscopy at frequency f_r. On the input line, this signal is combined with a separate IQ-modulated tone also at f_r, only used for time-domain measurements. The IQ-modulated drive tone at frequency f_d and the pump tone at frequency f_p are both sent through the drive line. For time-domain measurements, the output signal is additionally split off into a separate branch and down-converted to be measured with a *Quantum Machines OPX*.

Data processing

Background subtraction for single-tone and two-tone spectroscopy measurements. For all single-tone spectroscopy measurements shown in the main text and Supplementary Information, we plot the amplitude of the transmitted signal, $|S_{21}|$, with the frequency-dependent background, $|S_{21,b}(f_r)|$, divided out, in dB: $10\log_{10}(|S_{21}|/|S_{21,b}|)$. The background is extracted from an independent measurement of the transmission through the feedline as a function of V_C. To determine the background for each f_r we do not consider transmission data for which the resonator frequency is more than 20 MHz close to f_r, so that the presence of the resonator does not impact the extracted background.

For two-tone spectroscopy measurements, we instead plot the transmitted signal, $|S_{21}|$, with the frequency-independent background, $|S_{21,m}|$, subtracted: $|S_{21}| - |S_{21,m}|$. In this case, the background is defined as the median of $|S_{21}|$ of each frequency trace.

Gaussian fits to extract J from spectroscopy measurements. To extract the value of the coupling strength from the peak splitting observed in spectroscopy measurements, we follow the following procedure:
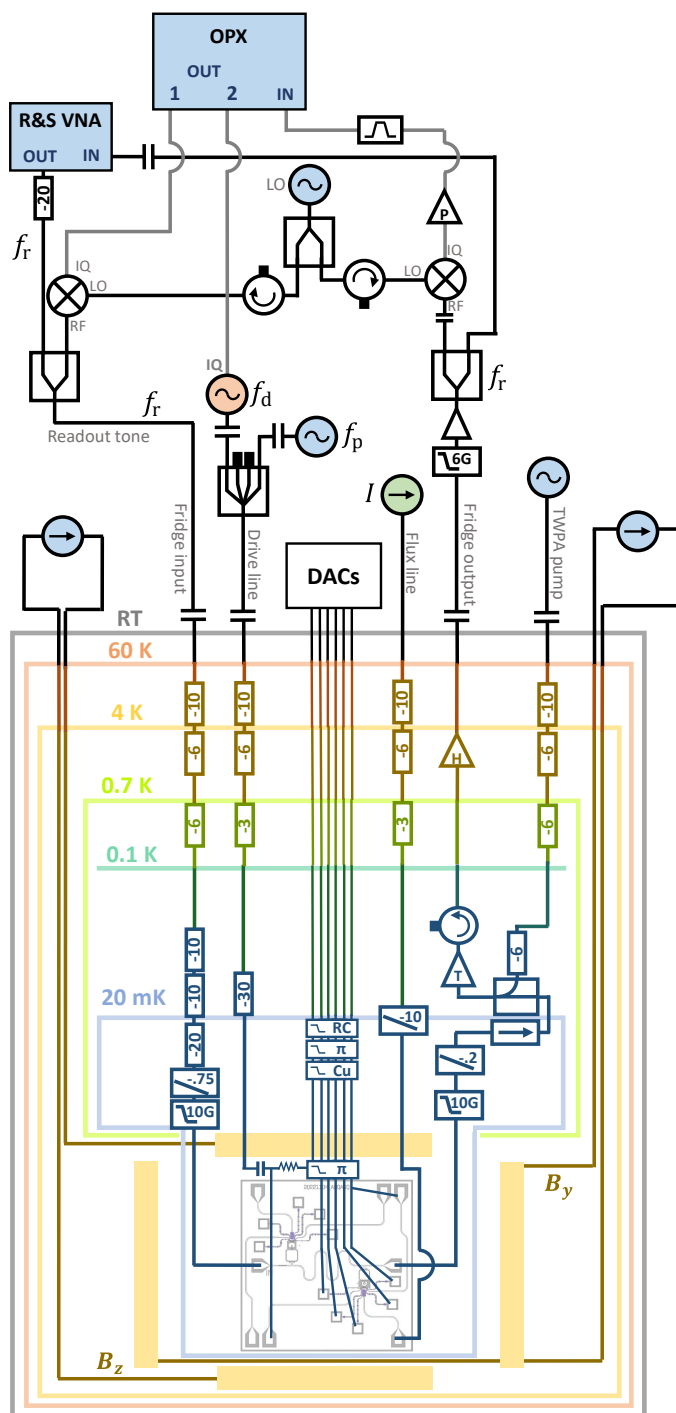
7

Figure 7.10: **Measurement setup.**

1. We first fit the two-tone spectroscopy signal in the absence of a pump tone with a single Gaussian function of the form

$$\frac{A}{\sqrt{2\pi\sigma^2}} \exp\left(\frac{-(f_\mathrm{d} - f_a)^2}{2\sigma^2}\right) + Bf_\mathrm{d} + C, \tag{7.19}$$

   from which we extract the position of the first peak, f_a, and its width, σ.

2. Next, we fit the two-tone spectroscopy signal in the presence of a pump tone with a double Gaussian function of the form

$$\frac{A_a}{\sqrt{2\pi\sigma^2}} \exp\left(\frac{-(f_\mathrm{d} - f_a)^2}{2\sigma^2}\right) + \frac{A_b}{\sqrt{2\pi\sigma^2}} \exp\left(\frac{-(f_\mathrm{d} - f_b)^2}{2\sigma^2}\right) + Bf_\mathrm{d} + C, \tag{7.20}$$

   for which the peak widths σ, as well as the position of the first peak, f_a, are fixed to their values extracted from the previous fit. From this fit, we extract the position of the second peak, f_b, as well as the chi-square of the fit, χ^2_double.

3. Next, we repeat a fit to the two-tone spectroscopy signal in the presence of a pump tone with a single Gaussian function (Eq. (7.19)) and extract the chi-square of the fit, χ^2_single.

4. To determine whether a double Gaussian fits better than a single Gaussian, we compare the goodness of fit of a double and single Gaussian fit. If $(\chi^2_\mathrm{single} - \chi^2_\mathrm{double})/\chi^2_\mathrm{double} \geq 0.1$, we conclude that the data shows two peaks and extract J as $J = (f_a - f_b)/2$ and the error of J as the error of f_b extracted from the double Gaussian fit (its one-sigma confidence interval).

5. If, else, $(\chi^2_\mathrm{single} - \chi^2_\mathrm{double})/\chi^2_\mathrm{double} < 0.1$, we conclude that the data shows a single peak and thus $J = 0$. For these data points, we do not observe a peak splitting at any third tone powers comparable to those used for setpoints where we do observe splitting.

Determination of the flux axis. To determine the flux axis for data that we display in the main text as a function of Φ_i, we map the corresponding flux control parameter (I for the loop containing ASQ1 and B_y for the loop containing ASQ2) to the fluxes Φ_1 and Φ_2. To do so, we need to determine the value of the control parameter corresponding to $\Phi_i = 0$ (denoted as $I_{\Phi_1=0}$ and $B_{y,\Phi_2=0}$, respectively) as well as the one flux quanta (denoted as I_{Φ_0} and B_{y,Φ_0}, respectively). The former is independently determined for each separate measurement, from fits of the data to the expected transitions.

The values of the flux quanta ($I_{\Phi_0} = 9.62\,\mathrm{mA}$ for Φ_1 and $B_{y,\Phi_0} = 3.16\,\mathrm{mT}$ for Φ_2) are fixed throughout all main text and supplementary figures and is extracted from fits to the data in Fig. 2a and b in the main text. The data in Fig. 2b is fitted with a sinusoidal dependence of the form

$$2E^\sigma_{\mathrm{J},2} \sin\left(2\pi \frac{B_y - B_{y,\Phi_2=0}}{B_{y,\Phi_0}}\right) + C, \tag{7.21}$$

as expected for a quantum dot Josephson junction (Padurariu and Nazarov, 2010; Bargerbos et al., 2023a). The data in Fig. 2a is instead fitted with a phenomenological skewed sinusoidal dependence of the form

$$2E_{J,1}^{\sigma} \sin\left(2\pi \frac{I - I_{\Phi_1=0}}{I_{\Phi_0}} + S\sin\left(2\pi \frac{I - I_{\Phi_1=0}}{I_{\Phi_0}}\right)\right) + C, \tag{7.22}$$

where $-1 < S < 1$ is the skewness parameter. For the data in Fig. 1a, we extract $S = -0.39$. The observed skewness of the spin-flip is, to our knowledge, not predicted by existing models (Padurariu and Nazarov, 2010; Bargerbos et al., 2023a), so further investigation is needed to explain its origin.

7.7.3 Basic characterization and tuneup

Readout resonator characterization

In this section, we perform a fit to a bare resonator spectroscopy trace and extract the resonator parameters shown in Tab. 7.1. The result of a single-tone resonator trace, performed with all Josephson junctions pinched off, is shown with black markers in Fig. 7.11. The grey lines show the best fit of the complex transmission to the expected dependence (Khalil et al., 2012; Flanigan)

$$S_{21}(f_r) = 1 - \frac{1 + i\alpha}{1 + \frac{Q_c}{Q_i} + 2Q_c i \frac{f_r - f_{r,0}}{f_{r,0}}}, \tag{7.23}$$

where $f_{r,0}$ is the bare resonator resonance frequency, Q_c and Q_i are the coupling and internal quality factors, respectively, and α is a real number to account for the resonator asymmetry.
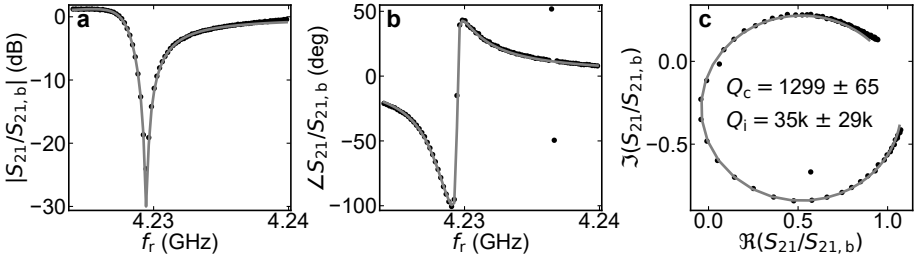

Figure 7.11: **Single-tone spectroscopy of the resonator and quality factor extraction.** All panels show the measured data (black markers) and a fit to Eq. (7.23) (grey line). **a** and **b** show, respectively, the amplitude and phase of the S_{21} signal as a function of frequency. **c** shows the imaginary and real parts of the complex S_{21} signal. From the fit, we extract a resonator bare frequency of $f_{r,0} = 4.228\,50\,\text{GHz} \pm 91\,\text{kHz}$ and the quality factors indicated in **c**.

Gate and flux characterization

Throughout this manuscript, we use B_y, which affects both Φ_1 and Φ_2, to tune Φ_2 and the current through the flux line, I, to tune Φ_1. Fig. 7.12a shows the B_y tunability of Φ_2, for which the period corresponds to 3.25 mT. Note that this value is slightly larger than

the actual flux quantum due to the small flux jumps present in the signal. Fig. 7.12c and b show how the current through the flux line, I, controls Φ_1, for which a flux quantum corresponds to 9.61 mA, while leaving Φ_2 unaffected.
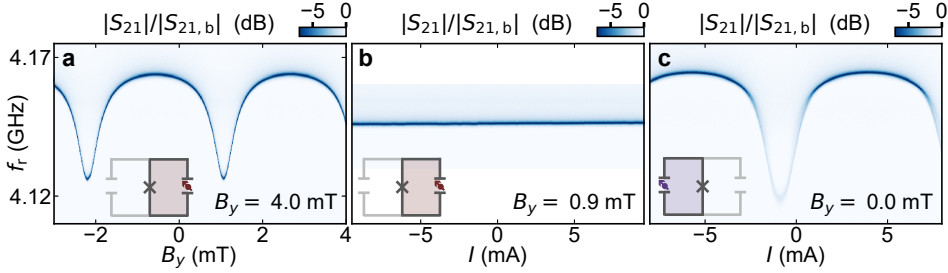

Figure 7.12: **Flux control.** Amplitude of the transmission through the readout circuit, $|S_{21}|$, with background, $|S_{21,b}|$, divided out. **a, b** With ASQ1 closed ($V_{LP1} = V_{R1} = -1000$ mV) and ASQ2 open to a singlet state with large Josephson energy. **a** shows the dependence on B_y, which tunes Φ_2, while **b** shows the dependence on the current through the flux line, I, which leaves Φ_2 unaffected. **c** With ASQ1 open to a singlet state with large Josephson energy and ASQ2 closed ($V_{L2} = V_{P2} = V_{R2} = -1000$ mV), plotted versus I, which controls Φ_1. For all panels, $B_x = B_z = 0$ and $V_C = 1995$ mV.

We now investigate the performance of all electrostatic gates. Fig. 7.13 shows the resonator frequency, measured by single-tone spectroscopy, while various combinations of gates are varied. In all cases, only at most one of the three junctions is open, thus not defining any loops. All junctions can be fully pinched off using any of the gates that control them while leaving the rest of the gates open, which confirms the proper functionality of all gates.

Panels a-c show the effect of varying the gates of ASQ1 either simultaneously (a) or separately (b, c). Note that the left and plunger gates of ASQ1 are connected to each other on-chip and thus are always set at the same voltage, V_{LP1}, while the right gate of ASQ1 is set at voltage V_{R1}. The effect of the left, plunger and right gates of ASQ2, respectively set at voltages V_{L2}, V_{P2} and V_{R2}, is shown in panels e-h. Although the pinch-off voltages for ASQ2 are slightly lower, this junction displays a behavior similar to that of ASQ1. Panel d shows the effect of V_C, the voltage of the coupling Josephson junction gate, which tunes $E_{J,C}$. By varying V_C, the transmon frequency can be tuned to values above the bare resonator frequency, thus resulting in an avoided crossing between the resonator and transmon frequencies at around $V_C = 500$ mV. We find a transmon-resonator coupling strength $g/h \sim 287$ MHz as half of the distance between the two resonances observed at the avoided crossing.

Next, we measure the V_C-dependence of the transmon frequency f_t with both ASQs pinched off, from which we calibrate the V_C to $E_{J,C}$ map which is used for the data processing behind Fig. 4 in the main text.

The black markers in Fig. 7.14a show the transmon frequency as a function of V_C, measured directly after the data shown in Fig. 4 of the main text and at the same magnetic field conditions ($B_r = 35$ mT applied in the chip plane and six degrees away from the z direction). For comparison, we also show the transmon frequencies measured while taking the data in Fig. 4e (teal markers), with both ASQs open. In this case, the measured frequencies deviate from the black markers, since they instead result from a parallel combination of
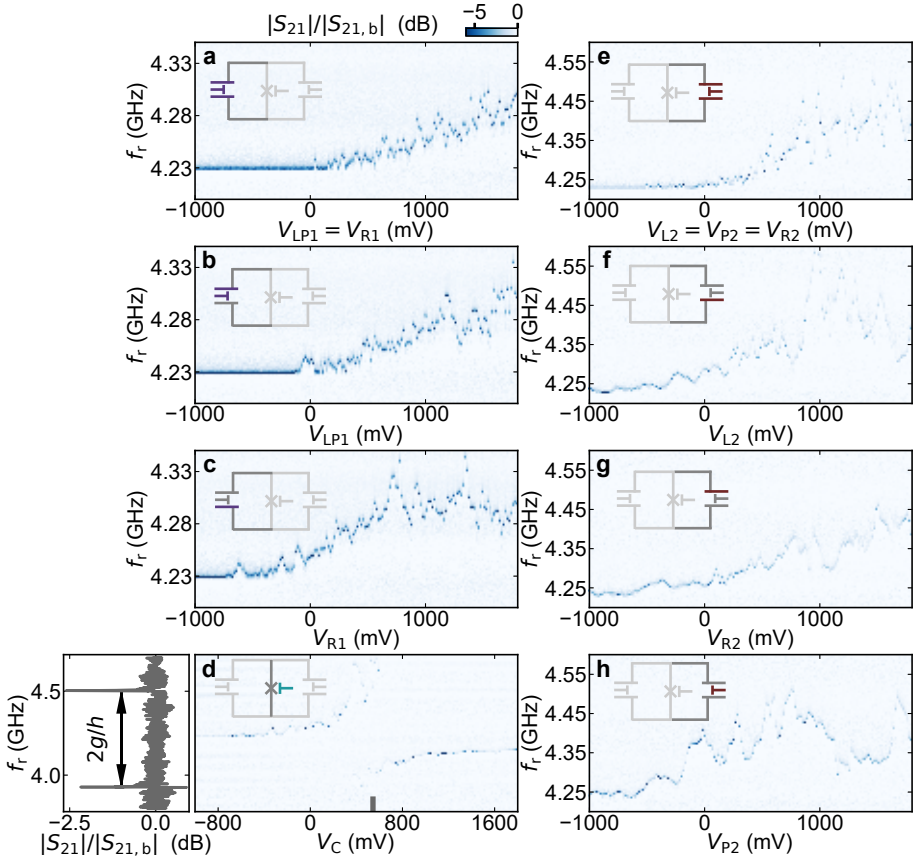
Figure 7.13: **Individual characterization of electrostatic gates.** All panels show single-tone spectroscopy of the resonator versus different gate voltages. The gate voltages that are being varied in each case are highlighted with colors in the insets. Dark grey shaded gates indicate open gates set to 1800 mV. Light grey shaded gates indicate closed gates set to −1000 mV. The panel to the left of **d** shows a line cut of the data in **d** taken at the V_C value indicated with a grey line in the x-axis. From this line cut we extract the transmon-resonator coupling energy g.

$E_{J,C}$ and the Josephson energies of both qubits. The black markers in Fig. 7.14a are used to determine the V_C-dependence of $E_{J,C}$ shown in Fig. 7.14b, given the value of E_c independently determined from a measurement of the transmon anharmonicity (see Tab. 7.1). These data are used to determine the x-axis of Fig. 4e in the main text.

ASQ gate setpoints

In this section, we discuss the tune-up of each individual ASQs, which results in the chosen gate setpoints specified in Tab. 7.2.

The tune-up of ASQ1 is presented in Fig. 7.15. We first set the junction containing ASQ2 to pinch-off by setting its three gates to −1000 mV and set the ASQ1 gates to a region where we detect a sizable spin-splitting energy in a low-resolution measurement.
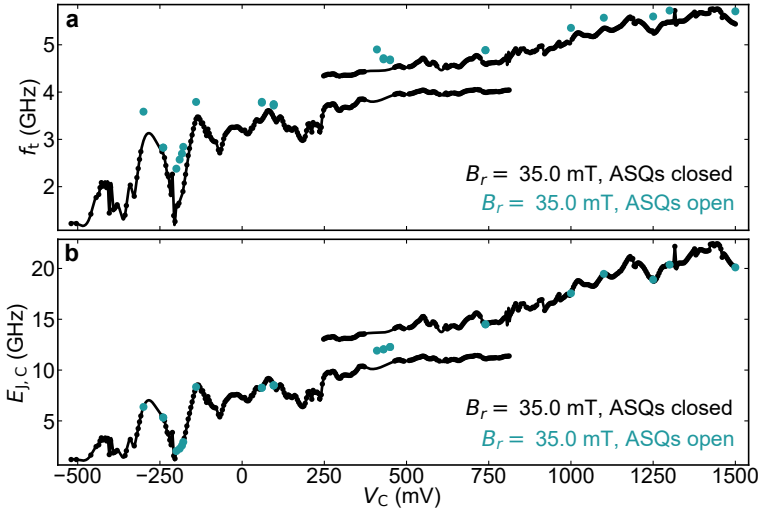
Figure 7.14: **Coupling junction characterization a** Transmon frequency, f_t, versus the coupling junction gate voltage, V_C, extracted by peak-finding in two-tone spectroscopy data. The black markers are taken at the magnetic field conditions at which we measured main text Fig. 4 but with both ASQ junctions fully closed (all quantum dot gates set to -1000 mV). The continuous line is a cubic interpolation to the measured data. The teal markers indicate the V_C, f_t points at which we measured longitudinal coupling in Fig. 4e. Note that, the teal markers deviate from the black markers, because there f_t is determined by the combination of $E_{J,C}$, $E_{J,1}^I$, $E_{J,1}^I$, $E_{J,1}^\sigma$, $E_{J,1}^\sigma$, Φ_1 and Φ_2, and not solely by $E_{J,C}$ as for the black markers. **b** Coupling junction Josephson energy $E_{J,C}$ versus V_C obtained directly from the corresponding data in **a**, given the measured E_c value specified in Tab. 7.1. The mapping between V_C and $E_{J,C}$ indicated with a continuous black line is used to obtain the x-axis of Fig. 4e in the main text.

From the transmon frequency at $\Phi_1 = 0, \Phi_0/2$ we estimate the spin-independent Josephson energy $E_{J,1}^I$ and map it out over a region in gate space using the two gate voltages of ASQ1 (Fig. 7.15a). Then, we proceed to investigating the value of the spin-dependent Josephson energy, $E_{J,1}^\sigma$. One way of doing so would be directly mapping out the spin-flip frequency f_1 in gate space. However, the visibility of the transition is significantly reduced at $B = 0$ due to the thermal population of the ASQ as well as to the smaller matrix element from driving the spin transition. We instead perform Φ_1-dependent transmon spectroscopy at a few selected gate points indicated with markers in Fig. 7.15a (Fig. 7.15b-g). For each gate setpoint we estimate the values of $E_{J,1}^\sigma/h$ by matching the distance between transmon frequencies at $\Phi_1 = \Phi_0/4$ to its theoretically expected value extracted from numerical diagonalization of Eq. (7.16) in the phase basis. Similarly, $E_{J,1}^I$ is estimated by fitting the measured transmon frequencies at $\Phi_1 = 0, \Phi_0/2$ to their theoretically expected values. The resulting quantities are indicated as labels on each panel. We choose the gate setpoint used for ASQ1 in the main text by maximizing $E_{J,1}^\sigma$ while keeping the value of $E_{J,1}^I$ low, since a high value negatively impacts the maximal coupling strength J. The chosen ASQ1 gate setpoint (see Tab. 7.2) is indicated in Fig. 7.15a with a purple marker.

Next, we pinch off the junction containing ASQ1 to tune-up the gate configuration of ASQ2. We perform an investigation analogous to the one detailed above, as shown in
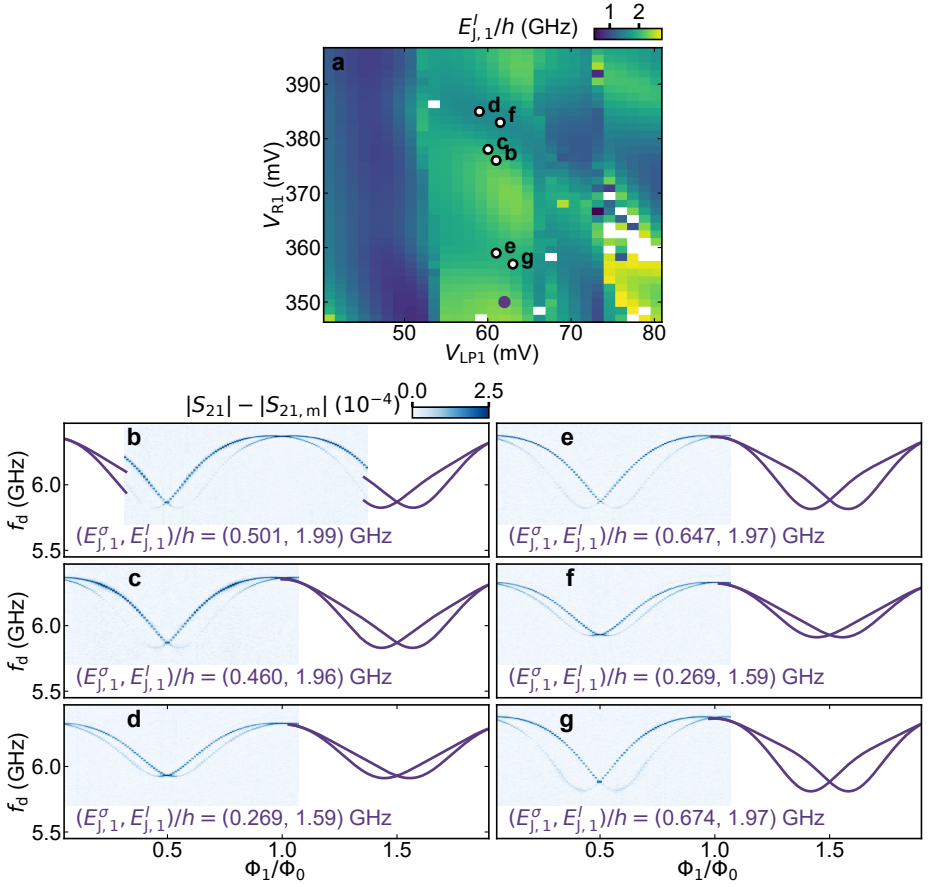
Figure 7.15: **ASQ1 gate dependence around its gate setpoint. a** Estimate of spin-independent Josephson energy of ASQ1, $E_{J,1}^I$, versus the two gate voltages of ASQ1, derived from the transmon transition frequency measured with two-tone spectroscopy at $B_r = 0$ and at two different flux values: $\Phi_1 = 0$ and $\Phi_1 = \Phi_0/2$. The purple marker indicates the gate setpoint of ASQ1 in the main text. **b** - **g** Transmon spectroscopy at various gate configurations, indicated with markers in **a**. The values of $E_{J,1}^I/h$ indicated in the labels are extracted by fitting the measured transmon frequencies at $\Phi_1 = 0$ and $\Phi_1 = \Phi_0/2$ to their theoretical values. The value of $E_{J,1}^\sigma/h$ is extracted from the distance between transmon frequencies at $\Phi_1 = \Phi_0/4$. The continuous lines are the corresponding transmon frequencies obtained by numerical diagonalization of an adapted Eq. (7.16) in which the spin-dependent potential of ASQ1 is replaced by a skewed sinusoidal shape $E_{J,1}^\sigma \sigma_1^z \sin(\varphi_1 + S \sin \varphi_1)$, where $\varphi_1 = \frac{2\pi}{\Phi_0} \Phi_1$. Panels **b** - **g** share the color map.

Fig. 7.16. Fig. 7.16a is measured in the same way as Fig. 7.15a and displays the evolution of $E_{J,2}^I$ with the tunnel gates, V_{L2} and V_{R2}, while V_{P2} is kept at 0 mV. Fig. 7.16b shows the tunnel gate dependence of $E_{J,2}^\sigma$, determined from direct spin-flip spectroscopy of ASQ2 at $B = 0$: $E_{J,2}^\sigma/h = f_2(B = 0, \Phi_2 = \Phi_0/4)/2$. Similarly to the strategy for ASQ1, we choose a gate setpoint for ASQ2 by maximizing $E_{J,2}^\sigma$ while keeping $E_{J,2}^I$ as low as possible. However, for some gate points in this region of gate space, a singlet state is also slightly visible in transmon spectroscopy (as can be seen in Fig. 7.16c, around $\Phi_2 = 0$). The presence of the
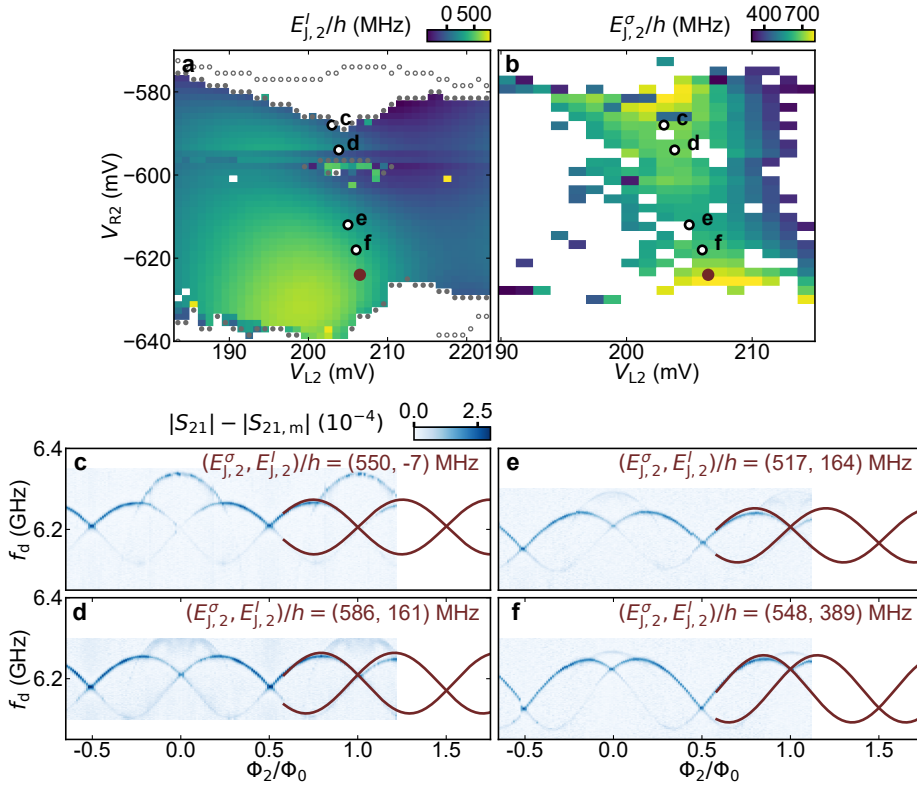
Figure 7.16: **ASQ2 gate dependence around its gate setpoint. a** Estimate of spin-independent Josephson energy of ASQ2, $E_{J,2}^I/h$, versus the two tunnel gates of ASQ2, for fixed $V_{P2} = 0$, obtained from two-tone spectroscopy measurements of the transmon transitions at $B_r = 0$ and at two different flux values: $\Phi_2 = 0$ and $\Phi_2 = \Phi_0/2$. The open and filled grey markers indicate the boundaries of the singlet-doublet transition at $\Phi_2 = 0$ and $\Phi_2 = \Phi_0/2$, respectively. **b** Estimate of spin-dependent Josephson energy of ASQ2, $E_{J,2}^\sigma/h$, versus the two tunnel gates of ASQ2, for fixed $V_{P2} = 0$, obtained from two-tone spectroscopy measurements of the spin-flip transition, f_2, at $B_r = 0$ and $\Phi_2 = \Phi_0/4$. The maroon marker in **a** and **b** indicates the gate setpoint of ASQ2 in the main text. **c** - **f** Transmon spectroscopy at various gate configurations indicated with markers in **a** and **b**. The values of $E_{J,2}^I/h$ indicated in the labels are extracted by fitting the measured transmon frequencies at $\Phi_2 = 0$ and $\Phi_2 = \Phi_0/2$ to their theoretical values. The value of $E_{J,2}^\sigma/h$ is extracted from the distance between transmon frequencies at $\Phi_2 = \Phi_0/4$. The continuous lines are the corresponding transmon frequencies obtained by numerical diagonalization of Eq. (7.16). Panels **c** - **f** share the color map.

singlet state indicates that the singlet phase of the system is only separated by an energy gap comparable to the thermal energy of the system. Consequently, while choosing the ASQ2 setpoint we also minimize the visibility of the singlet state. The chosen setpoint (see Tab. 7.2 is indicated in Fig. 7.16a and b with a maroon marker).

Finally, we perform in-field spin-flip spectroscopy of both ASQs, as well as transmon spectroscopy at zero field, to more accurately determine their Josephson energies detailed in Tab. 7.2.

The spin-flip spectroscopy shown in Fig. 7.17a and b is performed under the same mag-
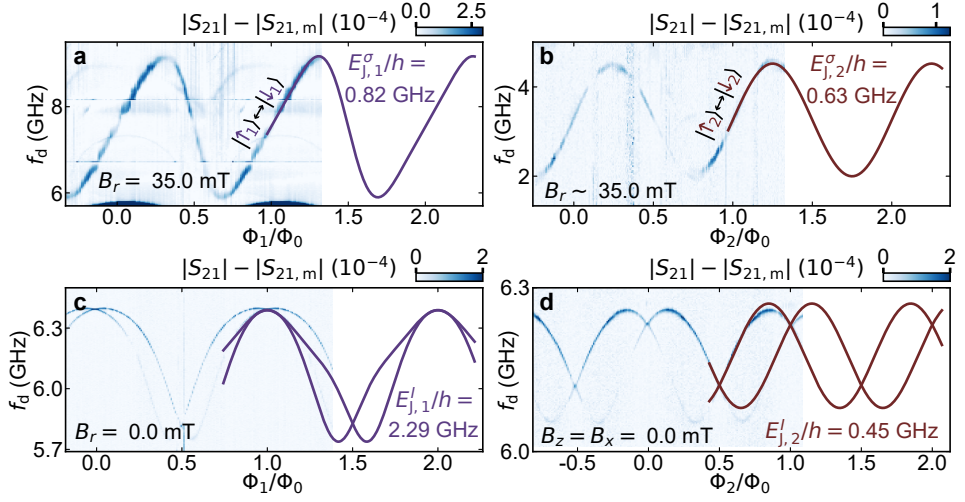
Figure 7.17: **Parameter estimation for both ASQs. a** Spin-flip spectroscopy of ASQ1 versus Φ_1, at $B_r = 35$ mT. The line shows a fit to a skewed sinusoidal dependence (Eq. (7.22)) from which we extract the value of $E_{J,1}^\sigma/h = 0.82$ GHz. **b** Spin-flip spectroscopy of ASQ2 versus Φ_2, at $B_r \sim 35$ mT. The line shows a fit to a sinusoidal dependence (Eq. (7.21)) from which we extract the value of $E_{J,2}^\sigma/h = 0.63$ GHz. **c** Transmon spectroscopy versus Φ_1, at $B_r = 0$ mT with ASQ1 open to its setpoint (see Tab. 7.2) and ASQ2 closed. The two transmon frequencies correspond to the two possible states of ASQ1. **d** Transmon spectroscopy versus Φ_2, at $B_r = 0$ mT with ASQ2 open to its setpoint (see Tab. 7.2) and ASQ1 closed. The two transmon frequencies correspond to the two possible states of ASQ2. For **a** and **b**, $V_C = 1500$ mV, while for **c** and **d**, $V_C = 1995$ mV. The continuous lines in **c** and **d** show the transmon transition spectrum given the spin-dependent part of the ASQ potentials found in **a**, **b** and the measured value of E_c (see Tab. 7.1). In both cases, the frequencies are obtained by numerical diagonalization of the Hamiltonian in Eq. (7.16) and are best fits of the measured data at Φ_i being integer multiples of $\Phi_0/2$. From these transmon spectra, we extract the values of the spin-independent Josephson energies $E_{J,1}^I/h = 2.29$ GHz and $E_{J,2}^I/h = 0.45$ GHz.

	V_{Li} (mV)	V_{Pi} (mV)	V_{Ri} (mV)	$E_{J,i}^I/h$ (GHz)	$E_{J,i}^\sigma/h$ (GHz)
ASQ1	62.0	62.0	350.0	2.29	0.82
ASQ2	206.50	0.0	-624.0	0.45	0.63

Table 7.2: ASQ1 and ASQ2 gate voltage set points and extracted model parameters from the measurements in Fig. 7.17.

netic field conditions as the ones where we measured coupling in the main text. We extract $E_{J,1}^\sigma/h = 0.82$ GHz and $E_{J,2}^\sigma/h = 0.63$ GHz from fits of a skewed and non-skewed sine, respectively, to the measured data (see Sec. 7.7.2). The $E_{J,i}^\sigma/h =$ values are determined as one fourth of the flux dispersion of the fit result. $E_{J,1}^I/h = 2.29$ GHz and $E_{J,2}^I/h = 0.45$ GHz are determined similarly to how it was done for Figs. 7.15 and 7.16, by fitting the Φ_i-dependent data to the expected transmon frequencies obtained by numerical diagonalization of the Hamiltonian in Eq. (7.16) at Φ_i being integer multiples of $\Phi_0/2$. In both cases, we fix the spin-dependent part of the transmon potential to that extracted from the fits in Fig. 7.17a and b.

Andreev spin qubit readout

In the main text (Fig. 1d) we discussed how, when both loops are open, we observe four possible resonator frequencies, depending on the four possible spin states of the ASQ1-ASQ2 system, $\{|\uparrow_1\uparrow_2\rangle, |\uparrow_1\downarrow_2\rangle, |\downarrow_1\uparrow_2\rangle, |\downarrow_1\downarrow_2\rangle\}$. This allows us to perform two-tone spectroscopy of either one of the two qubit transitions, f_1 and f_2, which are present when both ASQ junctions are open. Here, we show the analogous situation when only *one* out of the two ASQs is open, while the junction containing the other one is fully pinched off (Fig. 7.18).

Fig. 7.18a shows the Φ_1-dependence of resonator spectroscopy, at zero magnetic field and when only ASQ1 is open. In this case, we observe two branches of the resonator frequency, corresponding to the two possible states of ASQ1: $|\uparrow_1\rangle$ or $|\downarrow_1\rangle$). The different visibility of each of the branches is a consequence of the different thermal populations of the two states at $B_r = 0$. This is expected, since the spin-splitting of ASQ1 varies with flux reaching up to $2E_{J,1}^{\sigma}/h = 1.64\,\text{GHz}$, comparable, when transformed into an effective temperature, to typical electron temperatures found in other experiments (Jin et al., 2015; Pita-Vidal et al., 2023a; Uilhoorn et al., 2021). Fig. 7.18b shows the analogous situation but now for ASQ2. In this case, the resonator also displays two separate frequencies. After fixing B_y so that $\Phi_2 \sim -\Phi_0/4$ and so that the separation between the resonator frequencies corresponding to $|\uparrow_2\rangle$ and $|\downarrow_2\rangle$ is sizable, we open ASQ1 to its setpoint. In such situation, when performing resonator spectroscopy versus Φ_1, we observe four different transitions, labeled with their corresponding states in Fig. 7.18c. Note that, in this case, the difference in visibility becomes more perceptible due to the larger energy separation between the different states $\{|\uparrow_1\uparrow_2\rangle, |\uparrow_1\downarrow_2\rangle, |\downarrow_1\uparrow_2\rangle, |\downarrow_1\downarrow_2\rangle\}$.
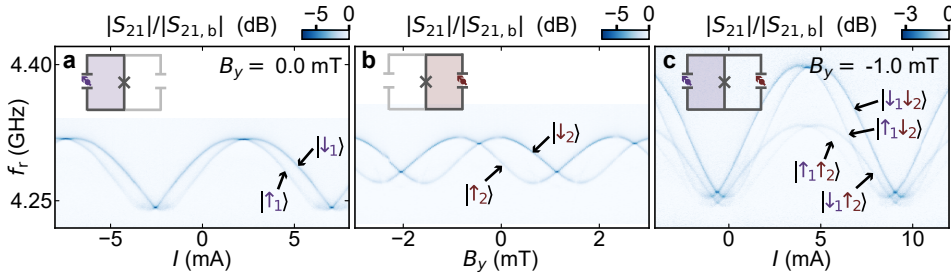

Figure 7.18: **Readout.** Amplitude of the transmission through the readout circuit, $|S_{21}|$, with background, $|S_{21,b}|$, divided out. **a** With ASQ1 open at its setpoint (see Tab. 7.2) and ASQ2 closed ($V_{L2} = V_{P2} = V_{R2} = -1000\,\text{mV}$). **b** With ASQ1 closed ($V_{LP1} = V_{R1} = -1000\,\text{mV}$) and ASQ2 open at its setpoint (see Tab. 7.2). **c** With both ASQ1 and ASQ2 open, as also displayed in Fig. 1d of the main text. **a, c** are plotted vs. the current through the flux line I, which controls Φ_1. **b** is plotted vs. B_y, which controls Φ_2. For all panels, $B_x = B_z = 0$ and $V_C = 180\,\text{mV}$.

Magnetic field angle dependence and determination of the spin-orbit direction

In this section, we specify the measurements performed to determine the zero-field spin-polarization direction for each Andreev spin qubit. For each qubit, we perform spin-flip spectroscopy measurements, like those shown in Fig. 7.17a and b, for different magnetic field directions. As reported previously in Bargerbos et al. (2023a), we observe that both the flux dispersion of the spin-flip transition, df, as well as the g-factor, depend strongly on the direction of the applied magnetic field. To determine these quantities, the maxima,

f_i^{max}, and minima, f_i^{min}, of the spin-flip frequencies are first extracted by hand from two-tone spectroscopy measurements of the spin-flip transition, analogous to those in Fig. 2a-c of the main text. The g-factors are calculated from the average of these maximum and minimum frequencies, as $g = (f_i^{\mathrm{max}} + f_i^{\mathrm{min}})/(2\mu_{\mathrm{B}}B_r)$, where μ_{B} is the Bohr magnetron and B_r is the magnitude of the applied magnetic field. The frequency dispersion is determined as $df = (f_i^{\mathrm{max}} - f_i^{\mathrm{min}})/2$. The dependence of g and df on the magnetic field direction is shown in Fig. 7.19 with purple and maroon markers for ASQ1 and ASQ2, respectively.

First, we investigate the angle dependence on the angle within the chip plane and away from the nanowire axis, $\theta_{\phi=90}$. $\theta_{\phi=90} = 0$ indicates that the field is applied approximately along the nanowires axis, while $\theta_{\phi=90} = 90$ degrees indicates that the field is applied in-plane but approximately perpendicular to the nanowire axis. We find that the g-factor of ASQ1 depends strongly on $\theta_{\phi=90}$, while that of ASQ2 stays almost constant, fluctuating only between 5.5 and 6.5 (Fig. 7.19a). Within this plane, the g-factor of ASQ1 is found to be maximal when the magnetic field B_r is applied approximately along the nanowires axis, while for ASQ2 it is maximized for $\theta_{\phi=90} \sim 31$ degrees away from the nanowire axis. Performing the same experiment while varying the field direction in the x-z plane, the plane perpendicular to the chip and containing the nanowires axis, we observe a similar dependence (Fig. 7.19c). This time, the ASQ1 g-factor is again maximized along the nanowires axis, while that of ASQ2 becomes maximal when B_r is applied $\theta_{\phi=0} \sim 60$ degrees away from the nanowires axis. This variability of the g-factor dependence for different configurations is consistent with previous observations of quantum dots implemented in InAs nanowires and is thought to be due to mesoscopic fluctuations of the electrostatic environment at the quantum dot (Han et al., 2023; Bargerbos et al., 2023a).

To learn about the zero-field spin-polarization direction of each qubit, we now focus on the field-direction dependence of the flux dispersion of the spin-flip transition. We denote by df the difference in frequency between the maximum and minimum of the spin-flip frequency versus flux. When the field is applied along the zero-field spin-polarization direction, we expect that $df = 4E_{\mathrm{J},i}^{\sigma}$ (see Sec. 7.7.1). However, when a component of the applied magnetic field is perpendicular to the zero-field spin-polarization direction, df is reduced due to the hybridization of the two spin states (Bargerbos et al., 2023a). Fig. 7.19b shows the $\theta_{\phi=90}$ dependence of df for both ASQs. We find that, in both cases, df becomes minimal at a direction approximately perpendicular to the nanowire axis. We also perform a similar experiment in the x-z plane (see Fig. 7.19d). The extracted angles constitute two of the directions perpendicular to the spin-polarization axis. Their cross-product thus returns the zero-field spin polarization directions for each qubit, which are indicated in Tab. 7.3 in spherical coordinates, where $\theta_\parallel$ denotes the polar angle away from the nanowire axis and $\phi_\parallel$ denotes the azimuthal angle measured away from the x-axis (see Fig. 7.19). The angle between this direction and the direction of the applied magnetic field in Figs. 3 and 4 of the main text ($\theta = 185, \phi = 90$) is indicated in the last column of Tab. 7.3.

The angle used for all measurements in the main text, except for Fig. 2c,d, is indicated with vertical dotted lines in Fig. 7.19a and b. We chose this angle following various considerations. First, we wanted to minimize the field component perpendicular to the spin directions of each of the ASQs. The reason for this is that we expect transverse qubit-qubit coupling terms to emerge under the presence of a large perpendicular Zeeman energy compared to $E_{\mathrm{J},i}^{\sigma}$, at the cost of the longitudinal component. Second, we wanted to maximize
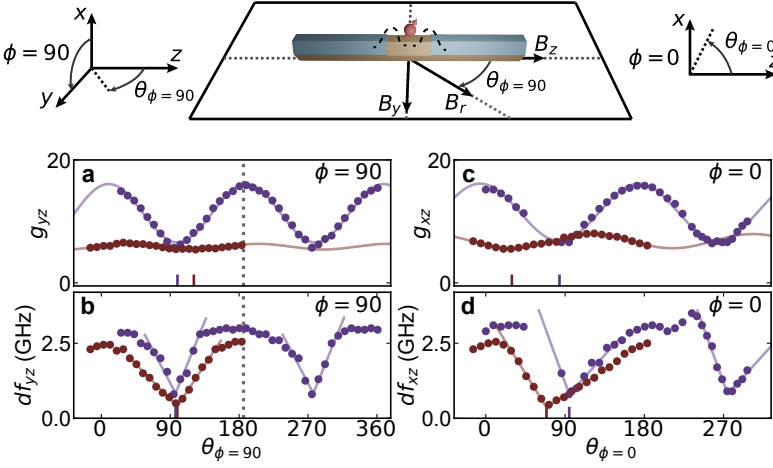
Figure 7.19: **Magnetic field angle dependence. a** g-factor for both ASQs for varying magnetic field direction in the chip plane, $y - z$, plotted as a function of the angle between the applied field and the nanowire axis, $\theta_{\phi=90}$. The g-factor is calculated as the average between its maximum and minimum values versus flux. Data points corresponding to ASQ1 and ASQ2 are colored purple and maroon, respectively. The continuous lines are cosinusoidal fits to the data. **b** Flux-dispersion of the spin-flip, df_{yz}, for both ASQs versus $\theta_{\phi=90}$. df_{yz} is calculated as the difference between the maximum and minimum of the spin-flip frequency f_i versus flux. The continuous lines are fits to the data around their minima and the colored vertical lines on the x-axis indicate the positions of the minima extracted from the fits, which are interpreted as the directions perpendicular to the zero-field spin-polarization direction for each qubit. Note that these lines do not coincide with the minima of the g-factors found in **a**. The vertical dotted lines in **a**, **b** indicate the field angle along which all measurements in the main text, except for Fig. 2c,d, were taken. **c**, **d** Same as **a**, **b** but in the $x - z$ plane, the plane perpendicular to the chip which contains the nanowires axis.

the difference in g-factors to avoid crossings between the qubit frequencies versus flux. This enables the possibility of spectroscopically measuring the coupling strength at every flux point. Finally, we chose the total field magnitude $B_r = 35\,\text{mT}$ to set the ASQ frequencies at setpoints that did not cross neither the resonator nor any transmon transition frequency for any value of flux.

	$\theta_{\parallel}$	$\phi_{\parallel}$	α
ASQ1	8.54	54.76	5.1
ASQ2	22.73	157.15	21.5

Table 7.3: **Zero-field spin-polarization directions for ASQ1 and ASQ2 in degrees.** The zero-field spin-polarization direction $(\theta_{\parallel}, \phi_{\parallel})$ is calculated as the vector product of the two perpendicular directions indicated with colored lines in the x-axis of Fig. 7.19b,d. α denotes the angle between the field applied in the main text measurements and the spin-polarization direction for each qubit.

7.7.4 Supplementary coherence data

We now describe the functions used for extracting the coherence times quoted in the main text. To determine T_1 we fit an exponential decay

$$y(t) = a \cdot \exp[t/T_1] + c \tag{7.24}$$

where a, T_1 and c are free fit parameters. For Ramsey and Hahn echo (see Figure 7.20) experiments we fit a sinusoide with a exponential decay envelope and sloped background

$$y(t) = a \cdot \cos\left(\frac{2\pi}{p}t - \phi\right) \cdot \exp\left[(-t/T_2)^{d+1}\right] + c + et \tag{7.25}$$

where a, T_2, ϕ, c, e and p are free fit parameters and d was fixed to 1, resulting in a Gaussian decay envelope. We found that $d = 1$ gave the least χ-squared in the fit compared to $d = 0, 2$. The tilted background was included to compensate for a slightly non-linear Rabi response.

Hahn echo decay time measurements of ASQ1 and ASQ2

To verify the slow nature of the noise causing dephasing, we performed Hahn-echo experiments with artificial detuning, shown in Figure 7.20. The resulting data was fit using Equation (7.25). Note that for these measurement we found that the data was not always within the range of the identity and π-pulse calibration points. We suspect this is due to the additional echo pulse inducing leakage to other states outside the spin-subspace. We therefore normalized the data setting 0 and 1 to the minimum and maximum of the fit envelope at $\tau = 0$ instead of using the calibration points as was done in the main text.
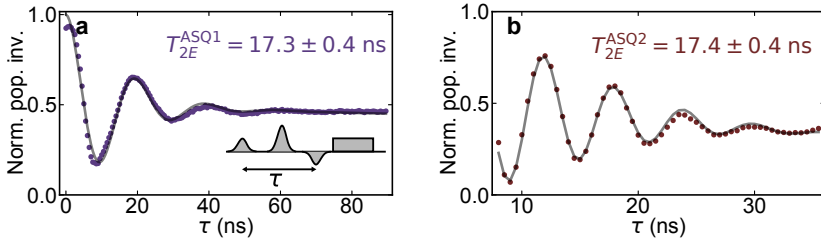

Figure 7.20: **Hahn echo experiment on ASQ1 and ASQ2. a, b** Measurement of T_2-echo for ASQ1 and ASQ2, respectively, with artificial detuning at the setpoints indicated in Fig. 2 of the main text. The pulse sequence is shown in the inset of **a**. This is the same sequence as used in the Ramsey experiment, but with a π-pulse added between the two $\pi/2$ pulses. In **a**, an artificial detuning corresponding to a period of 20 ns was set and in **b** it was set to 6 ns. This data was taken using Gaussian pulses with FWHM of 4 ns and averaged over $3 \cdot 10^5$ shots for each data point. The y-axis is normalized using the fit (for details, see the accompanying text in Section 7.7.4).

Coherence properties of the transmon

Although the transmon was used in this work to facilitate spin readout, we now demonstrate its coherence properties. Figure 7.21 shows measurements of the transmon's Rabi oscillations, Ramsey coherence time and energy decay time.

The transmon T_1 was found to be lower than that of previous implementations of a transmon using gate-tunable nanowires (Larsen et al., 2015; Casparis et al., 2016; Luthi

et al., 2018; Kringhøj et al., 2021; Pita-Vidal et al., 2023a; Bargerbos et al., 2023b), which we suspect may be due to it being too strongly coupled to the flux-bias line or drive lines. This in turn limits the ASQs T_1 due to Purcell decay via the transmon. Given a transmon T_1 of 53.6 ns, we can estimate the limit set by Purcell decay for each ASQ. At their setpoints in Fig. 2 in the main text, the detunings from the transmon were $\Delta_1 = 1.7$ GHz and $\Delta_2 = 2.2$ GHz for ASQ1 and ASQ2, respectively. From measurements of the avoided crossing between the ASQ spin-flip and transmon transitions under similar conditions, we extract that the coupling strengths between transmon and ASQ, $g_i \in$, are in the range 50 MHz to 100 MHz for both qubits. These quantities allow us to estimate the Purcell limit of T_1 for both qubits. to be 14-56 μs for ASQ2 and 23-92 μs for ASQ1. The higher harmonics of the transmon can reduce these lifetimes even more, especially for ASQ1 which resides close to the first higher harmonic. However, we did not measure the lifetime of that transition.
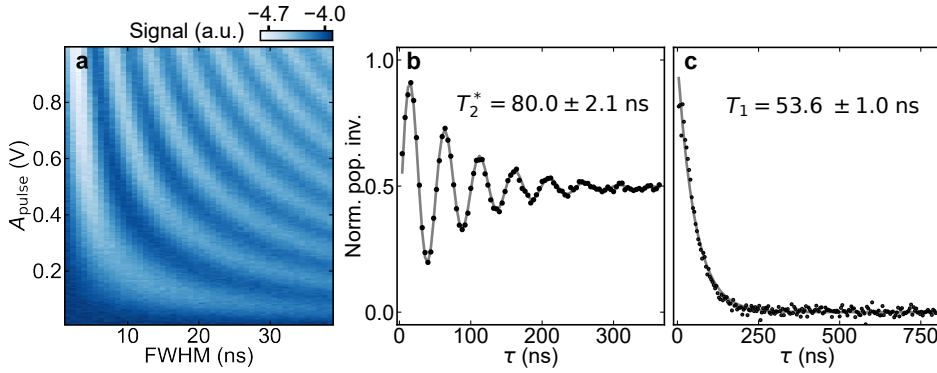

Figure 7.21: **Transmon coherence properties.** **a** Rabi oscillations versus the full-width at half maximum (FWHM) and amplitude of the Gaussian pulse. **b** Standard T_2^* measurement using a Ramsey sequence with Gaussian pulses of FWHM = 5.5 ns. The fit to Equation (7.25) (grey line) was performed here with $d = 0$. **c** T_1 measurement. For panels **b** and **c** the data was normalized using the fitted scaling constants of Equations (7.24) and (7.25).

Scaling of extracted T2* with pulse length

Due to the short dephasing time of ASQs with respect to the pulse length, the pulse length influences the observed life time of the ASQs when the pulses are (partly) overlapping (see Figure 7.22). This is the case because, during the part of the decay time τ, the ASQ is being driven. Therefore, care should be taken when pulses of length comparable to T_2^* are used. In the main text we report values obtained using short 4 ns FWHM pulses.
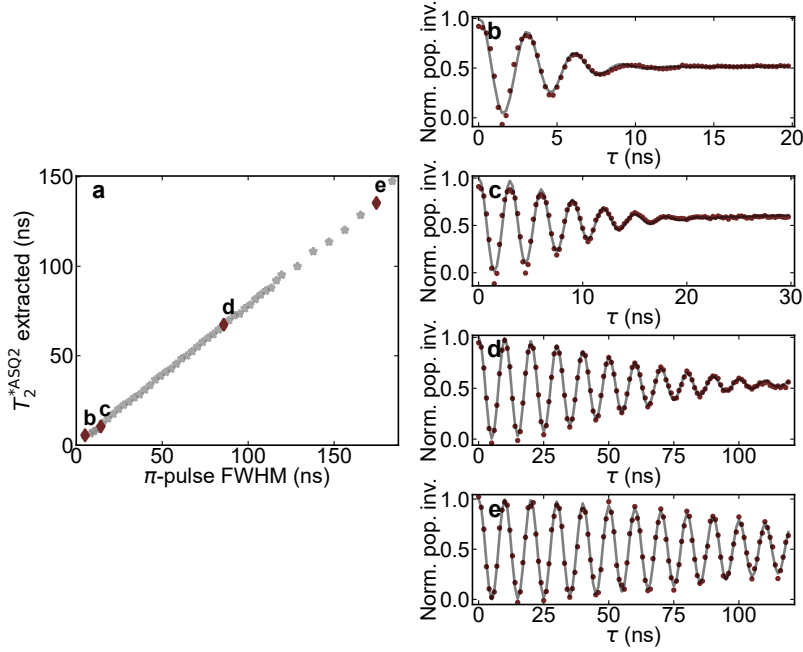
Figure 7.22: **Effect of overlapping pulses on the extracted** T_2^{*ASQ2} **for ASQ2.** **a** Extracted T_2^{*ASQ2} by performing Ramsey experiments on ASQ2 as a function of the $\pi/2$-pulse FWHM. For each data point we reduced the amplitude of the $\pi/2$-pulse by the same factor as we increased the pulse length to keep an approximate $\pi/2$-pulse, using the calibration for the shortest pulse length. **b-d** Examples of the data with T_2^{*ASQ2} fits indicated with maroon markers in **a**. The artificial detuning period was varied with pulse length to make sure there were enough points in each period and enough oscillations in the length of the traces.

Single-shot readout contrast of individual ASQs

In Figure 7.23 we show examples of single-shot readout outcomes. These are measured at the setpoints used in the main text and at magnetic field settings of the main text for ASQ1 and for ASQ2 we go to a higher magnetic field in order to reduce thermal population of the excited spin state. We obtain an average signal-to-noise ratio for distinguishing spin-up and spin-down, based on double Gaussian fits to the up and down initializations SNR $= |\mu_\uparrow - \mu_\downarrow|/(2\sigma)$ where μ_i, σ are the mean and width of the fitted Gaussian corresponding to state i, of 1.5 and 1.3 in a integration time of 1 μs, 1.5 μs for ASQ1 and ASQ2 respectively. Note that we use the fit parameters of the initialization without a π-pulse here as the pulse can cause excitations of other states, which we suspect to be the transmon excited states, visible as an extra tail in the Gaussian corresponding to the excited spin state in Figure 7.23b, c. Additionally, these values are strongly flux and magnetic field dependent and thus could be optimized further in future works, as we did not perform an exhaustive study here.

The SNR is a measurement of the pure readout contrast, rather than the more standard readout fidelity $F = 1 - P(\uparrow | \downarrow)/2 - P(\downarrow | \uparrow)/2$, where $P(a|b)$ denotes the probability of obtaining state a when preparing state b. This is because F includes the effects of thermal

population and imperfect π-pulse, due to dephasing during the π-pulse and imperfect calibrations. At the main text gate setpoint, and the magnetic field settings mentioned above using the indicated threshold (black dashed line in Figure 7.23) we obtain $F = 0.75$ and $F = 0.67$ for ASQ1 and ASQ2 respectively.
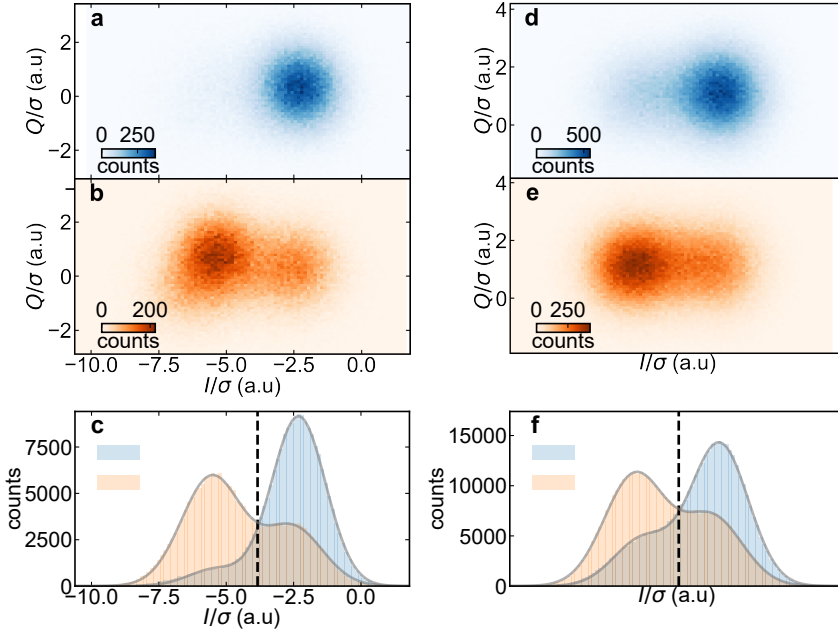

Figure 7.23: **Individual qubit readout shots**. **a-c** Histograms of single shot readout of ASQ1 near the maximum of the transition ($I = -2$ mA) at $B_z = 35$ mT (same setpoint as for the coherence measurements in the main text). **a**, **b** Histogram of single shot measurements in the $I - Q$ plane after initializing in $|\downarrow_1\rangle$ and $|\uparrow_1\rangle$, respectively. **c** Projection of the data in **a** and **b** along the I-axis fitted with a double Gaussian function (grey line) for each initialization. A 1000 ns readout pulse and a ~2 ns FWHM π-pulse were used. The black dashed line in **c** indicates the optimal threshold to distinguish spin-up from spin-down states and is used to calculate the fidelity F. **d-f** Histograms of single-shot readout of ASQ2 at $B_z = 80$ mT for a 1500 ns-long readout pulse and a ~ 4.7 ns FWHM π-pulse, at $B_y = 5.96$ mT.

7

7.7.5 Supporting data for the longitudinal coupling measurements

Fig. 7.24 shows data taken in the same way as in Fig. 3 of the main text and under the same field, gate and flux conditions, but for varying frequency of the pump tone f_p. We find that, when f_p matches the transition frequency of one of the qubits, and thus continuously drives it to its excited state, the frequency of the other qubit splits in two, as discussed in the main text (red lines in Fig. 7.24c and d). When the pump tone frequency instead does not match the transition frequency of the first qubit, the frequency of the second qubit does not split, as expected (black lines in Fig. 7.24c and d). This confirms that the frequency splitting observed in the main text is indeed the result of both states of the other ASQ being populated.

In Fig. 7.25 we perform a similar experiment for two fixed pump frequencies away from the spin-flip transitions and as a function of the pump tone power. For Fig. 7.25a and b, the pump tone drives the transmon transition and for Fig. 7.25c and d its frequency is set to a value $f_p = 5.8\,\text{GHz}$ where no transition is driven. In neither of the two cases do we observe a splitting of any of the two ASQ transitions at any power, as expected (the disappearance of the signal at high drive powers was generally seen throughout the work independent of drive frequency and corresponds to disappearance of the readout resonator resonance). Note that the instability that can be observed in the measured transition frequencies was also observed versus time and is thus unrelated to the presence of the pump tone.
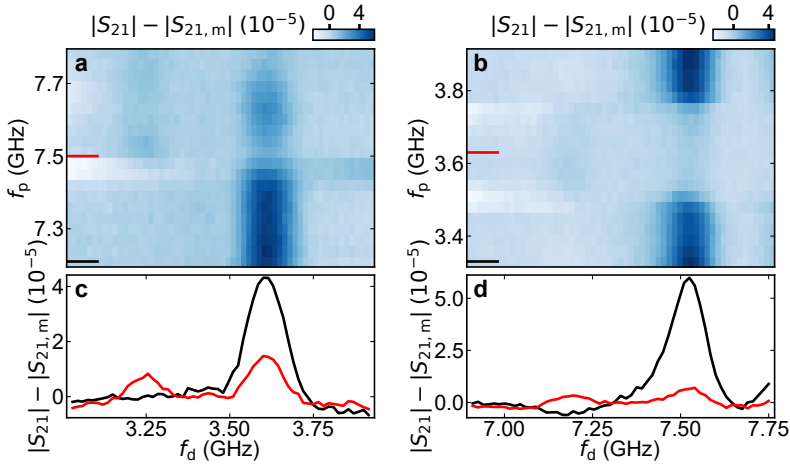

Figure 7.24: **Third tone frequency dependence of the longitudinal coupling signal. a** Spectroscopy of ASQ2 as a function of the drive frequency f_d while continuously applying a pump tone at varying frequency f_p. The red line indicates the pump tone frequency used in Fig. 3b,d of the main text, $f_p = f_1 - J$. **b** Same as in **a** but with the roles of ASQ1 and ASQ2 exchanged. In this case, the pump tone has a frequency close to that of ASQ2, while performing spectroscopy of ASQ1. **c** and **d** show line-cuts of **a** and **b**, respectively, at two fixed pump frequencies indicated in **a** and **b** with color matching lines.

7.7.6 Longitudinal coupling at different gate sepoint

In this section, we present longitudinal coupling measurements similar to those in the main text, but now taken at a different gate configuration for both Andreev spin qubits.
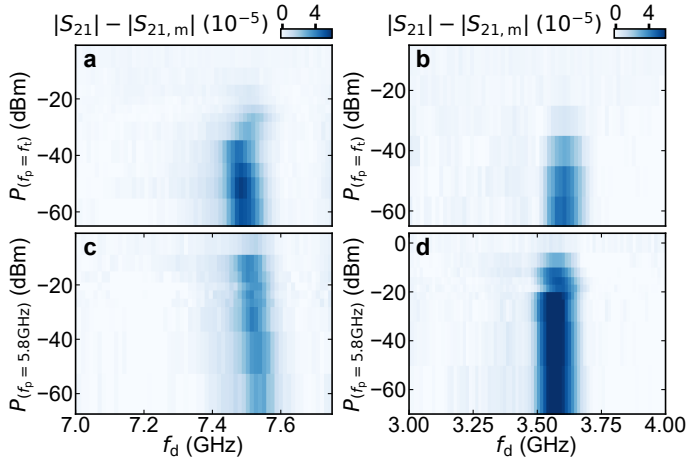
Figure 7.25: **Qubit spectroscopy while driving at different frequencies with the third pump tone. a** Two-tone spectroscopy of ASQ1 while driving with the third pump tone at the transmon frequency $f_p = f_t$ with varying power. **c** Same as **a** but for $f_p = 5.8$ GHz, not in resonance with any visible transition. **b** and **d** Same as **a** and **c** but for ASQ2.

The new gate setpoints, at which the two qubits are set for all results discussed in this section, are indicated in Tab. 7.4.

	V_{Li} (mV)	V_{Pi} (mV)	V_{Ri} (mV)	$E^I_{J,i}/h$ (GHz)	$E^\sigma_{J,i}/h$ (GHz)
ASQ1	61.0	61.0	376.0	1.79	0.66
ASQ2	53.0	0.0	-700.0	0.53	1.3

Table 7.4: ASQ1 and ASQ2 gate voltage set points and extracted model parameters from the measurements in Fig. 7.26 .

We start by performing basic characterization measurements. The values of the spin-independent, $E^I_{J,i}$, and spin-dependent, $E^\sigma_{J,i}$, Josephson energies for both qubits are extracted from spin-flip and transmon spectroscopy measurements (see Fig. 7.26). Fig. 7.26a and b show in-field spectroscopy of the ASQ1 and ASQ2 spin-flip transitions, respectively. The values of $E^\sigma_{J,1}$ and $E^\sigma_{J,2}$ are extracted from fits to a skewed (Eq. 7.22) and a non-skewed (Eq. 7.21) sinusoidal relation, respectively. Fig. 7.26c and d show transmon spectroscopy measurements performed at zero magnetic field, each with only one of the two ASQs open (ASQ1 in panel c and ASQ2 in panel d). The values of $E^I_{J,i}$ are estimated by fitting the measured transmon transitions with Eq. 7.16 at Φ_i being integer multiples of $\Phi_0/2$.

Before investigating the longitudinal coupling strength at the new gate setpoints, we characterize their magnetic field dependence. The characterization is done analogously to that for the previous gate setpoint (discussed around Fig. 7.19) and can be found in the data repository. The relevant extracted parameters are summarized in Tab. 7.5. By performing spin-flip spectroscopy of each of the two qubits at different field directions, we extract their g-factors on the chip plane, which range between 6 and 15 for ASQ1 and between 9 and 15 for ASQ2. The values along the B_z and B_y directions are reported in
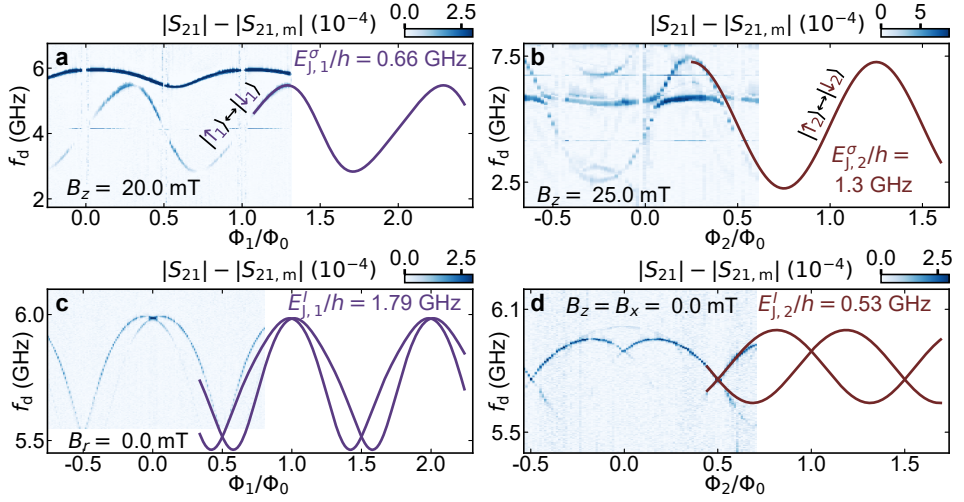
Figure 7.26: **Parameter estimation for both ASQs at the gate setpoints specified in Tab. 7.4.** **a** Spin-flip spectroscopy of ASQ1 versus Φ_1, at $B_z = 20\,\text{mT}$. The line shows a fit to a skewed sinusoidal dependence (Eq. 7.22) from which we extract the value of $E_{J,1}^\sigma/h = 0.66\,\text{GHz}$. **b** Spin-flip spectroscopy of ASQ2 versus Φ_2, at $B_z \sim 25\,\text{mT}$. The line shows a fit to a sinusoidal dependence (Eq. 7.21) from which we extract the value of $E_{J,2}^\sigma/h = 1.3\,\text{GHz}$. **c** Transmon spectroscopy versus Φ_1, at $B_r = 0\,\text{mT}$ with ASQ1 open to its setpoint (see Tab. 7.4) and ASQ2 closed. The two transmon frequencies correspond to the two possible states of ASQ1. **d** Transmon spectroscopy versus Φ_2, at $B_r = 0\,\text{mT}$ with ASQ2 open to its setpoint (see Tab. 7.4) and ASQ1 closed. The two transmon frequencies correspond to the two possible states of ASQ2. For all panels, $V_C = 1500\,\text{mV}$. The lines in **c** and **d** show the transmon transition spectrum given the spin-dependent part of the ASQ potentials found in **a**, **b** and the measured value of E_c (see Tab. 7.1). The lines in **c** and **d** are best fits to the measured data at Φ_i being integer multiples of $\Phi_0/2$. From these transmon spectra, we estimate the values of the spin-independent Josephson energies $E_{J,1}^I/h = 1.79\,\text{GHz}$ and $E_{J,2}^I/h = 0.53\,\text{GHz}$.

Tab. 7.5. As before, we determine the spin-flip polarization direction for ASQ1 by finding two perpendicular directions in the $y-z$ and $x-z$ planes. The resulting spin-polarization direction is reported in Tab. 7.5 and is this time found to be approximately 1.85 degrees away from the nanowire axis. For ASQ2 we did not determine the full spin-orbit direction as we only data measured in the $y-z$ plane.

	ASQi g_z	ASQi g_y	$\theta_\parallel$	$\phi_\parallel$	α
ASQ1	14.9	6.7	1.85	64.4	1.36
ASQ2	14.1	-	-	-	-

Table 7.5: **Summary of g-factors and relevant angles for ASQ1 and ASQ2 at their alternative setpoint.** The zero-field spin-polarization direction ($\theta_\parallel, \phi_\parallel$ in spherical coordinates) is calculated as the vector product of the two perpendicular directions $\theta_{yz,\perp}$ and $\theta_{xz,\perp}$. α denotes the angle between the field applied for the longitudinal coupling measurements of Fig. 7.27 and the spin-polarization direction for each qubit.

Next, we measure the longitudinal coupling energy at the selected gate setpoints in the same way as for Fig. 3 in the main text. Fig. 7.27a-d show a longitudinal coupling measurement for fixed control parameters $B_z = 25\,\text{mT}$, $\Phi_1 = 0.1\Phi_0$, $\Phi_2 = 0.48\Phi_0$ and $V_C = 180\,\text{mV}$.
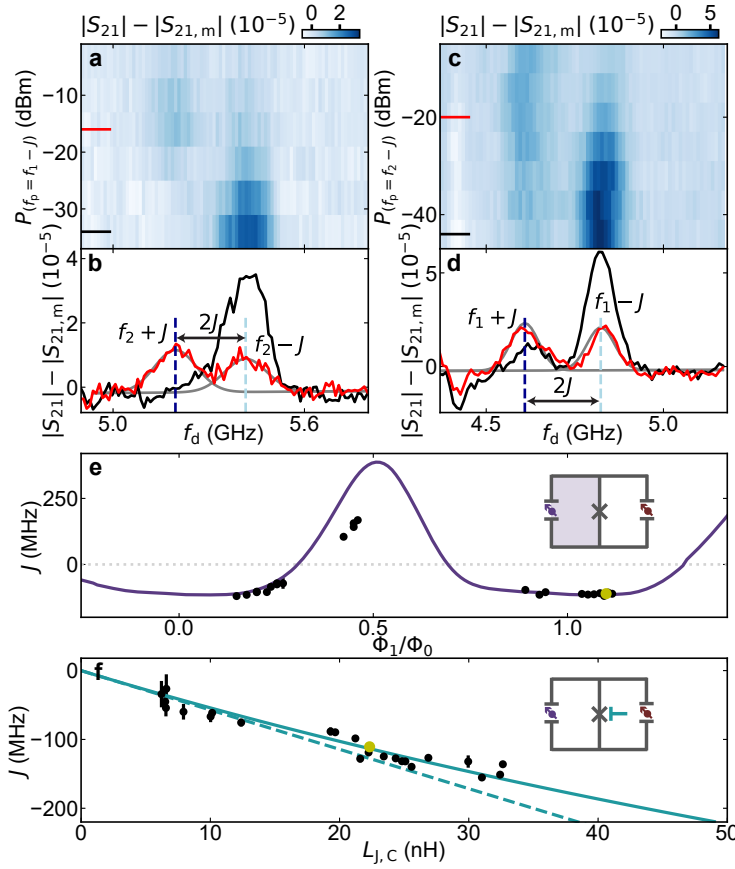
Figure 7.27: **Longitudinal coupling between the two Andreev spin qubits at different gate setpoint.** Data measured and processed in the same way as for Figs. 3 and 4 in the main text, but now for alternative ASQ1 and ASQ2 gate setpoints, reported in Tab. 7.4. **a** Spectroscopy of ASQ2 as a function of the drive frequency, f_d and the power of a pump tone resonant with ASQ1 at frequency $f_p = f_1 - J$. **b** Linecuts of **a** at the powers indicated with color-matching lines. The grey line shows the result of a double-Gaussian fit to the signal in red (see Sec. 7.7.2) and the vertical lines indicate the best-fit values of the two Gaussian centers. **c**, **d** Similar to the situation of **a**, **b**, but with the roles of ASQ1 and ASQ2 exchanged. In this case, the pump tone drives ASQ2 at a frequency $f_p = f_2 - J$, while performing spectroscopy of ASQ1. The longitudinal coupling strength, J, extracted from the fits is -110.0 ± 3.2 MHz and -107.0 ± 3.1 MHz, respectively for **b** and **d**. For **a** - **d**, $\Phi_1 = 0.1\Phi_0$. **e** Qubit-qubit coupling strength, J, as a function of flux in the loop for ASQ1, Φ_1, see also inset. The values of J are determined from a double Gaussian fit to a spectroscopy trace of one ASQ taken while driving the other ASQ. The markers and error bars represent the best-fit values and their estimated standard errors (one-sigma confidence intervals), respectively. The purple line shows the expected dependence $hJ(\Phi_1) = A \frac{L_{J,C}L_{ASQ}}{L_{J,C}+L_{ASQ}} I_1(\Phi_1)I_2/2$ for the value of A extracted from panel **f**. **f** Qubit-qubit coupling strength J at fixed $\Phi_1 = 1.1\Phi_0$ and as a function of $L_{J,C}$, which is varied using the gate-voltage at the coupling junction (see inset). The continuous line shows a fit to the dependence $hJ(L_{J,C}) = A \frac{L_{J,C}L_{ASQ}}{L_{J,C}+L_{ASQ}} I_1 I_2/2$. We extract a value $A = 0.79 \pm 0.02$ from this fit. The dashed line shows the linear dependence $hJ(L_{J,C}) = AL_{J,C}I_1 I_2/2$. The yellow marker in **e** and in **f** is a shared point between the two panels. For all panels, $B_z = 25$ mT, $B_y = 0.25$ mT, $B_x = 0.0$ mT and $\Phi_2 = 0.48\Phi_0$.

These parameters set $f_1 = 4.7\,\mathrm{GHz}$, $f_2 = 5.3\,\mathrm{GHz}$ and $L_{\mathrm{J,C}} = 22.3\,\mathrm{nH}$. Similarly to Fig. 3 in the main text, we find that the frequency of each of the qubits splits by $2J$ when the other qubit is driven with a pump tone f_{p}. From spectroscopy of ASQ2 while ASQ1 is driven (Fig. 7.27a, b), we find $J = -110.0 \pm 3.2\,\mathrm{MHz}$, while from spectroscopy of ASQ1 while ASQ2 is driven (Fig. 7.27c, d), we find $-107.0 \pm 3.1\,\mathrm{MHz}$. These two values are equal within their one-sigma confidence intervals, consistent with the theory prediction.

Finally, we investigate the flux and $L_{\mathrm{J,C}}$ dependence of the coupling strength, similarly to how it is done in Fig. 4 of the main text. Fig. 7.27e, f show the tunability of J at the setpoint of Tab. 7.4. These measurements are taken at the same B_z and Φ_2 conditions as in Fig. 7.27a-d, which result on a fixed supercurrent difference through ASQ2, $I_2 = -5.6\,\mathrm{nA}$. Panel e shows the Φ_1 dependence of J at $V_{\mathrm{C}} = 180\,\mathrm{mV}$, which fixes $L_{\mathrm{J,C}} = 22.3\,\mathrm{nH}$. Similarly to what was found in the main text, we observe that J can take both positive and negative values and that it follows a similar shape as that predicted by Eq. 7.5. We however note that, especially around $\Phi_1 = \Phi_0$, the data deviates from the behavior predicted by Eq. 7.5. This is due to the fact that this data is not taken for parameters consistent with the limit $L_{\mathrm{J,C}} \ll L_{\mathrm{J},i}^\sigma, L_{\mathrm{J},i}^I \forall i$. As shown in Fig. 7.6, when this limit is not met Eq. 7.5 overestimates the value of J in the region of $\Phi_1 \sim \Phi_0$.

Finally, Fig. 7.27f shows the evolution of J with $L_{\mathrm{J,C}}$ at a fixed $\Phi_1 = 1.1\Phi_0$ setpoint, indicated with a yellow marker in Fig. 7.27e, which sets $I_1 = 1.7\,\mathrm{nA}$. As expected, we find an increase of the magnitude of J with $L_{\mathrm{J,C}}$, which is proportional, with a scaling factor $A = 0.79 \pm 0.02$, to Eq. 2 from the main text given $L_{\mathrm{ASQ}} = \frac{\Phi_0^2}{4\pi^2}/(E_{\mathrm{J,1}}^I \cos(\frac{2\pi}{\Phi_0}\Phi_1) + E_{\mathrm{J,2}}^I \cos(\frac{2\pi}{\Phi_0}\Phi_2)) = 176.9\,\mathrm{nH}$.

7.8 Acknowledgements

Data availability

The data and analysis that support the findings and code to generate the figures of this study are publicly available via 4TU.ResearchData at
`https://doi.org/10.4121/e10185d0-026e-480f-bbaa-3448c6e1b9a2.`

Author contributions

J.J.W., M.P.V., and C.K.A. conceived the experiment. Y.L. developed and provided the nanowire materials. J.J.W, M.P.V., L.S. and A.B. prepared the experimental setup and data acquisition tools. L.S. deposited the nanowires. J.J.W, M.P.V. and A.B designed the device.

7

8

Conclusions and outlook

Forecasts may tell you a great deal about the forecaster; they tell you nothing about the future.

Warren Buffet

8.1 Flux control in a magnetic field

Key to the results was the development of flux control in field-compatible thin-film superconducting circuits in the early stages of this thesis, on which we build from previous works and experience in the group in Delft with thin-film sputtered NbTiN (Kroll et al., 2018, 2019; Samkharadze et al., 2016; Pita-Vidal et al., 2020) and flux qubits (Plantenberg, 2007). As explained in Chapters 3 and 5, to mitigate flux noise in presence of large external fields we use gradiometric loops that have effective sizes on the order of one μm^2, hence the flux period is on the order of mT.

The simple discovery of being able to apply an in-plane field for flux biasing, due to the height difference between the nanowire and the rest of the loop circuit (see Figure 3.18), was a large contributor to the ability of taking any of the flux-dependent data of all chapters in this thesis (see Figure 5.9 for a one to one comparison). A big challenge in this thesis, and potentially other experimental works that focus on flux-biased devices in substantial magnetic fields, has been to avoid flux jumps. Several iterations of test resonator devices have struggled with these jumps. Although more and denser flux trapping pinning sites (small hole layers) mitigate most the jumps, applying an out-of-plane magnetic field for flux biasing, as we originally envisioned, will likely always be accompanied with flux jumps, due to the naturally large perpendicular area of superconducting material exposed to the field. As described in Chapter 3, even with in-plane flux-biasing, superconducting bond wires can create superconducting loops that cause flux jumps due to circulating supercurrent. One solution used was to apply a magnetic field of ~ 10 mT to turn the bond wires normal and thus avoid these jumps. Another option is to align the bond wires with the preferred field direction. However, sometimes it is not desirable to work in finite fields alone, or other field directions are required. The use of dedicated flux-bias lines (described in Chapters 6 and 7) is an alternative solution, as the field generated by the flux-line current is local enough to cause much less jumps. However, this requires introducing additional control lines and when changing global magnetic fields, even when aligned in plane, flux jumps can still occur.

8

A potential alternative solution, that we did not explore, could be to make normal metal airbridges, similar to conventional superconducting airbridges (Stavenga et al., 2023) in an additional fabrication step. Airbridges normally consist of superconducting material, which would allow for circulating supercurrents, and thus flux jumps. Replacing them by normal metal could prevent this. For coplanar waveguide resonators typically used in zero-field circuit-QED experiments, this could reduce the internal quality factor. But, since we in general use lumped element resonators, the normal-metal airbridges would only go over transmission lines and gate-lines, for which the added losses should not matter too much[1]. If the bridges are stable enough to allow subsequent processing, they preferably should be placed before the nanowire placement to avoid temperature restrictions of sensitive material interfaces like in Chapter 6.

---

[1]It might cost SNR for the signal traveling to the amplification chain, but generally the RF-lines on printed circuit boards are also made of normal metal.

8.2 Physical mechanisms responsible for dynamical parity polarization

In Chapter 4 we found that it was possible to change the fermion parity of a Josephson junction by driving transitions between ABS. Although this is expected at frequencies on the order of the gap (Olivares et al., 2014; Bretheau et al., 2013b), we found this could also occur at driving frequencies much lower than the gap. Furthermore, we found the resulting polarization after driving a transition from an initial state in a certain parity sector, to end up being opposite to the initial state parity. In Chapter 4 we modeled the work with a phenomenological rate model, that could help with determining what process is responsible for the polarization, but has no assumption on what microscopic process is taking place. After (pre-)publication of Chapter 4, two interesting theoretical works (Ackermann et al., 2023; Kurilovich et al., 2023) were published that point to the need for interactions to be present for the polarization to occur. These works elucidated the possible microscopic process that could take place in the experiment, which we will summarize below.

Both of these works focus on the case of having at least two Andreev bound state manifolds in the junction, as was the case in Chapter 4. In Ackermann et al. (2023), the even to odd polarization is shown to occur if, after a microwave drive excites a mixed pair transition from the ground state, one of the excited Andreev levels is close to the superconducting gap edge on the order of the resonator frequency (or another circuit mode), such that there is a finite escape rate to the continuum when that state is excited. Similarly, odd to even polarization can occur if from one of the odd parity states of the lower energy Andreev manifold, a microwave pulse excites that quasiparticle to the second manifold and subsequently it escapes via the same mechanism as for even to odd polarization.

Although Ackermann et al. (2023) did not model the effect of electron-electron interactions, they did make a key observation that the parity polarization effects are mitigated if there are no electron-electron interactions. Kurilovich et al. (2023) worked this out in detail. Focusing on the case of even to odd polarization, if there is no interaction present in the junction, the microwave driven process of breaking a Cooper pair and exciting one quasiparticle to a each of the manifolds can be repeated once one of the two quasiparticles has left one of the manifolds. This results in three quasiparticles present in the junction, one in the higher manifold, which can be excited out, and two in the lowest manifold, which can relax quickly to the ground state as there is no change of parity required. Electron-electron interaction breaks this degeneracy, and thus is a requirement for this process to occur. From the spin-splitting of the interband transitions of Chapter 4, it is clear that spin-orbit coupling is present, which could also break this degeneracy. However, as the authors of Kurilovich et al. (2023) point out, this is not true for $\varphi = 0, \pi$, where the data still shows parity polarization.

Thus, the above discussion serves as an independent argument for the requirement of electron-electron interactions in the modeling of the proximitized InAs/Al Josephson junction, as pointed out in Chapter 5 for other reasons. In future work it would be interesting to measure the rates of polarization together with coherence decay rates and Rabi rates, in order to allow for a more quantitative comparison of the various polarization mechanisms.

8

8.3 Spectroscopy of Andreev states in nanowire Josephson junctions

In this thesis, we investigated the properties of Andreev bound states in a magnetic field using circuit-QED techniques. Adding to a growing body of works utilzing circuit-QED techniques to probe Andreev states (Janvier et al., 2015; Hays et al., 2018, 2020; Tosi et al., 2019; Hays et al., 2021; Metzger et al., 2021; Matute-Cañadas et al., 2022; Chidambaram et al., 2022; Fatemi et al., 2022; Bargerbos et al., 2023a; Pita-Vidal et al., 2023a; Hinderling et al., 2023) we were able to probe Andreev bound states and their spin with sub-μeV resolution. This allowed for high-resolution investigation into the physics that arises in the combination of superconductivity, spin-orbit coupling, magnetic fields and electron-electron interactions. Additionally, the experiments opened up the path to a field of "superconducting spin qubits" (Hays et al. (2021); Pita-Vidal et al. (2023a), Chapter 7), where the properties of superconducting circuits and spin qubits are combined, and could optimistically yield the best of both worlds.

In Chapter 5 we performed microwave spectroscopy of Andreev bound states in an InAs/Al nanowire Josephson junction in a magnetic field. This Chapter starts with reproducing signatures of pair transitions and of spin-orbit splitting in Andreev states as seen in earlier works using similar setups (Janvier et al., 2015; Hays et al., 2018; Tosi et al., 2019; Hays et al., 2020). We then moved on to apply a magnetic field and observed several new features related to the spin of Andreev states.

8.3.1 Detecting the doublet transition

A useful observation in this chapter for the following chapters was the direct spin-flip transition in the lowest Andreev manifold (doublet) $D_a : |\uparrow\rangle \leftrightarrow |\downarrow\rangle$. Although in Hays et al. (2021); Metzger et al. (2021) the ability to manipulate the Andreev spin with microwave control signals was by then already demonstrated, for us the observation of D_a together with the parallel development of transmons as a sensor for quantum dot based junctions by my colleagues (Bargerbos et al., 2022, 2023a), kicked off the process of working towards a directly driven spin qubit (Pita-Vidal et al., 2023a) and two of them in Chapter 7.

8.3.2 Detecting singlet and triplet transitions

The gist of the work focuses on the observation of pair transitions into final states of the lowest two manifolds that have a large parallel spin-component i.e. $T_\pm : |g\rangle \leftrightarrow |T_\pm\rangle$. These transitions are enabled by the spin-orbit coupling and the Zeeman effect, and their spinful nature is confirmed by the linear dispersion with magnetic field. While we were attempting to explain the data using non-interacting tight-binding simulations, two works came out by Matute-Cañadas et al. (2022) and Fatemi et al. (2022) that detailed the need for including interactions to explain the spectra, so we collaborated with some of the authors of Matute-Cañadas et al. (2022), which had seen similar transitions at zero magnetic field, and they obtained the theoretical results with interactions shown in Chapter 6. Finally we could understand most of the important transitions that we observed and their ordering!

An interesting avenue for future research would be to measure the coherence time and energy lifetime of the singlet and triplet Andreev pair excitations. As suggested by Padurariu and Nazarov (2012) spin blockade could prevent relaxation between singlet

and triplet states. This effect is mitigated by spin-orbit coupling, as it hybridizes the singlet and triplet states and breaks spin rotation symmetry. This coupling was also seen directly in the data of Figure 5.3. Nevertheless, this opens up the way to a superconducting equivalent of singlet-triplet proposals for spins in semiconducting quantum dots (Burkard et al., 2023).

The observed hybridization of triplet and singlet Andreev transitions at finite magnetic field is consistent with the superconducting pairing having a triplet component (Lutchyn et al., 2010; Oreg et al., 2010). However, we want to emphasize that we could only prove that this pairing is locally present in the junction, due to the local nature of the Andreev bound states that we probe. Additionally, the high density of states and lack of gap reopening (see Figure 5.18) demonstrate that in the device measured in this thesis, there was no use for an attempt at detecting signatures of the associated bulk topological phases with Majorana zero modes (Kitaev, 2001; Ivanov, 2001; Read and Green, 2000). This is consistent with current understanding of the requirements on disorder in these nanowires (Das Sarma and Pan, 2021).

8.3.3 Combining DC and RF access

In essence Chapter 5 contains an extensive set of microwave spectroscopy measurements of a ~ 150 nm InAs/Al nanowire Josephson junction versus flux, gate voltage and magnetic field. In the modeling of the data, there are many parameters to be estimated that vary per device and per magnetic field or gate setpoint. In Figure 8.1 we propose a setup for having an *in-situ* DC access (Kringhøj et al., 2020) to the nanowire Josephson junction by introducing additional junctions as field-effect transistors (FET). These FETs can serve as a switch between RF spectroscopy or time domain access and DC access. Kringhøj et al. (2020) showed a similar setup for a nanowire-based gatemon and demonstrated coherence times of 6 μs. The DC access could provide valuable additional information about the device under test using transport measurements and aid complex device tune-up. This could prove useful in the future when replacing the single junction with more complex systems such as those discussed in Section 8.4.
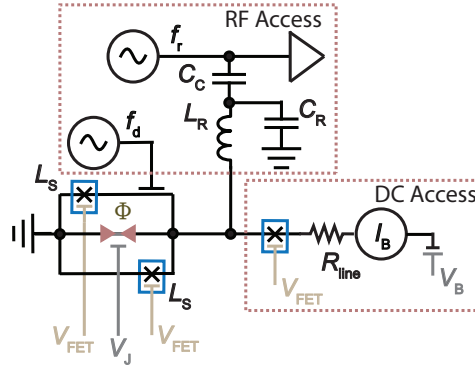
8

Figure 8.1: **Schematic for adding DC access to ABS spectroscopy experiments** based on Kringhøj et al. (2020). This yields an equivalent circuit as shown in Figure 5.1 from an RF perspective. The shunt inductors are replaced by nanowire Josephson junctions field effect transistors (FETs) (blue boxes) and can be switched off to force all current from the DC bias to go through the nanowire. An additional FET is introduced before the nanowire SQUID to allow turning off connection to the DC access. Symbols indicate the various components.

8.4 Shadow-wall lithography with circuit-QED

In Chapter 6 we demonstrated shadow-wall lithography techniques on a superconducting NbTiN circuit to study Andreev bound states in gate-tunable InSb-Al hybrid Josephson junctions. Qualitatively, compared to InAs/Al devices of similar junction length shown in this thesis and theses from other groups (Hays, 2021; Metzger, 2022), the density of states was lower, consistent with a lower effective mass and longer elastic scattering length in the InSb. However, the linewidth of observed transitions was consistently higher over several devices, reaching a minimum of $\sim 150\,\mathrm{MHz}$ for the pair transition, appearing limited by charge noise. Thus for this material combination to become used in coherent applications, more work is needed to study the origin of charge noise in these devices. On the other hand, 150 MHz corresponds to an energy resolution less than $1\,\mu\mathrm{eV}$. This is an order of magnitude lower than achievable with tunneling spectroscopy at 50 mK ($\sim 15\,\mu\mathrm{eV}$). Thus, as a spectroscopic tool, the results of Chapter 6 could prove beneficial for studying condensed matter physics with high resolution, and serve as a first step to combine superconducting circuits with more advanced materials and geometries. We now provide some suggestions for those combinations.

A first example, that should be within reach with the demonstrated fabrication techniques, is a device with two Josephson junctions separated by a section of grounded superconductor on the order of the coherence length ξ (Figure 8.2a). This geometry has been proposed as a way to create Andreev molecules, where the wavefunctions of two Andreev bound states overlap to form superconducting molecular states (Su et al., 2017; Pillet et al., 2019; Kornich et al., 2020; Matsuo et al., 2023). As typically $\xi \sim 100\,\mathrm{nm}$ for the Al shell (see Table 2.1), shadow wall lithography is especially suited for this purpose, as it allows for grounding small sections of the wire (Wang et al., 2022). A schematic on how to embed such a molecule in the rf-SQUID loop of the circuit of Chapter 6 to be measured using microwave spectroscopy in practise, is shown in Figure 8.2c. An extension of this geometry would be to make quantum dot Josephson junctions tuned to the odd-parity ground state

(see Figure 8.2b) similar to Chapter 7 and attempt to couple two Andreev spins directly via wavefunction overlap (Spethmann et al., 2022).

A second example is the embedding of artificial Kitaev chains in such a circuit. This has recently has been experimentally demonstrated in our group as a promising route to create well-controlled Majorana zero modes with less stringent requirements on the disorder (Leijnse and Flensberg, 2012; Dvir et al., 2023; Bordin et al., 2023). It would be interesting to investigate the possibility of detecting signatures of the fractional Josephson effect (Kitaev, 2001; Lutchyn et al., 2010; Väyrynen et al., 2015; van Heck et al., 2017; Peng et al., 2016; Cayao et al., 2018) in future versions of such devices in a circuit-QED architecture. For example, a recent proposal by Pino et al. (2023) suggests it is possible to measure the Majorana polarization by embedding a four site kitaev chain in a transmon SQUID-loop, which, would require combining the developments of using a transmon as a sensor (Chapter 7, Bargerbos et al. (2022, 2023a); Pita-Vidal et al. (2023a)) and the fabrication methods of Chapter 6.
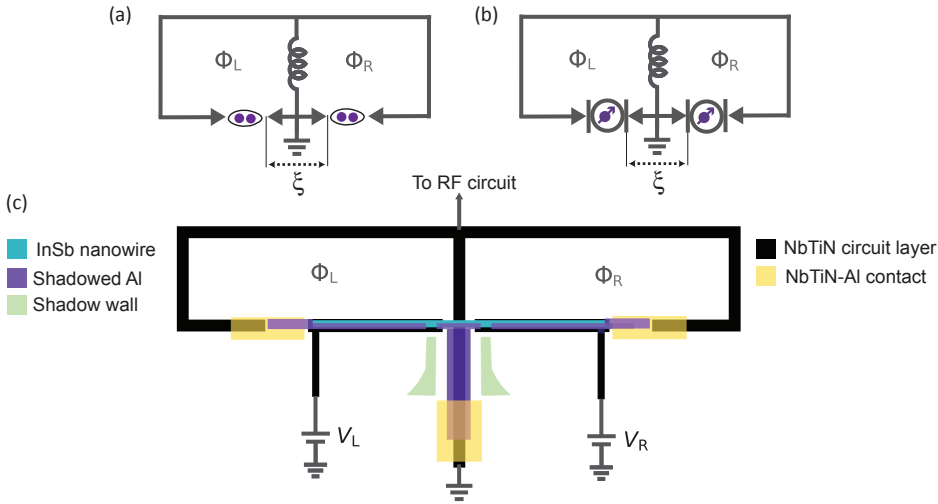

Figure 8.2: **Example of an advanced geometry using shadow wall lithography: Andreev molecule.** (a) SQUID loop schematic for coupling two even parity Andreev many body states via wavefunction overlap. The bound states reside in different Josephson junctions and are separated by a grounded section of superconductor on the order of the coherence length ξ. (b) Equivalent schematic for coupling two Andreev spin qubits via wavefunction overlap. (c) Schematic for a device implementation of (a), compatible with fabrication techniques demonstrated in Chapter 6. The phase difference over the left and right junction can be controlled with Φ_1, Φ_2 respectively, and the density tuned using electrostatic gates voltage biased with V_L, V_R. The inductance shown in (a,b) can be made by the kinetic inductance of the NbTiN base layer, similar to Chapter 6. For (b), if a larger inductance is needed, the inductor could be replaced with a nanowire junction similar to Chapter 7.

8.5 Coupled Andreev spin qubits

In Chapter 7, building on the demonstration of a single Andreev spin qubit (ASQ) in Hays (2021); Pita-Vidal et al. (2023a), we demonstrated the first two-qubit device with Andreev spin-qubits. This device was designed following a theoretical proposal by Padurariu and Nazarov (2010) and showed strong longitudinal spin-spin coupling over a distance of a few tens of micrometers. The demonstration of spin-spin coupling (178 MHz) over a distance much larger than the size of their individual wavefunctions, has been a long standing goal in the spin-qubit community and could pave the way to larger connected qubit arrays (Vandersypen and Eriksson, 2019).

An immediate further step using the device of Chapter 7 would be to demonstrate the effect of longitudinal coupling coherently. For example, a controlled Z gate can be done by starting with one ASQ biased with $\phi = 0, \pi$, i.e. the "OFF" state, and one qubit with $\phi = \pm\pi/2$, i.e. the "ON" state (see also Figure 8.3a). To then perform the gate, a flux pulse should be sent to the "OFF" qubit, turning on the coupling for a time τ_{flux} followed by single qubit phase rotations. Given the measured coherence times in Chapter 7, we estimated the limit on average gate fidelity to be 85% for $\tau_{\text{flux}} = 1.4$ ns. However, this would in practise require applying very short flux pulses and could suffer from flux tails and distortions[2] Rol et al. (2019, 2020). An alternative way to demonstrate two-qubit logic without flux pulses making use of the longitudinal coupling, is to drive frequency selective Rabi oscillations (Hendrickx et al., 2020; Plantenberg et al., 2007). This would require both qubits to be set to the "ON" point during the procedure, i.e. $\phi_i = \pi/2$ for ASQi. A drive at frequency $f_1 - J$ causes a controlled Rabi oscillation to occur from $|\downarrow_1, \downarrow_2\rangle \rightarrow |\uparrow_1, \downarrow_2\rangle$. Observing a lack of oscillations when starting in $|\downarrow_1, \uparrow_2\rangle$ versus starting in $|\downarrow_1, \downarrow_2\rangle$ then demonstrates the possibility of performing conditional qubit rotations. This also serves as a calibration for a CNOT gate if the pulse amplitude is taken to be so that the oscillation reaches its peak, however during the "ON"-"ON" state, both qubits will continuously have strong ZZ interaction. Note that in the device of Chapter 7, readout contrast is maximal at $\phi = 0, \pi$ and zero at $\phi = \pi/2$. Thus, if flux pulsing is not available, the experiment should be performed as far away from $\phi = \pi/2$ as possible while still retaining selectivity, or use an alternative readout design (Pita-Vidal et al., 2024).

Other types of operations might be possible if the coupling is not purely longitudinal. From the minimal model of the quantum dot (Equation (2.29), Padurariu and Nazarov (2010)), one can see that if the two quantum dots have a different effective spin-orbit direction, a magnetic field yields a transverse component to the coupling. Experimentally this should be observable as an avoided crossing between the two spin-qubits when their resonance frequency approaches each other, and could be explored in future work.

For future parallel operation of multiple ASQs, described in Section 8.5.1, it would be good to experimentally characterize the residual coupling strength in the "OFF" setting. Residual ZZ interaction acts as an always on entangling rate and can limit simultaneous qubit control fidelity. For superconducting qubits these interactions have reached values below 10 kHz (Ding et al., 2023; Marxer et al., 2022; Yan et al., 2018; AI, 2019). Measuring this residual coupling accurately, for example by comparing Ramsey experiments on one qubit conditioned on the state of the other to extract the qubit frequency, could yield

---

[2]Note that pulses this short would additionally be limited by the bandwidth of our arbitrary waveform generators

information on the limits that can be achieved.
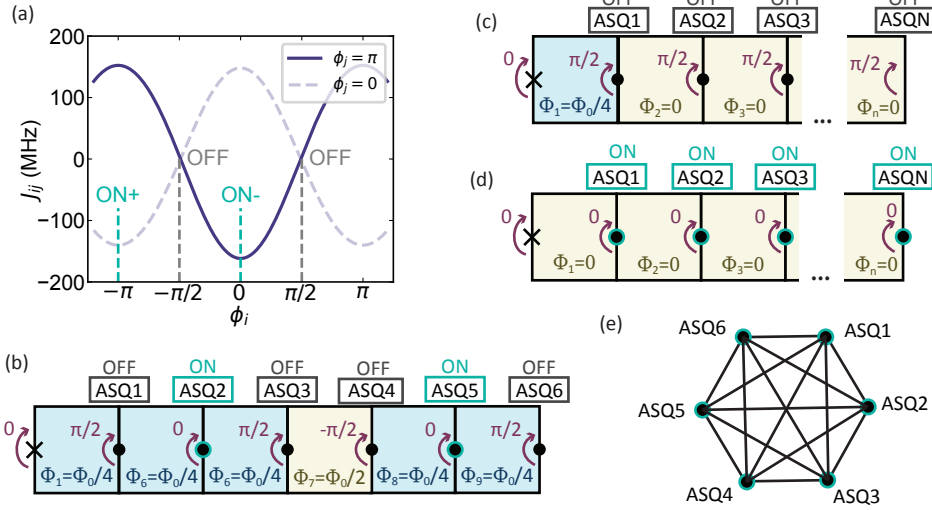
8.5.1 Scaling up Andreev spin qubit systems

Figure 8.3: **Schematic for creating all-to-all connected Andreev spin qubits with tunable coupling**. (a) Coupling strength between ASQi and ASQj as a function of phase drop over ASQi with the setpoints of coupling J_{ij} being positive (ON+), negative (ON-) and 0 (OFF) indicated using the circuit of (b). Parameters are the same as in Figure 7.5 for $L_J = 24$ nH. (b) Circuit and flux-bias settings for a six-ASQ array that turn on coupling between two out six ASQs. (c) flux-bias setting that turns off coupling between all ASQs. (d) Flux settings that turn on coupling between all ASQs. (e) Schematic indicating the all to all ASQ coupling created by (d) for $n = 6$.

For creating larger arrays of Andreev spin qubits, one option we envision is a direct galvanically connected grid of ASQ squid loops, soon to be proposed in (Pita-Vidal et al., 2024), which we summarize here. The main concept is displayed in Figure 8.3. This architecture is a direct extension of the two spin-qubit coupling proposed in Padurariu and Nazarov (2010) and demonstrated in Chapter 7. By adding $N - 2$ additional loop arms with an ASQ to the two-qubit circuit of Figure 7.1, the coupled two-qubit Hamiltonian of Equation (7.1) can be extended to an n-qubit version $H = \sum_i^N \hbar \omega_i \sigma_i^z / 2 + \sum_{j<i}^N h J_{ij} \sigma_i^z \sigma_j^z / 2$. The individual phase drop over each ASQ $\phi_i = \sum_{j=0}^i 2\pi \Phi_j / \Phi_0$ can be tuned by setting the appropriate fluxes, relying on the fact that the phase drop over the coupling junction E_J can be fixed to 0, if we keep E_J larger than the spin-dependent Josephson energies of the ASQs. In Figure 7.3, Equation (7.2) we demonstrated that the coupling between two spin-qubits i and j, J_{ij} can be turned to a maximally positive value, negative value or off by turning the phase drop over ASQ1 to $\phi_1 = -\pi/2, \{0, \pi\}, \pi/2$ respectively. At these points the supercurrent is either maximally spin-dependent (on), or independent (off). The setpoints are indicated in Figure 8.3a. By a judicious choice of the fluxes in the loops (Figure 8.3b,c), the phase drops over each ASQ can thus be tuned either to set the qubit to couple with others, i.e. "ON", or remain uncoupled, i.e. "OFF". A transmon based readout architecture similar

to that used in Chapter 7 can be utilized to readout the individual qubits sequentially in the "OFF" state, which is maximally (in)sensitive to the qubit states in the "OFF" ("ON") state. This allows for tunable all-to-all connectivity (Figure 8.3d,e), with $n-1$ coupling parameters that can be set positive, zero or negative. The larger connectivity has recently gained popularity as a way to reduce the overhead, i.e. the required number of qubits per logical qubit, and fault-tolerant threshold for quantum error correcting codes based on low-density parity-checks (Bravyi et al., 2024) as opposed to codes based on a square topology (Bravyi and Kitaev, 1998; Fowler et al., 2012). A second natural application is that of quantum simulation, as the coupled ASQ Hamiltonian represents an Ising spin glass model with a magnetic field (Barahona, 1982; Lechner et al., 2015; Kim et al., 2023).

Photon-mediated spin-spin coupling

As the distance of this coupling could be limited by maximum loop-sizes and the accompanying flux noise it could be worthwile to pursue photon mediated superconducting spin-spin interaction.

A worthy mention is a recent effort from a neighbouring pure semiconducting spin-qubit group in Delft using spin-qubits defined in double quantum dots in a ^{28}Si/SiGe heterostructure (Harvey-Collard et al., 2022; Dijkema et al., 2023). Here the double quantum dot in combination with a magnetic field gradient introduced by a cobalt micromagnet allows coupling spin to charge (the location of the trapped electron). Hence, via a high-impedance resonator, which has large voltage zero-point fluctuations, a large coupling strength can be achieved between the electron charge and resonator photons, which subsequently mediate virtual charge coupling between the two charge qubits and finally via spin-to charge conversion their distant spin-spin coupling of $\sim 17\,\text{MHz}$.

Due to their spin-to-current coupling, Andreev spin qubits naturally couple well inductively (much stronger than pure spins), so a similar resonator mediated coupling as shown in Harvey-Collard et al. (2022), but inductive, can be imagined to couple spins over larger distances on chip than a direct galvanic connection would allow. In fact, a recent experiment managed to couple two Andreev qubits using a resonator galvanically shunted with nanowire SQUIDs to mediate the coupling over a distance of 6 mm (Cheung et al., 2023). Here they achieved a qubit-photon coupling of $\sim 100\,\text{MHz}$. For Andreev spin qubits, the photon-mediated coupling could serve as long-distance couplers between unit cells discussed in Figure 8.3.

8.6 Exploring Andreev states in alternative hybrid material platforms

In this thesis, we have investigated hybrid InAs/Al and InSb/Al nanowires. The spin-coherence in these systems is arguably low and is suspected to be limited by dephasing due to hyperfine interactions with nuclear spins of indium or arsenic in the semiconductor (Nadj-Perge et al. (2010); van den Berg et al. (2013); Hays (2021); Pita-Vidal et al. (2023a)). I refer the interested reader to an excellent overview of the possible causes of noise presented by my colleague in her thesis Pita-Vidal (2023).

Trying out semiconducting materials with weak or purifiable nuclear spin baths could potentially improve the spin-coherence of ABS. Two candidates jump out: proximitized

Ge/SiGe (Hendrickx et al., 2018; Tosato et al., 2023; Valentini et al., 2023) and stacks of 2-dimensional materials with graphene, where sizable Rashba spin-orbit coupling has been demonstrated (Zihlmann et al., 2018; Wakamura et al., 2022), few-electron quantum dots have been created with $\sim 50\,$ms spin relaxation time (Eich et al., 2018; Gächter et al., 2022; Banszerus et al., 2023) and high-transparancy superconducting contacts have been made (Bretheau et al., 2017; Calado et al., 2015; Ben Shalom et al., 2016; Portolés et al., 2022). New materials could also aid the investigation of the effect of other types of spin-orbit coupling than linear Rashba spin-orbit coupling seen in (Tosi et al. (2019); Hays et al. (2020), Chapters 4 and 6) on the spin-splitting of ABS, such as the intrinsic Kane-Mele type present in graphene or qubic terms in Ge hole gases (Luethi et al., 2023b,a). A first challenge for these new platforms would be to demonstrate the observation of isolated Andreev bound states as has been done in InAs and InSb based nanowire systems.

8

A

2-Dimensional tight-binding simulation code and notes

The tight-binding simulations performed in Chapters 2 and 5 can be reproduced using the code from `https://www.doi.org/10.4121/20311137`. There, under the folder *kwant_simulations* you can find the simulated datasets for Chapter 5[1] as well as a general template to perform the simulations. This simulation code is based on Laeven et al. (2020) and slightly adapted. Some notable adaptions are:

- We added matrix element calculation using the native *kwant* (Groth et al., 2014) current operator.

- We added the calculation of microwave absorption spectra following van Heck et al. (2017), via the function *add_spectrum_to_dataset*, in the notebook that is runnable after the simulation is done and uses the current matrix elements.

- In the file *simulation_template.ipynb* you can find a basic template of code to generate a *kwant* system, and classes to perform 1-dimensional sweeps versus a parameter and also perform 2-dimensional sweeps versus two parameters. The sweep classes are written following the methods presented in Section 3.3.4, such that after a sweep, the used simulation parameters and data is saved in an *xarray* (".nc") file, to allow easy inspection and separate plotting and analysis from the simulations.

---

[1]The datasets from Chapter 2 are available on request.

Bibliography

References

A. Abrikosov. The magnetic properties of superconducting alloys. *Journal of Physics and Chemistry of Solids*, 2(3):199–208, Jan. 1957. ISSN 00223697. doi: 10.1016/0022-3697(57)90083-5.

N. Ackermann, A. Zazunov, S. Park, R. Egger, and A. L. Yeyati. Dynamical parity selection in superconducting weak links. *Physical Review B*, 107(21):214515, June 2023. ISSN 2469-9950, 2469-9969. doi: 10.1103/PhysRevB.107.214515.

F. Afshar, S. Nazarpour, and A. Cirera. Survey of the theory and experimental measurements of residual stress in Pd thin film. *Journal of Applied Physics*, 108(9):093513, Nov. 2010. ISSN 0021-8979. doi: 10.1063/1.3505725.

H. G. Ahmad, M. Minutillo, R. Capecelatro, A. Pal, R. Caruso, G. Passarelli, M. G. Blamire, F. Tafuri, P. Lucignano, and D. Massarotti. Coexistence and tuning of spin-singlet and triplet transport in spin-filter Josephson junctions. *Communications Physics*, 5(1):2, Dec. 2022. ISSN 2399-3650. doi: 10.1038/s42005-021-00783-1.

G. AI. Quantum supremacy using a programmable superconducting processor. *Nature*, 574(7779), Oct. 2019. doi: 10.1038/s41586-019-1666-5.

A. Akhmerov and G. Steele. Open Data Policy of the Quantum Nanoscience Department, TU Delft. Feb. 2019. doi: 10.5281/ZENODO.2556949.

S. M. Albrecht, A. P. Higginbotham, M. Madsen, F. Kuemmeth, T. S. Jespersen, J. Nygård, P. Krogstrup, and C. M. Marcus. Exponential protection of zero modes in Majorana islands. *Nature*, 531(7593):206–209, Mar. 2016. ISSN 0028-0836, 1476-4687. doi: 10.1038/nature17162.

J. Alicea. Majorana fermions in a tunable semiconductor device. *Physical Review B*, 81(12):125318, Mar. 2010. ISSN 1098-0121, 1550-235X. doi: 10.1103/PhysRevB.81.125318.

P. W. Anderson. Localized Magnetic States in Metals. *Physical Review*, 124(1):41–53, Oct. 1961. ISSN 0031-899X. doi: 10.1103/PhysRev.124.41.

P. W. Anderson. How Josephson discovered his effect. *Physics Today*, 23(11):23–29, Nov. 1970. ISSN 0031-9228, 1945-0699. doi: 10.1063/1.3021826.

A. F. Andreev. The thermal conductivity of the intermediate state in superconductors. *Soviet Physics JETP*, 19(5), Nov. 1964.

J. F. Annett. *Superconductivity, Superfluids, and Condensates.* Number 5 in Oxford Master Series in Physics Condensed Matter Physics. Oxford Univ. Press, Oxford, repr edition, 2011. ISBN 978-0-19-850755-0 978-0-19-850756-7.

A. J. Annunziata, D. F. Santavicca, L. Frunzio, G. Catelani, M. J. Rooks, A. Frydman, and D. E. Prober. Tunable superconducting nanoinductors. *Nanotechnology*, 21(44):445202, Nov. 2010. ISSN 0957-4484, 1361-6528. doi: 10.1088/0957-4484/21/44/445202.

A. E. Antipov, A. Bargerbos, G. W. Winkler, B. Bauer, E. Rossi, and R. M. Lutchyn. Effects of gate-induced electric fields on semiconductor Majorana nanowires. *Physical Review X*, 8(3):031041, Aug. 2018. ISSN 2160-3308. doi: 10.1103/PhysRevX.8.031041.

A. Aspuru-Guzik, A. D. Dutoi, P. J. Love, and M. Head-Gordon. Simulated Quantum Computation of Molecular Energies. *Science*, 309(5741):1704–1707, Sept. 2005. ISSN 0036-8075, 1095-9203. doi: 10.1126/science.1113479.

A. Assouline, C. Feuillet-Palma, N. Bergeal, T. Zhang, A. Mottaghizadeh, A. Zimmers, E. Lhuillier, M. Eddrie, P. Atkinson, M. Aprili, and H. Aubin. Spin-Orbit induced phase-shift in Bi2Se3 Josephson junctions. *Nature Communications*, 10(1):126, Dec. 2019. ISSN 2041-1723. doi: 10.1038/s41467-018-08022-y.

J. Aumentado, M. W. Keller, J. M. Martinis, and M. H. Devoret. Nonequilibrium Quasiparticles and 2 e Periodicity in Single-Cooper-Pair Transistors. *Physical Review Letters*, 92(6):066802, Feb. 2004. ISSN 0031-9007, 1079-7114. doi: 10.1103/PhysRevLett.92.066802.

G. Badawy, S. Gazibegovic, F. Borsoi, S. Heedt, C.-A. Wang, S. Koelling, M. A. Verheijen, L. P. Kouwenhoven, and E. P. A. M. Bakkers. High Mobility Stemless InSb Nanowires. *Nano Letters*, 19(6):3575–3582, June 2019. ISSN 1530-6984, 1530-6992. doi: 10.1021/acs.nanolett.9b00545.

P. F. Bagwell. Suppression of the Josephson current through a narrow, mesoscopic, semiconductor channel by a single impurity. *Physical Review B*, 46(19):12573–12586, Nov. 1992. ISSN 0163-1829, 1095-3795. doi: 10.1103/PhysRevB.46.12573.

L. Banszerus, S. Möller, K. Hecker, E. Icking, K. Watanabe, T. Taniguchi, F. Hassler, C. Volk, and C. Stampfer. Particle-hole symmetry protects spin-valley blockade in graphene quantum dots, Mar. 2023.

F. Barahona. On the computational complexity of Ising spin glass models. *Journal of Physics A: Mathematical and General*, 15(10):3241–3253, Oct. 1982. ISSN 0305-4470, 1361-6447. doi: 10.1088/0305-4470/15/10/028.

J. Bardeen, L. N. Cooper, and J. R. Schrieffer. Theory of Superconductivity. *Physical Review*, 108(5):1175–1204, Dec. 1957. ISSN 0031-899X. doi: 10.1103/PhysRev.108.1175.

A. Bargerbos. *Nanowire Josephson Junctions in Superconducting Circuits.* PhD thesis, Delft University of Technology, 2023.

A. Bargerbos, W. Uilhoorn, C.-K. Yang, P. Krogstrup, L. P. Kouwenhoven, G. de Lange, B. van Heck, and A. Kou. Observation of vanishing charge dispersion of a nearly-open superconducting island. *Physical Review Letters*, 124(24):246802, June 2020. ISSN 0031-9007, 1079-7114. doi: 10.1103/PhysRevLett.124.246802.

A. Bargerbos, M. Pita-Vidal, R. Žitko, J. Ávila, L. J. Splitthoff, L. Grünhaupt, J. J. Wesdorp, C. K. Andersen, Y. Liu, L. P. Kouwenhoven, R. Aguado, A. Kou, and B. van Heck. Singlet-doublet transitions of a quantum dot Josephson junction detected in a transmon circuit. *PRX Quantum*, 3(3):030311, July 2022. ISSN 2691-3399. doi: 10.1103/PRXQuantum.3.030311.

A. Bargerbos, M. Pita-Vidal, R. Žitko, L. J. Splitthoff, L. Grünhaupt, J. J. Wesdorp, Y. Liu, L. P. Kouwenhoven, R. Aguado, C. K. Andersen, A. Kou, and B. Van Heck. Spectroscopy of Spin-Split Andreev Levels in a Quantum Dot with Superconducting Leads. *Physical Review Letters*, 131(9):097001, Aug. 2023a. ISSN 0031-9007, 1079-7114. doi: 10.1103/PhysRevLett.131.097001.

A. Bargerbos, L. J. Splitthoff, M. Pita-Vidal, J. J. Wesdorp, Y. Liu, P. Krogstrup, L. P. Kouwenhoven, C. K. Andersen, and L. Grünhaupt. Mitigation of quasiparticle loss in superconducting qubits by phonon scattering. *Physical Review Applied*, 19(2):024014, Feb. 2023b. ISSN 2331-7019. doi: 10.1103/PhysRevApplied.19.024014.

M. S. Bartlett. Smoothing Periodograms from Time-Series with Continuous Spectra. *Nature*, 161(4096):686–687, May 1948. ISSN 1476-4687. doi: 10.1038/161686a0.

G. Batey, S. Chappell, M. N. Cuthbert, M. Erfani, A. J. Matthews, and G. Teleberg. A rapid sample-exchange mechanism for cryogen-free dilution refrigerators compatible with multiple high-frequency signal connections. *Cryogenics*, 60:24–32, Mar. 2014. ISSN 0011-2275. doi: 10.1016/j.cryogenics.2014.01.007.

C. W. J. Beenakker. Universal limit of critical-current fluctuations in mesoscopic Josephson junctions. *Physical Review Letters*, 67(27):3836–3839, Dec. 1991. ISSN 0031-9007. doi: 10.1103/PhysRevLett.67.3836.

C. W. J. Beenakker and H. van Houten. Resonant Josephson current through a quantum dot. *arXiv:cond-mat/0111505*, 31:175–179, 1992. doi: 10.1007/978-3-642-77274-0_20.

M. Ben Shalom, M. J. Zhu, V. I. Fal'ko, A. Mishchenko, A. V. Kretinin, K. S. Novoselov, C. R. Woods, K. Watanabe, T. Taniguchi, A. K. Geim, and J. R. Prance. Quantum oscillations of the critical current and high-field superconducting proximity in ballistic graphene. *Nature Physics*, 12(4):318–322, Apr. 2016. ISSN 1745-2473, 1745-2481. doi: 10.1038/nphys3592.

A. Benfenati, A. Maiani, F. N. Rybakov, and E. Babaev. Vortex nucleation barrier in superconductors beyond the Bean-Livingston approximation: A numerical approach for the sphaleron problem in a gauge theory. *Physical Review B*, 101(22):220505, June 2020. ISSN 2469-9950, 2469-9969. doi: 10.1103/PhysRevB.101.220505.

F. S. Bergeret and I. V. Tokatly. Theory of diffusive Φ0 Josephson junctions in the presence of spin-orbit coupling. *Europhysics Letters*, 110(5):57005, June 2015. ISSN 0295-5075. doi: 10.1209/0295-5075/110/57005.

B. Béri, J. H. Bardarson, and C. W. J. Beenakker. Splitting of Andreev levels in a Josephson junction by spin-orbit coupling. *Physical review. B*, 77(4), Jan. 2008. doi: 10.1103/physrevb.77.045311.

A. Blais, R.-S. Huang, A. Wallraff, S. M. Girvin, and R. J. Schoelkopf. Cavity quantum electrodynamics for superconducting electrical circuits: An architecture for quantum computation. *Physical Review A*, 69(6):062320, June 2004. ISSN 1050-2947, 1094-1622. doi: 10.1103/PhysRevA.69.062320.

N. Bogoliubov, V. Tolmachev, and D. Shirkov. *A New Method in the Theory of Superconductivity*. 1959.

J. D. S. Bommer, H. Zhang, Ö. Gül, B. Nijholt, M. Wimmer, F. N. Rybakov, J. Garaud, D. Rodic, E. Babaev, M. Troyer, D. Car, S. R. Plissard, E. P. A. M. Bakkers, K. Watanabe, T. Taniguchi, and L. P. Kouwenhoven. Spin-Orbit Protection of Induced Superconductivity in Majorana Nanowires. *Physical Review Letters*, 122(18):187702, May 2019. ISSN 0031-9007, 1079-7114. doi: 10.1103/PhysRevLett.122.187702.

A. Bordin, X. Li, D. van Driel, J. C. Wolff, Q. Wang, S. L. D. ten Haaf, G. Wang, N. van Loo, L. P. Kouwenhoven, and T. Dvir. Crossed Andreev reflection and elastic co-tunneling in a three-site Kitaev chain nanowire device. *arXiv:2306.07696*, June 2023.

F. Borjans, X. G. Croot, X. Mi, M. J. Gullans, and J. R. Petta. Resonant microwave-mediated interactions between distant electron spins. *Nature*, 577(7789):195–198, Jan. 2020. ISSN 0028-0836, 1476-4687. doi: 10.1038/s41586-019-1867-y.

F. Borsoi, G. P. Mazur, N. Van Loo, M. P. Nowak, L. Bourdet, K. Li, S. Korneychuk, A. Fursina, J.-Y. Wang, V. Levajac, E. Memisevic, G. Badawy, S. Gazibegovic, K. Van Hoogdalem, E. P. A. M. Bakkers, L. P. Kouwenhoven, S. Heedt, and M. Quintero-Pérez. Single-Shot Fabrication of Semiconducting–Superconducting Nanowire Devices. *Advanced Functional Materials*, 31(34):2102388, Aug. 2021. ISSN 1616-301X, 1616-3028. doi: 10.1002/adfm.202102388.

F. Boscherini, Y. Shapira, C. Capasso, C. Aldao, M. del Giudice, and J. H. Weaver. Exchange reaction, clustering, and surface segregation at the Al/InSb(110) interface. *Physical Review B*, 35(18):9580–9585, June 1987. doi: 10.1103/PhysRevB.35.9580.

S. Bravyi, A. W. Cross, J. M. Gambetta, D. Maslov, P. Rall, and T. J. Yoder. High-threshold and low-overhead fault-tolerant quantum memory. *arXiv:2308.07915*, Feb. 2024.

S. B. Bravyi and A. Y. Kitaev. Quantum codes on a lattice with boundary, Nov. 1998.

L. Bretheau. *Localized Excitations in Superconducting Atomic Contacts: Probing the Andreev Doublet*. PhD thesis, Ecole Poly- technique X, 2013.

L. Bretheau, Ç. Ö. Girit, H. Pothier, D. Esteve, and C. Urbina. Exciting Andreev pairs in a superconducting atomic contact. *Nature*, 499(7458):312–315, July 2013a. ISSN 0028-0836, 1476-4687. doi: 10.1038/nature12315.

L. Bretheau, Ç. Ö. Girit, C. Urbina, D. Esteve, and H. Pothier. Supercurrent Spectroscopy of Andreev States. *Physical Review X*, 3(4):041034, Dec. 2013b. ISSN 2160-3308. doi: 10.1103/PhysRevX.3.041034.

L. Bretheau, J. I.-J. Wang, R. Pisoni, K. Watanabe, T. Taniguchi, and P. Jarillo-Herrero. Tunnelling spectroscopy of Andreev states in graphene. *Nature Physics*, 13(8):756–760, Aug. 2017. ISSN 1745-2473, 1745-2481. doi: 10.1038/nphys4110.

A. Brunetti, A. Zazunov, A. Kundu, and R. Egger. Anomalous Josephson current, incipient time-reversal symmetry breaking, and Majorana bound states in interacting multilevel dots. *Physical Review B*, 88(14):144515, Oct. 2013. ISSN 1098-0121, 1550-235X. doi: 10.1103/PhysRevB.88.144515.

A. Bruno, G. de Lange, S. Asaad, K. L. van der Enden, N. K. Langford, and L. DiCarlo. Reducing intrinsic loss in superconducting resonators by surface treatment and deep etching of silicon substrates. *Applied Physics Letters*, 106(18):182601, May 2015. ISSN 0003-6951, 1077-3118. doi: 10.1063/1.4919761.

G. Burkard, T. D. Ladd, A. Pan, J. M. Nichol, and J. R. Petta. Semiconductor spin qubits. *Reviews of Modern Physics*, 95(2):025003, June 2023. doi: 10.1103/RevModPhys.95.025003.

A. I. Buzdin. Proximity effects in superconductor-ferromagnet heterostructures. *Reviews of Modern Physics*, 77(3):935–976, Sept. 2005. ISSN 0034-6861, 1539-0756. doi: 10.1103/RevModPhys.77.935.

R. Cai, Y. Yao, P. Lv, Y. Ma, W. Xing, B. Li, Y. Ji, H. Zhou, C. Shen, S. Jia, X. C. Xie, I. Žutić, Q.-F. Sun, and W. Han. Evidence for anisotropic spin-triplet Andreev reflection at the 2D van der Waals ferromagnet/superconductor interface. *Nature Communications*, 12 (1):6725, Dec. 2021. ISSN 2041-1723. doi: 10.1038/s41467-021-27041-w.

V. E. Calado, S. Goswami, G. Nanda, M. Diez, A. R. Akhmerov, K. Watanabe, T. Taniguchi, T. M. Klapwijk, and L. M. K. Vandersypen. Ballistic Josephson junctions in edge-contacted graphene. *Nature Nanotechnology*, 10(9):761–764, Sept. 2015. ISSN 1748-3387, 1748-3395. doi: 10.1038/nnano.2015.156.

G. Campagnano, P. Lucignano, D. Giuliano, and A. Tagliacozzo. Spin–orbit coupling and anomalous Josephson effect in nanowires. *Journal of Physics: Condensed Matter*, 27(20): 205301, May 2015. ISSN 0953-8984, 1361-648X. doi: 10.1088/0953-8984/27/20/205301.

L. Casparis, T. W. Larsen, M. S. Olsen, F. Kuemmeth, P. Krogstrup, J. Nygård, K. D. Petersson, and C. M. Marcus. Gatemon Benchmarking and Two-Qubit Operations. *Physical Review Letters*, 116(15):150505, Apr. 2016. ISSN 0031-9007, 1079-7114. doi: 10.1103/PhysRevLett.116.150505.

L. Casparis, M. R. Connolly, M. Kjaergaard, N. J. Pearson, A. Kringhøj, T. W. Larsen, F. Kuemmeth, T. Wang, C. Thomas, S. Gronin, G. C. Gardner, M. J. Manfra, C. M. Marcus, and K. D. Petersson. Superconducting gatemon qubit based on a proximitized two-dimensional electron gas. *Nature Nanotechnology*, 13(10):915–919, Oct. 2018. ISSN 1748-3387, 1748-3395. doi: 10.1038/s41565-018-0207-y.

J. Cayao, A. M. Black-Schaffer, E. Prada, and R. Aguado. Andreev spectrum and supercurrents in nanowire-based SNS junctions containing Majorana bound states. *Beilstein Journal of Nanotechnology*, 9:1339–1357, May 2018. ISSN 2190-4286. doi: 10.3762/bjnano.9.127.

W. Chang, S. M. Albrecht, T. S. Jespersen, F. Kuemmeth, P. Krogstrup, J. Nygård, and C. M. Marcus. Hard gap in epitaxial semiconductor-superconductor nanowires. *Nature Nanotechnology*, 10(3):232–236, Mar. 2015. ISSN 1748-3387, 1748-3395. doi: 10.1038/nnano.2014.306.

M. Cheng and R. M. Lutchyn. Josephson Current through a Semiconductor Nanowire: Effect of strong spin-orbit coupling and Zeeman splitting. *Physical Review B*, 86(13):134522, Oct. 2012. ISSN 1098-0121, 1550-235X. doi: 10.1103/PhysRevB.86.134522.

L. Y. Cheung, R. Haller, A. Kononov, C. Ciaccia, J. H. Ungerer, T. Kanne, J. Nygård, P. Winkel, T. Reisinger, I. M. Pop, A. Baumgartner, and C. Schönenberger. Photon-mediated long range coupling of two Andreev level qubits, Oct. 2023.

V. Chidambaram, A. Kringhøj, L. Casparis, F. Kuemmeth, T. Wang, C. Thomas, S. Gronin, G. C. Gardner, Z. Cui, C. Liu, K. Moors, M. J. Manfra, K. D. Petersson, and M. R. Connolly. Microwave sensing of Andreev bound states in a gate-defined superconducting quantum point contact. *Physical Review Research*, 4(2):023170, May 2022. ISSN 2643-1564. doi: 10.1103/PhysRevResearch.4.023170.

I. Chiorescu, Y. Nakamura, C. J. P. M. Harmans, and J. E. Mooij. Coherent Quantum Dynamics of a Superconducting Flux Qubit. *Science*, 299(5614):1869–1871, Mar. 2003. ISSN 0036-8075, 1095-9203. doi: 10.1126/science.1081045.

N. M. Chtchelkatchev and Yu. V. Nazarov. Andreev Quantum Dots for Spin Manipulation. *Physical Review Letters*, 90(22):226806, June 2003. ISSN 0031-9007, 1079-7114. doi: 10.1103/PhysRevLett.90.226806.

J. Clarke and A. I. Braginski, editors. *The SQUID Handbook: Fundamentals and Technology of SQUIDs and SQUID Systems*. Wiley, 1 edition, May 2004. ISBN 978-3-527-40229-8 978-3-527-60364-0. doi: 10.1002/3527603646.

A. J. Daley, I. Bloch, C. Kokail, S. Flannigan, N. Pearson, M. Troyer, and P. Zoller. Practical quantum advantage in quantum simulation. *Nature*, 607(7920):667–676, July 2022. ISSN 0028-0836, 1476-4687. doi: 10.1038/s41586-022-04940-6.

S. Das Sarma and H. Pan. Disorder-induced zero-bias peaks in Majorana nanowires. *Physical Review B*, 103(19):195158, May 2021. doi: 10.1103/PhysRevB.103.195158.

S. Datta and P. F. Bagwell. Can the Bogoliubov–de Gennes equation be interpreted as a 'one-particle' wave equation? *Superlattices and Microstructures*, 25(5-6):1233–1250, May 1999. ISSN 07496036. doi: 10.1006/spmi.1999.0747.

S. De Franceschi, L. Kouwenhoven, C. Schönenberger, and W. Wernsdorfer. Hybrid superconductor–quantum dot devices. *Nature Nanotechnology*, 5(10):703–711, Oct. 2010. ISSN 1748-3387, 1748-3395. doi: 10.1038/nnano.2010.173.

P. G. de Gennes. *Superconductivity Of Metals And Alloys*. Taylor & Francis Inc, Boca Raton London New York, first edition, Mar. 1999. ISBN 978-0-7382-0101-6.

D. de Jong, J. van Veen, L. Binci, A. Singh, P. Krogstrup, L. P. Kouwenhoven, W. Pfaff, and J. D. Watson. Rapid detection of coherent tunneling in an InAs nanowire quantum dot through dispersive gate sensing. *Physical Review Applied*, 11(4):044061, Apr. 2019. ISSN 2331-7019. doi: 10.1103/PhysRevApplied.11.044061.

G. de Lange and J. J. Wesdorp. Superconducting quantum interference devices and uses thereof, Aug. 2023.

G. de Lange, B. van Heck, A. Bruno, D. J. van Woerkom, A. Geresdi, S. R. Plissard, E. P. A. M. Bakkers, A. R. Akhmerov, and L. DiCarlo. Realization of Microwave Quantum Circuits Using Hybrid Superconducting-Semiconducting Nanowire Josephson Elements. *Physical Review Letters*, 115(12):127002, Sept. 2015. ISSN 0031-9007, 1079-7114. doi: 10.1103/PhysRevLett.115.127002.

M. W. A. de Moor, J. D. S. Bommer, D. Xu, G. W. Winkler, A. E. Antipov, A. Bargerbos, G. Wang, N. van Loo, R. L. M. Op het Veld, S. Gazibegovic, D. Car, J. A. Logan, M. Pendharkar, J. S. Lee, E. P. A. M Bakkers, C. J. Palmstrøm, R. M. Lutchyn, L. P. Kouwenhoven, and H. Zhang. Electric field tunable superconductor-semiconductor coupling in Majorana nanowires. *New Journal of Physics*, 20(10):103049, Oct. 2018. ISSN 1367-2630. doi: 10.1088/1367-2630/aae61d.

M. A. Despósito and A. Levy Yeyati. Controlled dephasing of Andreev states in superconducting quantum point contacts. *Physical Review B*, 64(14):140511, Sept. 2001. ISSN 0163-1829, 1095-3795. doi: 10.1103/PhysRevB.64.140511.

M. H. Devoret and R. J. Schoelkopf. Superconducting Circuits for Quantum Information: An Outlook. *Science*, 339(6124):1169–1174, Mar. 2013. doi: 10.1126/science.1231930.

J. Dijkema, X. Xue, P. Harvey-Collard, M. Rimbach-Russ, S. L. de Snoo, G. Zheng, A. Sammak, G. Scappucci, and L. M. K. Vandersypen. Two-qubit logic between distant spins in silicon. *arXiv:2310.16805*, Oct. 2023.

L. Ding, M. Hays, Y. Sung, B. Kannan, J. An, A. Di Paolo, A. H. Karamlou, T. M. Hazard, K. Azar, D. K. Kim, B. M. Niedzielski, A. Melville, M. E. Schwartz, J. L. Yoder, T. P. Orlando, S. Gustavsson, J. A. Grover, K. Serniak, and W. D. Oliver. High-Fidelity, Frequency-Flexible Two-Qubit Fluxonium Gates with a Transmon Coupler, Apr. 2023.

D. P. DiVincenzo. The Physical Implementation of Quantum Computation. *Fortschritte der Physik*, 48(9-11):771–783, Sept. 2000. ISSN 00158208, 15213978. doi: 10.1002/1521-3978(200009)48:9/11<771::AID-PROP771>3.0.CO;2-E.

Y.-J. Doh. Tunable Supercurrent Through Semiconductor Nanowires. *Science*, 309(5732):272–275, July 2005. ISSN 0036-8075, 1095-9203. doi: 10.1126/science.1113523.

T. Dvir, G. Wang, N. Van Loo, C.-X. Liu, G. P. Mazur, A. Bordin, S. L. D. Ten Haaf, J.-Y. Wang, D. Van Driel, F. Zatelli, X. Li, F. K. Malinowski, S. Gazibegovic, G. Badawy, E. P. A. M. Bakkers, M. Wimmer, and L. P. Kouwenhoven. Realization of a minimal Kitaev chain in coupled quantum dots. *Nature*, 614(7948):445–450, Feb. 2023. ISSN 0028-0836, 1476-4687. doi: 10.1038/s41586-022-05585-1.

M. Eich, F. Herman, R. Pisoni, H. Overweg, A. Kurzmann, Y. Lee, P. Rickhaus, K. Watanabe, T. Taniguchi, M. Sigrist, T. Ihn, and K. Ensslin. Spin and Valley States in Gate-Defined Bilayer Graphene Quantum Dots. *Physical Review X*, 8(3):031023, July 2018. ISSN 2160-3308. doi: 10.1103/PhysRevX.8.031023.

J. T. Farmer, A. Zarassi, D. M. Hartsell, E. Vlachos, H. Zhang, and E. M. Levenson-Falk. Continuous real-time detection of quasiparticle trapping in aluminum nanobridge Josephson junctions. *Applied Physics Letters*, 119(12):122601, Sept. 2021. ISSN 0003-6951. doi: 10.1063/5.0063445.

V. Fatemi, P. D. Kurilovich, M. Hays, D. Bouman, T. Connolly, S. Diamond, N. E. Frattini, V. D. Kurilovich, P. Krogstrup, J. Nygård, A. Geresdi, L. I. Glazman, and M. H. Devoret. Microwave Susceptibility Observation of Interacting Many-Body Andreev States. *Physical Review Letters*, 129(22):227701, Nov. 2022. ISSN 0031-9007, 1079-7114. doi: 10.1103/PhysRevLett.129.227701.

D. Feldstein Bofill. Magnetic field resilient lumped element superconducting resonators. 2022.

R. P. Feynman. Simulating physics with computers. *International Journal of Theoretical Physics*, 21(6,7), 1982.

D. Flanigan. To perform the fits we used the code available in the following GitHub repository: https://github.com/danielflanigan/resonator.

A. G. Fowler, M. Mariantoni, J. M. Martinis, and A. N. Cleland. Surface codes: Towards practical large-scale quantum computation. *Physical Review A*, 86(3):032324, Sept. 2012. ISSN 1050-2947, 1094-1622. doi: 10.1103/PhysRevA.86.032324.

S. friedel. How to Calculate a Capacitance Matrix in COMSOL Multiphysics®, 2017.

L. Fu and C. L. Kane. Josephson current and noise at a superconductor/quantum-spin-Hall-insulator/superconductor junction. *Physical Review B*, 79(16):161408, Apr. 2009. ISSN 1098-0121, 1550-235X. doi: 10.1103/PhysRevB.79.161408.

L. M. Gächter, R. Garreis, J. D. Gerber, M. J. Ruckriegel, C. Tong, B. Kratochwil, F. K. de Vries, A. Kurzmann, K. Watanabe, T. Taniguchi, T. Ihn, K. Ensslin, and W. W. Huang. Single-Shot Spin Readout in Graphene Quantum Dots. *PRX Quantum*, 3(2):020343, May 2022. ISSN 2691-3399. doi: 10.1103/PRXQuantum.3.020343.

S. T. Gill, J. Damasco, D. Car, E. P. A. M. Bakkers, and N. Mason. Hybrid superconductor-quantum point contact devices using InSb nanowires. *Applied Physics Letters*, 109(23): 233502, Dec. 2016. ISSN 0003-6951, 1077-3118. doi: 10.1063/1.4971394.

V. L. Ginzburg. *On Superconductivity and Superfluidity: A Scientific Autobiography*. Springer-Verlag, Berlin, 2009. ISBN 978-3-540-68004-8 978-3-540-68008-6.

S. M. Girvin. Circuit QED: Superconducting qubits coupled to microwave photons. In M. Devoret, B. Huard, R. Schoelkopf, and L. F. Cugliandolo, editors, *Quantum Machines: Measurement and Control of Engineered Quantum Systems: Lecture Notes of the Les Houches Summer School: Volume 96, July 2011*, page 0. Oxford University Press, June 2014. ISBN 978-0-19-968118-1. doi: 10.1093/acprof:oso/9780199681181.003.0003.

L. I. Glazman and G. Catelani. Bogoliubov Quasiparticles in Superconducting Qubits. *SciPost Physics Lecture Notes*, page 31, June 2021. ISSN 2590-1990. doi: 10.21468/SciPostPhysLectNotes.31.

L. I. Glazman and K. A. Matveev. Resonant Josephson current through Kondo impurities in a tunnel barrier. *JETP Letters [translation of Pisma v Zhurnal Eksperimentalnoi i Teoreticheskoi Fiziki]*, 49(10), 1994, 1989.

M. F. Goffman, C. Urbina, H. Pothier, J. Nygård, C. M. Marcus, and P. Krogstrup. Conduction channels of an InAs-Al nanowire Josephson weak link. *New Journal of Physics*, 19 (9):092002, Sept. 2017. ISSN 1367-2630. doi: 10.1088/1367-2630/aa7641.

Gor'kov. Microscopic Derivation of the Ginzburg-Landau Equations in the Theory of Superconductivity. *JETP*, 9(6):1364, Dec. 1959.

L. P. Gor'kov and E. I. Rashba. Superconducting 2D System with Lifted Spin Degeneracy: Mixed Singlet-Triplet State. *Physical Review Letters*, 87(3):037004, July 2001. ISSN 0031-9007, 1079-7114. doi: 10.1103/PhysRevLett.87.037004.

A. Goswami, S. R. Mudi, C. Dempsey, P. Zhang, H. Wu, B. Zhang, W. J. Mitchell, J. S. Lee, S. M. Frolov, and C. J. Palmstrøm. Sn/InAs josephson junctions on selective area grown nanowires with in situ shadowed superconductor evaporation. *Nano Letters*, 23(16): 7311–7318, Aug. 2023. doi: 10.1021/acs.nanolett.3c01320.

M. Governale and U. Zülicke. Spin accumulation in quantum wires with strong Rashba spin-orbit coupling. *Physical Review B*, 66(7):073311, Aug. 2002. ISSN 0163-1829, 1095-3795. doi: 10.1103/PhysRevB.66.073311.

C. W. Groth, M. Wimmer, A. R. Akhmerov, and X. Waintal. Kwant: A software package for quantum transport. *New Journal of Physics*, 16(6):063065, June 2014. ISSN 1367-2630. doi: 10.1088/1367-2630/16/6/063065.

Ö. Gül, D. J. V. Woerkom, I. V. Weperen, D. Car, S. R. Plissard, E. P. A. M. Bakkers, and L. P. Kouwenhoven. Towards high mobility InSb nanowire devices. *Nanotechnology*, 26(21): 215202, May 2015. ISSN 0957-4484, 1361-6528. doi: 10.1088/0957-4484/26/21/215202.

L. Han, M. Chan, D. de Jong, C. Prosko, G. Badawy, S. Gazibegovic, E. P. Bakkers, L. P. Kouwenhoven, F. K. Malinowski, and W. Pfaff. Variable and orbital-dependent spin-orbit field orientations in an InSb double quantum dot characterized via dispersive gate sensing. *Physical Review Applied*, 19(1):014063, Jan. 2023. doi: 10.1103/PhysRevApplied. 19.014063.

R. Hanson, L. P. Kouwenhoven, J. R. Petta, S. Tarucha, and L. M. K. Vandersypen. Spins in few-electron quantum dots. *Reviews of Modern Physics*, 79(4):1217–1265, Oct. 2007. ISSN 0034-6861, 1539-0756. doi: 10.1103/RevModPhys.79.1217.

P. Harvey-Collard, G. Zheng, J. Dijkema, N. Samkharadze, A. Sammak, G. Scappucci, and L. M. K. Vandersypen. On-Chip Microwave Filters for High-Impedance Resonators with Gate-Defined Quantum Dots. *Physical Review Applied*, 14(3):034025, Sept. 2020. ISSN 2331-7019. doi: 10.1103/PhysRevApplied.14.034025.

P. Harvey-Collard, J. Dijkema, G. Zheng, A. Sammak, G. Scappucci, and L. M. K. Vandersypen. Coherent Spin-Spin Coupling Mediated by Virtual Microwave Photons. *Physical Review X*, 12(2):021026, May 2022. ISSN 2160-3308. doi: 10.1103/PhysRevX.12.021026.

M. Hays. *Realizing an Andreev Spin Qubit: Exploring Sub-gap Structure in Josephson Nanowires Using Circuit QED*. Springer Theses. Springer International Publishing, Cham, 2021. ISBN 978-3-030-83878-2 978-3-030-83879-9. doi: 10.1007/ 978-3-030-83879-9.

M. Hays, G. de Lange, K. Serniak, D. J. van Woerkom, D. Bouman, P. Krogstrup, J. Nygård, A. Geresdi, and M. H. Devoret. Direct microwave measurement of Andreev-bound-state dynamics in a proximitized semiconducting nanowire. *Physical Review Letters*, 121(4): 047001, July 2018. ISSN 0031-9007, 1079-7114. doi: 10.1103/PhysRevLett.121.047001.

M. Hays, V. Fatemi, K. Serniak, D. Bouman, S. Diamond, G. de Lange, P. Krogstrup, J. Nygård, A. Geresdi, and M. H. Devoret. Continuous monitoring of a trapped, superconducting spin. *Nature Physics*, 16(11):1103–1107, Nov. 2020. ISSN 1745-2473, 1745-2481. doi: 10.1038/s41567-020-0952-3.

M. Hays, V. Fatemi, D. Bouman, J. Cerrillo, S. Diamond, K. Serniak, T. Connolly, P. Krogstrup, J. Nygård, A. L. Yeyati, A. Geresdi, and M. H. Devoret. Coherent manipulation of an Andreev spin qubit. *Science*, 373(6553):430–433, July 2021. ISSN 0036-8075, 1095-9203. doi: 10.1126/science.abf0345.

S. Heedt, M. Quintero-Pérez, F. Borsoi, A. Fursina, N. van Loo, G. P. Mazur, M. P. Nowak, M. Ammerlaan, K. Li, S. Korneychuk, J. Shen, M. A. Y. van de Poll, G. Badawy, S. Gazibegovic, N. de Jong, P. Aseev, K. van Hoogdalem, E. P. A. M. Bakkers, and L. P. Kouwenhoven. Shadow-wall lithography of ballistic superconductor–semiconductor quantum devices. *Nature Communications*, 12(1):4914, Dec. 2021. ISSN 2041-1723. doi: 10.1038/s41467-021-25100-w.

N. W. Hendrickx, D. P. Franke, A. Sammak, M. Kouwenhoven, D. Sabbagh, L. Yeoh, R. Li, M. L. V. Tagliaferri, M. Virgilio, G. Capellini, G. Scappucci, and M. Veldhorst. Gate-controlled quantum dots and superconductivity in planar germanium. *Nature Communications*, 9(1):2835, July 2018. ISSN 2041-1723. doi: 10.1038/s41467-018-05299-x.

N. W. Hendrickx, D. P. Franke, A. Sammak, G. Scappucci, and M. Veldhorst. Fast two-qubit logic with holes in germanium. *Nature*, 577(7791):487–491, Jan. 2020. ISSN 0028-0836, 1476-4687. doi: 10.1038/s41586-019-1919-3.

N. W. Hendrickx, W. I. L. Lawrie, M. Russ, F. Van Riggelen, S. L. De Snoo, R. N. Schouten, A. Sammak, G. Scappucci, and M. Veldhorst. A four-qubit germanium quantum processor. *Nature*, 591(7851):580–585, Mar. 2021. ISSN 0028-0836, 1476-4687. doi: 10.1038/s41586-021-03332-6.

M. Hinderling, D. Sabonis, S. Paredes, D. Haxell, M. Coraiola, S. Ten Kate, E. Cheah, F. Krizek, R. Schott, W. Wegscheider, and F. Nichele. Flip-Chip-Based Microwave Spectroscopy of Andreev Bound States in a Planar Josephson Junction. *Physical Review Applied*, 19(5):054026, May 2023. ISSN 2331-7019. doi: 10.1103/PhysRevApplied.19.054026.

R. P. Huebener and J. R. Clem. Magnetic flux structures in superconductors—a conference summary. *Reviews of Modern Physics*, 46(2):409–422, Apr. 1974. ISSN 0034-6861. doi: 10.1103/RevModPhys.46.409.

D. A. Ivanov. Non-Abelian Statistics of Half-Quantum Vortices in p -Wave Superconductors. *Physical Review Letters*, 86(2):268–271, Jan. 2001. ISSN 0031-9007, 1079-7114. doi: 10.1103/PhysRevLett.86.268.

C. Janvier. *Coherent Manipulation of Andreev Bound States in an Atomic Contact*. PhD thesis, Université Paris-Saclay, 2016.

C. Janvier, L. Tosi, L. Bretheau, Ç. Ö. Girit, M. Stern, P. Bertet, P. Joyez, D. Vion, D. Esteve, M. F. Goffman, H. Pothier, and C. Urbina. Coherent manipulation of Andreev states in superconducting atomic contacts. *Science*, 349(6253):1199–1202, Sept. 2015. ISSN 0036-8075, 1095-9203. doi: 10.1126/science.aab2179.

K.-R. Jeon, X. Montiel, S. Komori, C. Ciccarelli, J. Haigh, H. Kurebayashi, L. F. Cohen, A. K. Chan, K. D. Stenning, C.-M. Lee, M. Eschrig, M. G. Blamire, and J. W. A. Robinson. Tunable Pure Spin Supercurrents and the Demonstration of Their Gateability in a Spin-Wave Device. *Physical Review X*, 10(3):031020, July 2020. ISSN 2160-3308. doi: 10.1103/PhysRevX.10.031020.

X. Y. Jin, A. Kamal, A. P. Sears, T. Gudmundsen, D. Hover, J. Miloshi, R. Slattery, F. Yan, J. Yoder, T. P. Orlando, S. Gustavsson, and W. D. Oliver. Thermal and residual excited-state population in a 3D transmon qubit. *Physical Review Letters*, 114(24):240501, June 2015. doi: 10.1103/PhysRevLett.114.240501.

J. R. Johansson, P. D. Nation, and F. Nori. QuTiP 2: A Python framework for the dynamics of open quantum systems. *Computer Physics Communications*, 184(4):1234–1240, Apr. 2013. ISSN 0010-4655. doi: 10.1016/j.cpc.2012.11.019.

B. Josephson. Possible new effects in superconductive tunnelling. *Physics Letters*, 1(7): 251–253, July 1962. ISSN 00319163. doi: 10.1016/0031-9163(62)91369-0.

J. Kammhuber, M. C. Cassidy, H. Zhang, Ö. Gül, F. Pei, M. W. A. De Moor, B. Nijholt, K. Watanabe, T. Taniguchi, D. Car, S. R. Plissard, E. P. A. M. Bakkers, and L. P. Kouwenhoven. Conductance Quantization at Zero Magnetic Field in InSb Nanowires. *Nano Letters*, 16(6):3482–3486, June 2016. ISSN 1530-6984, 1530-6992. doi: 10.1021/acs.nanolett. 6b00051.

J. Kammhuber, M. C. Cassidy, F. Pei, M. P. Nowak, A. Vuik, Ö. Gül, D. Car, S. R. Plissard, E. P. A. M. Bakkers, M. Wimmer, and L. P. Kouwenhoven. Conductance through a helical state in an Indium antimonide nanowire. *Nature Communications*, 8(1):478, Sept. 2017. ISSN 2041-1723. doi: 10.1038/s41467-017-00315-y.

T. Karzig, C. Knapp, R. M. Lutchyn, P. Bonderson, M. B. Hastings, C. Nayak, J. Alicea, K. Flensberg, S. Plugge, Y. Oreg, C. M. Marcus, and M. H. Freedman. Scalable Designs for Quasiparticle-Poisoning-Protected Topological Quantum Computation with Majorana Zero Modes. *Physical Review B*, 95(23):235305, June 2017. ISSN 2469-9950, 2469-9969. doi: 10.1103/PhysRevB.95.235305.

G. Katsaros, J. Kukučka, L. Vukušić, H. Watzinger, F. Gao, T. Wang, J.-J. Zhang, and K. Held. Zero Field Splitting of Heavy-Hole States in Quantum Dots. *Nano Letters*, 20(7):5201–5206, July 2020. ISSN 1530-6984, 1530-6992. doi: 10.1021/acs.nanolett.0c01466.

T. S. Khaire, M. A. Khasawneh, W. P. Pratt, and N. O. Birge. Observation of Spin-Triplet Superconductivity in Co-Based Josephson Junctions. *Physical Review Letters*, 104(13): 137002, Mar. 2010. ISSN 0031-9007, 1079-7114. doi: 10.1103/PhysRevLett.104.137002.

M. S. Khalil, M. J. A. Stoutimore, F. C. Wellstood, and K. D. Osborn. An analysis method for asymmetric resonator transmission applied to superconducting devices. *Journal of Applied Physics*, 111(5):054510, Mar. 2012. ISSN 0021-8979, 1089-7550. doi: 10.1063/1. 3692073.

S. A. Khan, C. Lampadaris, A. Cui, L. Stampfer, Y. Liu, S. J. Pauka, M. E. Cachaza, E. M. Fiordaliso, J.-H. Kang, S. Korneychuk, T. Mutas, J. E. Sestoft, F. Krizek, R. Tanta, M. C. Cassidy, T. S. Jespersen, and P. Krogstrup. Transparent Gatable Superconducting Shadow Junctions, Mar. 2020.

Y. Kim, A. Eddins, S. Anand, K. X. Wei, E. Van Den Berg, S. Rosenblatt, H. Nayfeh, Y. Wu, M. Zaletel, K. Temme, and A. Kandala. Evidence for the utility of quantum computing before fault tolerance. *Nature*, 618(7965):500–505, June 2023. ISSN 0028-0836, 1476-4687. doi: 10.1038/s41586-023-06096-3.

A. Kitaev. Unpaired Majorana fermions in quantum wires. *Physics-Uspekhi*, 44(10S):131–136, Oct. 2001. ISSN 1468-4780. doi: 10.1070/1063-7869/44/10S/S29.

M. Kjaergaard, M. E. Schwartz, J. Braumüller, P. Krantz, J. I.-J. Wang, S. Gustavsson, and W. D. Oliver. Superconducting Qubits: Current State of Play. *Annual Review of Condensed Matter Physics*, 11(1):369–395, Mar. 2020. ISSN 1947-5454, 1947-5462. doi: 10.1146/annurev-conmatphys-031119-050605.

T. M. Klapwijk. Proximity Effect From an Andreev Perspective. *Journal of Super-conductivity*, 17(5):593–611, Oct. 2004. ISSN 0896-1107, 1572-9605. doi: 10.1007/s10948-004-0773-0.

R. L. Klees, G. Rastelli, and W. Belzig. Nonequilibrium Andreev bound states population in short superconducting junctions coupled to a resonator. *Physical Review B*, 96(14):144510, Oct. 2017. ISSN 2469-9950, 2469-9969. doi: 10.1103/PhysRevB.96.144510.

J. Koch, T. M. Yu, J. Gambetta, A. A. Houck, D. I. Schuster, J. Majer, A. Blais, M. H. Devoret, S. M. Girvin, and R. J. Schoelkopf. Charge insensitive qubit design derived from the Cooper pair box. *Physical Review A*, 76(4):042319, Oct. 2007. ISSN 1050-2947, 1094-1622. doi: 10.1103/PhysRevA.76.042319.

F. Konschelle, I. V. Tokatly, and F. S. Bergeret. Theory of the spin-galvanic effect and the anomalous phase shift φ 0 in superconductors and Josephson junctions with intrinsic spin-orbit coupling. *Physical Review B*, 92(12):125443, Sept. 2015. ISSN 1098-0121, 1550-235X. doi: 10.1103/PhysRevB.92.125443.

F. Konschelle, F. S. Bergeret, and I. V. Tokatly. Semiclassical Quantization of Spinning Quasiparticles in Ballistic Josephson Junctions. *Physical Review Letters*, 116(23):237002, June 2016. ISSN 0031-9007, 1079-7114. doi: 10.1103/PhysRevLett.116.237002.

V. Kornich, H. S. Barakov, and Y. V. Nazarov. Fine energy splitting of overlapping Andreev bound states in multi-terminal superconducting nanostructures. *Physical Review Research*, 1(3):033004, Oct. 2019. ISSN 2643-1564. doi: 10.1103/PhysRevResearch.1.033004.

V. Kornich, H. S. Barakov, and Y. V. Nazarov. Overlapping Andreev states in semiconducting nanowires: Competition of 1D and 3D propagation. *Physical Review B*, 101(19):195430, May 2020. ISSN 2469-9950, 2469-9969. doi: 10.1103/PhysRevB.101.195430.

L. P. Kouwenhoven, D. G. Austing, and S. Tarucha. Few-electron quantum dots. *Reports on Progress in Physics*, 64(6):701–736, June 2001. ISSN 0034-4885, 1361-6633. doi: 10.1088/0034-4885/64/6/201.

A. Kringhøj, T. W. Larsen, B. van Heck, D. Sabonis, O. Erlandsson, I. Petkovic, D. I. Pikulin, P. Krogstrup, K. D. Petersson, and C. M. Marcus. Controlled DC Monitoring of a Superconducting Qubit. *Physical Review Letters*, 124(5):056801, Feb. 2020. ISSN 0031-9007, 1079-7114. doi: 10.1103/PhysRevLett.124.056801.

A. Kringhøj, T. W. Larsen, O. Erlandsson, W. Uilhoorn, J. Kroll, M. Hesselberg, R. McNeil, P. Krogstrup, L. Casparis, C. Marcus, and K. Petersson. Magnetic-Field-Compatible Superconducting Transmon Qubit. *Physical Review Applied*, 15(5):054001, May 2021. ISSN 2331-7019. doi: 10.1103/PhysRevApplied.15.054001.

S. Krinner, S. Storz, P. Kurpiers, P. Magnard, J. Heinsoo, R. Keller, J. Lütolf, C. Eichler, and A. Wallraff. Engineering cryogenic setups for 100-qubit scale superconducting circuit systems. *EPJ Quantum Technology*, 6(1):2, Dec. 2019. ISSN 2662-4400, 2196-0763. doi: 10.1140/epjqt/s40507-019-0072-0.

S. Krinner, N. Lacroix, A. Remm, A. Di Paolo, E. Genois, C. Leroux, C. Hellings, S. Lazar, F. Swiadek, J. Herrmann, G. J. Norris, C. K. Andersen, M. Müller, A. Blais, C. Eichler, and A. Wallraff. Realizing repeated quantum error correction in a distance-three surface code. *Nature*, 605(7911):669–674, May 2022. ISSN 0028-0836, 1476-4687. doi: 10.1038/s41586-022-04566-8.

I. V. Krive, L. Y. Gorelik, R. I. Shekhter, and M. Jonson. Chiral symmetry breaking and the Josephson current in a ballistic superconductor–quantum wire–superconductor junction. *Low Temperature Physics*, 30(5):398–404, May 2004. ISSN 1063-777X, 1090-6517. doi: 10.1063/1.1739160.

P. Krogstrup, N. L. B. Ziino, W. Chang, S. M. Albrecht, M. H. Madsen, E. Johnson, J. Nygård, C. M. Marcus, and T. S. Jespersen. Epitaxy of semiconductor-superconductor nanowires. *Nature Materials*, 14, 2015. ISSN 1476-1122. doi: 10.1038/nmat4176.

J. G. Kroll, W. Uilhoorn, K. L. van der Enden, D. de Jong, K. Watanabe, T. Taniguchi, S. Goswami, M. C. Cassidy, and L. P. Kouwenhoven. Magnetic field compatible circuit quantum electrodynamics with graphene Josephson junctions. *Nature Communications*, 9(1):4615, Dec. 2018. ISSN 2041-1723. doi: 10.1038/s41467-018-07124-x.

J. G. Kroll, F. Borsoi, K. L. van der Enden, W. Uilhoorn, D. de Jong, M. Quintero-Pérez, D. J. van Woerkom, A. Bruno, S. R. Plissard, D. Car, E. P. A. M. Bakkers, M. C. Cassidy, and L. P. Kouwenhoven. Magnetic field resilient superconducting coplanar waveguide resonators for hybrid cQED experiments. *Physical Review Applied*, 11(6):064053, June 2019. ISSN 2331-7019. doi: 10.1103/PhysRevApplied.11.064053.

I. Kulik. Macroscopic quantization and the proximity effect in S-N-S junctions. *Soviet Journal of Experimental and Theoretical Physics*, 30(5):944, 1970.

P. D. Kurilovich, V. D. Kurilovich, V. Fatemi, M. H. Devoret, and L. I. Glazman. Microwave response of an Andreev bound state. *Physical review. B*, 104(17), Nov. 2021. doi: 10.1103/PhysRevB.104.174517.

P. D. Kurilovich, V. D. Kurilovich, A. E. Svetogorov, W. Belzig, M. H. Devoret, and L. I. Glazman. On-demand population of Andreev levels by their ionization in the presence of Coulomb blockade. *arXiv:2312.07512*, Dec. 2023.

I. L. Kurland, I. L. Aleiner, and B. L. Altshuler. Mesoscopic magnetization fluctuations for metallic grains close to the Stoner instability. *Physical Review B*, 62(22):14886–14897, Dec. 2000. ISSN 0163-1829, 1095-3795. doi: 10.1103/PhysRevB.62.14886.

T. Laeven, B. Nijholt, M. Wimmer, and A. R. Akhmerov. Enhanced Proximity Effect in Zigzag-Shaped Majorana Josephson Junctions. *Physical Review Letters*, 125(8):086802, Aug. 2020. ISSN 0031-9007, 1079-7114. doi: 10.1103/PhysRevLett.125.086802.

A. J. Landig, J. V. Koski, P. Scarlino, U. C. Mendes, A. Blais, C. Reichl, W. Wegscheider, A. Wallraff, K. Ensslin, and T. Ihn. Coherent spin–photon coupling using a resonant exchange qubit. *Nature*, 560(7717), Aug. 2018. ISSN 1476-4687. doi: 10.1038/s41586-018-0365-y.

D. Laroche, D. Bouman, D. J. van Woerkom, A. Proutski, C. Murthy, D. I. Pikulin, C. Nayak, R. J. J. van Gulik, J. Nygård, P. Krogstrup, L. P. Kouwenhoven, and A. Geresdi. Observation of the 4π-periodic Josephson effect in indium arsenide nanowires. *Nature Communications*, 10(1):245, Dec. 2019. ISSN 2041-1723. doi: 10.1038/s41467-018-08161-2.

T. W. Larsen, K. D. Petersson, F. Kuemmeth, T. S. Jespersen, P. Krogstrup, J. Nygård, and C. M. Marcus. Semiconductor-Nanowire-Based Superconducting Qubit. *Physical Review Letters*, 115(12):127001, Sept. 2015. ISSN 0031-9007, 1079-7114. doi: 10.1103/PhysRevLett.115.127001.

W. Lechner, P. Hauke, and P. Zoller. A quantum annealing architecture with all-to-all connectivity from local interactions. *Science Advances*, 1(9):e1500838, Oct. 2015. ISSN 2375-2548. doi: 10.1126/sciadv.1500838.

E. J. H. Lee, X. Jiang, M. Houzet, R. Aguado, C. M. Lieber, and S. De Franceschi. Spin-resolved Andreev levels and parity crossings in hybrid superconductor–semiconductor nanostructures. *Nature Nanotechnology*, 9(1):79–84, Jan. 2014. ISSN 1748-3387, 1748-3395. doi: 10.1038/nnano.2013.267.

J. Lee, D. W. Berry, C. Gidney, W. J. Huggins, J. R. McClean, N. Wiebe, and R. Babbush. Even More Efficient Quantum Computations of Chemistry Through Tensor Hypercontraction. *PRX Quantum*, 2(3):030305, July 2021. ISSN 2691-3399. doi: 10.1103/PRXQuantum.2.030305.

M. Leijnse and K. Flensberg. Parity qubits and poor man's Majorana bound states in double quantum dots. *Physical Review B*, 86(13):134528, Oct. 2012. ISSN 1098-0121, 1550-235X. doi: 10.1103/PhysRevB.86.134528.

M. Lenander, H. Wang, R. C. Bialczak, E. Lucero, M. Mariantoni, M. Neeley, A. D. O'Connell, D. Sank, M. Weides, J. Wenner, T. Yamamoto, Y. Yin, J. Zhao, A. N. Cleland, and J. M. Martinis. Measurement of energy decay in superconducting qubits from nonequilibrium quasiparticles. *Physical Review B*, 84(2):024501, July 2011. ISSN 1098-0121, 1550-235X. doi: 10.1103/PhysRevB.84.024501.

E. M. Levenson-Falk, F. Kos, R. Vijay, L. Glazman, and I. Siddiqi. Single-Quasiparticle Trapping in Aluminum Nanobridge Josephson Junctions. *Physical Review Letters*, page 5, 2014.

D. Liang and X. P. Gao. Strong Tuning of Rashba Spin–Orbit Interaction in Single InAs Nanowires. *Nano Letters*, 12(6):3263–3267, June 2012. ISSN 1530-6984, 1530-6992. doi: 10.1021/nl301325h.

J. Linder and J. W. A. Robinson. Superconducting spintronics. *Nature Physics*, 11(4):307–315, Apr. 2015. ISSN 1745-2473, 1745-2481. doi: 10.1038/nphys3242.

J.-F. Liu and K. S. Chan. Relation between symmetry breaking and the anomalous Josephson effect. *Physical Review B*, 82(12):125305, Sept. 2010. ISSN 1098-0121, 1550-235X. doi: 10.1103/PhysRevB.82.125305.

S. Lloyd. Universal Quantum Simulators. *Science*, 273(5278):1073–1078, Aug. 1996. ISSN 0036-8075, 1095-9203. doi: 10.1126/science.273.5278.1073.

F. London, H. London, and F. A. Lindemann. The electromagnetic equations of the supra-conductor. *Proceedings of the Royal Society of London. Series A - Mathematical and Physical Sciences*, 149(866):71–88, Mar. 1935. doi: 10.1098/rspa.1935.0048.

D. López-Núñez, Q. P. Montserrat, G. Rius, E. Bertoldo, A. Torras-Coloma, M. Martínez, and P. Forn-Díaz. Magnetic penetration depth of Aluminum thin films, Nov. 2023.

D. Loss and D. P. DiVincenzo. Quantum computation with quantum dots. *Physical review. A*, 57(1), Jan. 1998. doi: 10.1103/PhysRevA.57.120.

M. Luethi, K. Laubscher, S. Bosco, D. Loss, and J. Klinovaja. Planar Josephson junctions in germanium: Effect of cubic spin-orbit interaction. *Physical Review B*, 107(3):035435, Jan. 2023a. ISSN 2469-9950, 2469-9969. doi: 10.1103/PhysRevB.107.035435.

M. Luethi, H. F. Legg, K. Laubscher, D. Loss, and J. Klinovaja. Majorana bound states in germanium Josephson junctions via phase control. *Physical Review B*, 108(19):195406, Nov. 2023b. ISSN 2469-9950, 2469-9969. doi: 10.1103/PhysRevB.108.195406.

R. M. Lutchyn, J. D. Sau, and S. D. Sarma. Majorana Fermions and a Topological Phase Transition in Semiconductor-Superconductor Heterostructures. *Physical Review Letters*, 105(7):077001, Aug. 2010. ISSN 0031-9007, 1079-7114. doi: 10.1103/PhysRevLett.105.077001.

F. Luthi, T. Stavenga, O. W. Enzing, A. Bruno, C. Dickel, N. K. Langford, M. A. Rol, T. S. Jespersen, J. Nygård, P. Krogstrup, and L. DiCarlo. Evolution of Nanowire Transmon Qubits and Their Coherence in a Magnetic Field. *Physical Review Letters*, 120(10):100502, Mar. 2018. ISSN 0031-9007, 1079-7114. doi: 10.1103/PhysRevLett.120.100502.

S. Machlup. Noise in Semiconductors: Spectrum of a Two-Parameter Random Signal. *Journal of Applied Physics*, 25(3):341–343, Mar. 1954. ISSN 0021-8979. doi: 10.1063/1.1721637.

M. D. Maloney, F. De La Cruz, and M. Cardona. Superconducting Parameters and Size Effects of Aluminum Films and Foils. *Physical Review B*, 5(9):3558–3572, May 1972. ISSN 0556-2805. doi: 10.1103/PhysRevB.5.3558.

A. Martín-Rodero and A. Levy Yeyati. Josephson and Andreev transport through quantum dots. *Advances in physics*, 60(6), 2011. doi: 10.1080/00018732.2011.624266.

F. Marxer, A. Vepsäläinen, S. W. Jolin, J. Tuorila, A. Landra, C. Ockeloen-Korppi, W. Liu, O. Ahonen, A. Auer, L. Belzane, V. Bergholm, C. F. Chan, K. W. Chan, T. Hiltunen, J. Hotari, E. Hyyppä, J. Ikonen, D. Janzso, M. Koistinen, J. Kotilahti, T. Li, J. Luus, M. Papic, M. Partanen, J. Räbinä, J. Rosti, M. Savytskyi, M. Seppälä, V. Sevriuk, E. Takala, B. Tarasinski, M. J. Thapa, F. Tosto, N. Vorobeva, L. Yu, K. Y. Tan, J. Hassel, M. Möttönen, and J. Heinsoo. Long-distance transmon coupler with CZ gate fidelity above 99.8%, Dec. 2022.

S. Matsuo, T. Imoto, T. Yokoyama, Y. Sato, T. Lindemann, S. Gronin, G. C. Gardner, S. Nakosai, Y. Tanaka, M. J. Manfra, and S. Tarucha. Phase-dependent Andreev molecules and superconducting gap closing in coherently coupled Josephson junctions, Mar. 2023.

F. J. Matute-Cañadas, C. Metzger, S. Park, L. Tosi, P. Krogstrup, J. Nygård, M. F. Goffman, C. Urbina, H. Pothier, and A. L. Yeyati. Signatures of Interactions in the Andreev Spectrum of Nanowire Josephson Junctions. *Physical Review Letters*, 128(19):197702, May 2022. ISSN 0031-9007, 1079-7114. doi: 10.1103/PhysRevLett.128.197702.

W. Mayer, M. C. Dartiailh, J. Yuan, K. S. Wickramasinghe, E. Rossi, and J. Shabani. Gate controlled anomalous phase shift in Al/InAs Josephson junctions. *Nature Communications*, 11(1):212, Dec. 2020. ISSN 2041-1723. doi: 10.1038/s41467-019-14094-1.

G. P. Mazur, N. van Loo, J. Y. Wang, T. Dvir, G. Wang, A. Khindanov, S. Korneychuk, F. Borsoi, R. C. Dekker, G. Badawy, P. Vinke, S. Gazibegovic, E. P. A. M. Bakkers, M. Quintero-Perez, S. Heedt, and L. P. Kouwenhoven. Spin-mixing enhanced proximity effect in aluminum-based superconductor-semiconductor hybrids, Feb. 2022.

V. Meden. The Anderson–Josephson quantum dot—a theory perspective. *Journal of Physics: Condensed Matter*, 31(16):163001, Apr. 2019. ISSN 0953-8984, 1361-648X. doi: 10.1088/1361-648X/aafd6a.

W. Meissner and R. Ochsenfeld. Ein neuer Effekt bei Eintritt der Supraleitfähigkeit. *Naturwissenschaften*, 21(44):787–788, Nov. 1933. ISSN 1432-1904. doi: 10.1007/BF01504252.

T. Meng, P. Simon, and S. Florens. Self-consistent description of Andreev bound states in Josephson quantum dot devices. *Physical Review B*, 79(22):224521, June 2009. ISSN 1098-0121, 1550-235X. doi: 10.1103/PhysRevB.79.224521.

C. Metzger. *Effets de Spin et de Charge Dans Les États Liés d'Andreev*. PhD thesis, Université Paris-Saclay, May 2022.

C. Metzger, S. Park, L. Tosi, C. Janvier, A. A. Reynoso, M. F. Goffman, C. Urbina, A. L. Yeyati, and H. Pothier. Circuit-QED with phase-biased Josephson weak links. *Physical Review Research*, 3(1):013036, Jan. 2021. ISSN 2643-1564. doi: 10.1103/PhysRevResearch.3.013036.

X. Mi, J. V. Cady, D. M. Zajac, P. W. Deelman, and J. R. Petta. Strong coupling of a single electron in silicon to a microwave photon. *Science (New York, N.Y.)*, 355(6321), 2017a. doi: 10.1126/science.aal2469.

X. Mi, J. V. Cady, D. M. Zajac, J. Stehlik, L. F. Edge, and J. R. Petta. Circuit Quantum Electrodynamics Architecture for Gate-Defined Quantum Dots in Silicon. *Applied Physics Letters*, 110(4):043502, Jan. 2017b. ISSN 0003-6951, 1077-3118. doi: 10.1063/1.4974536.

X. Mi, M. Benito, S. Putz, D. M. Zajac, J. M. Taylor, G. Burkard, and J. R. Petta. A coherent spin–photon interface in silicon. *Nature*, 555(7698):599–603, Mar. 2018. ISSN 0028-0836, 1476-4687. doi: 10.1038/nature25769.

C. M. Moehle, P. K. Rout, N. A. Jainandunsing, D. Kuiri, C. T. Ke, D. Xiao, C. Thomas, M. J. Manfra, M. P. Nowak, and S. Goswami. Controlling Andreev Bound States with the Magnetic Vector Potential. *Nano Letters*, 22(21):8601–8607, Nov. 2022. ISSN 1530-6984, 1530-6992. doi: 10.1021/acs.nanolett.2c03130.

C. Murthy, V. D. Kurilovich, P. D. Kurilovich, B. van Heck, L. I. Glazman, and C. Nayak. Energy spectrum and current-phase relation of a nanowire Josephson junction close to the topological transition. *Physical Review B*, 101(22):224501, June 2020. ISSN 2469-9950, 2469-9969. doi: 10.1103/PhysRevB.101.224501.

S. Nadj-Perge, S. M. Frolov, E. P. A. M. Bakkers, and L. P. Kouwenhoven. Spin–orbit qubit in a semiconductor nanowire. *Nature*, 468(7327):1084–1087, Dec. 2010. ISSN 0028-0836, 1476-4687. doi: 10.1038/nature09682.

Y. Nakamura, Yu. A. Pashkin, and J. S. Tsai. Coherent control of macroscopic quantum states in a single-Cooper-pair box. *Nature*, 398(6730):786–788, Apr. 1999. ISSN 0028-0836, 1476-4687. doi: 10.1038/19718.

M. Newville, R. Otten, A. Nelson, A. Ingargiola, T. Stensitzki, D. Allan, A. Fox, F. Carter, Michał, R. Osborn, D. Pustakhod, Lneuhaus, S. Weigand, Glenn, C. Deil, Mark, A. L. R. Hansen, G. Pasquevich, L. Foks, N. Zobrist, O. Frost, A. Beelen, Stuermer, Azelcer, A. Hannum, A. Polloreno, J. H. Nielsen, S. Caldwell, A. Almarza, and A. Persaud. Lmfit/lmfit-py: 1.0.3. Zenodo, Oct. 2021.

D. G. Olivares, A. L. Yeyati, L. Bretheau, Ç. Ö. Girit, H. Pothier, and C. Urbina. Dynamics of quasiparticle trapping in Andreev levels. *Physical Review B*, 89(10):104504, Mar. 2014. ISSN 1098-0121, 1550-235X. doi: 10.1103/PhysRevB.89.104504.

Y. Oreg, G. Refael, and F. von Oppen. Helical liquids and Majorana bound states in quantum wires. *Physical Review Letters*, 105(17):177002, Oct. 2010. ISSN 0031-9007, 1079-7114. doi: 10.1103/PhysRevLett.105.177002.

C. Padurariu and Yu. V. Nazarov. Theoretical proposal for superconducting spin qubits. *Physical Review B*, 81(14):144519, Apr. 2010. ISSN 1098-0121, 1550-235X. doi: 10.1103/ PhysRevB.81.144519.

C. Padurariu and Yu. V. Nazarov. Spin blockade qubit in a superconducting junction. *EPL (Europhysics Letters)*, 100(5):57006, Dec. 2012. ISSN 0295-5075, 1286-4854. doi: 10.1209/ 0295-5075/100/57006.

S. Park and A. L. Yeyati. Andreev spin qubits in multichannel Rashba nanowires. *Physical Review B*, 96(12):125416, Sept. 2017. ISSN 2469-9950, 2469-9969. doi: 10.1103/PhysRevB. 96.125416.

S. Park, C. Metzger, L. Tosi, M. F. Goffman, C. Urbina, H. Pothier, and A. L. Yeyati. From adiabatic to dispersive readout of quantum circuits. *Physical Review Letters*, 125(7):077701, Aug. 2020. ISSN 0031-9007, 1079-7114. doi: 10.1103/PhysRevLett.125.077701.

L. Pavešić, M. Pita Vidal, A. Bargerbos, and R. Žitko. Impurity Knight shift in quantum dot Josephson junctions. *SciPost Physics*, 15(2):070, Aug. 2023. ISSN 2542-4653. doi: 10.21468/SciPostPhys.15.2.070.

Y. Peng, F. Pientka, E. Berg, Y. Oreg, and F. von Oppen. Signatures of topological Josephson junctions. *Physical Review B*, 94(8):085409, Aug. 2016. ISSN 2469-9950, 2469-9969. doi: 10.1103/PhysRevB.94.085409.

D. Phan, J. Senior, A. Ghazaryan, M. Hatefipour, W. M. Strickland, J. Shabani, M. Serbyn, and A. P. Higginbotham. Detecting induced $p \pm ip$ pairing at the Al-InAs interface with a quantum microwave circuit. *Physical Review Letters*, 128(10):107701, Mar. 2022. ISSN 0031-9007, 1079-7114. doi: 10.1103/PhysRevLett.128.107701.

J.-D. Pillet, V. Benzoni, J. Griesmar, J.-L. Smirr, and Ç. Ö. Girit. Nonlocal Josephson effect in Andreev molecules. *Nano Letters*, 19(10):7138–7143, Oct. 2019. ISSN 1530-6984, 1530-6992. doi: 10.1021/acs.nanolett.9b02686.

D. M. Pino, R. S. Souto, and R. Aguado. Minimal Kitaev-transmon qubit based on double quantum dots, Sept. 2023.

A. B. Pippard. An experimental and theoretical study of the relation between magnetic field and current in a superconductor. *Proceedings of the Royal Society of London. Series A. Mathematical and Physical Sciences*, 216(1127):547–568, Feb. 1953. ISSN 0080-4630, 2053-9169. doi: 10.1098/rspa.1953.0040.

M. Pita-Vidal. *Realizing Superconducting Spin Qubits*. PhD thesis, [object Object], 2023.

M. Pita-Vidal, A. Bargerbos, J. J. Wesdorp, and C. Andersen. A gradiometric device and an array of such gradiometric devices (Patent pending).

M. Pita-Vidal, A. Bargerbos, C.-K. Yang, D. J. van Woerkom, W. Pfaff, N. Haider, P. Krogstrup, L. P. Kouwenhoven, G. de Lange, and A. Kou. A gate-tunable, field-compatible fluxonium. *Physical Review Applied*, 14(6):064038, Dec. 2020. ISSN 2331-7019. doi: 10.1103/PhysRevApplied.14.064038.

M. Pita-Vidal, A. Bargerbos, R. Žitko, L. J. Splitthoff, L. Grünhaupt, J. J. Wesdorp, Y. Liu, L. P. Kouwenhoven, R. Aguado, B. van Heck, A. Kou, and C. K. Andersen. Direct manipulation of a superconducting spin qubit strongly coupled to a transmon qubit. *Nature Physics*, May 2023a. ISSN 1745-2481. doi: 10.1038/s41567-023-02071-x.

M. Pita-Vidal, J. J. Wesdorp, a. L. J. Splitthoff, A. Bargerbos, Y. Liu, and C. Andersen. Strong tunable coupling between two distant superconducting spin-qubits. *arXiv e-prints*, 2023b.

M. Pita-Vidal, J. J. Wesdorp, and C. K. Andersen. Blueprint for all-to-all connected superconducting spin qubits. *In preparation*, 2024.

J. H. Plantenberg. *Coupled Superconducting Flux Qubits*. s.n., S.l., 2007. ISBN 978-90-8593-036-5.

J. H. Plantenberg, P. C. de Groot, C. J. P. M. Harmans, and J. E. Mooij. Demonstration of controlled-NOT quantum gates on a pair of superconducting quantum bits. *Nature*, 447 (7146):836–839, June 2007. ISSN 0028-0836, 1476-4687. doi: 10.1038/nature05896.

S. R. Plissard, D. R. Slapak, M. A. Verheijen, M. Hocevar, G. W. G. Immink, I. Van Weperen, S. Nadj-Perge, S. M. Frolov, L. P. Kouwenhoven, and E. P. A. M. Bakkers. From InSb Nanowires to Nanocubes: Looking for the Sweet Spot. *Nano Letters*, 12(4):1794–1798, Apr. 2012. ISSN 1530-6984, 1530-6992. doi: 10.1021/nl203846g.

I. M. Pop, K. Geerlings, G. Catelani, R. J. Schoelkopf, L. I. Glazman, and M. H. Devoret. Coherent suppression of electromagnetic dissipation due to superconducting quasi-particles. *Nature*, 508(7496):369–372, Apr. 2014. ISSN 0028-0836, 1476-4687. doi: 10.1038/nature13017.

E. Portolés, S. Iwakiri, G. Zheng, P. Rickhaus, T. Taniguchi, K. Watanabe, T. Ihn, K. Ensslin, and F. K. de Vries. A tunable monolithic SQUID in twisted bilayer graphene. *Nature Nanotechnology*, 17(11):1159–1164, Nov. 2022. ISSN 1748-3387, 1748-3395. doi: 10.1038/s41565-022-01222-0.

A. C. Potter and P. A. Lee. Majorana end states in multiband microstructures with Rashba spin-orbit coupling. *Physical Review B*, 83(9):094525, Mar. 2011. ISSN 1098-0121, 1550-235X. doi: 10.1103/PhysRevB.83.094525.

D. M. Pozar. *Microwave Engineering*. John Wiley & Sons, Inc, Hoboken, NJ, fourth edition edition, 2012. ISBN 978-0-470-63155-3.

E. Prada, P. San-Jose, M. W. A. de Moor, A. Geresdi, E. J. H. Lee, J. Klinovaja, D. Loss, J. Nygård, R. Aguado, and L. P. Kouwenhoven. From Andreev to Majorana bound states in hybrid superconductor-semiconductor nanowires. *Nature Reviews Physics*, 2(10):575–594, Sept. 2020. ISSN 2522-5820. doi: 10.1038/s42254-020-0228-y.

J. Preskill. Quantum Computing in the NISQ era and beyond. *Quantum*, 2:79, Aug. 2018. ISSN 2521-327X. doi: 10.22331/q-2018-08-06-79.

J. Preskill. Quantum computing 40 years later, Feb. 2023.

A. Rasmussen, J. Danon, H. Suominen, F. Nichele, M. Kjaergaard, and K. Flensberg. Effects of spin-orbit coupling and spatial symmetries on the Josephson current in SNS junctions. *Physical Review B*, 93(15):155406, Apr. 2016. ISSN 2469-9950, 2469-9969. doi: 10.1103/PhysRevB.93.155406.

N. Read and D. Green. Paired states of fermions in two dimensions with breaking of parity and time-reversal symmetries, and the fractional quantum Hall effect. *Physical Review B*, 61(15):10267–10297, Apr. 2000. ISSN 0163-1829, 1095-3795. doi: 10.1103/PhysRevB.61.10267.

C. R. Reeg and D. L. Maslov. Proximity-induced triplet superconductivity in Rashba materials. *Physical Review B*, 92(13):134512, Oct. 2015. ISSN 1098-0121, 1550-235X. doi: 10.1103/PhysRevB.92.134512.

A. A. Reynoso, G. Usaj, C. A. Balseiro, D. Feinberg, and M. Avignon. Anomalous Josephson Current in Junctions with Spin Polarizing Quantum Point Contacts. *Physical Review Letters*, 101(10):107001, Sept. 2008. ISSN 0031-9007, 1079-7114. doi: 10.1103/PhysRevLett. 101.107001.

A. A. Reynoso, G. Usaj, C. A. Balseiro, D. Feinberg, and M. Avignon. Spin-orbit-induced chirality of Andreev states in Josephson junctions. *Physical Review B*, 86(21):214519, Dec. 2012. ISSN 1098-0121, 1550-235X. doi: 10.1103/PhysRevB.86.214519.

D. Ristè, C. C. Bultink, M. J. Tiggelman, R. N. Schouten, K. W. Lehnert, and L. DiCarlo. Millisecond charge-parity fluctuations and induced decoherence in a superconducting transmon qubit. *Nature Communications*, 4(1):1913, Oct. 2013. ISSN 2041-1723. doi: 10.1038/ncomms2936.

R.-P. Riwar. Control of Andreev bound state population and related charge-imbalance effect. *J. Phys.*, page 7, 2015.

R. P. Riwar, M. Houzet, J. S. Meyer, and Y. V. Nazarov. Shooting quasiparticles from Andreev bound states in a superconducting constriction. *Journal of Experimental and Theoretical Physics*, 119(6):1028–1033, Dec. 2014. ISSN 1063-7761, 1090-6509. doi: 10.1134/S1063776114120164.

R.-P. Riwar, A. Hosseinkhani, L. D. Burkhart, Y. Y. Gao, R. J. Schoelkopf, L. I. Glazman, and G. Catelani. Normal-metal quasiparticle traps for superconducting qubits. *Physical Review B*, 94(10):104516, Sept. 2016. ISSN 2469-9950, 2469-9969. doi: 10.1103/PhysRevB. 94.104516.

J. W. A. Robinson, J. D. S. Witt, and M. G. Blamire. Controlled Injection of Spin-Triplet Supercurrents into a Strong Ferromagnet. *Science*, 329(5987):59–61, July 2010. ISSN 0036-8075, 1095-9203. doi: 10.1126/science.1189246.

S. Roelofs. *Impact of Design and III-V Materials on Losses of Superconducting Resonators by Using Simulations*. Bachelors Thesis, The Hague university of applied sciences, May 2019.

M. A. Rol, F. Battistel, F. K. Malinowski, C. C. Bultink, B. M. Tarasinski, R. Vollmer, N. Haider, N. Muthusubramanian, A. Bruno, B. M. Terhal, and L. DiCarlo. Fast, high-fidelity conditional-phase gate exploiting leakage interference in weakly anharmonic superconducting qubits. *Physical Review Letters*, 123(12):120502, Sept. 2019. doi: 10.1103/PhysRevLett.123.120502.

M. A. Rol, L. Ciorciaro, F. K. Malinowski, B. M. Tarasinski, R. E. Sagastizabal, C. C. Bultink, Y. Salathe, N. Haandbaek, J. Sedivy, and L. DiCarlo. Time-domain characterization and correction of on-chip distortion of control pulses in a quantum processor. *Applied Physics Letters*, 116(5):054001, Feb. 2020. ISSN 0003-6951. doi: 10.1063/1.5133894.

T. Ö. Rosdahl, A. Vuik, M. Kjaergaard, and A. R. Akhmerov. Andreev rectifier: A nonlocal conductance signature of topological phase transitions. *Physical Review B*, 97(4):045421, Jan. 2018. ISSN 2469-9950, 2469-9969. doi: 10.1103/PhysRevB.97.045421.

P. Rot. Microwave Spectroscopy of InSb-Al Shadow-Wall Nanowire Josephson Junctions. Master's thesis, Technical University of Delft, Apr. 2022.

A. Roy and M. Devoret. Introduction to parametric amplification of quantum signals with Josephson circuits. *Comptes Rendus Physique*, 17(7):740–755, Aug. 2016. ISSN 1631-0705. doi: 10.1016/j.crhy.2016.07.012.

N. Samkharadze, A. Bruno, P. Scarlino, G. Zheng, D. P. DiVincenzo, L. DiCarlo, and L. M. K. Vandersypen. High-Kinetic-Inductance Superconducting Nanowire Resonators for Circuit QED in a Magnetic Field. *Physical Review Applied*, 5(4):044004, Apr. 2016. ISSN 2331-7019. doi: 10.1103/PhysRevApplied.5.044004.

N. Samkharadze, G. Zheng, N. Kalhor, D. Brousse, A. Sammak, U. C. Mendes, A. Blais, G. Scappucci, and L. M. K. Vandersypen. Strong spin-photon coupling in silicon. *Science*, 359(6380):1123–1127, Mar. 2018. ISSN 0036-8075, 1095-9203. doi: 10.1126/science. aar4054.

G. Scappucci, C. Kloeffel, F. A. Zwanenburg, D. Loss, M. Myronov, J.-J. Zhang, S. De Franceschi, G. Katsaros, and M. Veldhorst. The germanium quantum information route. *Nature Reviews Materials*, 6(10):926–943, Dec. 2020. ISSN 2058-8437. doi: 10.1038/s41578-020-00262-z.

K. Serniak, M. Hays, G. de Lange, S. Diamond, S. Shankar, L. D. Burkhart, L. Frunzio, M. Houzet, and M. H. Devoret. Hot non-equilibrium quasiparticles in transmon qubits. *Physical Review Letters*, 121(15):157701, Oct. 2018. ISSN 0031-9007, 1079-7114. doi: 10. 1103/PhysRevLett.121.157701.

P. W. Shor. Scheme for reducing decoherence in quantum computer memory. *Physical Review A*, 52(4):R2493–R2496, Oct. 1995. ISSN 1050-2947, 1094-1622. doi: 10.1103/ PhysRevA.52.R2493.

C. Song. *Microwave Properties of Vortices in Superconducting Resonators*. PhD thesis, 2011.

M. Spethmann, X.-P. Zhang, J. Klinovaja, and D. Loss. Coupled superconducting spin qubits with spin-orbit interaction. *Physical Review B*, 106(11):115411, Sept. 2022. ISSN 2469-9950, 2469-9969. doi: 10.1103/PhysRevB.106.115411.

L. J. Splitthoff, A. Bargerbos, L. Grünhaupt, M. Pita-Vidal, J. J. Wesdorp, Y. Liu, A. Kou, C. K. Andersen, and B. van Heck. Gate-tunable kinetic inductance in proximitized nanowires. *Physical Review Applied*, 18(2):024074, Aug. 2022. ISSN 2331-7019. doi: 10.1103/PhysRevApplied.18.024074.

D. Sprungmann, K. Westerholt, H. Zabel, M. Weides, and H. Kohlstedt. Evidence for triplet superconductivity in Josephson junctions with ferromagnetic Cu$_{2}$MnAl-Heusler barriers, Mar. 2010.

G. Stan, S. B. Field, and J. M. Martinis. Critical Field for Complete Vortex Expulsion from Narrow Superconducting Strips. *Physical Review Letters*, 92(9):097003, Mar. 2004. ISSN 0031-9007, 1079-7114. doi: 10.1103/PhysRevLett.92.097003.

T. Stavenga, S. A. Khan, Y. Liu, P. Krogstrup, and L. DiCarlo. Lower-temperature fabrica-
tion of airbridges by grayscale lithography to increase yield of nanowire transmons in
circuit QED quantum processors. *Applied Physics Letters*, 123(2):024004, July 2023. ISSN
0003-6951. doi: 10.1063/5.0146814.

E. Strambini, A. Iorio, O. Durante, R. Citro, C. Sanz-Fernández, C. Guarcello, I. V. Tokatly,
A. Braggio, M. Rocci, N. Ligato, V. Zannier, L. Sorba, F. S. Bergeret, and F. Giazotto. A
Josephson phase battery. *Nature Nanotechnology*, 15(8):656–660, Aug. 2020. ISSN 1748-
3387, 1748-3395. doi: 10.1038/s41565-020-0712-7.

Z. Su, A. B. Tacla, M. Hocevar, D. Car, S. R. Plissard, E. P. A. M. Bakkers, A. J. Daley,
D. Pekker, and S. M. Frolov. Andreev molecules in semiconductor nanowire double
quantum dots. *Nature Communications*, 8(1):585, Sept. 2017. ISSN 2041-1723. doi: 10.
1038/s41467-017-00665-7.

L. Sun, L. DiCarlo, M. D. Reed, G. Catelani, L. S. Bishop, D. I. Schuster, B. R. John-
son, G. A. Yang, L. Frunzio, L. Glazman, M. H. Devoret, and R. J. Schoelkopf. Mea-
surements of Quasiparticle Tunneling Dynamics in a Band-Gap-Engineered Transmon
Qubit. *Physical Review Letters*, 108(23):230509, June 2012. ISSN 0031-9007, 1079-7114.
doi: 10.1103/PhysRevLett.108.230509.

D. B. Szombati, S. Nadj-Perge, D. Car, S. R. Plissard, E. P. A. M. Bakkers, and L. P. Kouwen-
hoven. Josephson Φ0-junction in nanowire quantum dots. *Nature Physics*, 12(6):568–572,
June 2016. ISSN 1745-2473, 1745-2481. doi: 10.1038/nphys3742.

C. Thomas, R. E. Diaz, J. H. Dycus, M. E. Salmon, R. E. Daniel, T. Wang, G. C. Gardner,
and M. J. Manfra. Toward durable Al-InSb hybrid heterostructures via epitaxy of 2ML
interfacial InAs screening layers. *Physical Review Materials*, 3(12):124202, Dec. 2019. doi:
10.1103/PhysRevMaterials.3.124202.

M. Tinkham. Effect of Fluxoid Quantization on Transitions of Superconducting Films.
Physical Review, 129(6):2413–2422, Mar. 1963. ISSN 0031-899X. doi: 10.1103/PhysRev.
129.2413.

M. Tinkham. *Introduction to Superconductivity*. Dover Books on Physics. Dover Publ,
Mineola, NY, 2 ed edition, 2015. ISBN 978-0-486-43503-9.

A. Tosato, V. Levajac, J.-Y. Wang, C. J. Boor, F. Borsoi, M. Botifoll, C. N. Borja, S. Martí-
Sánchez, J. Arbiol, A. Sammak, M. Veldhorst, and G. Scappucci. Hard superconducting
gap in germanium. *Communications Materials*, 4(1):23, Apr. 2023. ISSN 2662-4443. doi:
10.1038/s43246-023-00351-w.

L. Tosi, C. Metzger, M. F. Goffman, C. Urbina, H. Pothier, S. Park, A. L. Yeyati, J. Nygård, and
P. Krogstrup. Spin-orbit splitting of Andreev states revealed by microwave spectroscopy.
Physical Review X, 9(1):011010, Jan. 2019. ISSN 2160-3308. doi: 10.1103/PhysRevX.9.
011010.

W. Uilhoorn, J. G. Kroll, A. Bargerbos, S. D. Nabi, C.-K. Yang, P. Krogstrup, L. P. Kouwen-
hoven, A. Kou, and G. de Lange. Quasiparticle trapping by orbital effect in a hybrid
superconducting-semiconducting circuit. *arXiv:2105.11038 [cond-mat]*, May 2021.

A. Vaartjes. Microwave spectroscopy of Andreev Bound States in Al/InAs nanowires in the presence of a magnetic field. Master's thesis, Technical university of Delft, Dec. 2020.

S. Vaitiekėnas, M.-T. Deng, J. Nygård, P. Krogstrup, and C. M. Marcus. Effective g factor of subgap states in hybrid nanowires. *Physical Review Letters*, 121(3):037703, July 2018. doi: 10.1103/PhysRevLett.121.037703.

M. Valentini, O. Sagi, L. Baghumyan, T. de Gijsel, J. Jung, S. Calcaterra, A. Ballabio, J. Aguilera Servin, K. Aggarwal, M. Janik, T. Adletzberger, R. Seoane Souto, M. Leijnse, J. Danon, C. Schrade, E. Bakkers, D. Chrastina, G. Isella, and G. Katsaros. Radio frequency driven superconducting diode and parity conserving Cooper pair transport in a two-dimensional germanium hole gas. *arXiv e-prints*, (arXiv:2306.07109):arXiv:2306.07109, June 2023. doi: 10.48550/arXiv.2306.07109.

J. A. van Dam, Y. V. Nazarov, E. P. A. M. Bakkers, S. De Franceschi, and L. P. Kouwenhoven. Supercurrent reversal in quantum dots. *Nature*, 442(7103):667–670, Aug. 2006. ISSN 0028-0836, 1476-4687. doi: 10.1038/nature05018.

J. W. G. van den Berg, S. Nadj-Perge, V. S. Pribiag, S. R. Plissard, E. P. A. M. Bakkers, S. M. Frolov, and L. P. Kouwenhoven. Fast spin-orbit qubit in an indium antimonide nanowire. *Physical review letters*, 110(6), Feb. 2013. doi: 10.1103/physrevlett.110.066806.

B. van Heck, J. I. Väyrynen, and L. I. Glazman. Zeeman and spin-orbit effects in the Andreev spectra of nanowire junctions. *Physical Review B*, 96(7):075404, Aug. 2017. ISSN 2469-9950, 2469-9969. doi: 10.1103/PhysRevB.96.075404.

N. van Loo, G. P. Mazur, T. Dvir, G. Wang, R. C. Dekker, J.-Y. Wang, M. Lemang, C. Sfiligoj, A. Bordin, D. van Driel, G. Badawy, S. Gazibegovic, E. P. A. M. Bakkers, and L. P. Kouwenhoven. Electrostatic control of the proximity effect in the bulk of semiconductor-superconductor hybrids. *Nature Communications*, 14(1):3325, June 2023. ISSN 2041-1723. doi: 10.1038/s41467-023-39044-w.

I. Van Weperen, S. R. Plissard, E. P. A. M. Bakkers, S. M. Frolov, and L. P. Kouwenhoven. Quantized Conductance in an InSb Nanowire. *Nano Letters*, 13(2):387–391, Feb. 2013. ISSN 1530-6984, 1530-6992. doi: 10.1021/nl3035256.

I. van Weperen, B. Tarasinski, D. Eeltink, V. S. Pribiag, S. R. Plissard, E. P. A. M. Bakkers, L. P. Kouwenhoven, and M. Wimmer. Spin-orbit interaction in InSb nanowires. *Physical Review B*, 91(20):201413, May 2015. ISSN 1098-0121, 1550-235X. doi: 10.1103/PhysRevB.91.201413.

D. J. van Woerkom, A. Proutski, B. van Heck, D. Bouman, J. I. Väyrynen, L. I. Glazman, P. Krogstrup, J. Nygård, L. P. Kouwenhoven, and A. Geresdi. Microwave spectroscopy of spinful Andreev bound states in ballistic semiconductor Josephson junctions. *Nature Physics*, 13(9):876–881, Sept. 2017. ISSN 1745-2473, 1745-2481. doi: 10.1038/nphys4150.

L. M. K. Vandersypen and M. A. Eriksson. Quantum computing with semiconductor spins. *Physics Today*, 72(8):38–45, Aug. 2019. ISSN 0031-9228, 1945-0699. doi: 10.1063/PT.3.4270.

L. M. K. Vandersypen, H. Bluhm, J. S. Clarke, A. S. Dzurak, R. Ishihara, A. Morello, D. J. Reilly, L. R. Schreiber, and M. Veldhorst. Interfacing spin qubits in quantum dots and donors—hot, dense, and coherent. *npj Quantum Information*, 3(1):34, Sept. 2017. ISSN 2056-6387. doi: 10.1038/s41534-017-0038-y.

J. I. Väyrynen, G. Rastelli, W. Belzig, and L. I. Glazman. Microwave signatures of Majorana states in a topological Josephson junction. *Physical Review B*, 92(13):134508, Oct. 2015. ISSN 1098-0121, 1550-235X. doi: 10.1103/PhysRevB.92.134508.

F. Vigneau, R. Mizokuchi, D. C. Zanuz, X. Huang, S. Tan, R. Maurand, S. Frolov, A. Sammak, G. Scappucci, F. Lefloch, and S. De Franceschi. Germanium Quantum-Well Josephson Field-Effect Transistors and Interferometers. *Nano Letters*, 19(2):1023–1027, Feb. 2019. ISSN 1530-6984, 1530-6992. doi: 10.1021/acs.nanolett.8b04275.

U. Vool and M. Devoret. Introduction to quantum electromagnetic circuits. *International Journal of Circuit Theory and Applications*, 45(7):897–934, 2017. doi: 10.1002/cta.2359.

U. Vool, I. M. Pop, K. Sliwa, B. Abdo, C. Wang, T. Brecht, Y. Y. Gao, S. Shankar, M. Hatridge, G. Catelani, M. Mirrahimi, L. Frunzio, R. J. Schoelkopf, L. I. Glazman, and M. H. Devoret. Non-Poissonian Quantum Jumps of a Fluxonium Qubit due to Quasiparticle Excitations. *Physical Review Letters*, 113(24):247001, Dec. 2014. ISSN 0031-9007, 1079-7114. doi: 10.1103/PhysRevLett.113.247001.

T. Wakamura, S. Guéron, and H. Bouchiat. Novel transport phenomena in graphene induced by strong spin-orbit interaction. *Comptes Rendus. Physique*, 22(S4):145–162, Mar. 2022. ISSN 1878-1535. doi: 10.5802/crphys.93.

D. F. Walls and G. J. Milburn. *Quantum Optics*. Springer, Berlin, 2nd ed edition, 2008. ISBN 978-3-540-28573-1.

C. Wang, Y. Y. Gao, I. M. Pop, U. Vool, C. Axline, T. Brecht, R. W. Heeres, L. Frunzio, M. H. Devoret, G. Catelani, L. I. Glazman, and R. J. Schoelkopf. Measurement and control of quasiparticle dynamics in a superconducting qubit. *Nature Communications*, 5(1):5836, Dec. 2014. ISSN 2041-1723. doi: 10.1038/ncomms6836.

G. Wang, T. Dvir, G. P. Mazur, C.-X. Liu, and N. van Loo. Singlet and triplet Cooper pair splitting in superconducting-semiconducting hybrid nanowires, 2022.

G. Wendin. Quantum information processing with superconducting circuits: A review. *Reports on Progress in Physics*, 80(10):106001, Sept. 2017. ISSN 0034-4885. doi: 10.1088/1361-6633/aa7e1a.

J. Wenner, Y. Yin, E. Lucero, R. Barends, Y. Chen, B. Chiaro, J. Kelly, M. Lenander, M. Mariantoni, A. Megrant, C. Neill, P. J. J. O'Malley, D. Sank, A. Vainsencher, H. Wang, T. C. White, A. N. Cleland, and J. M. Martinis. Excitation of Superconducting Qubits from Hot Nonequilibrium Quasiparticles. *Physical Review Letters*, 110(15):150502, Apr. 2013. ISSN 0031-9007, 1079-7114. doi: 10.1103/PhysRevLett.110.150502.

J. J. Wesdorp, L. Grünhaupt, A. Vaartjes, M. Pita-Vidal, A. Bargerbos, L. J. Splitthoff, P. Krogstrup, B. van Heck, and G. de Lange. Dynamical Polarization of the Fermion Parity in a Nanowire Josephson Junction. *Physical Review Letters*, 131(11):117001, Sept. 2023. doi: 10.1103/PhysRevLett.131.117001.

J. J. Wesdorp, F. J. Matute-Cañadas, A. Vaartjes, L. Grünhaupt, T. Laeven, S. Roelofs, L. J. Splitthoff, M. Pita-Vidal, A. Bargerbos, D. J. Van Woerkom, P. Krogstrup, L. P. Kouwenhoven, C. K. Andersen, A. L. Yeyati, B. Van Heck, and G. De Lange. Microwave spectroscopy of interacting Andreev spins. *Physical Review B*, 109(4):045302, Jan. 2024. ISSN 2469-9950, 2469-9969. doi: 10.1103/PhysRevB.109.045302.

G. W. Winkler, A. E. Antipov, B. van Heck, A. A. Soluyanov, L. I. Glazman, M. Wimmer, and R. M. Lutchyn. A unified numerical approach to semiconductor-superconductor heterostructures. *Physical Review B*, 99(24):245408, June 2019. ISSN 2469-9950, 2469-9969. doi: 10.1103/PhysRevB.99.245408.

F. Yan, P. Krantz, Y. Sung, M. Kjaergaard, D. L. Campbell, T. P. Orlando, S. Gustavsson, and W. D. Oliver. Tunable Coupling Scheme for Implementing High-Fidelity Two-Qubit Gates. *Physical Review Applied*, 10(5):054062, Nov. 2018. ISSN 2331-7019. doi: 10.1103/PhysRevApplied.10.054062.

G. Yang, C. Ciccarelli, and J. W. A. Robinson. Boosting spintronics with superconductivity. *APL Materials*, 9(5):050703, May 2021. ISSN 2166-532X. doi: 10.1063/5.0048904.

T. Yokoyama, M. Eto, and Y. V. Nazarov. Josephson Current through Semiconductor Nanowire with Spin-Orbit Interaction in Magnetic Field. *Journal of the Physical Society of Japan*, 82(5):054703, May 2013. ISSN 0031-9015, 1347-4073. doi: 10.7566/JPSJ.82.054703.

T. Yokoyama, M. Eto, and Y. V. Nazarov. Anomalous Josephson effect induced by spin-orbit interaction and Zeeman effect in semiconductor nanowires. *Physical Review B*, 89(19):195407, May 2014. ISSN 1098-0121, 1550-235X. doi: 10.1103/PhysRevB.89.195407.

C. X. Yu, S. Zihlmann, J. C. Abadillo-Uriel, V. P. Michal, N. Rambal, H. Niebojewski, T. Bedecarrats, M. Vinet, É. Dumur, M. Filippone, B. Bertrand, S. De Franceschi, Y.-M. Niquet, and R. Maurand. Strong coupling between a photon and a hole spin in silicon. *Nature Nanotechnology*, Mar. 2023. doi: 10.1038/s41565-023-01332-3.

A. Zazunov, V. S. Shumeiko, E. N. Bratus', J. Lantz, and G. Wendin. Andreev Level Qubit. *Physical Review Letters*, 90(8):087003, Feb. 2003. ISSN 0031-9007, 1079-7114. doi: 10.1103/PhysRevLett.90.087003.

A. Zazunov, V. S. Shumeiko, G. Wendin, and E. N. Bratus'. Dynamics and phonon-induced decoherence of Andreev level qubit. *Physical Review B*, 71(21):214505, June 2005. doi: 10.1103/PhysRevB.71.214505.

A. Zazunov, R. Egger, T. Jonckheere, and T. Martin. Anomalous Josephson current through a spin-orbit coupled quantum dot. *Physical Review Letters*, 103(14):147004, Oct. 2009. ISSN 0031-9007, 1079-7114. doi: 10.1103/PhysRevLett.103.147004.

M. Zgirski, L. Bretheau, Q. Le Masne, H. Pothier, D. Esteve, and C. Urbina. Evidence for Long-Lived Quasiparticles Trapped in Superconducting Point Contacts. *Physical Review Letters*, 106(25):257003, June 2011. ISSN 0031-9007, 1079-7114. doi: 10.1103/PhysRevLett.106.257003.

S. Zihlmann, A. W. Cummings, J. H. Garcia, M. Kedves, K. Watanabe, T. Taniguchi, C. Schönenberger, and P. Makk. Large spin relaxation anisotropy and valley-Zeeman spin-orbit coupling in WSe 2 /graphene/ h -BN heterostructures. *Physical Review B*, 97(7):075434, Feb. 2018. ISSN 2469-9950, 2469-9969. doi: 10.1103/PhysRevB.97.075434.

K. Zuo, V. Mourik, D. B. Szombati, B. Nijholt, D. J. van Woerkom, A. Geresdi, J. Chen, V. P. Ostroukh, A. R. Akhmerov, S. R. Plissard, D. Car, E. P. A. M. Bakkers, D. I. Pikulin, L. P. Kouwenhoven, and S. M. Frolov. Supercurrent Interference in Few-Mode Nanowire Josephson Junctions. *Physical Review Letters*, 119(18):187704, Nov. 2017. ISSN 0031-9007, 1079-7114. doi: 10.1103/PhysRevLett.119.187704.

Curriculum Vitæ

Jaap Joachim Wesdorp

25-03-1993	Born in Columbia, United States of America
2005-2011	Pre-university education C.S.G Calvijn, Rotterdam, The Netherlands
2011-2015	B.Sc. Applied Physics, B.Sc. Applied Mathematics Delft University of Technology, The Netherlands
Thesis subject	*A Real-Time Adaptive Sampling Algorithm and its Application in Quantum Transport Measurements*
Thesis supervisors	Prof. dr. A. Akhmerov, Dr. M. Cassidy, Dr. V. Guerra Ones
2015-2018	M.Sc. Applied Physics Delft University of Technology, The Netherlands
Thesis subject	*Generating chip-to-chip entanglement by measurement with transmon qubits using engineered driving fields*
Thesis supervisors	Prof. dr. L. Dicarlo, Dr. C. Dickel
2018-2023	PhD Applied Physics Qutech, Delft University of Technology, The Netherlands
Thesis subject	*Spinful Andreev States in Superconducting Circuits*
Promotor	Prof. dr. ir. L.P. Kouwenhoven, Delft University of Technology
Copromotor	Dr. C.K. Andersen, Delft University of Technology

List of Publications

📄 Included in this thesis.
* Equal contributors

📄 12. **J. J. Wesdorp**, P. A. Rot, N. van Loo, A. Vaartjes, M. Pita-Vidal, L. J. Splitthoff, A. Bargerbos, J. C. Wolff, G. P. Mazur, L. P. Kouwenhoven, and C. K. Andersen, *Andreev bound states in InSb-Al nanowire Josephson junctions defined using shadow-wall lithography in a circuit-QED architecture*, In preparation (2024)

11. M. Pita-Vidal, **J. J. Wesdorp**, and C. K. Andersen, *Blueprint for all-to-all connected superconducting spin qubits*, In preparation (2024)

📄 10. M. Pita-Vidal*, **J. J. Wesdorp***, L. J. Splitthoff, A. Bargerbos, Y. Liu, L. P. Kouwenhoven, C. K. Andersen, *Strong tunable coupling between two distant superconducting spin qubits*, arXiv preprint arXiv:2307.15654 (2023), accepted for publication in Nature Physics (2024)

9. L. J. Splitthoff, **J. J. Wesdorp**, M. Pita-Vidal, A. Bargerbos, Y. Liu, and C. K. Andersen, *A gate-tunable kinetic inductance parametric amplifier*, Physical Review Applied **21**, 014052 (2024)

8. M. Pita-Vidal*, A. Bargerbos*, R. Žitko, L. J. Splitthoff, L. Grünhaupt, **J. J. Wesdorp**, Y. Liu, L. P. Kouwenhoven, R. Aguado, B. van Heck, A. Kou and C. K. Andersen, *Direct manipulation of a superconducting spin qubit strongly coupled to a transmon qubit*, Nature Physics, **19**, 1110–1115 (2023)

7. A. Bargerbos*, M. Pita-Vidal*, R. Žitko, L. J. Splitthoff, L. Grünhaupt, **J. J. Wesdorp**, Y. Liu, L. P. Kouwenhoven, R. Aguado, C. K. Andersen, A. Kou, and B. van Heck, *Spectroscopy of Spin-Split Andreev Levels in a Quantum Dot with Superconducting Leads*, Physical Review Letterrs **131**, 09700 (2023)

📄 6. **J. J. Wesdorp**, F. J. Matute-Cañadas, A. Vaartjes, L. Grünhaupt, T. Laeven, S. Roelofs, L. J. Splitthoff, M. Pita-Vidal, A. Bargerbos, D.J. van Woerkom, P. Krogstrup, L.P. Kouwenhoven, C. K. Andersen, A. Levy Yeyati, B. van Heck, and G. De Lange, *Microwave spectroscopy of interacting Andreev spins*, Physical Review B **109**, 045302 (2024), *Editors suggestion.*

📄 5. **J.J. Wesdorp**, L. Grünhaupt, A. Vaartjes, , M. Pita-Vidal, A. Bargerbos, L. Splitthoff, P. Krogstrup, B. van Heck, and G. De Lange, *Dynamical polarization of the fermion parity in a nanowire Josephson junction*, Physical Review Letters **131**, 117001 (2023)

4. L. J. Splitthoff, A. Bargerbos, L. Grünhaupt, M. Pita-Vidal, **J. J. Wesdorp**, Y. Liu, A. Kou, C. K. Andersen, B. Van Heck, *Gate-tunable kinetic inductance in proximitized nanowires*, Physical Review Applied **18**, 024074 (2022)

3. A. Bargerbos, L. J. Splitthoff, M. Pita-Vidal, **J. J. Wesdorp**, Y. Liu, P. Krogstrup, L. P. Kouwenhoven, C. K. Andersen, and L. Grünhaupt, *Mitigation of Quasiparticle Loss in Superconducting Qubits by Phonon Scattering*, Physical Review Applied **19**, 024014 (2023)

2. A. Bargerbos*, M. Pita-Vidal*, J. Ávila, L. J. Splitthoff, L. Grünhaupt, **J. J. Wesdorp**, C. K. Andersen, Y. Liu, L. P. Kouwenhoven, R. Aguado, A. Kou, and B. Van Heck, *Singlet-doublet transitions of a quantum dot Josephson junction detected in a transmon circuit*, PRX Quantum **3**, 030311 (2022)

1. C. Dickel, **J.J. Wesdorp**, N.K. Langford, S Peiter, R. Sagastizabal, A. Bruno, B. Criger, F. Motzoi, L. DiCarlo *Chip-to-chip entanglement of transmon qubits using engineered measurement fields* Physical Review B, **97**, 064508 (2018).

Patent Applications

3 M.Pita-Vidal, **J.J. Wesdorp**, C.K. Andersen, *Scalable architecture for coupling Andreev spin qubits, and methods of manufacturing and operating such*, Patent Pending

2 M. Pita-vidal, A. Bargerbos, **J.J. Wesdorp**, C.K. Andersen *A gradiometric device and an array of such gradiometric devices*, Patent pending

1 G. de Lange, **J.J. Wesdorp** *Superconducting quantum interference devices and uses thereof*, Patent pending

Acknowledgments

Doing a PhD has been a humbling experience in many ways. Often a PhD is described as an individual achievement, and I used to value my independence in working. However, during this trajectory I found strong evidence that productivity is highest (and anxiety is lowest) when having at least one person to work closely on something with to share ideas and worries. In that sense, I was lucky to have many periods of working with others during my PhD.

Leo In the beginning of my PhD you were mostly a person I would ask for resources for new project plans. I still remember our first conversation on what I should do during my PhD and you told me, well if I would decide that, it would be boring! But preferably something that results in six nines. I think this reflects well your hands off management style. It was great that I could hire my master students to stay after their projects. Thank you for coming to the third floor during my fourth year occasionally, asking how I was doing when times were less easy. You have a good sense of people. I wish you all the best with the new Kitaev chain efforts. **Christian**, your patience and incredibly fast feedback was exactly what I needed when you became my copromotor. I'm still amazed how you could make an accurate master equation simulation of ASQASQ coupling during a quick afternoon tea break. Thank you for your great support in helping me get this thesis done, including detailed comments all the way until the last day, and creating such a happy group of people around you. **Gijs**, your deep knowledge of all microwave taught me the best basis I could wish for with RF experiments and design during the first years of my phd at the Microsoft lab. Rewiring fridges between Christmas and new year was a great ritual in the first years. I always enjoyed the hour long chats about Andreev bound states and chip designs with the analog version of you (I hope one day you shall master the art of digital communication). I look forward to having one more in-person chat about Andreev bound states with you as a committee member during my defense. Hopefully not our last! PS: the quasiparticles on the cover are purple! **Bernard**, you are the master of ABS. In the beginning you served as a go to point whenever me and Gijs got lost in Andreev reflection analogies. Later you proved a great support in writing the papers and general councelling how the academic world functions, I learned so much from that. It was amazing that you managed to keep supporting me with the simulations and writing, even though you changed jobs at least 2 years before we finally published the papers! If only there was an option for equal contributing last authors. All the best and happiness to your latest addition in the family. **Lukas G**, you did not have the easiest of post-docs with a group of PhD students "in-between" supervisors after split between MS and the TUD. Nevertheless, for that period you took it upon you to help us out, and your management skills made sure the dynamical polarization datasets got done within three weeks, just in time before the fridge warmed up. It's great to have gained a friend in the process and perhaps, preferably not too often, we can repeat that good-conversation-5am-cigar once in while. I don't want you cycling off in Delft again. **Tom Dvir**, your can-do attitude,

dry humor and open conversations about physics definitely brought some fun to my PhD. Although we thought the results of the SAG multiterminal Josephson junctions were not "quantum enough" to publish, as the 3-terminal I-V diagrams were explained by a classical RCSJ model made by Gijs, recent literature seems to suggest otherwise!

CQED team Thanks for taking me in when I was a lone ABS-er after the SAG era. I think we had a great time, drinks and adventures, and a lot of output!
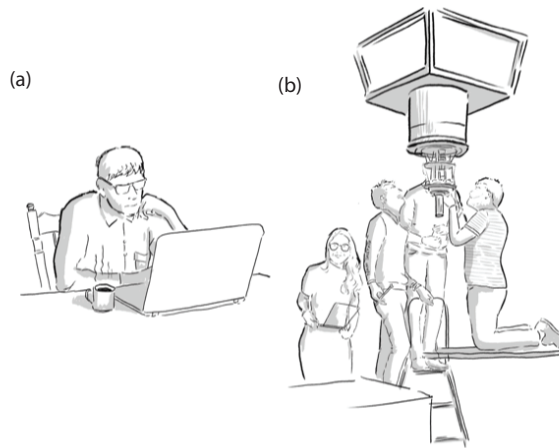

Figure A.1: Proximity effect of CQED team on one of its members. (a) before contacting (b) after contacting

Marta, although you started your PhD later, you were already around forever when I started somehow. It was a great experience to join forces on the final project with you on ASQx2. From our discussions about life and research, although you always thought they were too long, to your rapid matplotlib wizardry to compensate for it. I'm still impressed by your (from my point of view) lack of overthinking, which helped push the projects super fast. It was a lot of fun to do the job hunting and conference touring last year, meeting so many other groups and people, and that really felt like the cherry on our PhDs. PS: now that you have your first tattoo, there is no escape and your road is set to become "that cool professor", like the one from Singapore. PPS: Thanks again for proofreading my last minute sections of this thesis. All the best to you and **Hugo** in Zurich. And **Hugo** have fun picking out cars! Drive to finland one day. **Arno**, you have a great passion for science and that will no doubt pay off! arXiv must think you are a scraper-bot. I've learned the hard way not make $100 bets with you, which I am 100% confident to win, under the influence of green beers... Nice that we will be in the same field going forward! **Lukas**, you have a knack for living through strange experiences and telling stories about it. Your passion for extreme sports is commentable. Thinking about that happy post of your holiday "eating spaghetti in the rain on a swedish graveyard after a 230km bicycle ride with 5bft headwind" still makes me chuckle. I hope you visit Finland in the near future so we can make such a post together. **Willemijn**, You were one of the original CQED teamers. Nice that you are back around so we can have more CQEDrinks. Fun to hear we both share happy memories from a time in Colombia. **Guanzhong**, starting in the SAG team, you taught me (and Gijs?) DC transport methods. Your persistence,

after such a tough period with the retractions, towards the Kitaev effort is commendable. Let's have more no-bullshit discussions about physics soon. **Di** It's been great chatting with you on the third floor. I hope you finish those youtube series on how to pronounce Chinese one day. All the best with your postdoc, and perhaps we can eat Japanese food in Delft again someday. **Lin**, somehow when we started discussing life and politics it always quickly turned into a 3 hour long conversation. It was never boring. You gave me a unique view on another world and best of luck with wrapping up your phd, you deserve it! **Qingzhen** my favourite accross the street neighbour, karaoke one day? Good talks on the bike between our houses! Good luck finishing your phd and with the next steps. Thanks for sharing the secret Al etching recipe to our success. **Michael Chan**, TA-ing as an experimentalist for advanced quantum mechanics sounds crazy, but you made it sound easy. Good luck in the Veldhorst lab! **Tom Laeven**, thank you for helping me out with the ABS simulations, even after all the double work we had to do switching from the Microsoft QMS platform to pure Kwant. Your, and Bas Nijholts, code is still used in this theory section.

I've had the pleasure of (co-)guiding several students during this PhD, without whom there would be a lot less results! **Sebastiaan**, you were my first student during your bachelors. I hope I wasn't too harsh. You did great work simulating the ABS devices and resonators. It's good to see that you are now doing a PhD in our group! Let's compare notetaking software once more soon. **GijsB**, I co-supervised you with Tom on the SAG multiterminal project of my first year proposal. Covid and the distance between Delft and Eindhoven did not make for an easy project at all times. I think you must have made at least 8 iterations of the MTT chip design before we finally managed to get a working Al contact to the InSb. In the end your thesis is super complete and if I had more time it would definitely have become a chapter in this thesis. For now I hope people can simply read yours. Great to hear you are thinking of doing a PhD now. **Arjen**, the OG master student on the InAs ABS spectroscopy project. Thanks for staying on as a paid employee afterwards. What a huge amount of data to comb through. I defended your grade with pleasure and it's nice that the waiting for your Australian VISA paid off so you are now doing your PhD in UNSW. You always had that surfer's vibe going... **Pepijn**, you followed after Arjen and joined the challenge of the InSb spectroscopy project. Thanks for staying on afterwards in our attempt to measure coherent ABS in InSb. Is it a Rabi?? You must have been the most socially adept student I had, reflected in your double masters of Management of Technology. I believe you found a place to climb mountains now with your boyfriend, best of luck there!

Alfredo, thank you for the theory support on the ABS paper together with **Francisco**. The calls with you and **Bernard** were always a treasure of free information for me, and **Nico** thanks for spending the time modeling the dynamical parity polarization, it felt like a real taste of how the academic process functions. **Francisco** It's been great getting to know you also outside work, and I have no doubt you'll do great in your PhD. **Ramón**, good luck with getting your secret spanish network to dominate quantum and thanks for the Madrid visit and exchange of ideas **Eduardo, Angel, Nacho, Gorm**.

Greg and Nick thank you for being my go to guys for a pessimistic review of the latest majorana papers. Good luck with your own corner of QuRe now. And with **Jan Cornelis** all the work for the InSb paper. **Vukan**, Aii mamasita! we started together, your im-

attested to incredible foresight. **Giorgos** it was great to see someone so interested in the ASQASQ work, thanks for making HQT fun and I hope you guys succeed in the next steps of your project with Giorgo "measuring a shitty transmon" like we did. **Les houches party people**, as the name suggest, it was a great month and it seems like forever ago, let's see how long our reunions last! **Ferdinand, Andreas, Patrick** Thanks for letting me visit your labs as a candidate, it was a great experience. **People in Espoo** Thanks for showing me in 3 months of more qubits than I could have dreamed of in my PhD.

Also I would like to acknowledge those I met the Microsoft lab, where I spend my first years and learned the basics. **Davidvw**, AKA the cleanroom pirate. You taught me a lot on "how to cleanroom" and made sure the ABS device was designed such that the nanowire and gate part would work. Your humor though... **Amrita** your cleanroom skills are unparalleled thanks for sharing some of that with me. I always enjoyed our chats. **Elvedin** I still believe your laugh (mostly about your own joke) ruined my SAG AFM measurements. **Angela and Wolfgang**, you seemed like the perfect professor couple to me, great that you got a position in Urbana-Champaign and thanks for letting us visit there. I'm still embarassed by the ill-prepared explanation of the Kitaev chain I ended up presenting to your students. **Pavel, Frenk, Luca, Philippe, Lieuwe, Daan, Jonne** I have some good memories of the SAG days, even though they never made it in the thesis. **John** You alway knew how something should be done properly. Thanks for helping me with the US VISA lawyer. **Lydia**, thanks for always being kind even if I sneaked Gijs' parents into the top secret lab for a tour without telling you.

Also without the support of the **cleanroom staff**, nothing of this phd would have been fabricated. **Eugene**, nice to be the second Wesdorp you met. **Anja, Marco, Charles/Chuck, Pauline, Mark, Arnold, Bas and others** thanks!

Naast collegas zijn er ook veel oude vrienden die op hun eigen manier hebben bijgedragen aan de thesis, bedankt! **Royaal (en partners)**, het doorzettingsvermogen in de boot heeft zeker bijgedragen aan deze PhD. Ik ben erg dankbaar dat we al zo lang goede vrienden zijn samen. Binnenkort maar eens een lustrumreis naar Finland plannen! **Janneke** Leuk dat we nog steeds contact hebben! Wie plant het volgende jaarlijks weekend? **Bodemdrift**, Filmavond? **Mark** Bedankt voor mijn paranymph te zijn! Fijn dat ik jou als klankbord voor mijn leven kon gebruiken over de lange telefoongesprekken. Geen zorgen, komt goed die promotie!

Verder wil ook graag mijn **familie** bedanken. In het bijzonder, **Mama en Papa**, bedankt voor alle steun, liefde en raad en daad, ik denk dat het zaadje voor kritisch onderzoek is gelegd bij het discussieren dat was aangeleerd aan de eettafel. **Kees, Hielke**, thanks bros, en hoop dat we de gewoonte leren met elkaar te bellen binnenkort! Tot die tijd: Potje Starcraft? **Dorinda**, erg leuk dat we dezelfde rol in de relatie lijken als financieel beheerders, binnenkort maar eens strategieën overleggen? **Dorinda, Kees en Auke** veel geluk samen in jullie nieuwe huis. Hopelijk komt oom vaak op bezoek! **Lars, birgit en Naline, Ed en Judith, Henk**, ik heb me altijd erg welkom gevoeld bij jullie en **Mirjam, Dick, Loes, Bart** fijn dat we altijd welkom waren om lekker indonesich te eten. Ten slot, **Ilse**, jouw kern blijft een mysterie voor ons beiden, maar jouw liefde, kinderlijke vreugde en wijsheid heeft zijn plek gevonden in het centrum van mijn bestaan. Ik kijk uit naar de toekomst.